NASA/CR—1999-209164/VOL1

Stirling Space Engine Program
Volume 1—Final Report

Manmohan Dhar
Mechanical Technology Inc., Latham, New York

Prepared under Contract NAS3–25463

National Aeronautics and
Space Administration

Glenn Research Center

August 1999

Note that at the time of printing, the NASA Lewis Research Center was undergoing a name change to the NASA John H. Glenn Research Center at Lewis Field. Both names appear in these proceedings.

Available from

NASA Center for Aerospace Information
7121 Standard Drive
Hanover, MD 21076
Price Code: A10

National Technical Information Service
5285 Port Royal Road
Springfield, VA 22100
Price Code: A10

TABLE OF CONTENTS

SECTION **PAGE**

Volume I

TABLE OF CONTENTS (continued)

TABLE OF CONTENTS (continued)

SECTION **PAGE**

Volume II

TABLE OF CONTENTS (continued)

LIST OF FIGURES

LIST OF FIGURES (continued)

LIST OF FIGURES (continued)

LIST OF TABLES

1.0 SUMMARY

This report describes work performed by Mechanical Technology Incorporated (MTI) under NASA Contract NAS3-25463, "Stirling Space Engine (SSE) Program." The work was performed from August 1988 through September 1993. The objective of the SSE program was to develop the technology necessary for operating Stirling power converters in a space environment and to demonstrate this technology in full-scale engine test. The program required the design of a "paper" reference engine, the Reference Stirling Space Power Converter (RSSPC), and two experimental hardware engines: the Component Test Power Converter (CTPC) and the Stirling Space Power Converter (SSPC). The program concluded before the SSPC was built due to termination of the SP100 program funding.

At any particular time during the program, the RSSPC represented the best-known design approach for meeting the program objectives, which were:

- Power module net efficiency greater than 25%
- Power module specific mass less than 6.0 kg/kWe
- Operating life more than 60,000 hr
- 200 start-stop cycles
- Bilevel power control (80% and 100% power).

The final design configuration selected for the RSSPC was a stepped-bore arrangement with the displacer and power piston supported on internally pumped hydrostatic gas bearings. A two cylinder, linearly opposed arrangement was selected to meet the low vibration requirement without the weight penalty of an active vibration absorber. A sketch of one-half of the RSSPC power module is shown in Figure 1. In the full engine configuration, the two power module halves are connected at their hot end to produce a linearly opposed arrangement with a common expansion space.

To minimize the power module specific weight, the working fluid pressure and the operating frequency needed to be made as high as possible. The RSSPC uses helium at 150-bar mean pressure as the working fluid. The selection of 150-bar mean pressure was constrained by the requirement of adequate creep strength of high-temperature superalloy materials. The operating frequency was selected as 70 Hz, based on balancing the conflicting requirements of high thermodynamic efficiency (low frequency) and low alternator weight (high frequency). Table 1 summarizes the operating parameters of the RSSPC. Figure 2 shows the RSSPC power flow diagram for the total engine. The overall engine performance is summarized in Table 2.

The major challenge in the RSSPC design was proper mechanical operation of the power-module cold-end reciprocating elements (displacer and power piston assemblies) at the elevated temperature of 525 K. Dynamic operation of each unit at this temperature was a challenge since thermal growth and thermal distortions of moving and stationary parts and misalignment could, if not carefully controlled, reduce already tight seal clearances and cause the free pistons to bind. In this regard, the displacer and power piston assemblies were designed to maintain their clearances at the elevated temperature.

Due to the high temperature levels of both the hot side and cold side of the machine, significant component, material, and manufacturing development was required in addition to the customary design and analysis. Highlights of these activities follow:

- Initial power operation tests with the CTPC were performed using slot radiant heaters to transfer heat into the engine. With the hot-side temperature between 800 and 950 K, an output power of 12.5 kW was achieved at a temperature ratio of approximately 2 and an input power of approximately 60 kW.
- The Starfish heater head was a new approach to Stirling engine heater design. The two critical steps were the precise machining of 50 radial pockets into a solid ring of Inconel 718 followed by the machining of almost 2000, 40-mil-diameter holes, 2 in. through the 0.150-in.-thick wall between the pockets. Positional tolerances on the hole position were very tight since the edge of the holes was about 30 mil from the surface. This was accomplished successfully using a shaped-tube electrochemical milling process.

Table 1. Operating Parameters of RSSPC

Working fluid	Helium
Mean pressure, MPa	15
Frequency, Hz	73
Heater metal gas side temperature, K	1.05E+03
Cooler metal gas side temperature, K	5.25E+02
Displacer amplitude, mm	16
Piston amplitude, mm	14
Displacer/power piston phase, degrees	65

Table 2. Overall Performance of RSSPC

Power, kW	**Value**
Heater heat flux rate	95.2
Thermodynamic power	31.2
Alternator plunger shaft power	28.8
Net electrical power	25.4
Efficiency	
Carnot efficiency	0.5
Thermodynamic efficiency (fraction Carnot)	0.658
Mechanical efficiency	0.92
Electrical efficiency	0.88
System efficiency	0.27

97TR21

- The alternator must operate in a helium environment of about 275°C, which is above the temperature capability of most standard insulating materials. The temperature level is close to the upper bound for the best organic materials but well below the level at which glass or ceramics can operate. An important requirement was that small hard particles with the potential for degrading the close clearance seals be avoided. Polyimide coated wire with polyimide adhesive between turns and a polyimide impregnated fiberglass overwrap was selected for the CTPC.
- The magnet design temperature of 275°C was near the upper bound of practical application for the best rare earth magnets. Samarium cobalt (Sm2Co17) magnets were used. Based on sample tests, a very stringent specification was developed. Coupled with the high temperature acceptance testing, this specification resulted in magnets with adequate strength and demagnetization resistance at 275°C.
- The CTPC was designed with internally charged hydrostatic gas bearings that become activated when the piston and the displacer strokes are equal or at more than half of the design point stroke. Therefore, during start-up, the reciprocating members are in dry contact (it takes seven cycles, one-tenth of a second, of displacer and piston motion to fully charge the bearings). To select appropriate wear couple surfaces, friction and wear tests were performed on various surfaces at the CTPC cold-end operating temperature. Based on these tests, carbon graphite and aluminum oxide were selected for the mating reciprocating surfaces. The carbon graphite sleeves were installed as a shrink fit in cylinder bores and then machined to final dimensions. The aluminum oxide was plasma sprayed to the outer surface of the reciprocating pistons and then ground to finish dimensions. This wear couple combination worked very well on the motoring and engine tests performed. Some rework had to be performed due to an inadequate shrink fit but no other operational problems occurred.

- Udimet 700 (or variants: 720 and 720LI) was the material of choice to meet the long life requirement of the heater head at 1050 K. While Udimet material and fabrication development was in process, Inconel 718 was selected for the CTPC. Since 1050 K is above the normal working range for Inconel 718, various creep and other development tests were conducted to verify the design and provide a basis for setting operation limits during subsequent engine testing. Sodium compatibility issues were experimentally addressed. Heat treatment and sodium processing temperature cycles were worked out.
- Heat pipe development was conducted primarily at Thermacore with support by ETEC for sodium filling. A one-tenth segment was built and tested. The thermal performance of the concept was verified, and various processing procedures developed. The CTPC heat pipe heater head performed without problems.
- Testing with the heat pipe heater head was a success, demonstrating a power level of 12.5 kWe and an overall efficiency of 22% in the very first maiden test. These successful results indicate the value of the work performed in this program to demonstrate the viability of Stirling engine technology for space applications.
- The CTPC was subjected to a 1500-hour endurance test to demonstrate the long-term operating characteristics of the CTPC gas-bearing FPSE power converter and to establish a reliability database for FPSE linear alternator machinery. During this test, the CTPC operated in an unattended, stand-alone mode with no significant problems. The test was stopped three times to replace an O-ring that failed due to overheating/fatigue. Since the O-rings are only used to facilitate laboratory testing, it was not considered a problem for flight hardware. Aside from the influence of the O-ring failures, the CTPC performance was steady with no significant degradation. The demonstration of consistent performance under automatic control was a major advance in FPSE linear alternator technology.

Volume I of this report, contained herein, documents the work performed during the SSE Program, with a focus on the CTPC. Volume II, bound separately, presents additional detail on three key technology development areas: the heater head (Appendix A), CTPC component development (Appendix B), and Udimet testing (Appendix C). Photographs of CTPC hardware are presented in Appendix D.

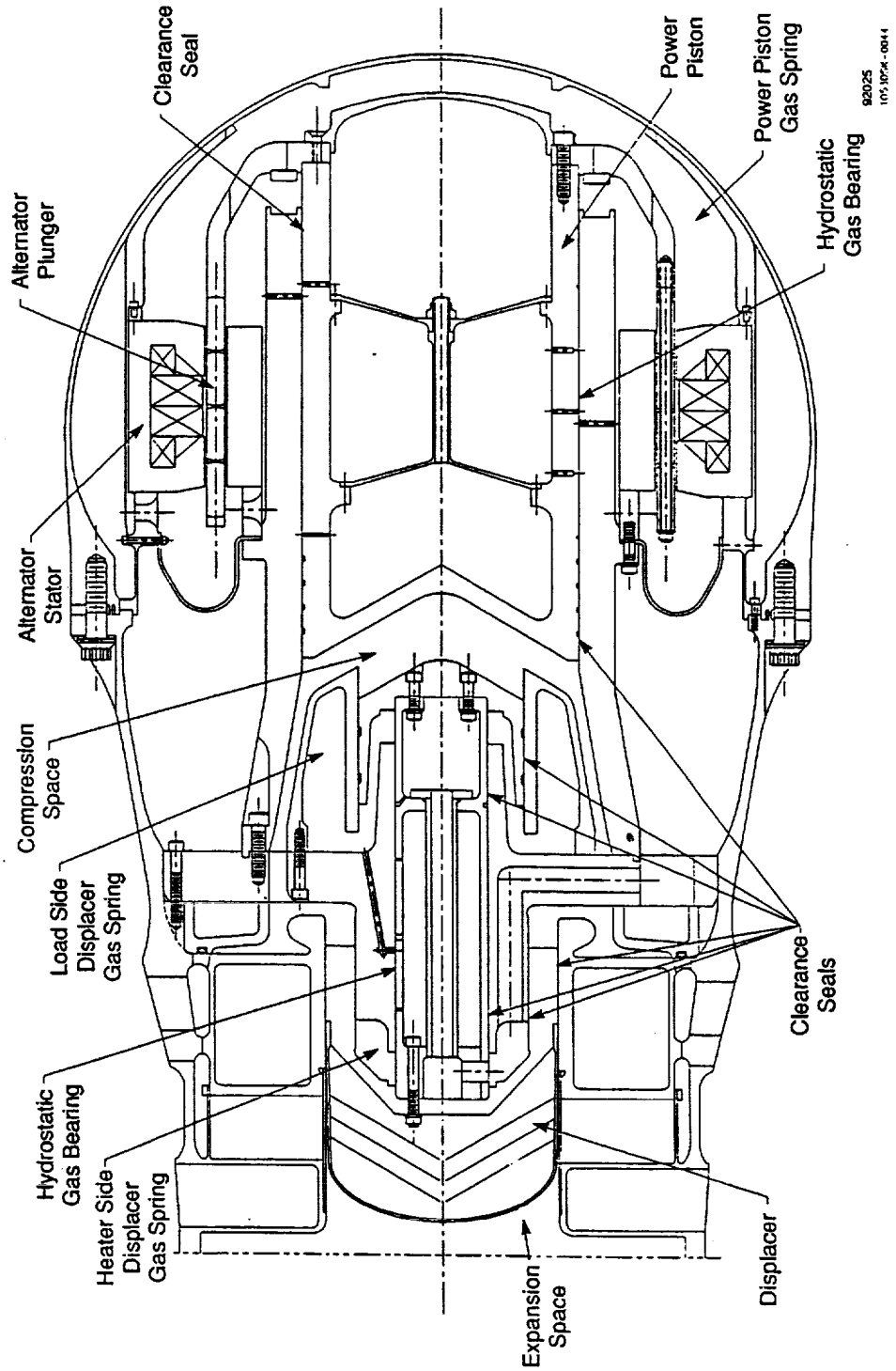

Figure 1. One-half of RSSPC Power Module

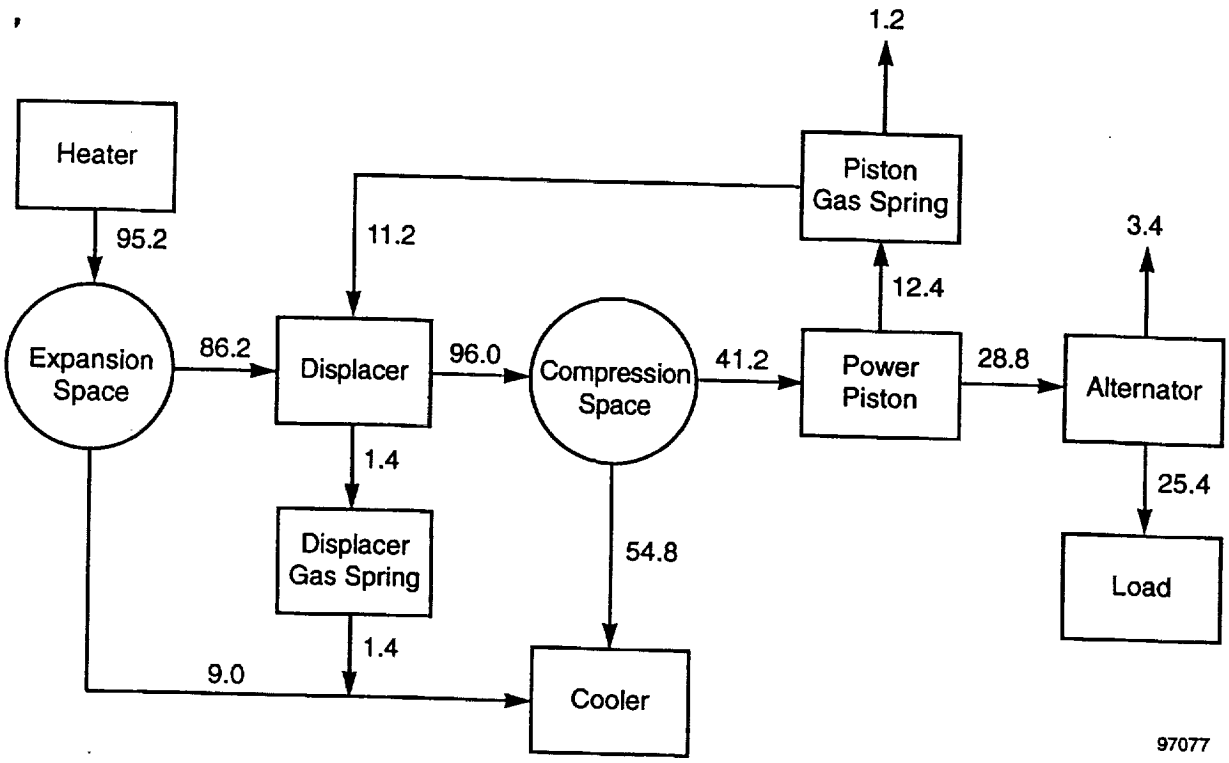

Figure 2. RSSPC Power Flow Diagram (kW)

2.0 BACKGROUND AND INTRODUCTION

2.1 Background

Free-Piston Stirling Engines (FPSE) have the potential to meet future space power requirements of high reliability, long life, and efficient operation for a wide variety of applications with less mass, better efficiency, and less total heat exchanger area (collector and radiator) than other power converter options. FPSEs can be coupled with many potential heat sources (solar, radioisotope, or nuclear reactor), various heat input systems (direct radiation or conduction, heat pipe, or pumped loop), various heat rejection systems (heat pipe or pumped loop), and various power management and distribution systems (ac, dc, and fixed or variable load).

Operation in space requires the FPSE to absorb heat from a high-temperature source and radiate unused heat to space via a radiator. Since the area of the radiator (and, therefore, its size and mass) is inversely proportional to the fourth power of the absolute temperature, the heat reject temperature for the space application optimizes, for a minimum specific mass, to a temperature much higher than the near ambient reject temperature for terrestrial systems. System studies along with material limitations establish the optimum source and reject temperatures. Based on various system studies for 100-kWe-class-size nuclear-reactor power systems, a heater head temperature of 1050 K and an engine temperature ratio of 2.0 have been established as a reference for superalloy Stirling engine power conversion systems (Dochat, 1991). Also based on these system studies, a heat pipe using a liquid metal working fluid has been identified as the appropriate approach to interface the power converter to a reactor heat source. For 1050 K operation, the thermodynamic properties of sodium make it the heat pipe fluid of choice. For the heat reject system, a liquid metal (NaK) pumped loop has been selected as the heat transport medium from the power converter to the radiator.

The National Aeronautics and Space Administration (NASA) Lewis Research Center (LeRC) has the responsibility to evaluate and develop power technologies that can satisfy anticipated future space mission power requirements. NASA awarded Mechanical Technology Incorporated (MTI) a contract in 1984 to demonstrate, within 18 months after program initiation, that a permanent magnet linear alternator directly coupled to an FPSE is a technology with the potential to meet the requirements of a space power generating system. This time constraint was imposed by the power converter selection decision process in the SP100 program.

The resulting Space Power Demonstrator Engine (SPDE) was operating 16 months after program initiation (Dhar, et al., 1987). The SPDE operated at a temperature ratio of 2.0, but at lower absolute temperature levels (650 K at the heater head and 325 K at the cooler) to reduce development time and cost. Note that the power density and efficiency of a Stirling cycle machine, to the first order, depend only on heat exchanger temperature ratio and are independent of the absolute temperature levels. The SPDE utilized an electrically heated molten salt loop as a heat source and a conventional water/glycol loop as a heat sink. To minimize casing vibration, it was designed in a two cylinder, linearly balanced opposed configuration, consisting of two 12.5 kWe modules connected at the hot end with a common expansion space.

In October 1986, the SPDE developed 25 kW of engine PV power. Measured vibration level of the SPDE casing was less than 1 mil peak-to-peak. Following successful demonstration, the SPDE was cut in half to create two 12.5 kWe power converters (designated Space Power Research Engines (SPRE)) to permit complementary testing to proceed at both NASA-LeRC and MTI. These engines were attached to a large inertial mass to limit the vibration associated with a single cylinder arrangement. The SPREs have served as test beds for evaluating key technology areas and components.

2.2 Stirling Space Technology Program Objectives and Approach

Based on the success of the SPDE and review of a subsequent proposal under a competitive procurement, NASA awarded MTI a multiyear Stirling Space Engine (SSE) program. The objective was to develop Stirling technology for space power applications and to demonstrate this technology in a full-scale power converter test by the end of 1994.

The program approach, as specified by the contract, was as follows:

1. Perform an assessment of technologies required to meet the goals of the Reference Stirling Space Power Converter (RSSPC) design. The RSSPC is a "paper engine" design that, at any particular time during the program, represents the best known approach for meeting the program objectives. The design goals established for the RSSPC were:
    - Output power: up to 25 kWe per cylinder
    - Efficiency: 25% (electrical power out/heat into heater head)
    - Heater wall temperature: 1050 K
    - Cooler wall temperature: 525 K
    - Specific mass: 6 kg/kW or less.
    - Design life: 60,000 hours of unattended operation with the power module capable of sustaining at least 200 start-stop cycles.
2. Select the reference design configuration and identify component technology needs to support the design and fabrication of Stirling space engines.
3. Perform component development, and in parallel, based on the selected reference design configuration, design and fabricate an experimental engine designated as the Component Test Power Converter (CTPC). The CTPC should allow easy assembly and disassembly, component modification, and instrumentation access.
4. Based on what is learned from testing of the CTPC, design, fabricate, and test the final experimental engine, the Stirling Space Power Converter (SSPC), to demonstrate the end program goals. With a change in focus and priority for space power requirements within the U.S. government and at NASA headquarters, the funding level on the SSE program was reduced in FY93 and suspended in FY94. Therefore, funds were not available to fabricate the SSPC.

2.3 Power Module Technology Assessment

The major changes in the design requirements for the CTPC from the SPDE were: 1) integration of a heat pipe to the hot end of the engine and operation of the hot end at 1050 K, and 2) the operation of cold end at 525 K. To avoid the high cost and facility complexity associated with handling a large inventory of liquid metal, a pumped loop using mineral oil (paratherm) and a conventional forced air 'radiator' was selected for the experimental CTPC and SSPC.

Requirement 1 primarily impacts the engine heat exchanger design, and requirement 2 impacts the design of the displacer, the power piston drive assemblies, and the linear alternator.

2.3.1 Engine Heat Exchanger Configuration

The SPDE heater and cooler were a tube-and-shell arrangement. Each contained over 1000 tubes brazed at each end into a tube sheet. These heat exchangers performed well, but, for space application, were judged to have inadequate reliability with such a large number of joints.

The heat exchanger assembly is the thermodynamic heart of the engine, where the conversion of thermal power to pneumatic power occurs. It consists of the heat source and heat sink connections, and the heater, regenerator, and cooler. The critical design objective here is to integrate the heat pipes, the cooling system, and high performance thermodynamics into a low mass, reliable, long-life assembly. This task is complicated by the high temperature, large thermal gradient, high pressure, and long operating life requirements. The following power module concepts were considered in the technology assessment study. All of these concepts used sodium heat-pipe heat transport to the heater and NaK (sodium-potassium eutectic mixture) pumped loop heat rejection from the cooler. The main differences were in the heat exchanger configuration. The power piston and displacer drive assemblies were essentially the same for all and similar to the SPDE.

- The Conceptual Stirling Space engine (CSSE) featured modular heat exchangers (see Figure 3, provided by NASA-LeRC, as Appendix A to the Request For Quotation). In this design approach, the heat exchanger is divided into a number of smaller heat exchanger modules, called Thermal Power Modules (TPM) (Penswick, 1988). Each TPM is connected on either end to the engine expansion and compression spaces via ducts, and each accepts heat from and rejects heat to the engine heat source and heat sink, respectively. Each heater is fed by a separate heat pipe. The heater heat pipes are externally finned with the engine gas flowing between fins, parallel to the heat pipe axis. The regenerator is a full disk, and the cooler is similar to the heater, but with NaK flowing over the outside of the module. The advantage of the TPM design is that division of the assembly into smaller diameter modules reduces both the thermal stresses resulting from the regenerator wall temperature gradient and the wall stresses arising from the engine gas pressure. The disadvantage is the complexity of the resulting structure and the complexity and level of the stresses in the ducts that connect the module to the respective engine spaces. These ducts must be large enough to avoid excessive pumping losses, flexible enough to avoid excessive thermal stresses, and strong enough to withstand the engine pressure stresses.
- The modified thermal power module design (Figure 4) is similar to the CSSE design, but is modified by using separate ducts to the modules to reduce thermal stresses.
- The double-wall annular configuration with heat pipe thermal wells (Figure 5) uncouples the pressure vessel wall temperature gradient from the regenerator matrix gradient and allows the use of a large-enough wall diameter to package the engine in a single vessel without compromising regenerator length. The main advantages of this approach are:
  - Its simplicity from ducting, structural, and fabrication considerations.
  - It is relatively easy to provide a large frontal area for the regenerator. Since the regenerator is located in the annulus between the displacer and the pressure vessel, a small increase in the outer diameter results in a large area increase.
  - It is much easier to remove and install the cooler and regenerator in this design than in the other concepts.

  A disadvantage of this approach is that there is less cross-sectional area available for the heat pipe heater elements. It is more difficult to provide the optimum heater surface area without increasing the hot pressure vessel diameter, which has a negative impact on the power converter specific mass. In addition, there is the potential for a large thermal resistance between the heat pipe and the well. Due to the large number of pressure vessel penetrations for the heat pipes, significant structural reinforcement is required in the penetration zone, resulting in a relatively heavy heater head.
- The radial flow heat exchanger design (Figure 6) is an alternative version of the double-wall annular configuration. In this arrangement, the heater, regenerator, and cooler are located in concentric annuli outboard of the displacer dome. The working fluid flows radially through the heater, regenerator, and cooler; hence, the name radial flow heat exchanger. The radial flow heat exchangers are constructed with stacks of thin metal plates to form rectangular channels through which the engine working fluid flows. The plates act as fins to conduct heat between the heat source or sink and the engine working fluid. One advantage of this arrangement is that the hot pressurized structure is confined to a small central region about the axis at the hot end of the engine, thus confining the requirement of high creep strength material to this small region. An additional advantage is that the regenerator frontal area and the heater and cooler geometric requirements do not significantly affect the design of the hot pressurized structure.

These power converter designs were presented to NASA-LeRC at the Technology Assessment Review Meeting on October 12-13, 1988. The major findings presented were:

- Of the various power module configurations reviewed, the radial configuration has the highest performance (efficiency at a given specific power) and the modified thermal power module the lowest. The double-wall annular configuration has an intermediate performance level.

- The radial configuration has the highest risk and represents the greatest departure from previous experience. Despite its somewhat higher predicted performance, it was not selected as a preferred concept for the RSSPC.
- The risk and departure from previous experience of the modified thermal power module and the double-wall annular were judged to be similar and not excessive.
- The double-wall annular and the modified thermal power module are both viable configurations for the reference and the experimental Stirling space power converters.
- The double-wall annular is more convenient from assembly and disassembly considerations for the experimental power converter.

The following decisions were made at the Technology Assessment Review Meeting:

- A two-cylinder, balanced-opposed, double-wall annular concept with heat pipe thermal wells was selected as the RSSPC configuration. The power and efficiency goals for the RSSPC were set at 25 kWe per cylinder and 25%, respectively.
- Because of the limited program funds, the following decisions were made relative to the CTPC:
  - The power level was set at 12.5 kWe per cylinder.
  - Since the feasibility of controlling vibration by using a two-cylinder, balanced-opposed arrangement was clearly demonstrated on the SPDE, a single-cylinder arrangement mounted on an inertial mass was selected for the CTPC.
  - Since the design and fabrication of the CTPC and the component technology development were to be carried out in parallel, the efficiency goal for the CTPC was set at 20%.
  - For the SSPC heater head, the superalloy selected to meet the long life creep strength requirement is Udimet 720. Like other superalloys with very high creep strength at 1050 K, Udimet 720 is not readily joined to itself or other alloys. It is therefore necessary to minimize the joints required, and, where joints are unavoidable, make them of a simple geometry in a location that permits radiographic inspection.
  - Recognizing that an extensive material and manufacturing development program was needed to generate the design database for Udimet 720 (determine material properties and evaluate joining processes) before a detail design could be finalized, it was decided to make the initial heater head of Inconel 718, which would permit early demonstration of the CTPC power output and efficiency. Inconel 718 can meet all strength requirements except for long life creep strength. The CTPC, with an Inconel 718 heater head, can operate at 950 K for thousands of hours, at 1000 K for hundreds of hours, and at 1050 K for tens of hours.

Although the technology assessment concluded that the annular heat exchanger design with heat pipe thermal wells would yield adequate performance and was manufacturable, it was concluded early on in the CTPC preliminary design phase that all the required joints were not readily inspectable. The same conclusion was reached for the modified thermal power module concept.

To avoid the joint problems associated with all previous designs, approaches using a monolithic heater head with no hot-side pressure wall penetrations were considered. An initial concept used fins on the gas side of the cylindrical heater pressure vessel wall, but the effective heater gas side surface area was not adequate because of the insufficient wall perimeter at the base of the fins. To provide adequate heater surface area, the "starfish" heater head design, Figure 7, was developed. The main pressure vessel wall was moved into the displacer diameter, and radial fins were added outboard of this wall to introduce a larger heated perimeter. Sodium condenses on the external surface of these fins, which are covered with wicks for gravity-unassisted heat pipe operation. Small diameter heater passages are evenly spaced in the fin interior, with only a thin wall required between the gas passages and fin surface due to the low pressure stresses. Because there are no wall reinforcements needed for penetrations, the head weight is significantly less than that of the thermal well head. The joints required are limited to two butt joints in the cylindrical pressure vessel wall and two butt joints where the heat pipe is joined to the

heater head. Since the starfish heater is machined from a single piece of superalloy material, the reliability of the heater head is greatly improved.

2.3.2 Elevated Temperature Cold-End Operation

The critical concern for the CTPC was proper mechanical operation of the cold end at 525 K. Multikilowatt free-piston Stirling power converters rely on close-clearance, noncontacting seals and bearings for ultra-long life. The CTPC is the first power converter in which the cold-end hardware must operate from ambient to 525 K and maintain close clearances between the reciprocating pistons and stationary cylinders.

2.3.2.1 Surface Treatment for Reciprocating Mating Elements

Based on the operating experience with different surface treatments, chrome oxide was used for the SPDE and several other free-piston engines as the surface coating for the reciprocating mating elements. The CTPC had the same tight clearance requirements and also would operate at higher temperatures with the potential for thermal distortion affecting seal and bearing clearances. For this reason, early component technology development focused on proper, reliable mechanical operation at the elevated cooler temperature of 525 K (see Section 3.0).

Based upon tests in two wear couple rigs, carbon graphite and aluminum oxide were selected as the mating reciprocating surfaces. Plasma-sprayed aluminum oxide was selected as the outer surface for the reciprocating element and a shrink-fit carbon graphite sleeve for the stationary cylinder bore.

2.3.2.2 Gas Bearings

Proper gas bearings for FPSEs are essential for meeting the zero maintenance, extremely long life (greater than 60,000 hours), and high reliability demands of any space power application. Most of the experience with gas bearings for FPSEs has been with externally pumped hydrostatic gas bearings. Hydrostatic gas bearings operate effectively, provide excellent bearing stiffness, and are well understood. The development concern with hydrostatic bearings is the method of supplying the high pressure to the bearing orifices. The simplest method is to pump the bearings externally with a bearing pump. This bearing pump would require a design life similar to the engine and, therefore, would impose a reliability penalty. An elegant, straightforward method of supplying bearing pressure is to provide it internally via a ported compressor that "clips" a pressure wave in the engine, usually the piston gas spring pressure wave. This method has been successfully demonstrated on the SPDE. A disadvantage of this approach is that it requires high amplitude aft piston gas springs (≅7 to 9 bar) and additional internal hardware complexity. The high pressure amplitude in the aft piston gas spring results in high gas spring hysteresis losses. Hardware complexity results because of the drillings, drains, ports, and orifices required for the hydrostatic gas bearings.

At the start of the SSE Program, the prime approach to gas bearings was hydrodynamic because of the following perceived advantages:

- Hydrodynamic gas bearings can be "pumped" by a rotary electric motor and, therefore, do not require a large-pressure-amplitude gas spring.
- Hydrodynamic bearings eliminate the need for orifices and feed and drain grooves and, therefore, reduce the complexity associated with hydrostatic bearings.
- Hydrodynamic gas bearings can allow a longer clearance seal between the compression space and the piston gas spring for the same overall length as hydrostatic bearings.

Because of the above advantages and the potential to improve overall system efficiency, MTI modified the SPRE to test and evaluate a hydrodynamic gas bearing piston (Spelter and Dhar, 1989). The engine was modified to incorporate a spin motor, hydrodynamic power piston, and cylinder. Experience with hydrodynamic gas bearings on the SPRE provided a great deal of information including:

- Hydrodynamic bearings need to be isolated from pressure amplitudes acting across the bearing.
- Plain journal bearings, while operating at design stroke, exhibited half-speed whirl and some indications (visual inspection) of light rubs on the ends of the piston.
- Spiral groove bearings (herringbone grooves) provide improvement over plain journal bearings.

During the preliminary design phase of the CTPC, a number of advantages initially associated with hydrodynamic bearings were eroded in the implementation of the design. For example, the need to isolate the hydrodynamic bearing from the engine and gas spring pressure waves resulted in a significantly reduced piston seal length. Increase in piston mass because of the spin motor required higher gas spring pressure amplitude. Incorporation of the spin motor into the design became increasingly complex, offsetting some of the advantages over hydrostatic bearings.

Prior to the CTPC preliminary design review, the hydrodynamic concept was reevaluated, and it was decided to also design the CTPC with a hydrostatic bearing and directly compare the two bearing configurations. The CTPC power piston hydrostatic bearing configuration incorporated bearing charge and drain plenums ported to the piston gas spring pressure wave in a manner so as to supply the bearings at a pressure higher than engine mean pressure and drain the bearings at lower than engine mean pressure. This approach is unlike the SPDE where the bearings are drained to engine mean pressure. This allowed a reduction of the piston gas spring pressure amplitude to 5 bar, thus significantly reducing the gas spring hysteresis losses. The two gas bearing configurations (hydrostatic and hydrodynamic) were presented for NASA review at the preliminary design review meeting. These configurations are shown in Figures 8 and 9, respectively. Both configurations have similar performance (power and efficiency) and specific mass. There was no clear discriminator that would permit recommendation of one over the other. At the preliminary design review, it was recommended that since there was no clear design choice, Sundstrand Aerospace Mechanical Systems should evaluate both systems from a Failure Modes and Effects Analysis (FMEA) consideration to determine the best bearing system for the CTPC. MTI subcontracted Sundstrand to provide guidance on space power system integration. Based on Sundstrand's FMEA results, the hydrostatic bearing configuration was selected for the CTPC.

2.3.2.3 Alternator

The CTPC alternator is required to operate in a helium environment at a temperature of about 275°C (548 K). This temperature level is above the capability of most standard insulating materials. The temperature level is close to the upper bound for the best organic materials but well below the level at which glass or ceramics can operate. An important requirement for the CTPC is that small, hard particles with the potential for degrading the close clearance seals must be avoided. Since the CTPC design had to be performed with the available technology, polyimide-coated wire with polyimide adhesive between turns and a polyimide-impregnated fiberglass overwrap was selected for CTPC. This coil design has an expected life of hundreds of hours at the coil operating temperature of about 600 K, but there is uncertainty about operation for several years. It is expected that glass or ceramic construction will be required to meet the life requirements.

2.4 CTPC Development Strategy

The manufacturing of the finned section of the starfish heater head involves complex processes. Several alternative methods of machining the slots and flow passages were identified for evaluation. The time to develop these processes and apply them to the actual head was judged to be significantly longer than the time to build the cold-end assemblies. It was therefore decided to build and install the cold-end assemblies into a dummy heater head and debug the cold-end components by operating in a motoring mode before the heater head and the heat pipe were available.

Sodium heat pipe technology is relatively well established for a simple configuration such as a hollow tube in which one end is the evaporator and the other end is the condenser. For a single large evaporator interfacing with a condenser formed by radial slots in the starfish arrangement, significant

development and demonstration on a reduced-size assembly were needed. The heat pipe development is summarized in Section 8. Since the engine-alternator assembly using the Inconel 718 head was scheduled to be available several months before the heat pipe would be ready and to reduce program risk if the heat pipe development required additional time, direct heating by flat radiant heaters mounted directly into the starfish slots was identified as a means of permitting engine/alternator tests to proceed independent of the heat pipe development schedule.

In summary, because of the cold-end mechanical operation concerns at the elevated temperatures and the long lead time anticipated for the procurement of the engine heat pipe and heater head, the overall CTPC development was organized in three sequential phases:

1. Cold-end testing where the heater head is replaced by a dummy heater head incorporating an SPDE cooler.
2. Engine testing with an Inconel 718 heater head with direct heating by flat silicon carbide heaters mounted in the heater head slots.
3. Engine testing with an Inconel 718 Starfish heater head with a sodium heat pipe. Heat input is by round silicon carbide radiant heaters in a cavity below the bottom plate of the heat pipe.

References[1]

Dochat, G. R. "Free-Piston Stirling Engine System Considerations for Various Space Power Applications." *Proceedings of the 8th Symposium on Space Nuclear Power Systems*, M. S. El-Genk and M. D. Hoover, eds., American Institute of Physics, New York, NY, 1991.

Dhar, M. et al. "Design and Performance of a 25-kWe Free-Piston Stirling Space Power Demonstrator Engine." Intersociety Energy Conversion Engineering Conference, Philadelphia, PA, August 1987.

Penswick, L. B. "1050 K Stirling Space Engine Design." NASA CR-182149, 1988.

Spelter, S. and M. Dhar. "Space Power Research Engine Power Piston Hydrodynamic Bearing Technology Development." NASA Contractor Report 182136, 1989.

[1] A complete bibliography of related material is presented at the end of this report volume.

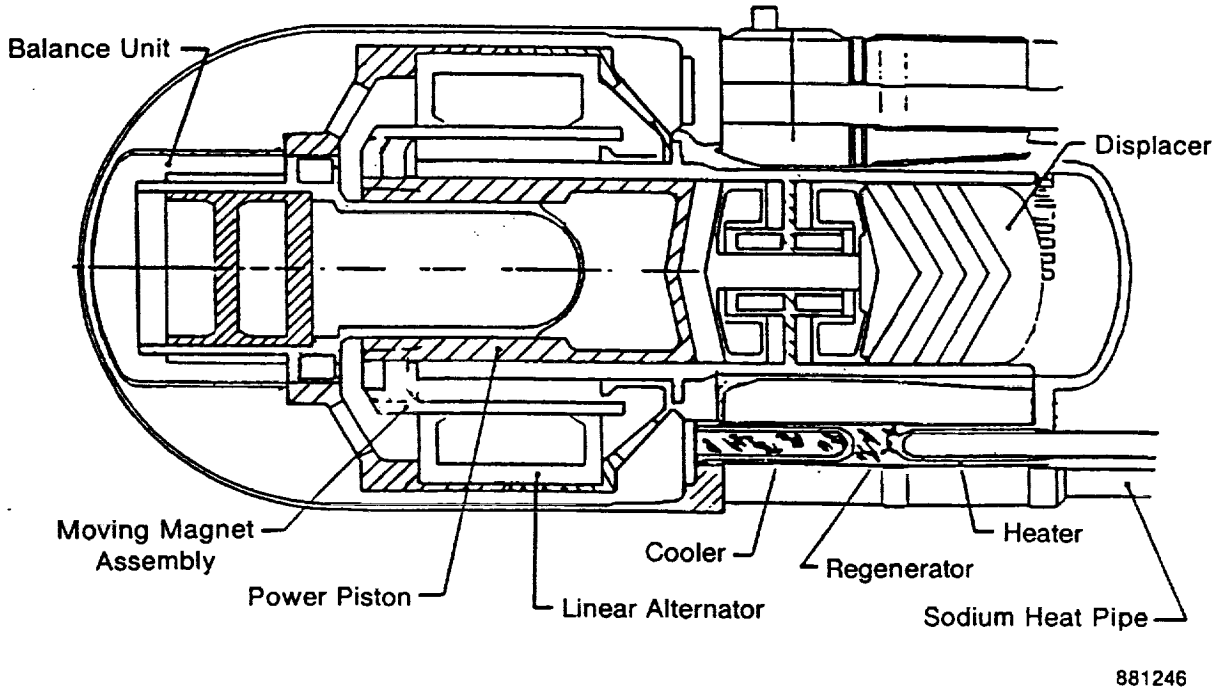

Figure 3. Conceptual Stirling Space Engine (CSSE)

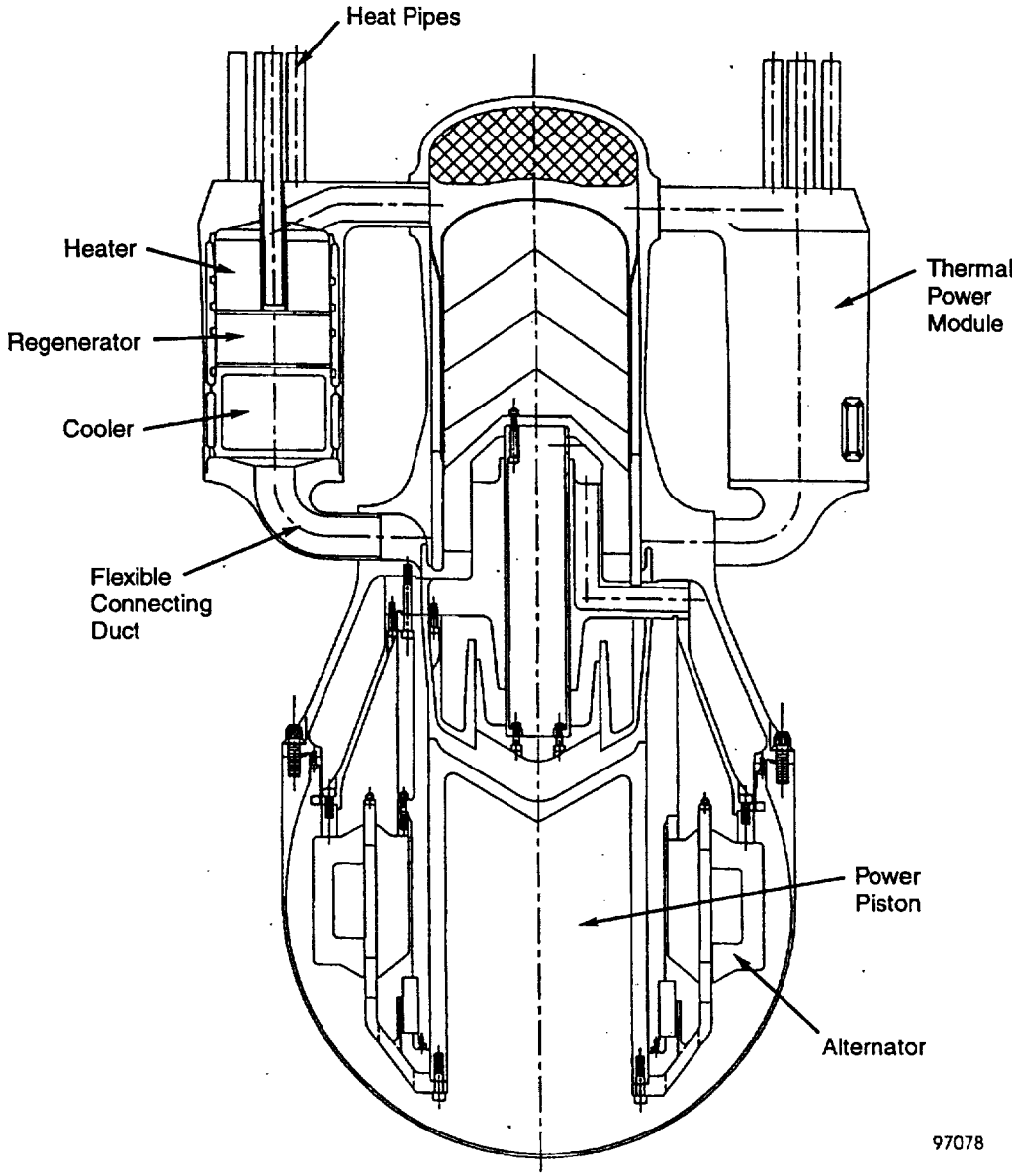

Figure 4. Modified Thermal Power Module Design

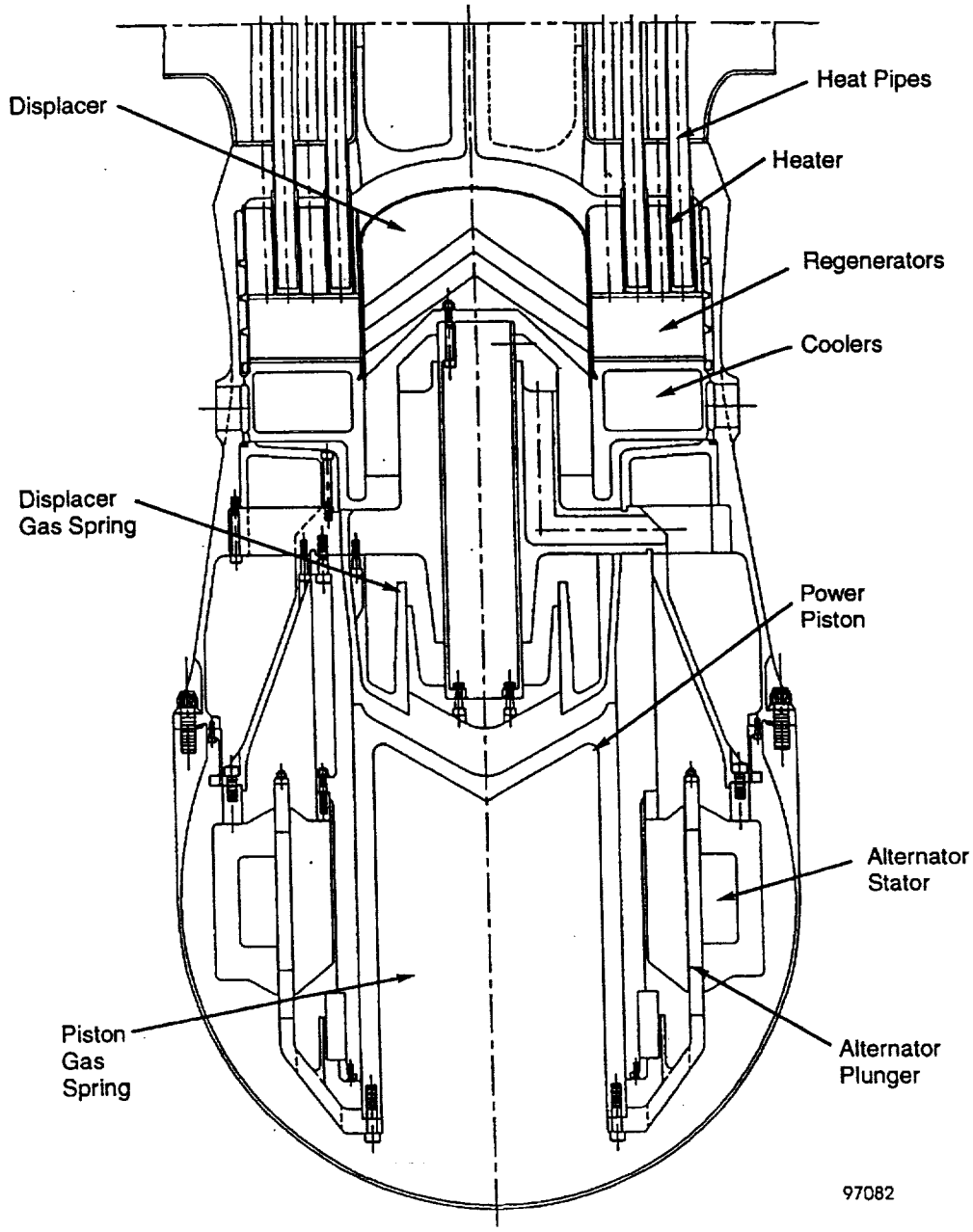

Figure 5. Double-Wall Annular Configuration with Heat Pipe Thermal Wells

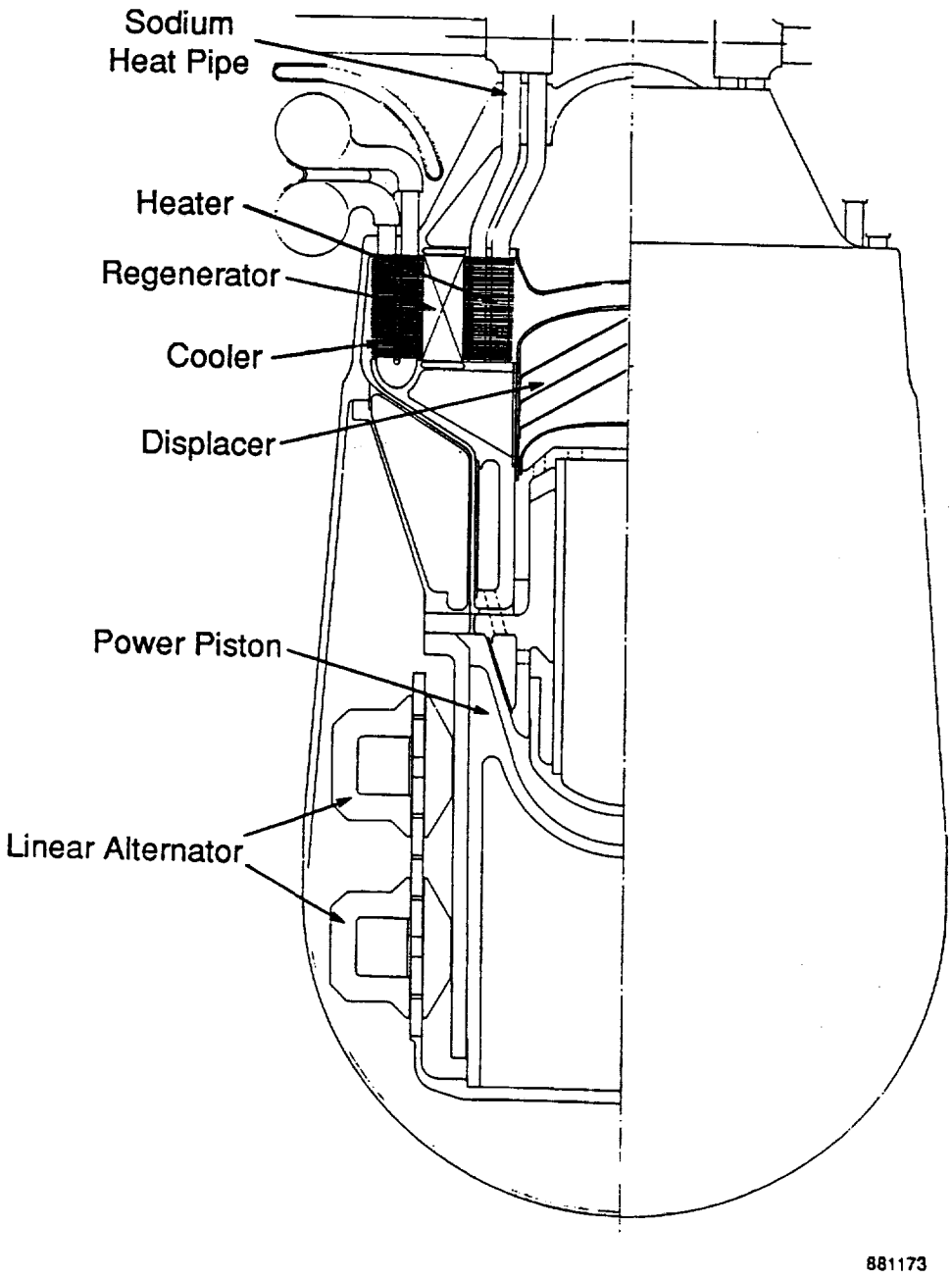

Figure 6. Engine Configuration with Radial-Flow Heat Exchangers

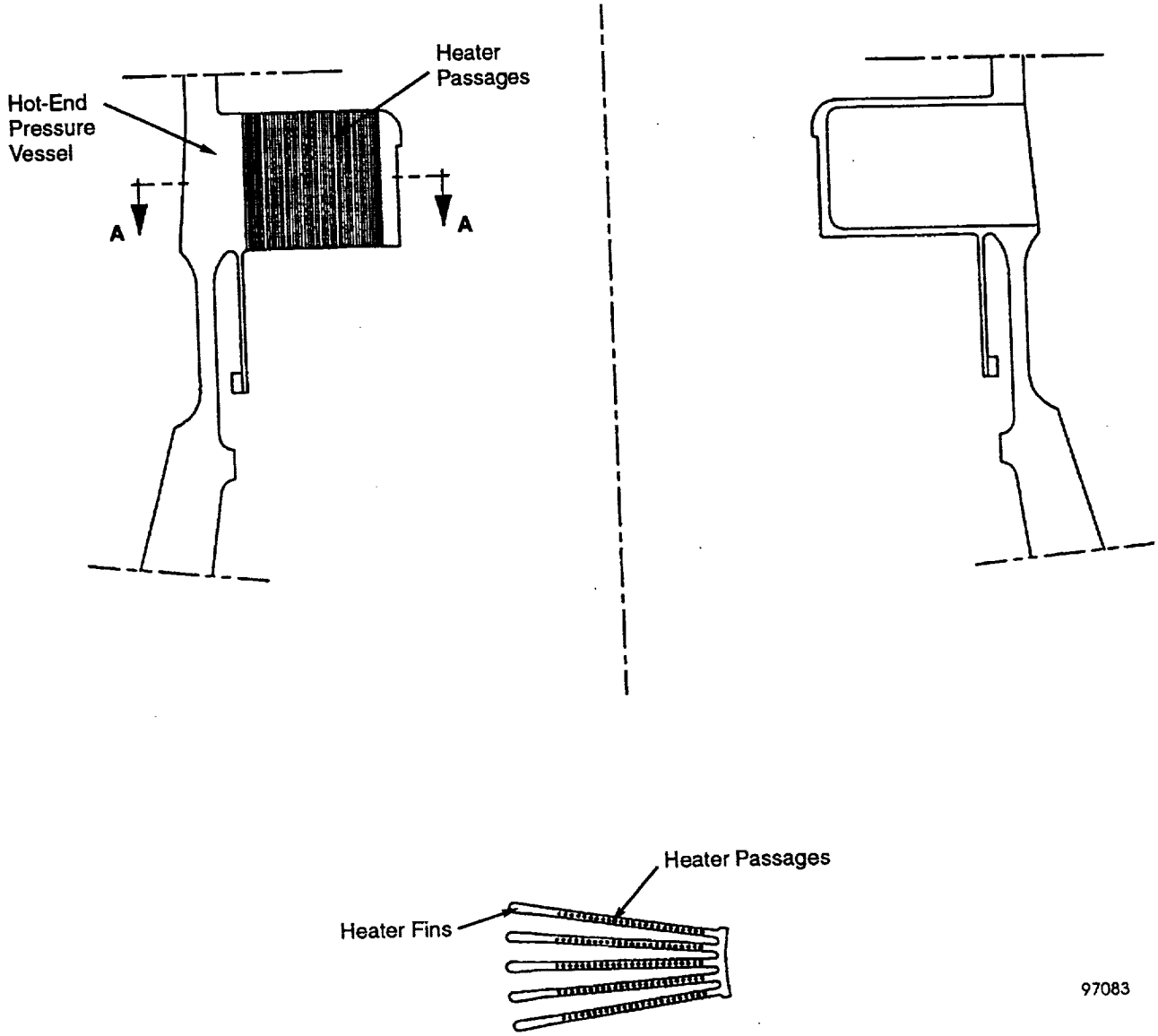

Figure 7. Starfish Heater Head Design

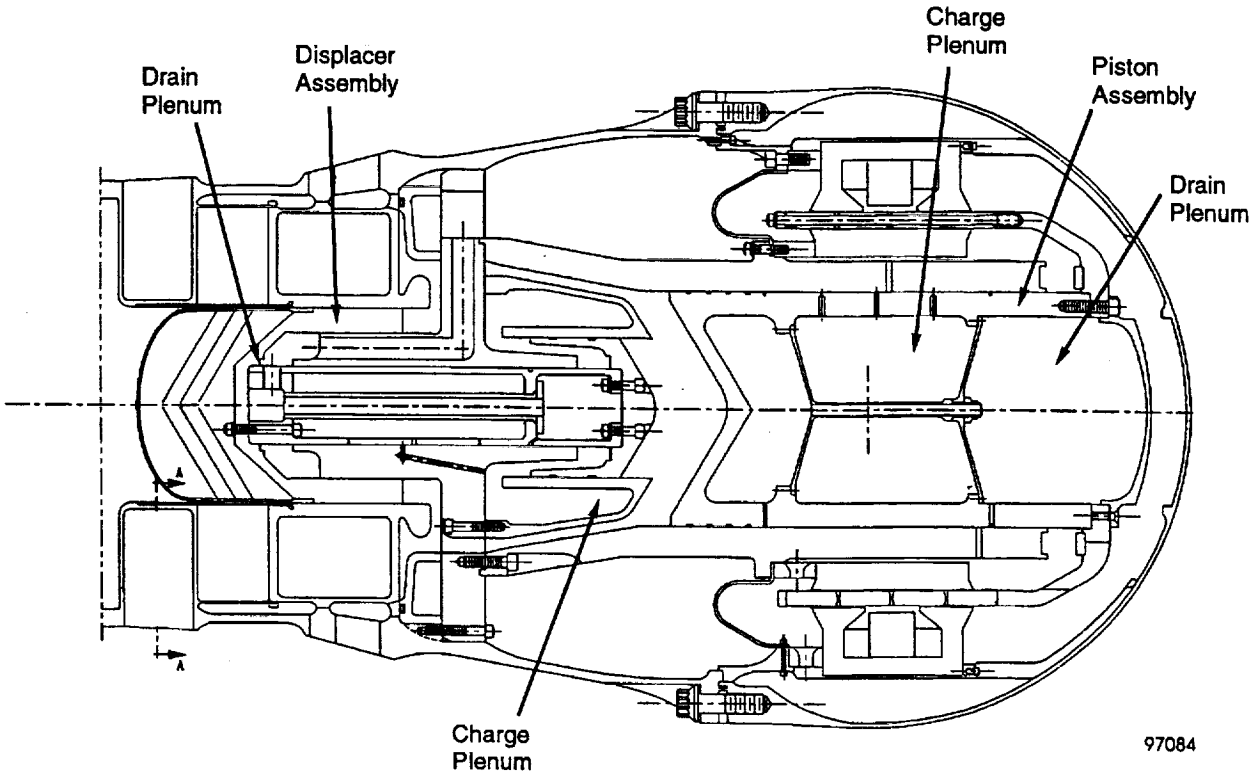

Figure 8. Hydrostatic Gas Bearing Configuration

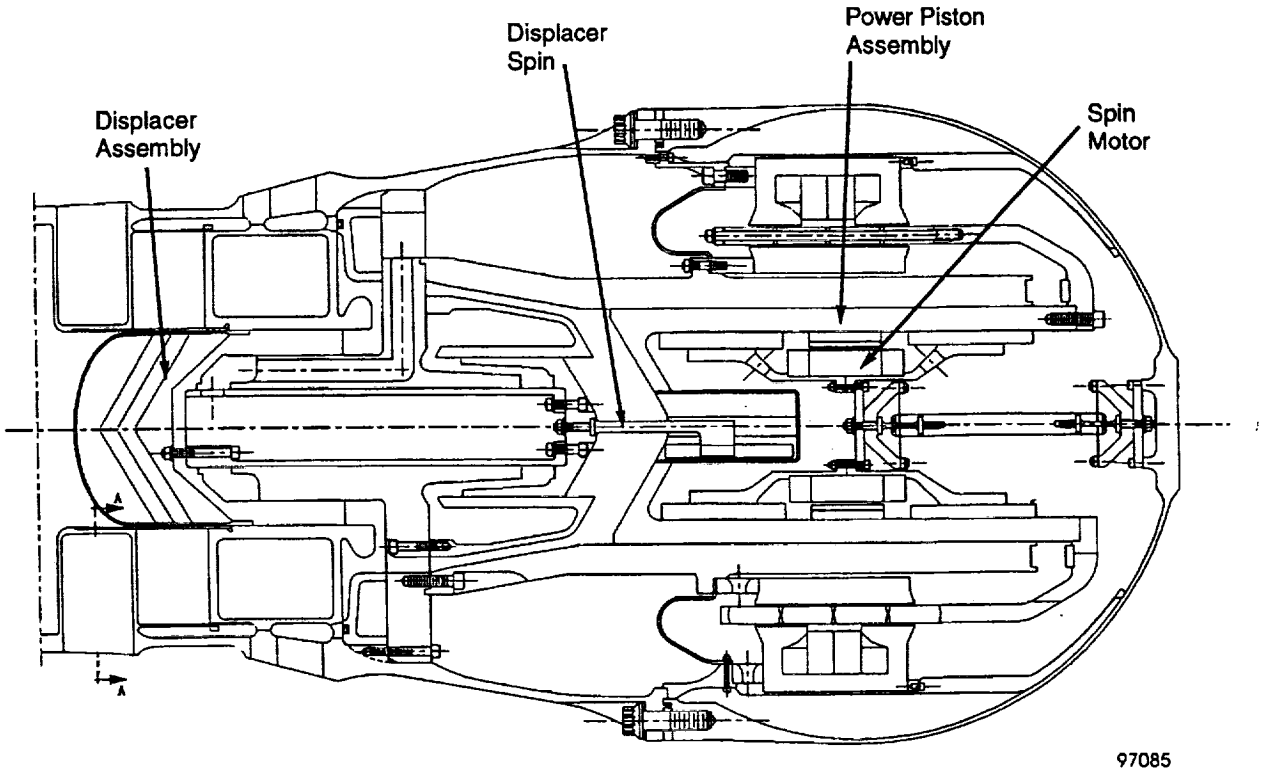

Figure 9. Hydrodynamic Gas Bearing Configuration

3.0 CTPC DESIGN DESCRIPTION

3.1 Introduction

The design objectives established for the CTPC were:

- Power: 12.5 kWe/cylinder
- Efficiency: 20%
- Hot-Side Interface: heat pipe
- Heater Temperature: 1050 K
- Cold-Side Interface: oil-pumped loop
- Cooler Temperature: 525 K
- Bearings: hydrostatic gas bearings.

Figure 10 shows a layout of the engine. Heat energy is input to the engine by interfacing an unconventional heat pipe design with a slotted starfish heater head. Heat is rejected at a tube-and-shell engine cooler to an external pumped cooling loop using a noncorrosive mineral oil (paratherm). A smaller cooling loop pumps coolant over the outer surface of the pressure vessel to remove heat that is generated in the alternator.

The engine can be broken down into three basic subsystems: the hot-end assembly (Figure 11), the displacer drive assembly (Figure 12), and the alternator assembly (or lower end) (Figure 13).

The hot-end assembly consists of the heater head, heat pipe, regenerator, and cooler. The displacer drive assembly incorporates the reciprocating displacer within the stationary post and flange. The lower end incorporates the reciprocating power piston within the stationary power piston cylinder. The magnetic plunger is attached to one end of the power piston and is driven through the gap between the stationary outer and inner alternator stators which are supported by the power piston cylinder. The lower end is enclosed within the joining ring and pressure vessel.

As the displacer and power piston oscillate within their stroke limits, the working fluid (high pressure helium) oscillates back and forth between the hot side (heater and expansion space) and cold side (cooler and compression space). During each cycle, gas passes back and forth through the regenerator. Heat transfer to and from the regenerator during each cycle maintains a constant axial temperature gradient across the regenerator. A similar gradient is experienced by the pressure shells at the inner and outer diameters of the regenerator. This is a source of significant thermal stress affecting the mechanical design of these components.

The Stirling cycle thermodynamics is discussed in Section 4.0. From these analyses, the thermal and hydraulic characteristics of the heater, regenerator, and cooler are defined. The heater and cooler typically require a large number of small hydraulic diameter flow passages closely coupled thermally to the heat source or heat sink. The porosity, wire size, frontal area, and length of the regenerator are also selected based on these analyses. The heat exchanger geometries of the CTPC are presented in Section 4.0.

3.2 Hot-End Assembly

The hot-end assembly is comprised of four components: the heater head/heat pipe assembly, the regenerator, the cooler, and the displacer cylinder (see Figure 11). Heat is added to the thermodynamic cycle through the heater head. Heat is removed from the cycle through the cooler. The regenerator acts as a thermal buffer between the hot and cold sections of the engine. The displacer cylinder provides the seal between the expansion space and the compression space.

3.2.1 Heater Head/Heat Pipe Assembly

The heater head was designed as a monolithic structure with the heat pipe as an integral part of the head. The heat pipe uses pure sodium as the working fluid. The goal of this design was to minimize the number of brazed or welded joints in the assembly and eliminate any joints that see both high stress and a sodium environment. This results in a significant increase in the reliability of the heater head by reducing the number of potential leak sites.

The heater head is a four-piece, welded assembly as shown in Figure 14. The inner and outer closure plates are butt welded to the expansion space side of the starfish heater head. The wall which surrounds the outer diameter of the regenerator is also welded to the starfish head. All welds are made by the electron-beam process. The double-closure plate arrangement is used for laboratory testing of a single-cylinder power converter. In an actual application, the starfish heater head design permits an opposed-cylinder configuration, resulting in a much lighter design (Figure 15).

The heat pipe is constructed of an upper and lower plate, an outer ring, and ten reinforcing gussets (Figure 16). The two plates are formed slightly conical to prevent "oil canning" as radial temperature gradients are experienced during start-up and shutdown. The lower plate is used as the evaporator section. Forty radiant heaters are used to provide heat to the heat pipe. The gussets add extra stiffness to reduce vibrational flexing of the assembly. They also increase the heat pipe's pressure-carrying capability in the event of a heater head rupture. In the event of a heater failure, a rupture disk is provided to relieve the pressure before the heat pipe structure fails.

The geometry of the heater section consists of 50 pockets machined radially inward from the outer diameter of a solid ring of material (see Sections 10.2.1 and 10.2.2). These pockets form an array of 50 fins oriented axially in the heater head. These fins act as the condensor for the heat pipe. Each fin contains 38 circular gas passages running through the length of the fin. Initially, a smaller number of oval passages was planned. The change to circular passages was made to reduce the manufacturing development associated with the oval shape. Figures 17 and 18 show the initial and final gas passage geometry.

In order to contain the pressure at the hot-end temperature for the design life of the engine and to minimize weight, the material selected must have good creep resistance. Although the starfish configuration requires only two joints on the pressure boundary and two joints at the heat pipe interface, the ability to join the heater head material is nevertheless a major consideration because high-creep-strength superalloys are inherently difficult to join reliably. Following a review of high-strength superalloy properties and the strength requirements of the CTPC head, UDIMET 720 was selected as the reference material. Udimet 720 exhibits good creep strength, has good long-term stability characteristics at elevated temperatures, and is available in wrought form (see Volume II, Appendix C).

Because of uncertainties in the joining characteristics and the lack of certain mechanical property data for Udimet 720, Inconel 718 was substituted for the material of the first heater head. This allowed time for the uncertainties and unknowns regarding Udimet 720 to be addressed by development activities proceeding in parallel with the first CTPC engine build and test. The design approach was to make the Inconel and Udimet heads geometrically identical to permit a Udimet head to be incorporated later. The heat pipe components are made of Inconel 718 because it resists sodium attack and is readily weldable. The heat pipe wicks are made from stainless steel screens and are spot welded to all internal surfaces of the heat pipe.

The creep strength of Inconel 718 is such that hundreds of hours of testing can be performed at temperatures up to 1000 K and tens of hours of testing can be performed up to 1050 K. This will allow the performance of the CTPC engine/alternator to be thoroughly characterized. Long-time endurance testing at design-level temperatures could then be conducted with a Udimet head.

3.2.2 Regenerator

The regenerator is constructed of a single stack of sintered felt metal (see Table 3 in Section 4.0 for regenerator parameters). Coarse screen mesh is sintered to each end of the felt metal to give the matrix

some rigidity and to help prevent small pieces from breaking off during engine operation. The inside and outside diameters are brazed to metal liners to prevent bypass leakage from occurring. The inside liner also forms one wall of the appendix gap on the outer diameter of the displacer dome (Figures 10 and 19).

The material selection for the regenerator is limited by the availability of small diameter wire (25 to 50 microns). Important properties for regenerator material are high heat capacity, good oxidation resistance at 1050 K, and a thermal expansion match with surrounding components. The primary material chosen for the regenerator matrix based on thermal expansion is Inconel 600. To allow different wire sizes to be tested, 300-series stainless-steel regenerators were also procured. The end screens are 316 stainless steel, and the liners on the inner and outer diameters are Inconel 718.

3.2.3 Cooler

The cooler is a tube-and-shell arrangement as shown in Figure 20. The outer shell has two inlets and two outlets in order to minimize the circumferential temperature variation around the cooler and, thus, the displacer with its close-clearance seals.

The cooler shell is a four-piece welded construction. The inner surfaces of each piece are finish machined while the outer surfaces are left with ample machining stock to allow for any warping due to welding. The parts are then full-penetration electron-beam welded to make the assembly. The tube sheets are drilled after welding to ensure proper alignment for easy installation of the tubes. Because the cooler shell is exposed to the full engine pressure, Inconel 718 was selected for the material of the shells because of its high yield, ultimate, and fatigue strengths.

The tubes are a two-piece construction consisting of an insert brazed into a thin-walled tube. The helium flow passages are axial slots milled into the outer surface of the insert. Commercially pure nickel was selected for the inserts because of its high thermal conductivity. The high conductivity minimizes the average temperature difference between the helium and the coolant which flows over the outer surface of the tubes. Inconel 625 was selected for the tubes based upon its strength, joining, and thermal expansion characteristics.

The slotted insert approach reduces the number of tube-to-tube sheet joints compared to a cooler of the SPRE configuration. Cooler parameters are listed in Table 3. Both electron-beam welding and brazing were evaluated experimentally for the tube-to-tube sheet joints. Welding was selected for the CTPC cooler because it provides a stronger, more reliable joint and can be easily repaired in the event there is a leak.

3.2.4 Displacer Cylinder

The displacer cylinder is located inside the cooler (see Figure 11). The flange of the displacer cylinder acts as a plenum for the cooler and connects the flow to the cold duct. The inner diameter of the cylinder and the outer diameter of the displacer body form a tight gap that seals the expansion space from the compression space. The inner diameter of the cylinder is plasma sprayed with chrome oxide and finish ground to meet the required dimension. The hard coating is applied to minimize wear and prevent galling in the event that any unexpected contact occurs between the moving displacer and the cylinder during operation due to such things as thermal distortion.

Misalignment of the displacer cylinder was a constant problem associated with the SPDE design. For this reason, the displacer cylinder on the CTPC was not welded to the heater assembly. Instead, the displacer cylinder is mounted directly to the post and flange, ensuring positive alignment with the critical diameters of the displacer drive assembly. The alignment can then be checked prior to final engine assembly, unlike the SPDE design, which was a blind assembly. Also, the pilots are replaceable by design. This allows reworking of the pilots if wear due to repeated assembly and disassembly occurs. The pilots on the displacer cylinder are mechanically attached Inconel 718 tabs. The pilots on the post and flange are hardened dowel pins with machined faces.

3.3 Displacer Drive Assembly

The displacer drive assembly (Figure 21) is comprised of the moving displacer assembly and the stationary post and flange/instrumentation ring assembly.

3.3.1 Displacer Assembly

The displacer assembly is comprised of the rod, the displacer, and the gas spring piston (see Figure 12). The displacer is attached to the forward end of the rod and the gas spring piston is attached to the aft end of the rod. Close-tolerance pilots are used to control the concentricities and alignments of these components.

The displacer body has a domed cylinder attached at its outer diameter. The domed section forms the interface with the expansion space. As stated in the previous section, the outer diameter of the displacer forms a close clearance seal with the inner diameter of the displacer cylinder between the expansion space and the compression space. The inner diameter of the displacer body and the outer diameter of the post form a close clearance seal between the forward gas spring and the compression space.

The rod is a 1.8-in.-diameter tube about 9 in. long. It is about 1.5 in. longer than the bore of the post and slightly smaller in diameter. The hydrostatic (noncontacting) gas bearings which support the displacer are located in the small clearance between the rod and post bore. One set of ports in the rod and post are arranged to pressurize a bearing supply plenum inside the rod. Bearing orifices, drain grooves, and drain ports are located as shown in Figure 22. Their geometries were determined by the analysis described in Section 4.0.

The displacer drive assembly incorporates two gas springs. These were sized based on the dynamic analysis of the engine described in Section 4.0. The aft gas spring is a high pressure amplitude spring (18 bar) which acts on the gas spring piston located on the cold side of the assembly. It is enclosed by the gas spring piston and gas spring cylinder. The small clearance between the gas spring piston and cylinder must be closely controlled because it provides the seal between the high-pressure-amplitude aft gas spring and the high-pressure-amplitude compression space. The forward gas spring is a low-pressure-amplitude spring (2 bar) located in the displacer body and is interconnected to the large volume enclosed by the joining ring.

The aft end of the displacer body and the aft side of the gas spring piston are exposed to the compression space. The displacer dome is exposed to the expansion space. The difference in area between the compression and expansion sides of the moving assembly is referred to as the rod area. This was sized based on the analysis described in Section 4.0 and can be adjusted by replacing the gas spring piston and gas spring piston cylinder with ones of different diameters.

To minimize the mechanical losses in the displacer gas springs, the pressure amplitudes in the gas springs must be kept low. To accomplish this, the inertial mass of the displacer drive must be minimized. The walls adjacent to the seals and bearings are subject to fluctuating pressure loads, causing them to deform. Excessive deformation results in an increase in seal leakage, a reduction in bearing stiffness, and a higher potential for rubs. Therefore, a material with a low density and a high modulus of elasticity is needed for the displacer drive. Beryllium has the high stiffness-to-weight ratio that makes it the optimum material choice for all of the high precision parts. Another benefit of beryllium is that it is a highly stable material capable of maintaining the tolerances necessary to control the tight clearances. Hot-pressed S200-F block is the product form specified for the displacer body, displacer rod, and gas spring piston.

The dome, which is exposed to the high temperature side of the engine, is made from Inconel 718 because of its high temperature properties. The wall of the dome must be thin to minimize its inertia and conduction loss, but must be capable of resisting the expansion space pressure amplitude without buckling or fatigue failure.

The initial approach to joining the dome to the outer diameter of the beryllium displacer body was a copper/silver braze. Based upon tests, the strength was marginal, and radial pins were added to carry the loads on the joint. The braze was retained primarily as a seal. Subsequent tests on the finished assembly after operation in the engine have indicated that the braze joint does not provide the required seal. The braze joint design was replaced with a shrink-fit with no braze alloy. This arrangement has demonstrated a lower leak rate than the design with the braze.

3.3.2 Post and Flange/Instrumentation Ring

The post and flange and instrumentation ring assembly make up the stationary member of the displacer drive assembly (see Figure 12). The post and flange houses the porting for the bearings and connecting ducts for the forward gas spring of the displacer. The instrumentation ring is an extension of the flange section of the post and flange and carries all feedthroughs for pressure and instrumentation access into the displacer region. The complete assembly is supported by the instrumentation ring, which is then sandwiched between the bolted flanges of the heater head and the joining ring.

Because the instrumentation ring is used for instrumentation access and gas supply to the post and flange, the joint between the beryllium flange section and the instrumentation ring required careful design. Each penetration must be sealed against leakage from the neighboring gas volume as well as adjacent penetrations, but must also be flexible to accommodate any thermal expansion differences between the parts. The post and flange is also made of beryllium S200-F. This reduces the overall mass and, being the same material as the displacer, minimizes the potential for differential thermal expansion causing contact in the close clearance seals and bearings.

The instrumentation ring material is Inconel 718. It is separable from the post and flange. This two-piece construction was selected to avoid damage to the beryllium flange from the large clamping loads imposed by the bolted joint.

3.4 Alternator Assembly (Lower End)

As shown in Figure 13, the alternator assembly consists of the power piston, the power piston cylinder, the plunger assembly, the alternator, the joining ring, the volume compensator, and the pressure vessel. The alternator is comprised of the plunger assembly and the inner and outer stator assemblies. Details of the alternator stator and alternator plunger are given in Section 7.0.

3.4.1 Power Piston and Cylinder

As the name implies, the power piston is the component which delivers the mechanical power of the engine to the alternator. This is accomplished by the cyclic pressure in the compression space acting on the forward face of the power piston to drive the plunger assembly. The flux from the magnets in the plunger assembly links the alternator coil to generate electrical power.

The power piston and power piston cylinder are a mating pair. As discussed above, they are constructed of S200-F beryllium for the same reasons as were the displacer and post and flange. The outer surface of the piston is plasma-sprayed aluminum oxide. The inner diameter of the cylinder is lined with a carbon graphite sleeve. Both are ground and lapped to final dimension.

The arrangement of power piston bearings, ports, and seals is described in Section 5.0. As discussed therein, two power pistons are provided. One is designed for operation on externally supplied bearings in which the helium system external to the engine is used to maintain a pressure across the bearings. The second piston is designed for operation on internally activated bearings in which the bearing pressure is provided by the power piston gas spring.

For external bearing operation, the port arrangement which controls the pressure level in the supply and drain plenums located inside the power piston is different from that used for internal bearings.

At the forward end of the power piston, a 2-in.-long section on the piston outer diameter provides the seal between the compression space and the gas spring. Midstroke ports interconnecting the two volumes are located in the seal section to stabilize the dynamic midstroke position of the piston.

The mass of the components inside the power piston which separate the bearing volumes are minimized by making them from a high strength material. Inconel 718 was selected since it has a coefficient of thermal expansion similar to beryllium.

3.4.2 Pressure Vessel

The pressure vessel is a large spherical end cap (see Figures 10 and 13) for the engine which contains the full engine pressure. It is also used to extract heat that is generated in the lower end. A cooling jacket encloses the pressure vessel and is welded to the outside of the vessel. An external cooling loop controls the vessel temperature. Helium circulation within the vessel transfers heat generated in the alternator and gas spring to the cooled pressure vessel wall.

The main function of the pressure vessel is to enclose the cold end of the engine and contain the high pressure helium. The material must have high yield and tensile strengths relative to its density to minimize its weight. Moderate fatigue properties are desirable since the cyclic pressure wave in the gas spring induces a stress amplitude on the mean stress. Inconel 718 was selected for the pressure vessel material.

The cooling jacket is made from Inconel 625 since it is readily welded to itself and to Inconel 718. The high strength of Inconel 718 is not required for the jacket material.

3.4.3 Joining Ring/Volume Compensator

The joining ring (see Figure 13) acts as the transition piece between the heater head and the alternator pressure vessel. In a space-application version of the engine, this would be an integral part of the heater head outer wall. For a test engine, many instrumentation leads must be brought out across the pressure boundary. Gas lines for engine pressurization and external gas bearings also are provided. By providing the instrumentation ring for displacer instrumentation and gas lines and the joining ring for lower end instrumentation and gas lines, engine assembly and disassembly are simplified.

The lower end assembly contains two separate gas volumes (see Figure 13) The first volume is located within the joining ring and includes the volume compensator. It is interconnected at the post and flange with the forward gas spring of the displacer. The second volume, which is within the pressure vessel and surrounds the alternator, is the power piston gas spring.

Due to the many penetrations in the joining ring, it is made heavier than would be the case for a space engine. Because of the reduction in internal volume associated with the thicker joining ring wall, the volume compensator is added to regain the needed volume to keep the forward displacer gas spring amplitude low. The volume compensator would not be required in a space engine.

From strength and thermal expansion compatibility reasons, the joining ring and volume compensator are made from Inconel 718.

3.5 Dynamic Seals - Close Clearance

Leakage losses in the seals are proportional to the cube of the clearance dimension. To limit these losses to acceptable levels, clearances in the range 0.0005 to 0.0006 in. are required. Experience on previous engines has shown that rubbing and jamming of the displacer can occur due to small misalignments induced by pressure and/or temperature gradients. Small particles of debris can also become trapped in the clearance and jam the displacer. The SPDE and other engines operated at MTI had used hard-coated surfaces on both the moving and stationary sides of the seals. For the CTPC, an experimental program was conducted to evaluate various material combinations for the seal surfaces. Based upon the tests, the decision was made to use plasma-sprayed aluminum oxide on the outer surfaces and a carbon graphite sleeve (Pure Carbon Co. Purebon P-3310) on the inner surfaces for developmental purposes.

A plasma-sprayed coating of aluminum oxide was specified to be applied on the outer diameter of the power piston and the rod, the outer diameter of the gas spring piston, and the outer diameter of the post. These surfaces are final ground and lapped to the precise dimensions required. On the adjacent surfaces, carbon graphite sleeves are installed. These were shrunk fit into place and were also ground and lapped to final dimension.

To prevent any damage to the hardware should the displacer or power piston exceed their normal stroke limits, gas snubbers are provided at both ends of the strokes (see Figure 12). These are small cavities which engage at overstroke conditions. The small clearance in the snubber cavity between the moving and stationary element coupled with the low compressibility of high pressure helium provides a decelerating force which eliminates high velocity impact.

3.6 Static Seals

Static seals are used on all stationary parts. Among the types of static seals used are zero gap, gaskets, O-rings, and metallic boss seals. Zero gap seals are essentially created by two mating parts that are tightly clamped together. Their surfaces are polished to a smooth finish, thus creating a low leakage joint. These types of seals are used on assemblies where space is limited and alignment and concentricity are critical.

Gaskets are used in areas where there is a sufficient clamping force between mating parts but space limitations preclude the use of O-rings. Gasket materials used are Grafoil and soft metal, such as annealed copper or silver plated stainless steel. Grafoil is made up of thin sheets of carbon graphite that are pressed into gasket material. It can withstand high temperatures and high pressures and comes in sheets as thin as 5 mils. A disadvantage of Grafoil is that it flakes easily, and extreme care is required to avoid the formation of debris.

O-rings are used in areas where space permits and gaskets would not allow adequate control of alignment. They are also used on diameters where no clamping force can be generated.

Since the O-rings are reusable, they are the preferred seal at the main pressure vessel joints which are frequently disassembled. The primary choice for O-ring material is Kalrez compound 4079. This material is rated for continuous operation at 535 K and for short-term use at 600 K with minimal compression set.

Kalrez is a very expensive material. For laboratory operations, it is more economical to use Viton. This is rated for continuous use at 480 K and can survive brief excursions to 600 K.

For sealing static pressures above 100 bar, O-ring manufacturers recommend using backup, or antiextrusion rings. Standard backup rings are only rated for 400 K, so special backup rings had to be designed for CTPC. These backup rings have the standard backup ring geometry, but are made of Vespel, a polyimide compound capable of continuous service to 600 K.

Many penetrations are made into the engine. These penetrations provide access for gas charging, power feedthrough, temperature measurements, and displacement measurements. Each one of these feedthroughs must have a seal to carry the full engine pressure. In the instrumentation ring, many of the feedthroughs also need internal seals to separate different volumes within the engine. A typical feedthrough assembly for the instrumentation ring is shown in Figure 23. The internal seal is made using a silver-plated Belleville washer which is pressed up against the post and flange with the seal positioner. On the outside of the seal positioner is an O-ring to seal against leakage around the threads. An adapter is then screwed onto the positioner with a copper gasket for the seal against the instrumentation ring. The adapter can then take a number of fittings depending on the feedthrough requirements. Because pipe thread fittings are characteristically difficult to seal against helium leakage, pipe threads have been avoided, and a straight thread fitting with an MS boss seal as shown in Figure 24 is used. These boss seals are capable of sealing very high pressures at temperatures up to 1100 K.

The seals around the instrumentation leads are made using off-the-shelf feedthrough fittings rated for the temperature and pressure of engine operation. These fittings use a crushable sealing gland made from Teflon.

3.7 CTPC Mass Breakdown

The mass breakdown for the CTPC is given below in Table 2A and was based on the CTPC preliminary design. The masses are representative of a spaceflight configuration, using an opposed-piston layout and including no bolted flanges or other elements needed just for laboratory testing. Alternative reference spaceflight designs were evaluated at various stages of the effort. The minimum projected specific mass achieved for these alternative designs was about 4.9 kg/kWe.

Table 2A. Mass Breakdown for Spaceflight Version of CTPC

CTPC Component	Specific Mass, kg/kWe
Heater Head	1.10
Regenerator	0.10
Cooler	0.56
Joining Ring	0.97
Post and Flange	0.22
Displacer	0.13
Power Piston (less magnets)	0.36
Power Piston Cylinder	0.33
Alternator Pressure Vessel	0.91
Alternator Stators	1.76
Alternator Magnets	0.38
Alternator Capacitors	0.15
Alternator Cooling Shell	0.09
Total	7.07

97TR21

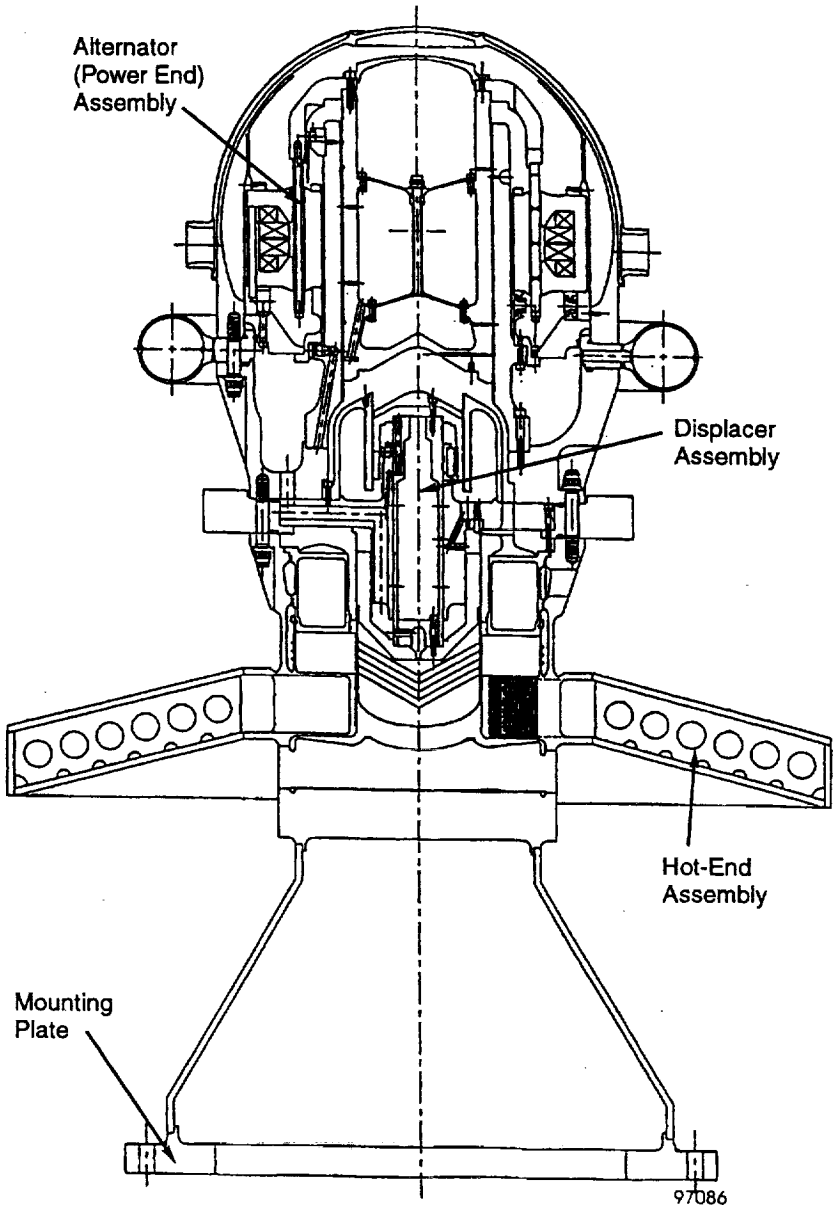

Figure 10. CTPC Engine Layout

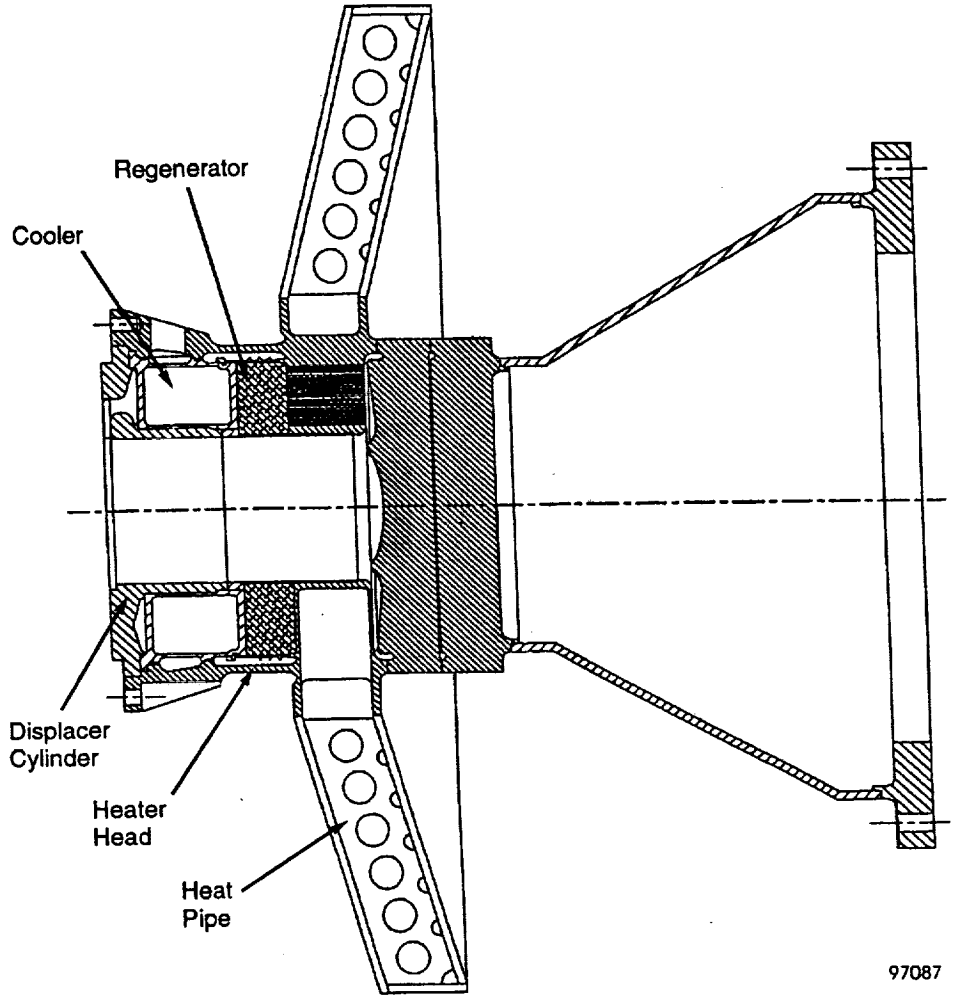

Figure 11. Hot-End Assembly

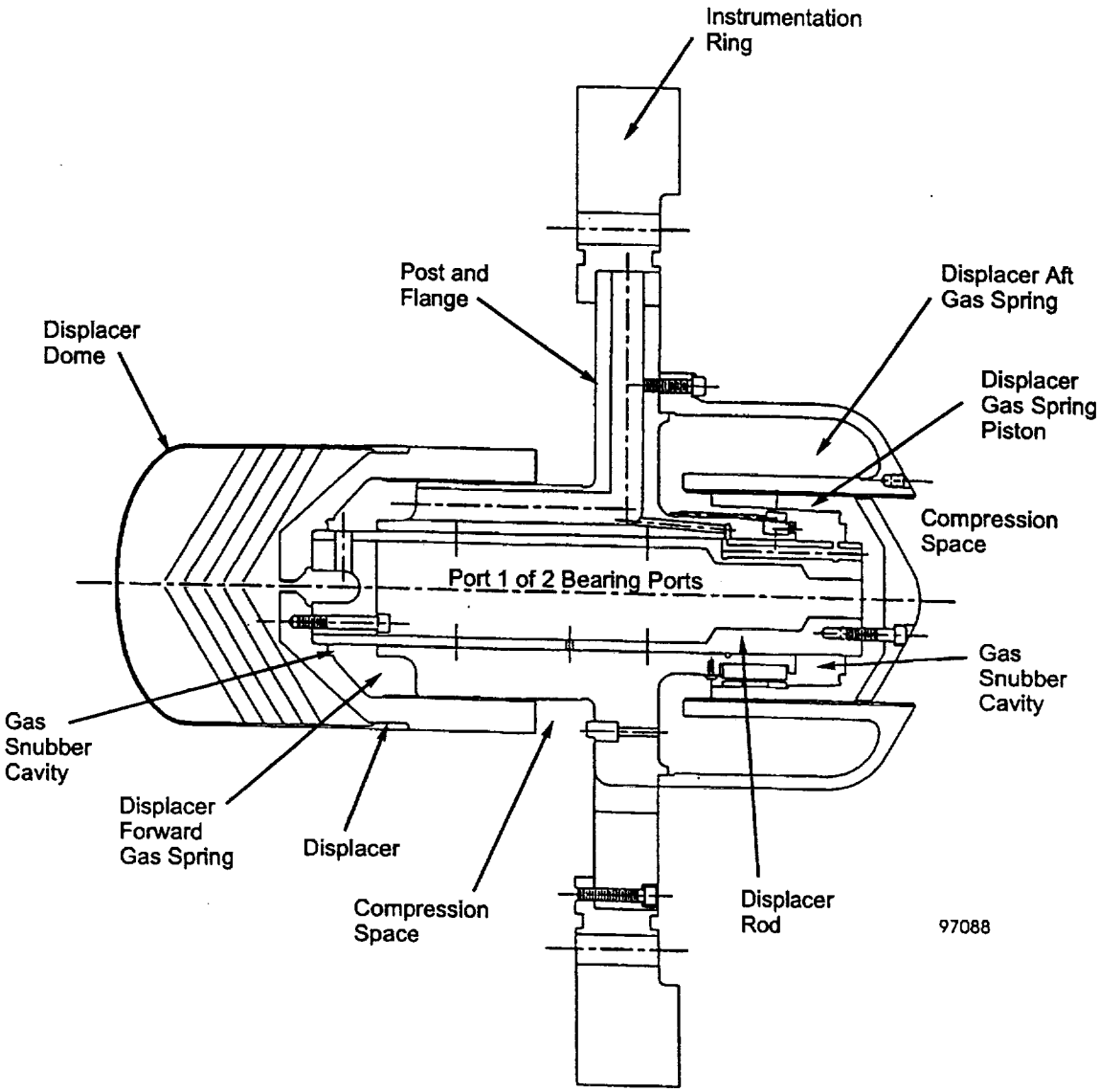

Figure 12. Displacer Drive Assembly

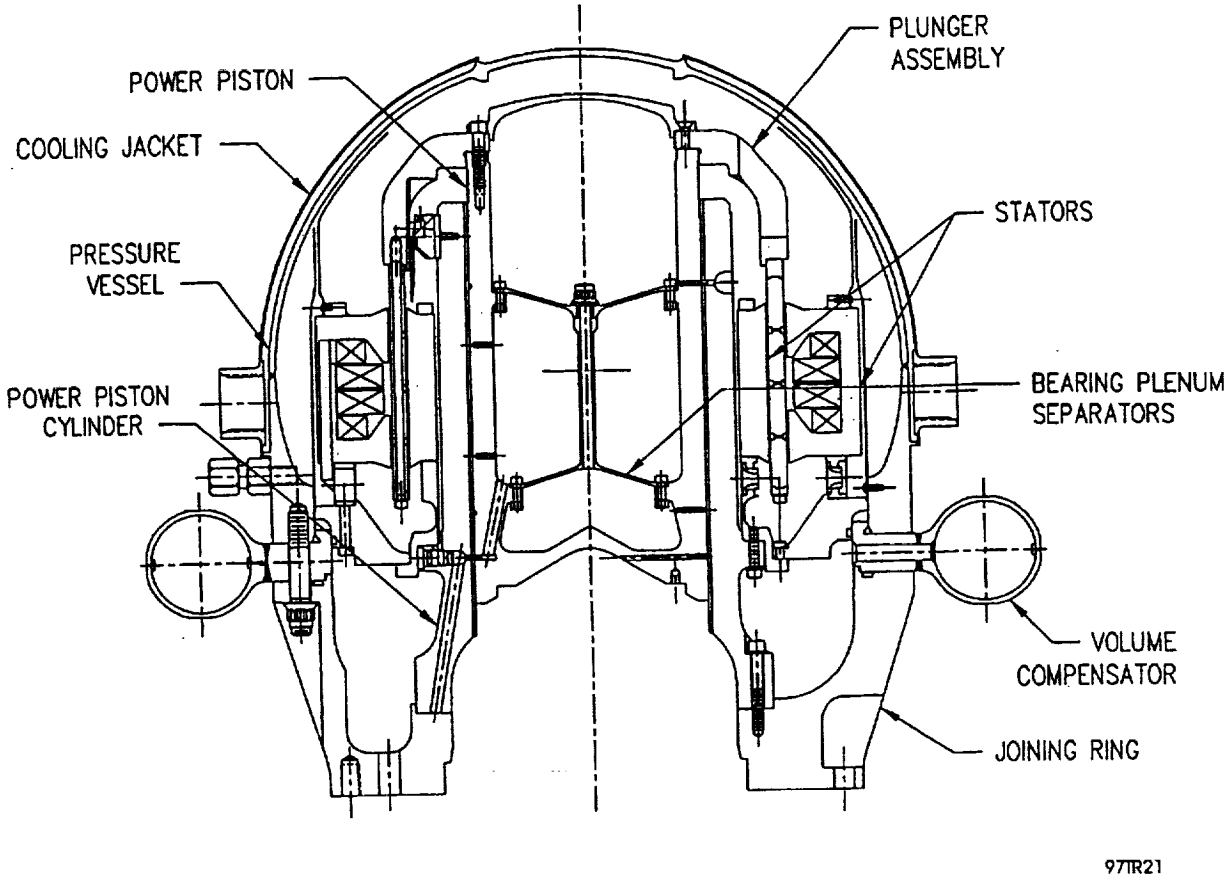

Figure 13. Alternator Assembly

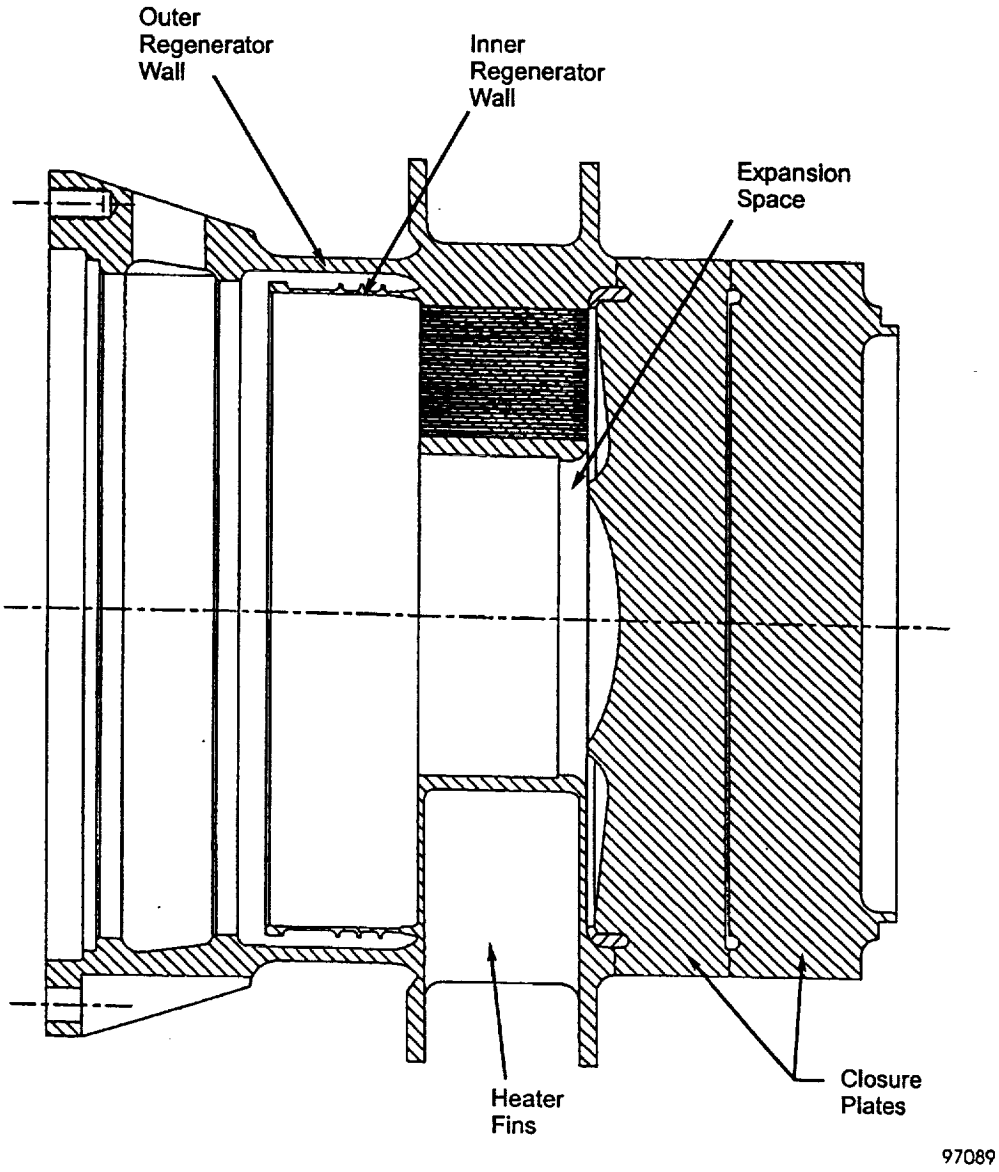

Figure 14. Heater Head Assembly

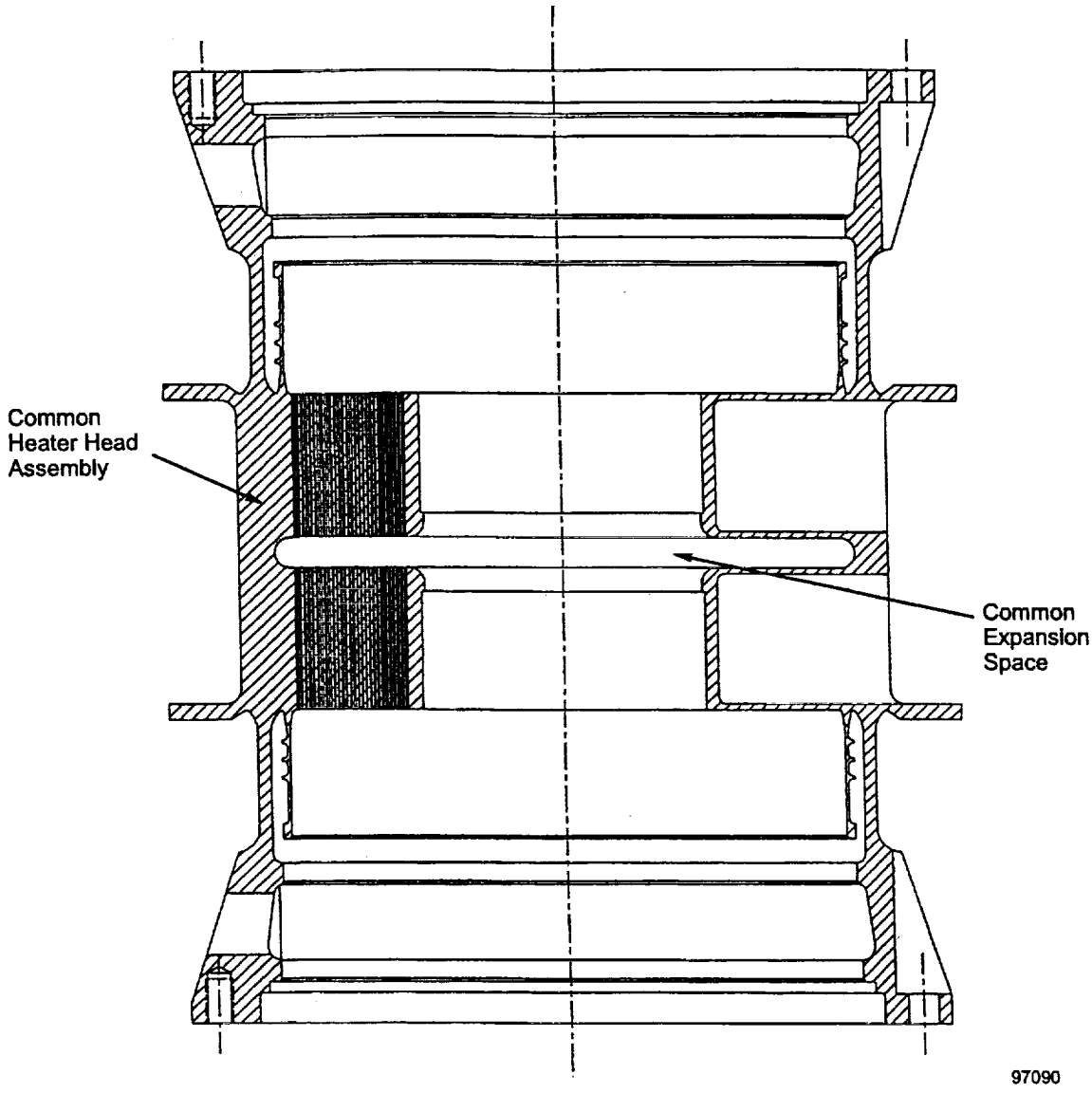

Figure 15. Opposed-Cylinder Configuration of Starfish Heater Head Design

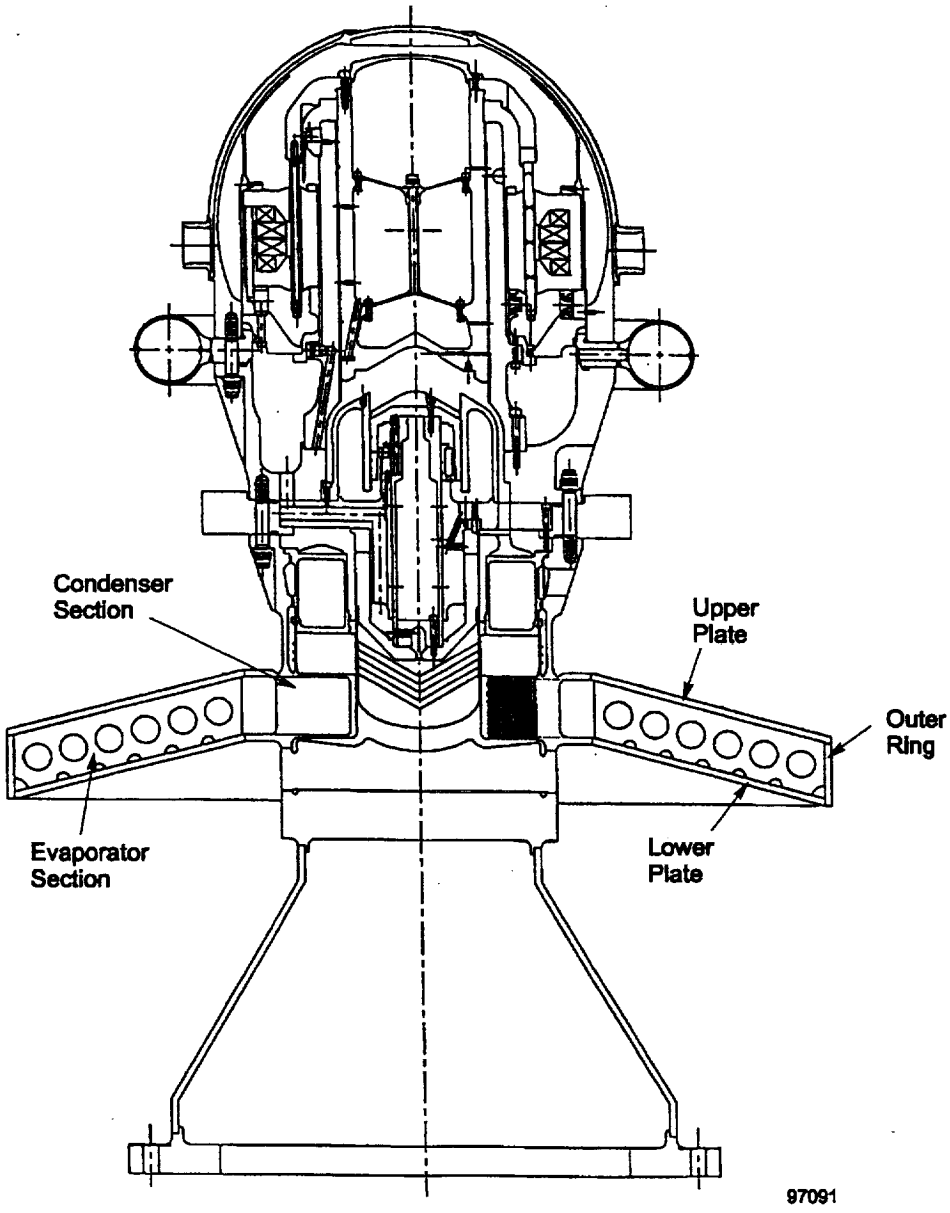

Figure 16. Heat Pipe Construction

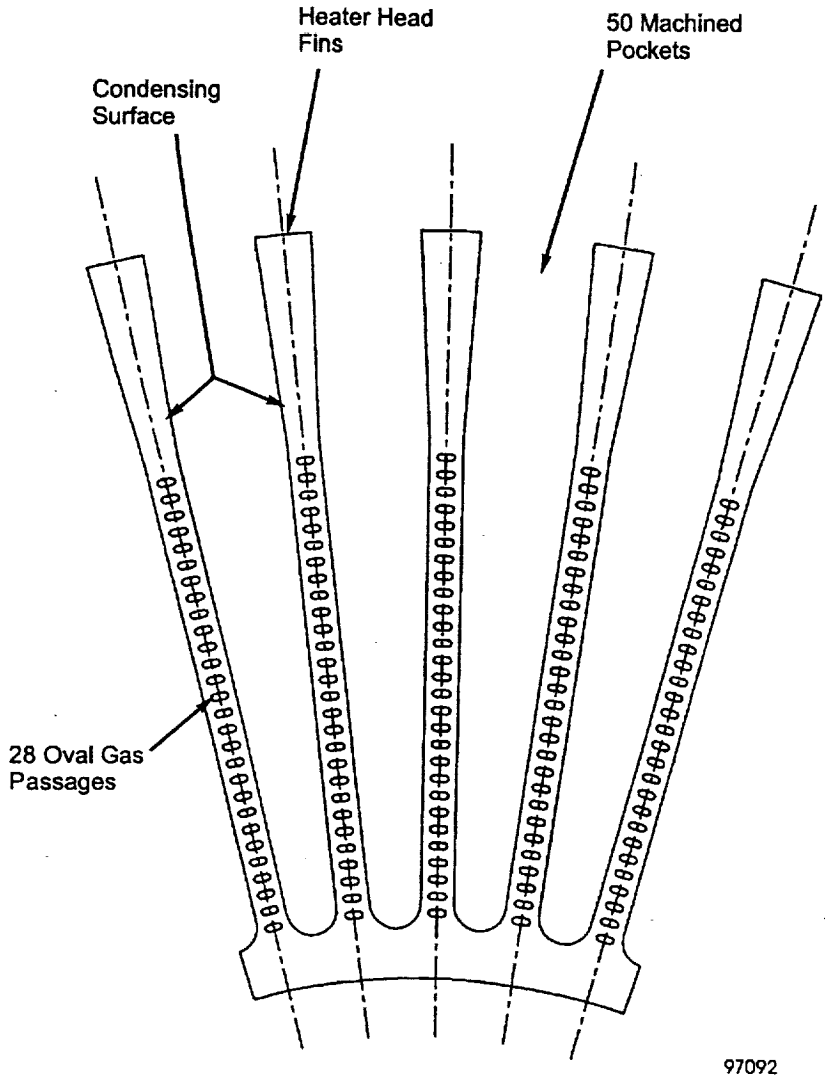

Figure 17. Initial Gas Passage Geometry of Heater Head Section

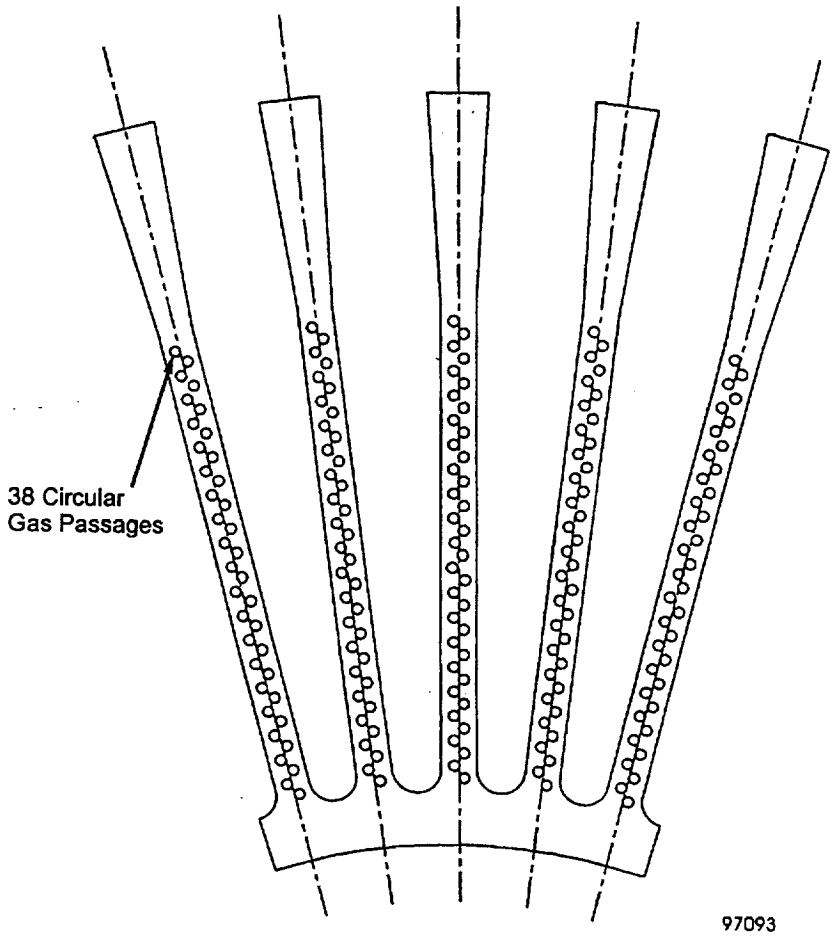

Figure 18. Final Gas Passage Geometry of Heater Head Section

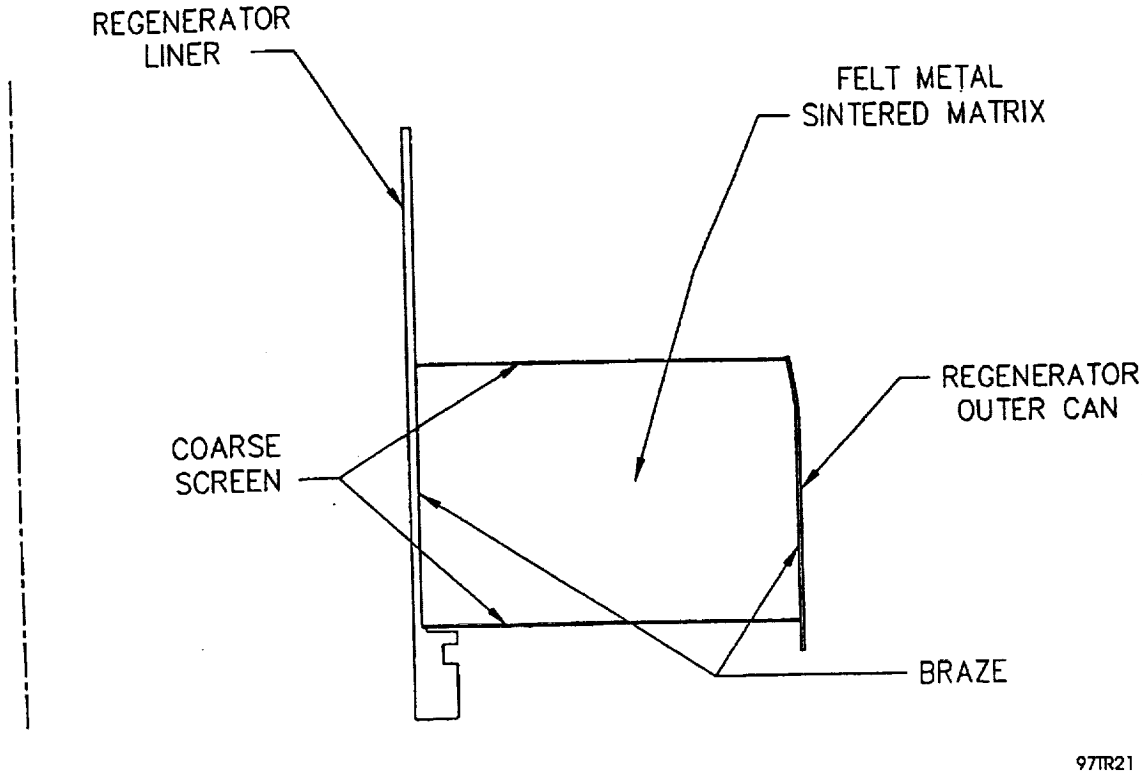

Figure 19. Regenerator Assembly

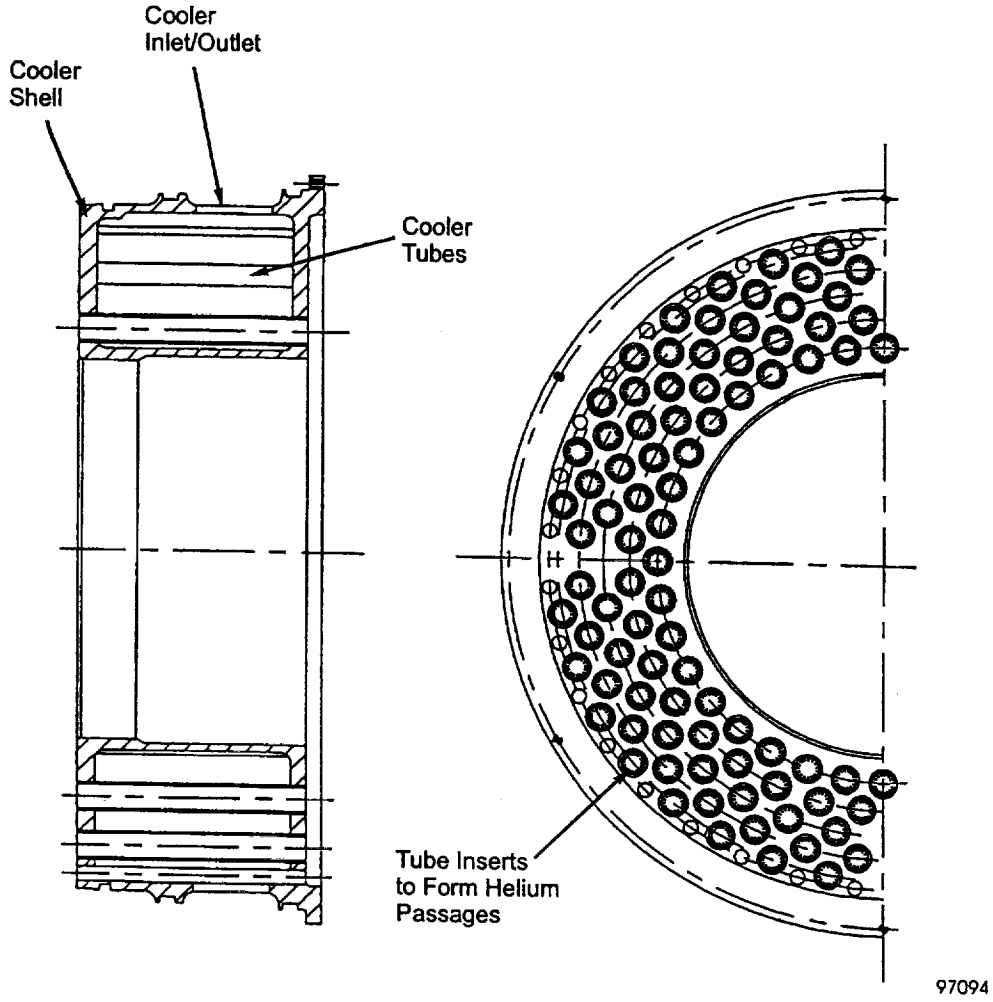

Figure 20. Cooler Arrangement

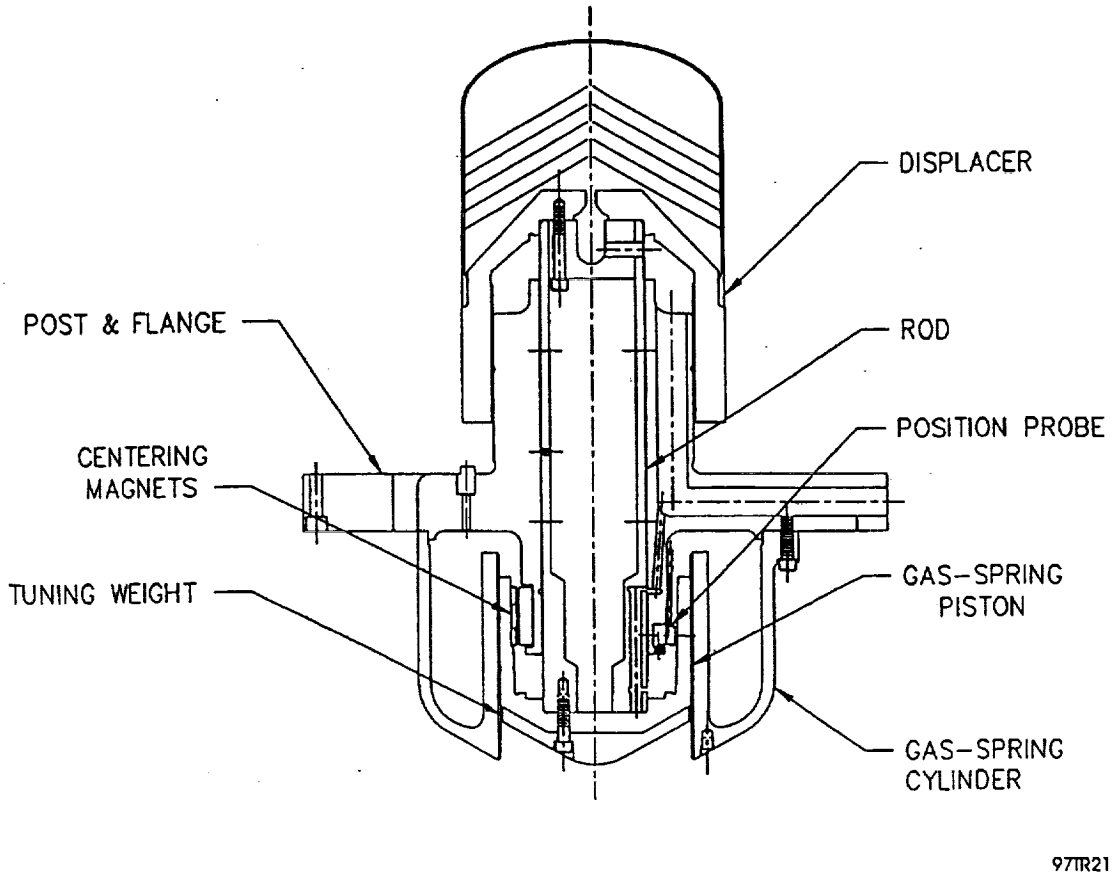

Figure 21. Displacer Drive Assembly

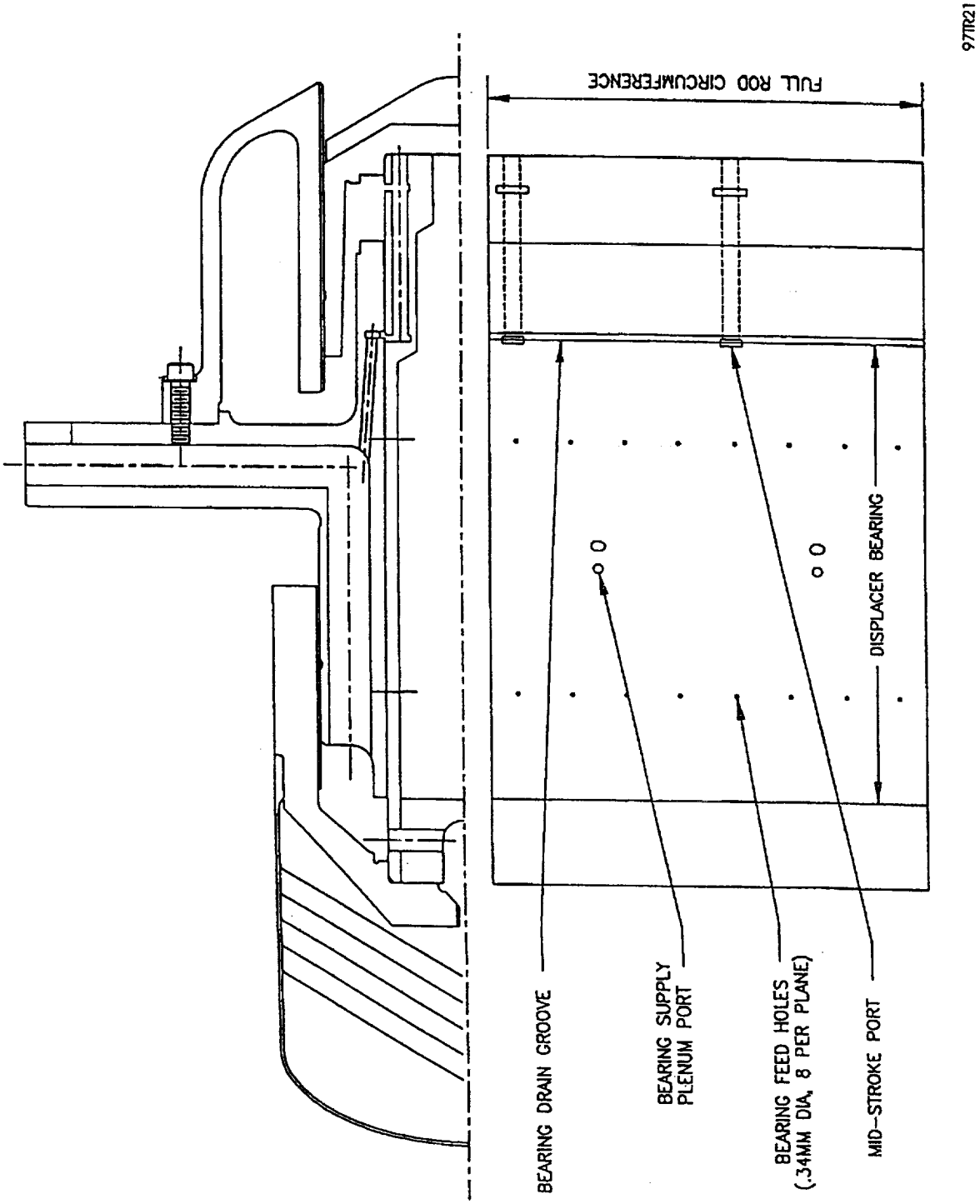

Figure 22. Location of Bearing Orifices, Drain Grooves, and Drain Ports in Displacer Assembly

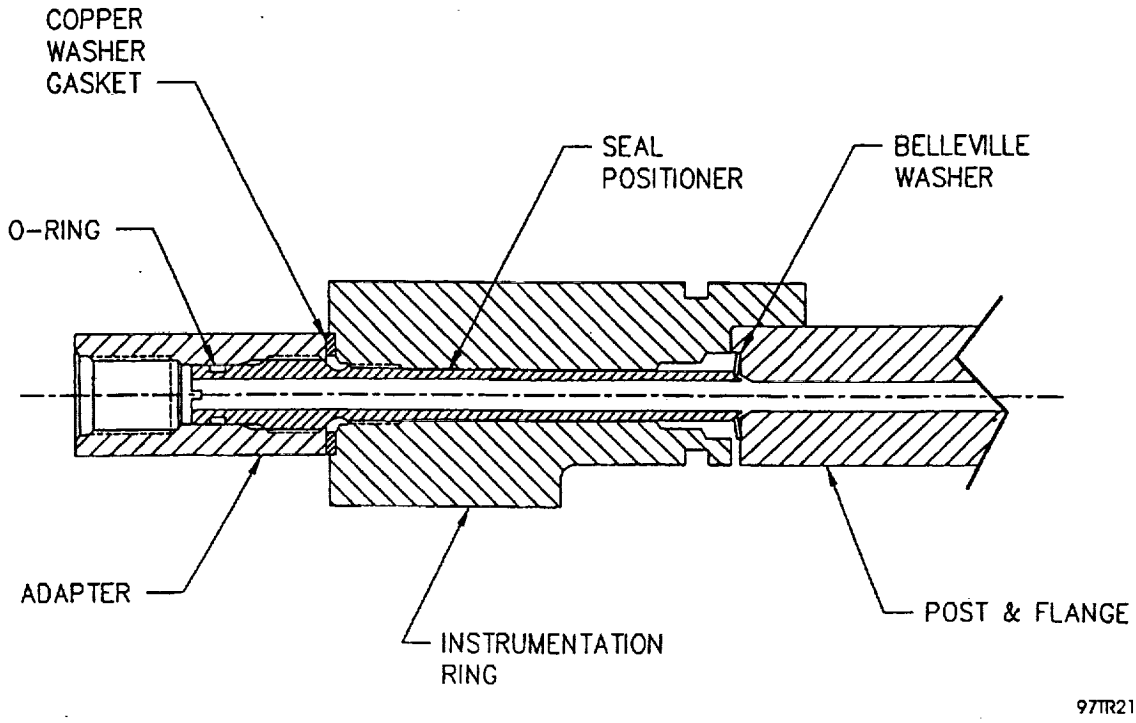

Figure 23. Typical Feedthrough Assembly for Static Seal Instrumentation Ring

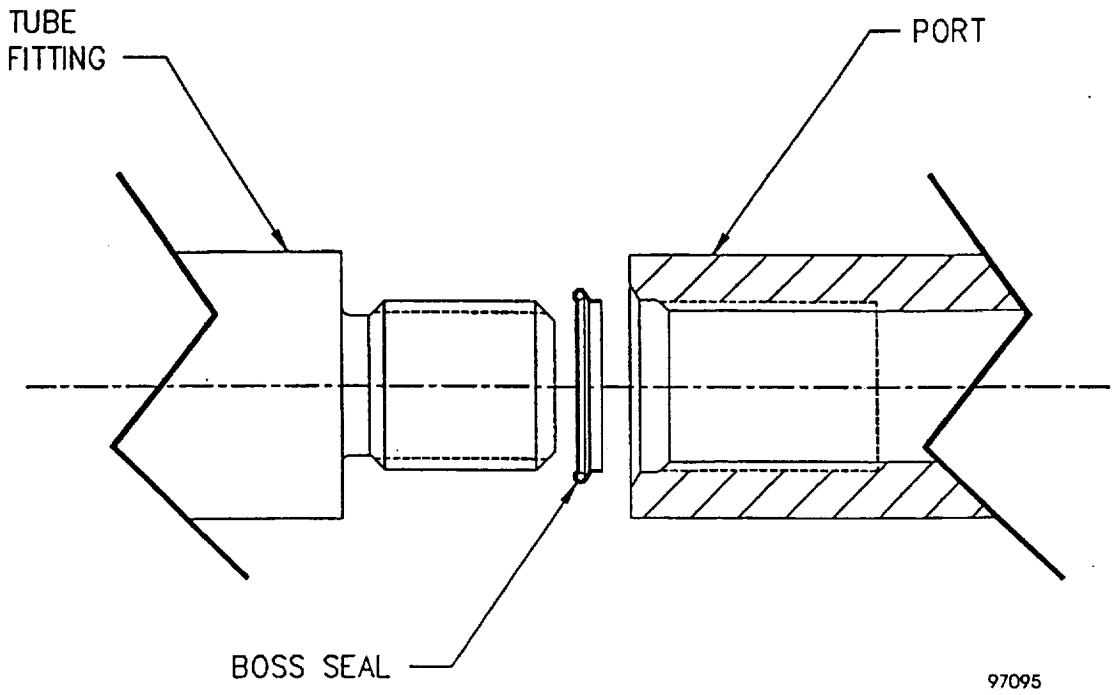

Figure 24. Straight Thread Fitting with MS Boss Seal

4.0 STIRLING THERMODYNAMICS AND DYNAMICS DESIGN

The MTI-developed harmonic analysis and design program for Stirling-cycle machines, HFAST (version 1.02), was used for the thermodynamics and dynamics design of the engine (Huang, 1992). HFAST analyzes the cyclic steady-state performance of the engine by solving one-dimensional governing equations of the working gas (continuity, momentum, and energy equations) through harmonic variables. The computational efficiency of the code allows parametric studies and optimization of the engine geometry to be performed quickly.

The thermodynamic design of the engine was guided by experience with the SPRE/SPDE engines. The HFAST code (version 1.02) was used to predict and compare the SPRE/SPDE engine performance. It was found that in order to match the test results, the thermodynamic inputs of the code needed to be modified by using:

- A multiplier of 1.75 for the regenerator friction factor.
- A compression-space seal clearance that was 2.5 times the clearance at room temperature. The increased operating clearance was possible if, during engine operation, the cylinder temperature was 20°C above the piston temperature. This was consistent with the known fact that there was significant eddy current loss in the steel cylinder structure to cause the increase in cylinder temperature.

For the gas springs, it was found that, by using the room temperature clearances,

- The predicted displacer gas spring losses were consistent with the measured results.
- The predicted piston gas spring losses were lower than the tests.

The regenerator friction factor multiplier of 1.75 obtained from the SPRE/SPDE performance study was used throughout the design phase of the CTPC . Since the multiplier increased the pumping power in the regenerator, the predicted thermodynamic performance of the engine was more conservative than if the multiplier was not used.

Since the CTPC and SPRE had the same required electrical power output at the design point, the SPRE/SPDE geometry was used as the starting point. Unconstrained HFAST optimization of the SPRE/SPDE geometry indicated that significant improvement of the thermodynamic efficiency could be achieved by:

- Increasing the regenerator frontal area.
- Reducing the heater and cooler lengths.
- Decreasing the operating frequency.

The above findings were used as the design guidelines for the CTPC.

In view of the potential errors of the code performance prediction, performance margins were added to the design goals so that:

- The electrical power output and efficiency of the engine at the nominal design operating conditions (1050 K heater and 525 K cooler temperatures) were set to be 14 kW and 25%, respectively. These design goals were higher than the minimum requirements of the engine: 12.5 kW electrical power output and 20% efficiency.
- A 20% overstroke capability was provided before the engagement of the end-of-stroke dampers.

To select the CTPC nominal design operating point, a parametric study of the Stirling-cycle performance was performed for a wide range of mean pressures, operating frequencies, piston strokes, and displacer phase angles. For each combination of parameters, a constrained optimization was performed to select the optimum heat exchanger (heater, cooler, regenerator) geometry that gave the maximum system efficiency. The optimization constraints included:

- The electrical power output of the engine was maintained at the required design level.
- The structural and geometrical constraints of the engine were satisfied.

After the constrained optimization, the efficiency and specific mass relationship was examined and the best combination was selected.

The results of the parametric study were:

- Performance improved with increasing mean pressure. A mean engine pressure of 15 MPa was selected based on past experience.
- Displacer phase angle of 60 to 70 degrees relative to the power piston gave the best efficiency and power characteristics.
- 14-mm piston amplitude at 70-Hz operating frequency gave the maximum efficiency without significant specific mass penalty. Piston amplitudes above 14 mm made the gas spring design increasingly difficult and resulted in lower mechanical efficiency.
- For the displacer, using the same stroke but a smaller diameter (relative to the power piston) gave a balanced overall engine design.

Extensive sensitivity study of the engine performance with respect to variations in the heat exchanger geometry at the above selected nominal operating conditions was performed to determine the risk and trade-offs. The sensitivity study included the following heat exchanger geometry parameters: number of heater passages, heater length and passage diameter, regenerator frontal area, regenerator length, matrix porosity and wire diameter, number of cooler passages, cooler length, cooler channel width and height, and the operating offsets of the displacer and piston. The performance sensitivity with respect to the heat transfer and friction coefficients as used by the code was also studied.

After selecting the operating conditions and heat exchanger geometries, the piston mass, gas spring volume, and the linear alternator characteristics were determined in order to obtain the required piston dynamics. To simulate the dynamic behavior of the engine, a system of governing equations for an equivalent mass-damper-spring model was used. Although the governing equations of the engine dynamics were nonlinear in nature, the equations were linearized near the point of operation so that conventional analysis methods for a linear system could be used.

The piston dynamics were determined by the balance of forces of the Stirling cycle, gas springs, and the linear alternator. The Stirling-cycle forces acting on the pistons were obtained from the HFAST code simulation and were represented in terms of the piston motions via proportional constants. The gas springs were represented by their damping and stiffness coefficients. The damping coefficients of the gas springs were determined by a detailed analysis of the power losses, which included the hysteresis, leakage, bearing, porting, and shuttle losses. The bearing loss was obtained from the MTI-developed bearing codes. The porting losses were obtained from an MTI-developed time-stepping code. The linear alternator was represented by an equivalent circuit that included effects of the coil inductance, the core losses, the copper losses, the tuning capacitance, and the electric load. Some of the parameter values used in the model were obtained from a more detailed analysis using an MTI-developed linear alternator code (LPMMA).

Figure 25 shows a representative phasor diagram of the force balance on the displacer for steady-state operation. Figure 26 shows a representative phasor diagram of the force balance on the power piston for steady-state operation.

The dynamic behavior of the engine was determined by solving the complex eigenvalues of the equivalent mass-damper-spring system. The real parts of the complex eigenvalues corresponded to the transient behavior of the system. Positive values indicated a growing response with time and were usually associated with an unstable situation. Negative values indicated a decaying response with time. The steady-state operation of the engine was associated with eigenvalues whose real parts were zero. For these steady-state eigenvalues, the imaginary parts were used to determine the operating frequency, while the eigenvectors were used to determine the amplitude and phase angles of the response. Here the response of the dynamic system refers to the displacer and power piston motions and the current in the linear alternator electrical circuit.

The simulation of the complete engine required the iteration between the HFAST prediction of the thermodynamic performance and the eigenvalue solution of the equivalent mass-damper-spring model of the piston dynamics. The iteration continued until convergence was reached.

The transient behavior of the engine was also studied by using a commercial integration package, SIMNON. SIMNON numerically integrated the governing equations of the equivalent mass-damper-spring model of the engine. The time history of the system response to a specified input could be graphically displayed to gain additional insight. To perform the simulation, the thermodynamic performance of the engine was provided by the HFAST prediction. The numerical integration was more flexible than the eigenvalue formulation and allowed the nonlinear behavior of the system to be modeled also.

Allowances were made for possible errors in the predicted piston dynamics. Interchangeable displacer tuning masses (0.260 to 0.587 kg) were made by using materials of different densities (steel and tungsten). Interchangeable aft displacer gas spring pistons were made to give different effective rod areas (4.7080E-4 and 5.5467E-4 m^2). Combinations of the various displacer tuning masses and effective rod areas allowed the piston dynamics to be fine-tuned during tests.

The nominal geometry of the engine design, as used for the first heat pipe tests, is given in Table 3.

After completion of the CTPC design, HFAST was updated to version 2.00 under the NASA contract "Stirling Engine Harmonic Code and Validation Analysis" (contract number NAS3-25330). Version 2.00 uses an improved solution method that removed several known deficiencies of earlier versions of the HFAST code.

For example, version 2.00 uses the same set of governing equations for manifolds as for heat exchangers. Version 1.02 treated manifolds differently and less rigorously due to potential numerical problems. Because of this modeling deficiency, the plenums on the hot and cold ends of the regenerator were lumped into the expansion space and compression space, respectively, in the analysis of the CTPC design. The revised HFAST code allows the regenerator plenums to be placed in their correct locations.

When HFAST version 2.00 was used, the predicted thermodynamic performance of the engine was found to be about 15% less than version 1.02. Since the manufacturing of the engine was already underway, it was impossible to revise the design. Fortunately, the engine was designed with a performance margin and an overstroke capability. As presented below, with the revised engine performance prediction, the program goal of 12.5-kW electrical power output could still be achieved.

The revised (HFAST version 2.00) prediction of the engine performance was made at the design operating conditions (15 MPa, 1050 K heater, and 525 K cooler temperatures) without the use of adjustment factors. As compared to the original design analysis made with HFAST version 1.02, the revised prediction had a smaller pressure drop in the working space and, consequently, a higher displacer amplitude. By limiting the displacer amplitude to 15 mm (versus 14 mm), the predicted piston amplitude was 13.5 mm (versus 14 mm). Thus, the displacer-piston amplitude ratio was 1.11. The corresponding operating frequency was 67.3 Hz instead of 70 Hz.

Figure 27 shows the Stirling-cycle power flow as compared to the ideal Carnot cycle (HFAST version 1.02). As shown, the predicted cycle efficiency was 56% of the Carnot-cycle efficiency. The difference between the predicted cycle power and the Carnot-cycle power represented the irreversible power loss that was converted into additional rejected heat. The irreversible power loss was a result of the convective heat transfer between the gas and the wall (and the regenerator matrix), the hysteresis heat transfer driven by the periodic pressure wave, the thermal mixing of the working gas, the pressure drop due to fluid friction and flow distribution, the heat conduction in the gas and the wall, the leakage flow through seals, and the appendix gap shuttle heat transfer. As noted, the heat transfer (convection and conduction) contributed the majority of the irreversible power loss. The pumping power loss represented a relatively small percentage (15.6%) of the total irreversible power loss.

Figure 28 shows the engine power flow. Accounting for gas spring losses, the mechanical efficiency of the engine was estimated to be 89%. The gas spring losses include the hysteresis heat transfer, the

leakage flow through seals, the port flow, the bearing flow, the shuttle fluid flow through connecting ducts, and the hysteresis and eddy current losses of the centering magnet (of the displacer). The alternator efficiency was estimated to be 88%, which was based on the estimated structural eddy current loss as well as the coil loss, the stator lamination loss, and the magnet (hysteresis and eddy current) losses. By using the above mechanical and alternator efficiencies, the predicted system power and efficiency were 12.96 kW and 22%, respectively. Both exceeded the minimum performance goals.

References

Huang, S. C. "HFAST: A Harmonic Analysis Program for Stirling Cycles." *Proceedings of the 27th Intersociety Energy Conversion Engineering Conference*, San Diego, CA, Vol. 5, pp. 5.47 to 5.52.

Table 3. CTPC Geometry

General and Nominal Design Conditions	
Number of cylinders	1
Type	Free-piston gamma configuration
Working gas	Helium
Frequency	70 Hz
Mean pressure	15 MPa
Heater wall temperature (working gas side)	1050 K
Cooler wall temperature (working gas side)	525 K
Heater/cooler wall temperature ratio	2
Piston and displacer amplitudes	14 mm
Displacer phase angle	67 degrees
Electrical power output at linear alternator terminals	12.5 kW
Engine efficiency	>20 %
Displacer	
Dome material	Inconel 718
Diameter (hot side)	1.1430E-1 m
Piston area (hot side)	1.0261E-2 m^2
Piston area (cold side)	9.7902E-3 m^2
Effective rod area	4.7080E-4 m^2
Amplitude at initial snubber engagement	1.6502E-2 m
Amplitude at final snubber engagement	1.9304E-2 m
Dome thickness	1.0160E-3 m
Conduction length	3.7640E-2 m
Mass (with steel tuning mass of 0.260 kg)	2.17 kg
Power Piston	
Wall material	Beryllium
Diameter	1.3716E-1 m
Piston area	1.4776E-2 m^2
Amplitude at initial snubber engagement	1.680E-2 m
Amplitude at full snubber engagement	2.0066E-2 m
Massp (includes plunger assembly)	13.176 kg
Appendix Gap	
Diameter	1.1430E-1 m
Effective gap (cold end)	1.3678E-4 m
Effective gap (hot end)	4.8884E-4 m
Effective gap (middle)	3.1113E-4 m
Effective length	8.7000E-2 m

97TR21

Table 3. continued

Expansion Space	
Wall material	Inconel 718
Mean surface area	7.2730E-2 m^2
Dead volume	2.2982E-4 m^3
Mean volume	4.2790E-4 m^3
Heater	
Type	Staggered circular passages in starfish fins
Heating element	Electrically heated radiant heater or heat pipe
Wall material	Inconel 718
Number of starfish fins	50
Number of circular passages per fin	38
Total number of circular passages	1900
Circular passage inside diameter	1.0160E-3 m
Length (total)	5.9690E-2 m
Length (active)	5.4610E-2 m
Length (inactive - top manifold)	2.5400E-3 m
Length (inactive - bottom manifold)	2.5400E-3 m
Wall thickness (approximate)	7.5000E-4 m
Connecting Duct 1 (between heater and regenerator)	
Type	Annual volume for regenerator top stand-off wire
Number of channels	1
Channel height	5.4300E-2 m
Channel width	5.3800E-1 m
Length	7.6200E-4 m
Regenerator	
Type	Annular screen matrix
Matrix material	SS 347
Wall material (outer)	Inconel 718
Wall material (inner)	Inconel 718
Matrix diameter (outer)	2.2780E-1
Matrix diameter (inner)	1.1690E-1 m
Matrix frontal area	2.9926E-2 m^2
Wire diameter	5.0800E-5 m
Porosity (design)	75.0%
Porosity (measured)	72.8%
Length	3.7600E-2 m
Wall thickness (outer and inner)	3.1750E-4 m and 1.2700E-3 m

97TR21

Table 3. continued

Connecting Duct 2 (between regenerator and cooler)	
Type	Annular volume for regenerator bottom stand-off wire
Number of channels	1
Channel height	5.5450E-2 m
Channel width	5.4153E-1 m
Length	7.6200E-4 m
Cooler	
Type	Modular internally finned tube for gas passages Cross-flow heat exchanger using paratherm oil as coolant
Tube shell material	Inconel 718
Fin material	Nickel 270
Number of tubes	172
Tube outside diameter	9.5000E-3 m
Tube inside diameter	8.0000E-3 m
Number of channels per tube	15
Total number of channels	2580
Channel height (fin height)	1.4640E-3 m
Channel width	5.3340E-4 m
Length (total)	7.4930E-2 m
Length (active)	6.4770E-2 m
Length (inactive - top manifold)	5.0800E-3 m
Length (inactive - bottom manifold)	5.0800E-3 m
Fin thickness (average)	9.1270E-4 m
Connecting Duct 3 (below cooler, excluding compression space volume below displacer)	
Wall material	Inconel 718
Number of channels	1
Channel height	4.3180E-2 m
Channel width	5.5850E-1 m
Length	6.1750E-3 m
Connecting Duct 4 (cold connecting duct)	
Wall material	Beryllium
Number of channels	8
Channel height	3.4540E-2 m
Channel width	1.0920E-2 m
Length	4.1000E-2 m

97TR21

Table 3. continued

Connecting Duct 5 (connecting duct)	
Wall material	Beryllium
Number of channels	1
Channel height	5.9690E-3 m
Channel width	5.0710E-1 m
Length	9.9505E-2 m
Compression Space (including volume below displacer)	
Wall material	Beryllium
Mean surface area	9.4420E-2 m^2
Dead volume	1.4980E-4 m^3
Mean volume	6.3529E-4 m^3
Aft (load side) Displacer Gas Spring	
Mean volume	8.7072E-4 m^3
Piston area	3.7865E-3 m^2
Wetted surface area (mean value)	1.5000E-1 m^2
Forward (heater side) Displacer Gas Spring	
Mean volume	7.9509E-3 m^3
Piston area	4.2573E-3 m^2
Wetted surface area (mean value)	7.2000E-1 m^2
Piston Gas Spring	
Mean volume	9.5065E-3 m^3
Piston area	1.4776E-2 m^2
Wetted surface area (mean value, excluding alternator lamination surface area)	1.7400E00 m^2
Seal (aft displacer gas spring to compression space)	
Effective length	5.1562E-2 m
Clearance (room temperature)	1.8593E-5 m
Clearance (design temperature)	2.1209E-5 m
Diameter	8.3135E-2 m
Eccentricity	0.8000E00
Seal (aft displacer gas spring to forward displacer gas spring)	
Effective length	2.6289E-2 m
Clearance (room temperature)	1.4161E-5 m
Clearance (design temperature)	1.5113E-5 m
Diameter	4.5720E-2 m
Eccentricity	5.0000E-1

97TR21

Table 3. continued

Seal (forward displacer gas spring to compression space)	
Effective length	4.4450E-2 m
Clearance (room temperature)	1.9685E-5 m
Clearance (design temperature)	2.1768E-5 m
Diameter	8.6665E-2 m
Eccentricity	0.8000E00
Seal (compression space to piston bearing drain plenum)	
Effective length	5.1816E-2 m
Clearance (room temperature)	1.2700E-5 m
Clearance (design temperature)	1.5900E-5 m
Diameter	1.3716E-1 m
Eccentricity	5.0000E-1
Seal (piston gas spring to piston bearing drain plenum)	
Effective length	3.7084E-2 m
Clearance (room temperature)	1.2700E-5 m
Clearance (design temperature)	1.5900E-5 m
Diameter	1.3716E-1 m
Eccentricity	5.0000E-1
Seal (expansion space to compression space)	
Effective length	5.0800E-2 m
Clearance	7.6200E-5 m
Diameter	1.1430E-1 m
Eccentricity	2.5000E-1

97TR21

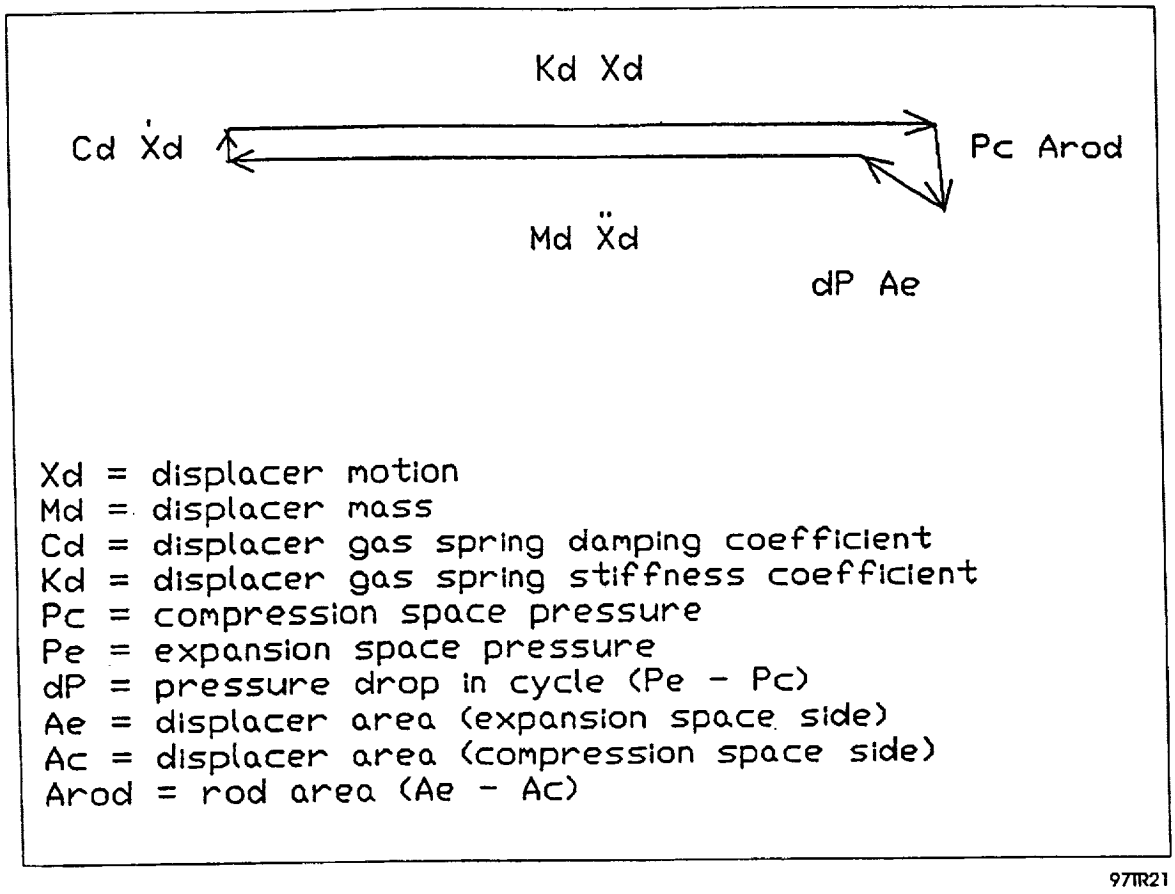

Figure 25. Phasor Diagram of Force Balance on Displacer

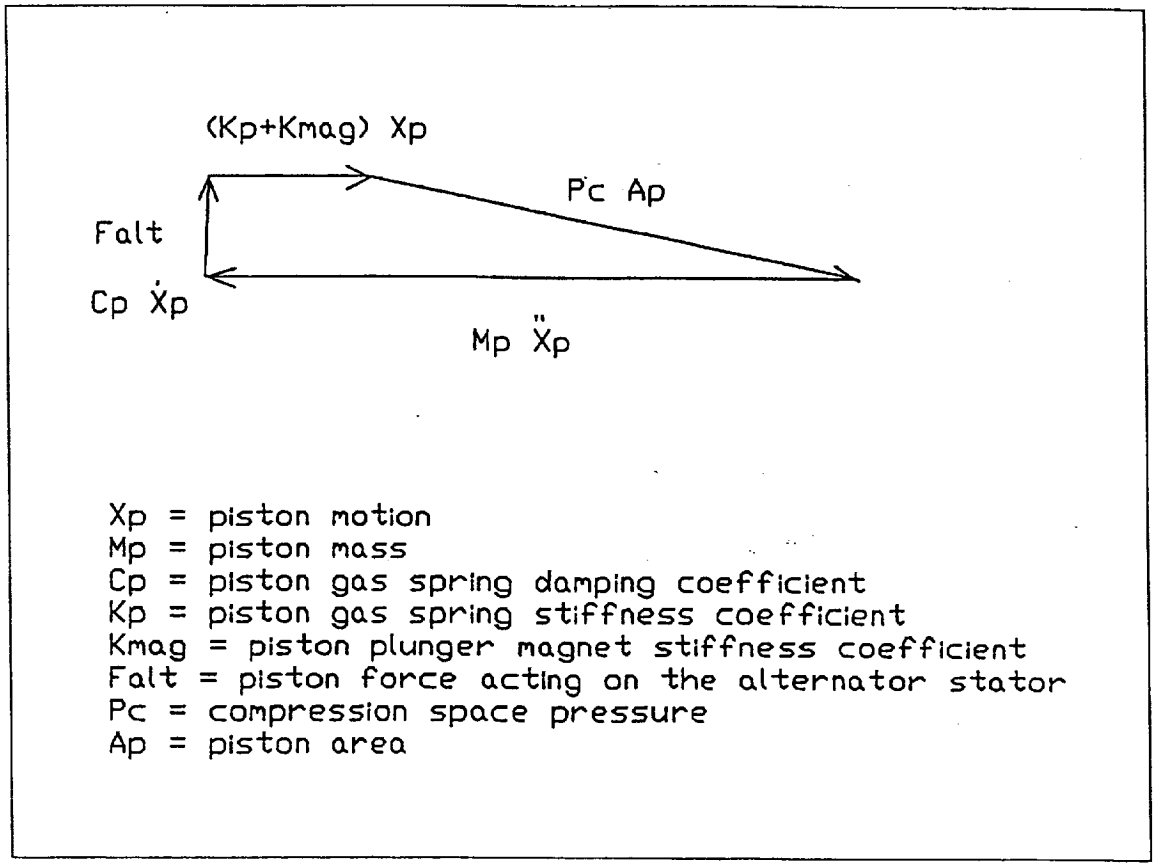

Figure 26. Phasor Diagram of Force Balance on Power Piston

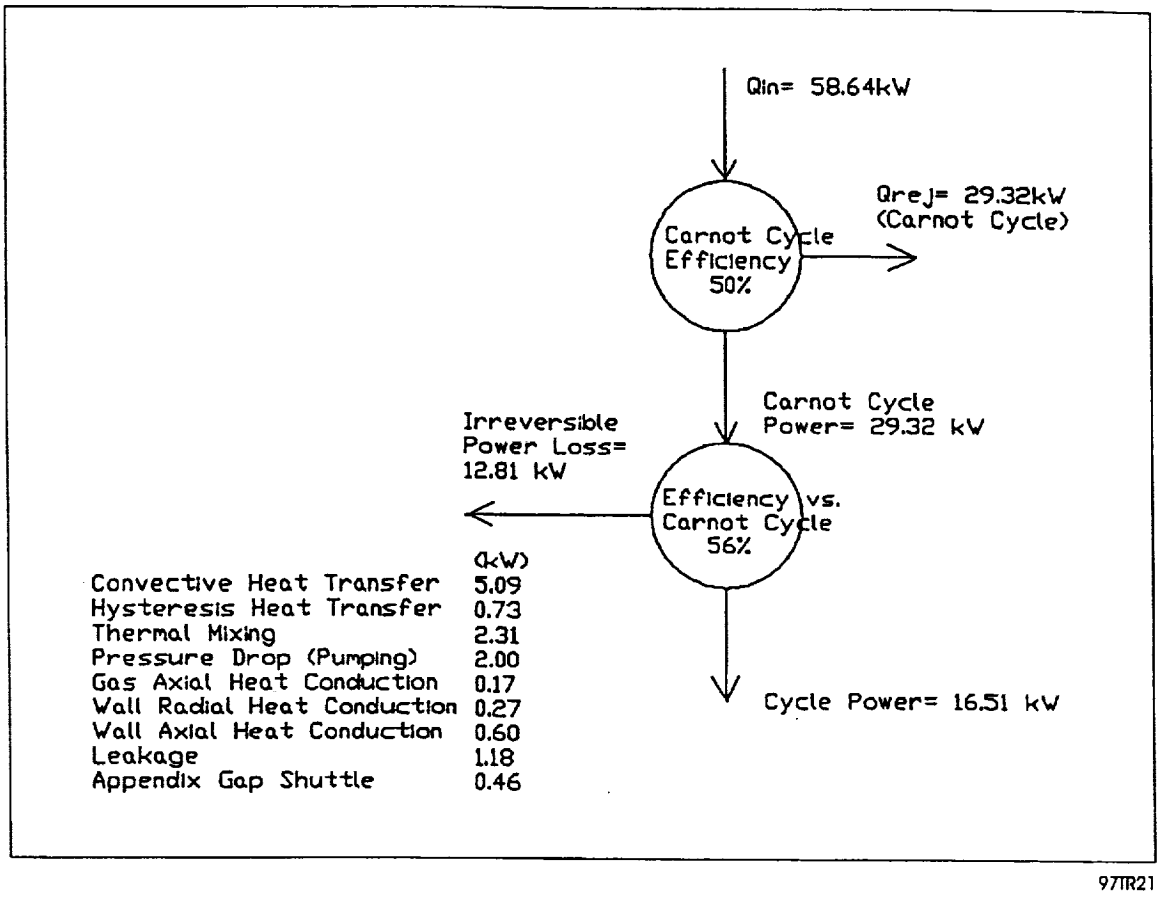

Figure 27. CTPC Stirling-Cycle Efficiency

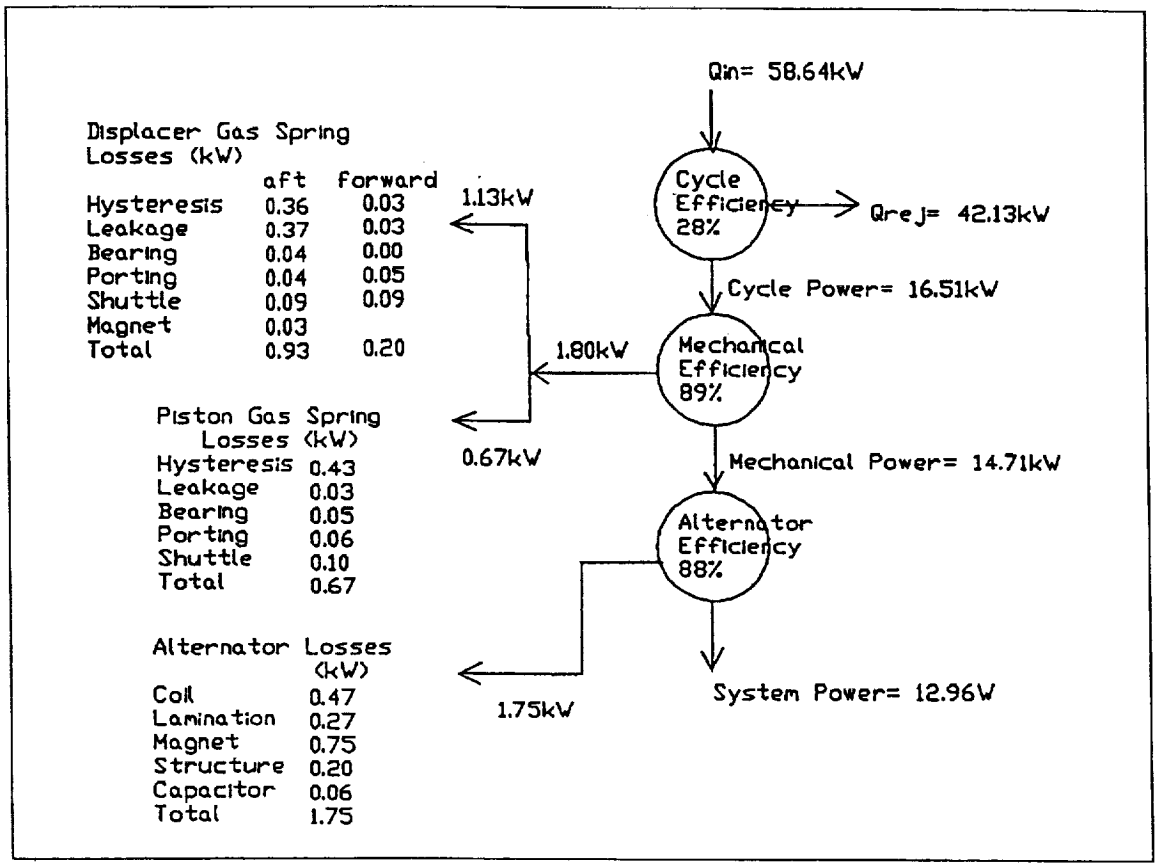

Figure 28. CTPC Power Flow Diagram

5.0 DISPLACER AND POWER PISTON DRIVE DESIGN

5.1 Introduction

The displacer and the power piston drive assemblies cause the flow processes that activate the heat exchangers to generate mechanical power and cause the alternator plunger motion that generates electrical power. In long-life Stirling engines, these reciprocating assemblies rely on the successful operation of three basic elements: clearance seals, gas springs, and noncontacting gas bearings.

5.1.1 Clearance Seals

A clearance seal is based on the flow restriction presented by the close clearance between non-contacting surfaces. Leakage through a clearance seal results in a power loss that is proportional to the radial clearance cubed and is inversely proportional to the seal length. Therefore, the primary design consideration relative to effective sealing is maintaining tight operating clearances. A secondary design consideration is to augment the tight clearance with long seal lengths. The CTPC has been designed with clearances in the 12- to 18-μm (0.5- to 0.7-mil) range. The tighter clearances are primarily for seals whose clearances are controlled directly by adjoining gas bearings, and the looser clearances are for seals whose clearances are controlled indirectly through assembly stack-ups from bearing surfaces.

The major challenge in the CTPC design was to ensure proper mechanical operation of the power module cold end reciprocating elements (the displacer and power piston assemblies) at the elevated temperature of 525 K. Dynamic operation of each unit at elevated temperature is a challenge since thermal growth, thermal distortions, and misalignments can, if not carefully controlled, reduce the already tight seal clearances and cause the free pistons to bind. In this regard, the displacer and power piston assemblies must be designed to maintain their clearances at the elevated temperature. The actual operating clearances depend on many factors, such as:

- Manufacturing tolerances and stack-up of tolerances during assembly.
- Wear and assembly damage to critical pilots and flat surfaces during repeated assembly and disassembly.
- Distortion resulting from assembly stresses.
- Distortion resulting from relaxation of residual stresses and aging of the hardware with time.
- Distortion of parts due to stresses imposed by engine pressure.
- Distortion of parts due to thermal effects, such as temperature gradients and variations in thermal expansion coefficients.

The above factors were taken into consideration during the preliminary design of the overall assembly and during the detail design of the individual components. Tolerances were held to less than 10% of the nominal clearance on all critical dimensions. Geometric control was specified in such a way as to minimize the cumulative number of stack-ups. All bolted joints were carefully designed such that minimal distortion due to the clamping load occurred in the part adjacent to the clearance surface. Wall thicknesses were sized to reduce pressure wave distortions to acceptable levels. For all tight fitting pilots, special arrangements were made to reduce the amount of wear that could occur during assembly and disassembly. Where feasible, the female part would be heated slightly to increase the sliding fit with the mating male part. Once cool, the original design fit was obtained.

On parts that could not be heated practically, fixtures were designed to align and guide the assembly and disassembly. Beryllium is a highly stable material and can retain very precise dimensions over long periods of time. Because beryllium is a relatively brittle material (tensile elongations of 2%), a significant amount of residual stress cannot build up due to machining. Beryllium is also very isotropic. Maximum variations in the coefficient of thermal expansion is less than 2% and occurs between the longitudinal and transverse directions. As a precaution, all beryllium hardware was machined with its centerline axis parallel to the longitudinal axis of the pressed block. Temperature variations in clearance seal areas, due

to losses generated in gas spring and working space volumes, were calculated and their impact on seal clearances was taken into account during the preliminary design phase. The results of a preliminary thermal analysis showing the operating temperatures at various locations are given in Figure 29. The differences in operating temperatures of each element impact the seal clearance gaps.

5.1.2 Gas Springs

The gas springs provide the reactive power flow required to alternately accelerate and decelerate the reciprocating pistons. The gas spring consists of a piston reciprocating in a closed-end cylinder filled with working fluid generally at engine mean pressure and at a temperature close to the cooler temperature. Reactive energy is stored as the fluid is compressed and is released as the fluid is expanded. Leakage losses occur in the clearance seal between the piston and the cylinder, and thermal hysteresis losses occur on the walls of the cylinder and face of the piston. In addition, gas springs have centering losses which are introduced by the porting system used to maintain the midstroke location of the gas spring piston. The total loss in the gas spring is proportional to the maximum amount of energy that the gas spring needs to store and, therefore, is proportional to the mass of the reciprocating elements. For the CTPC, the displacer and the power piston reciprocating elements are made of beryllium. Beryllium has relatively high dimensional stability, high modulus of elasticity, high thermal conductivity, and low density. For example, the elastic modulus to density ratio for beryllium is 6.6 times greater than that for steel. The thermal conductivity of beryllium is more than twice that of steel.

Gas springs are not the only way to store reactive energy in free-piston machines. Mechanical, liquid, and magnetic springs can also perform the same function. Mechanical springs impose stroke limitations and reliability concerns, liquid springs present sealing problems, and magnetic springs tend to be bulky.

5.1.3 Gas Bearings

The key design considerations for gas bearings are dynamic stability, response to static and dynamic loads, size and weight (length, diameter), power dissipation, achievable clearance levels, and complexity. The CTPC has been designed with hydrostatic gas bearings to provide radial support for the reciprocating elements. The CTPC displacer and power piston bearings have been designed such that the pressure across the bearings can be supplied from either gas springs internal to the engine (internally pumped bearing) or by external gas loops charged by boost pumps (externally pumped bearing). For the power piston, internally pumped bearings use a different piston from that used when the bearings are externally pumped (Figure 30). For the displacer, internally pumped bearings use a different rod from that used when the bearings are externally pumped (Figure 31). Both approaches have been successfully demonstrated in the cold-end motoring tests and engine tests. Internally pumped bearings are used for operation at full pressure (150 bar). The externally pumped option is available for initial hardware check out and testing at low engine pressures.

For the internally pumped hydrostatic bearings, the reciprocating members must undergo a start-up process that has the potential to result in surface wear. Bearing surface coatings have to be selected that are low in static and dynamic friction to allow start-up without excessive power dissipation, while not generating excessive wear and debris during repeated bearing starts. To select appropriate wear couple surfaces, friction and wear tests were performed on various surfaces at the CTPC cold-end operating temperature. Based on these tests, carbon graphite and aluminum oxide were selected. In the engine, the carbon graphite was installed as a shrink-fit sleeve in the bores and then machined to final dimension. The aluminum oxide was flame sprayed on the outer surface of the reciprocating pistons and then ground to finished dimensions.

5.2 Power Piston Drive: Internally Pumped Bearing Configuration

The purpose of the power piston drive is to alternately compress and expand the engine working fluid and to transfer the engine power to the alternator plunger. The power piston drive consists of a moving assembly (the power piston proper and alternator plunger that are mechanically connected through a

bolted joint) and the power piston cylinder. The purpose of the power piston cylinder is to support and guide the power piston as well as support the alternator stator. The volume enclosed by the power piston cylinder and the engine cold-side pressure vessel forms the power piston gas spring. The power piston spring action is provided by the power piston gas spring as well as the compression space. The power piston gas spring parameters were given earlier in Table 3. The power piston gas spring has a pressure amplitude of 5.5 bar at design conditions (150-bar mean pressure and 28-mm stroke). Recall that the maximum gas spring pressure amplitude is 5.5 bar at full stroke. The reciprocating mass of the piston assembly is 13.176 kg (29.05 lb), out of which the compression space pressure wave carries 9.85 kg (21.7 lb). The remaining 3.19 kg (7 lb) are carried by the power piston gas spring.

5.2.1 Bearing

Figures 32, 33, and 34 show the arrangement of the internally pumped bearings, the seals, and the ports in the power piston and power piston cylinder. The figures show the pressure amplitude in the various volumes, and the bearing, port, and seal flows. The geometries of the close clearance seals were given earlier in Table 3, with the geometries of the power piston bearings and ports summarized in Table 4.

Table 4. Power Piston Bearing and Port Geometry

Bearing Configuration	Double-plane hydrostatic, bearing moving with piston
Bearing diameter	137 mm (5.4 in.)
Total length	140 mm (5.5 in.)
Feed plane separation	70 mm (2.75 in.)
Number of feed holes	14 per plane
Feed hole diameter	0.51 mm (0.020 in.)
Nominal radial clearance	0.0127 mm (0.005 in.)
Bearing Supply Ports	
Number	4
Axial length	2.5 mm (0.1 in.)
Circumferential length	
Power piston	6.45 mm (0.25 in.)
Cylinder	7.6 mm (0.30 in.)
Offset from midstroke	6.9 mm (0.275 in.)
Bearing Drain Ports	
Number	6
Piston groove width	2.5 mm (0.1 in.)
Cylinder slots	
Axial	2.5 mm (0.1 in.)
Circumferential	1.3 mm (0.05 in.)
Offset from midstroke	-6.9 mm (-0.275 in.)
Midstroke Ports	
Number	4
Piston hole diameter	2.5 mm (0.10 in.)
Cylinder slots	2.5 x 3.8 mm (0.10 x 0.15 in.)
Offset from midstroke	1.4 mm (0.55 in.)
Transverse Moment of Inertia of Piston about Center of Gravity: 0.105 kg-m^2 (359 lb-in.^{2})	

97TR21

The bearing supply and drain plenums are located inside the power piston. The bearing supply plenum is maintained at about 2.25 bar above engine mean pressure by ports connecting it to the gas spring. These ports are offset so that they are fully open when the gas spring pressure is about 2.75 bar above mean pressure. This allows engine operation from full stroke to half stroke and output power modulation from full load power to one-quarter of the full load power.

The bearing flow drains into circumferential grooves located at each end of the bearing. These grooves are connected to the drain plenum which is maintained at about 2.25 bar below mean pressure by ports in the cylinder. These ports are fully open when the gas spring pressure is about 2.75 bar below mean pressure.

The volume of the plenums is relatively large so that plenum pressure variations due to bearing flow between port openings is small. Based on a conservative estimate of bearing flow, the calculated plenum pressure varies during a cycle from 5.0 to 4.0 bar.

Bearing stiffness requirements were established to give a large margin of safety against an increase in eccentricity from alternator side loads. At room temperature, the sidepull gradient is 1.58×10^6 N/m (9010 lb/in.). Dimensional control on the alternator plunger and stator assemblies will result in the magnetic center being within 50 microns (2 mils) of the geometric center. To provide ample margin, 127 microns (5 mils) was selected for the offset of the magnetic center for performing the bearing design. This results in a sidepull at the alternator centerline of 196 N (45 lb).

5.2.2 Supply and Drain Ports

Close clearance, noncontacting seals are located at each end of the power piston between the bearing drain grooves and the compression space and gas spring, respectively. Because of alternating pressure in the compression space and the gas spring, there is a net flow along these seals into the drain plenum. There is also a continuous gas flow across the bearing from the supply plenum into the drain plenum. The supply and drain port flows are intermittent but need to equal the combined bearing and seal flow on a time-averaged basis to achieve steady-state operation. The ports are sized to pass this flow and maintain the pressure differential across the bearing.

Circumferential alignment of the bearing supply ports and the midstroke ports require that the piston be constrained against rotation. This is accomplished by building 0.050-in.-wide axial grooves in the inner stator which are opposite the 0.050-in.-wide tie rod gaps in the plunger. This produces a magnetic resistance to rotation generally referred to as cogging. The ports are sized to accommodate up to ±.025-in. circumferential misalignment. Based on bench tests, it was judged that 6 grooves in the inner stator would provide adequate stiffness against rotation. After assembly of the CTPC power piston drive, the cogging torque was lower than expected. A Rulon post was located on the end of the power piston cylinder which passed through one of the slots in the carrier with a small clearance. No rubbing on the post was observed following engine tests, but it is being retained to provide a positive limit to piston rotation if, for any reason, cogging is inadequate.

The losses associated with the power piston drive are:

Gas spring thermal hysteresis:	430 W
Gas shuttle loss:	100 W
Gas spring leakage:	30 W
Midstroke ports:	60 W
Supply and drain ports (bearing):	50 W
Total loss:	670 W

The above losses results in a net mechanical efficiency of 95.4%.

5.3 Power Piston Drive: Externally Pumped Bearing Configuration

Figure 30 shows the bearing and port arrangement used for external bearing operation. The same cylinder is used as for the internally pumped bearings, but the openings to the gas spring at the supply ports are plugged. The external supply drilling in the cylinder interconnects at this location.

A different piston is used with the bearing supply ports relocated to open at midstroke. The ports between the drain plenum and the gas spring are also relocated to open at midstroke. These changes

were made because a lower than mean pressure drain plenum was not required and locating the bearing ports at midstroke allows operation at small stroke levels.

The external helium loop has ample capability to supply the bearing with the above-described port arrangement.

Gas is supplied to the bearings via drillings in the power piston cylinder and joining ring. Gas returns through a pressure vessel feedthrough from the power piston gas spring, which is the normal drain plenum for the bearings.

5.4 Displacer Drive: Internally Pumped Bearing Configuration

The displacer drive consists of an assembly of moving parts and an assembly of stationary parts. The moving assembly, called the displacer proper, is composed of the gas spring piston, the displacer rod (which contains the high-pressure plenum for the displacer hydrostatic bearing), and the displacer dome that thermally isolates the hot expansion space from the cold compression space and displacer gas spring volumes. The purpose of the displacer proper is to transfer gas from the expansion space to the compression space and back during engine operation.

The stationary assembly, called the displacer flange and post, contains the displacer gas spring cylinder and a number of clearance seal surfaces. The flange and post assembly supports, guides, and springs the displacer proper in its motion. The displacer gas spring piston, cylinder, and enclosed volume form the load side gas spring element. The load side gas spring pressure amplitude at the 28 mm (1.1 in) design stroke is 17.2 bar. The head side gas spring pressure amplitude is 1.8 bar. The reciprocating mass of the displacer assembly is 2.17 kg (4.78 lb), which requires the combined load and head side gas spring stiffness of 7.1×10^5 N/m (4050 lb/in.) for the displacer to reciprocate at 70-Hz frequency.

Figures 35, 36, and 37 show the displacer bearing, port, and seal arrangement. The displacer bearing and port geometries are summarized in Table 5.

The bearing supply plenum is located inside the displacer rod. It is pressurized by ports offset 0.275 in. (6.9 mm), connecting it to the load side gas spring. The ports are fully open when the gas spring pressure is 8.77 bar. The bearings drain directly to the head side gas spring.

Table 5. Displacer Bearing and Port Geometry

Bearing Configuration	Double-plane hydrostatic, bearing moving with displacer
Bearing diameter	45.7 mm (1.8 in.)
Total length	137 mm (5.4 in.)
Feed plane separation	76 mm (3.0 in.)
Number of feed holes	8
Feed hole diameter	0.34 mm (0.0135 in.)
Nominal radial clearance	0.0127 mm (0.005 in.)
Bearing Supply Ports	
Number	2
Cylinder Port Holes	2.75 mm (0.108 in.)
Piston Port Slots	2.75 x 4.0 mm (0.108 x 0.16 in.)
Offset from midstroke	6.9 mm (0.275 in.)
Midstroke Ports	
Number	2
Cylinder groove width	2.0 mm (0.08 in.)
Piston slots	2.0 x 6.4 mm (0.08 x 0.25 in.)
Offset from midstroke	-0.07 mm (-0.03 in.)
Transverse Moment of Inertia of Displacer about Displacer Center of Gravity: 0.018 kg-m^2 (61.5 lb-in.^{2})	

97TR21

Sideloads on the displacer are very small. Based on a bench test (see Figures 38 and 39) and installation tolerences, the sideload due to centering magnets was estimated to be 1.3 N (0.3 lb). As shown earlier in Figure 21, the purpose of the centering magnets is to hold the displacer close to the mid-stroke position during the shutdown mode.

Midstroke ports are located between the two gas springs as shown in Figure 36 to return the bearing and unbalanced seal flows to the forward gas spring. They also stabilize the midstroke position of the displacer.

There are no ports between the compression space and the gas springs. The mean pressure in the gas springs will self adjust until the flow along the two seals to the compression space balance each other. The mean pressure in the gas springs for the reference geometry and 0.6-mil clearance is 2 bar above the 150-bar level in the engine.

The losses associated with the displacer drive are:

Gas spring thermal hysteresis:	390 W
Gas spring leakage:	400 W
Gas shuttle:	180 W
Midstroke ports:	40 W
Supply and drain ports:	90 W
Port alignment magnet:	30 W
Total loss:	1130 W

These losses result in a net displacer mechanical efficiency of 93.2%.

5.5 Displacer Drive Configuration: External Bearing Supply

Figure 31 shows the arrangement for operation on externally supplied bearings. The port connection between the load side gas spring and the bearing plenum is plugged. A rod with bearing supply ports located at midstroke is used. Gas from the external loop enters the plenum through the bearing supply ports. Gas return to the loop is from the head-side gas spring, which is the normal drain plenum for the bearings.

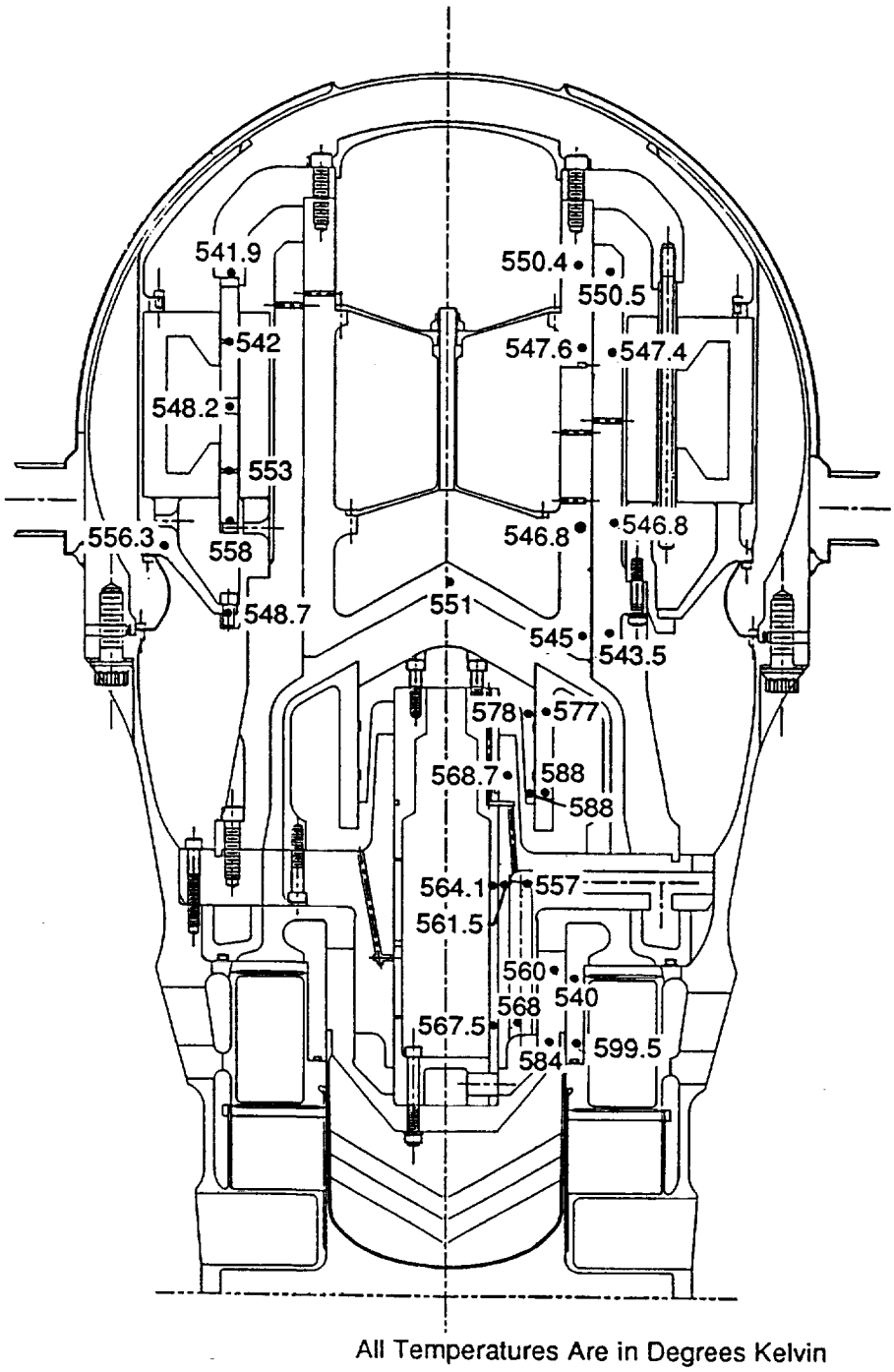

Figure 29. Operating Temperatures at Various Locations

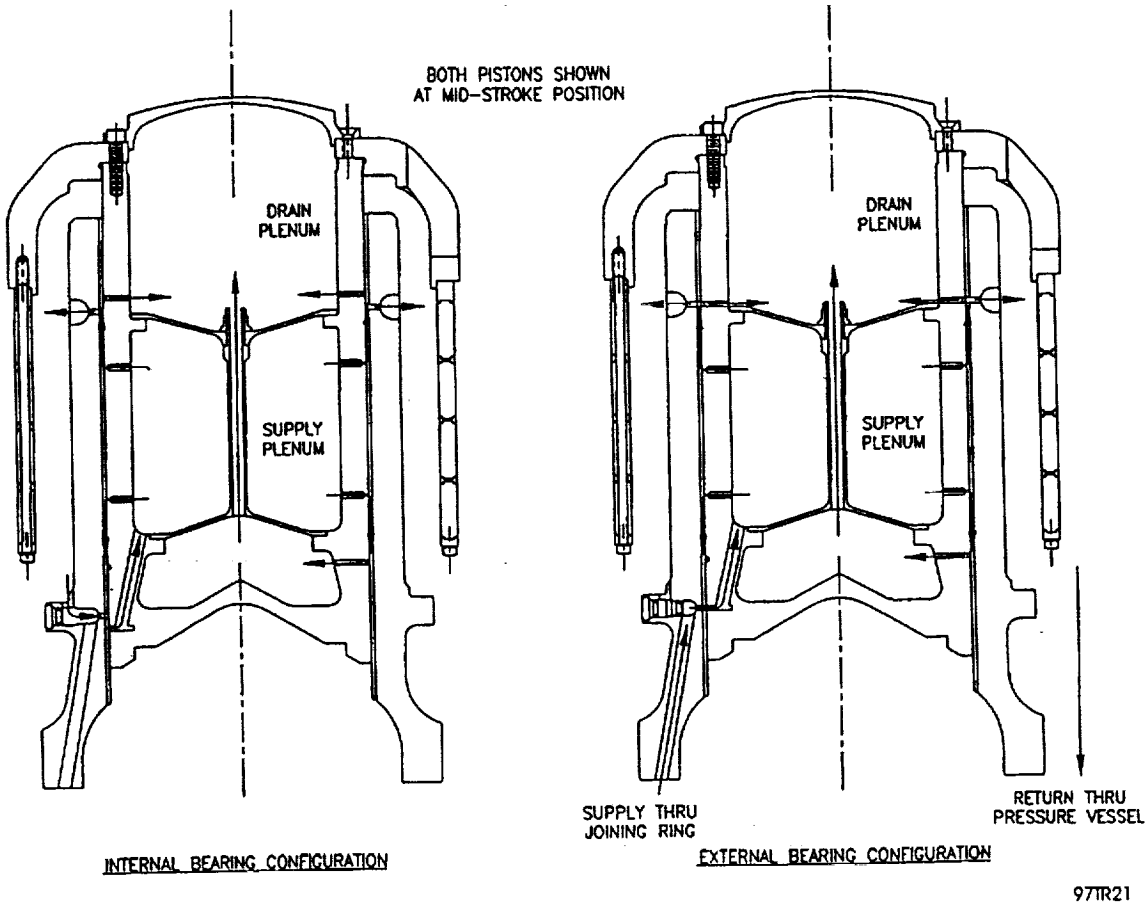

Figure 30. Power Piston: Gas Bearing Configurations

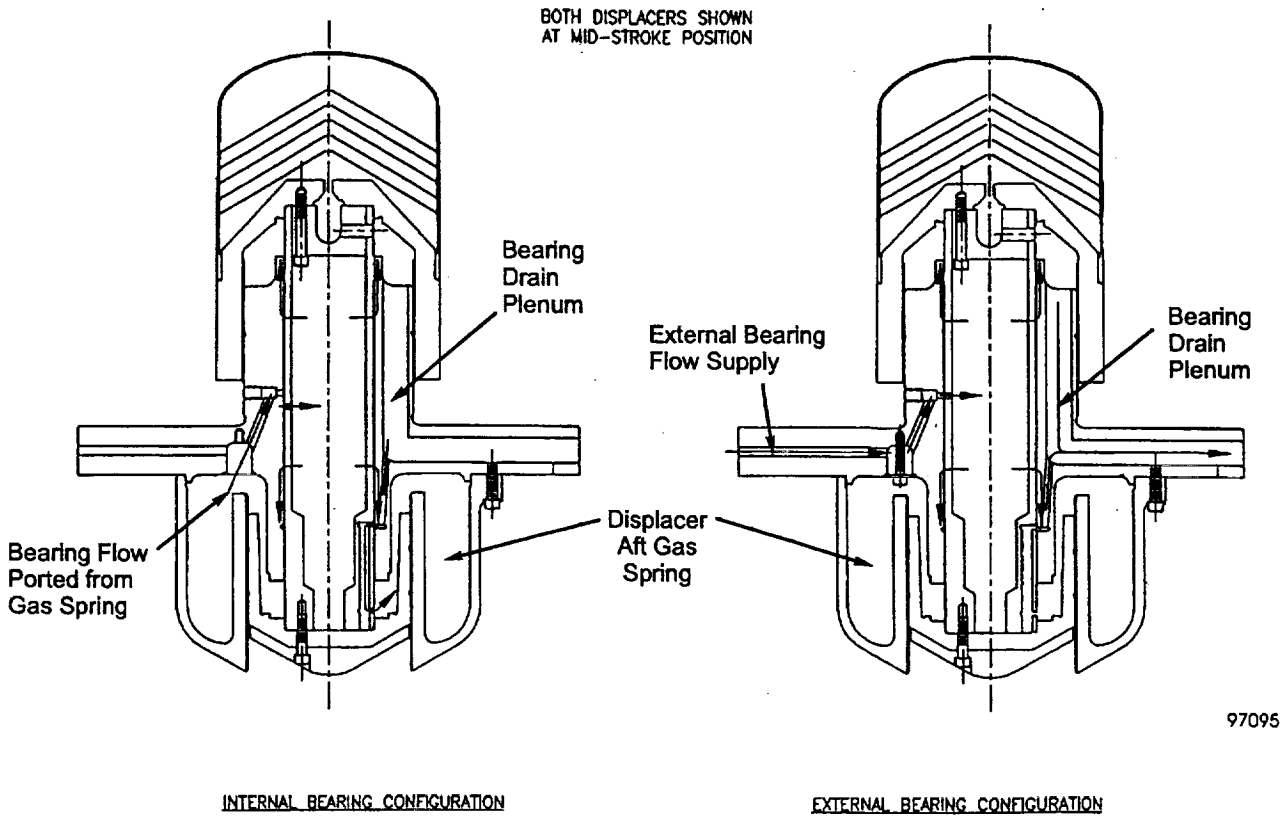

Figure 31. Displacer: Gas Bearing Configurations

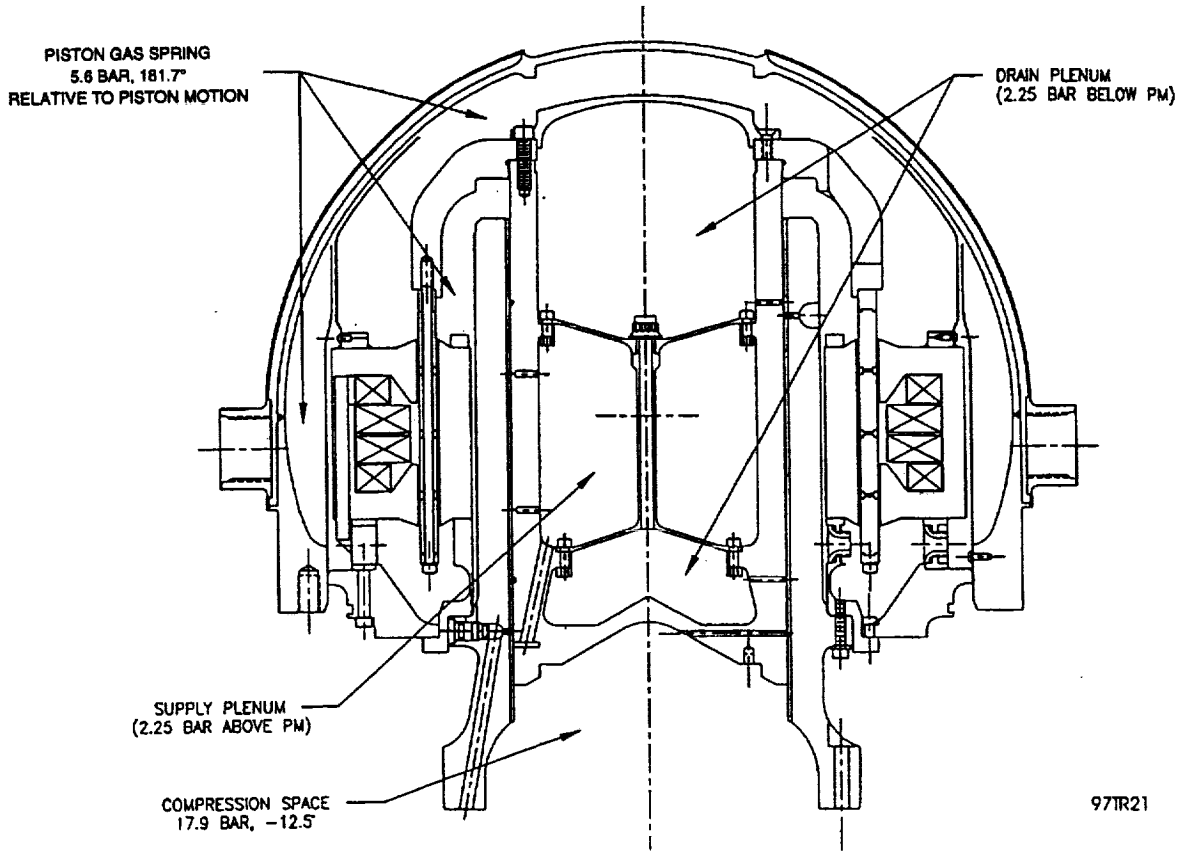

Figure 32. Arrangement of Internally Pumped Bearings and Seals in Power Piston Drive

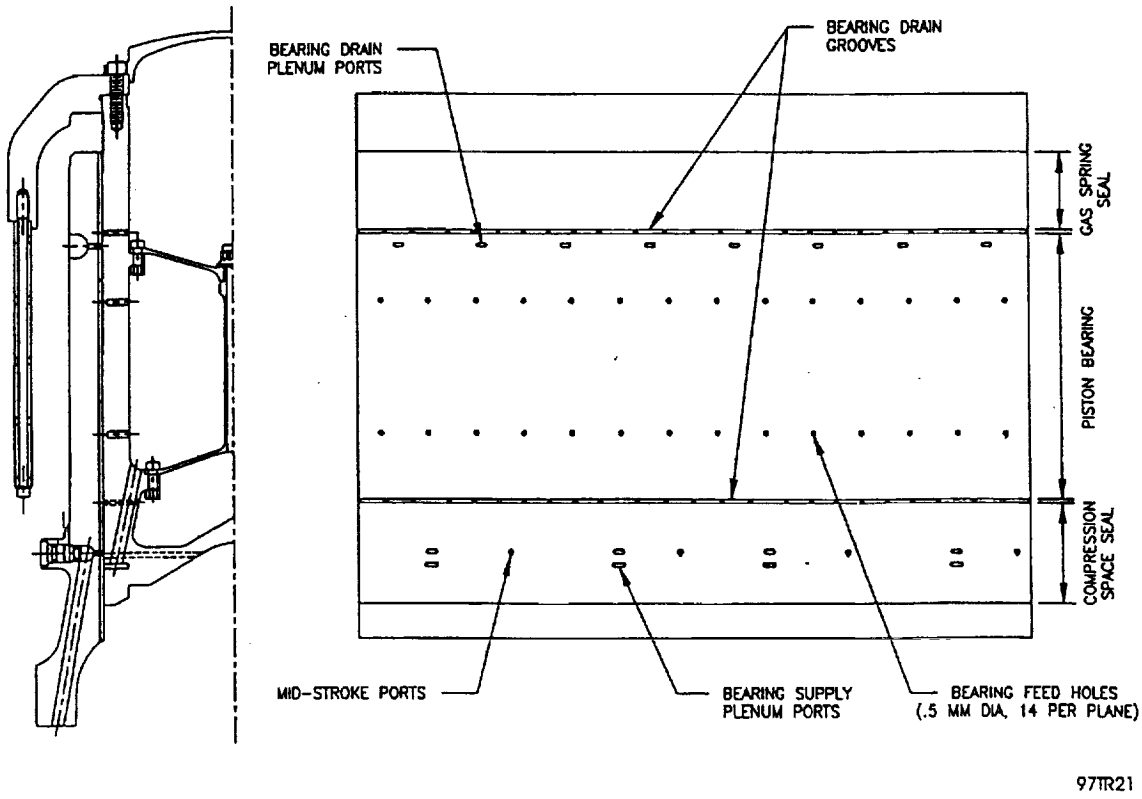

Figure 33. Arrangement of Bearing Ports, Grooves, and Feed Holes In Power Piston Drive

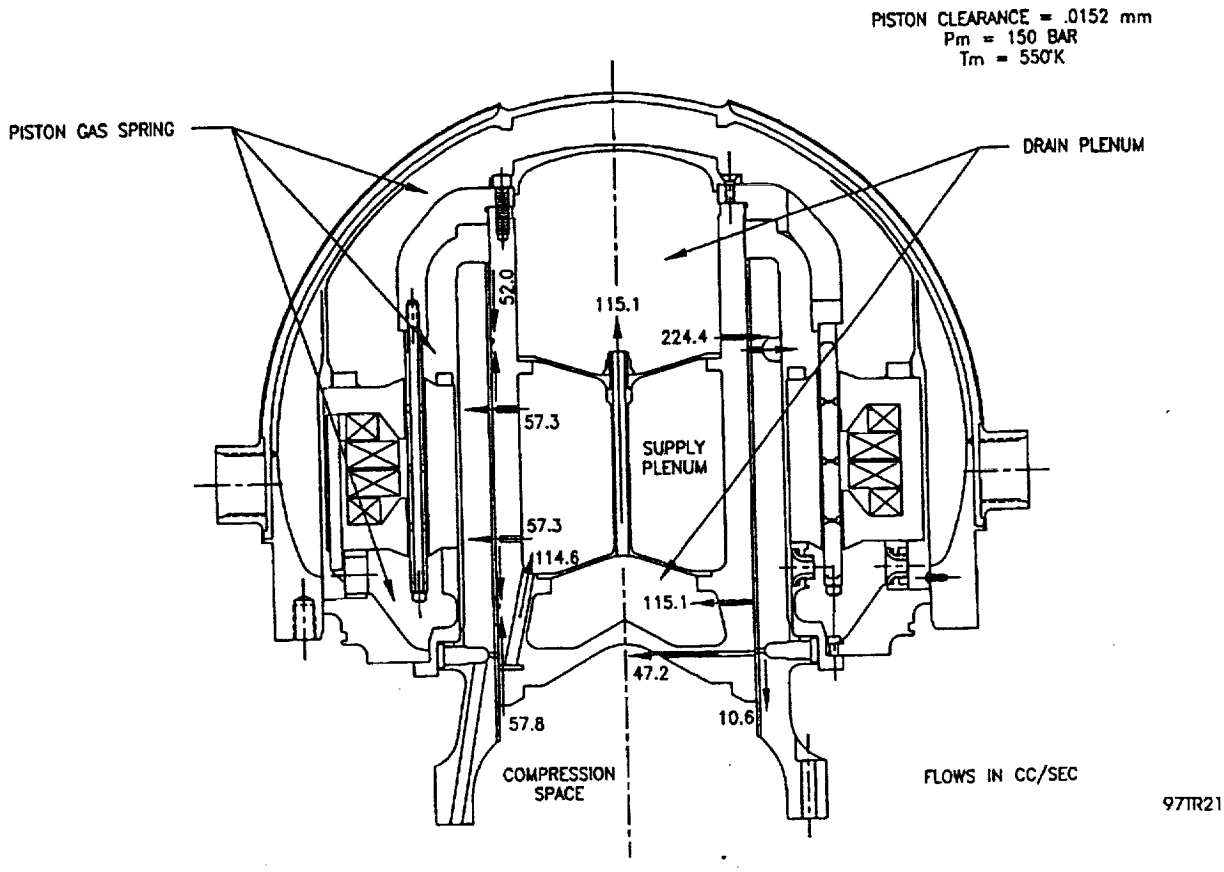

Figure 34. Flow Rates in Various Volumes of Power Piston Drive

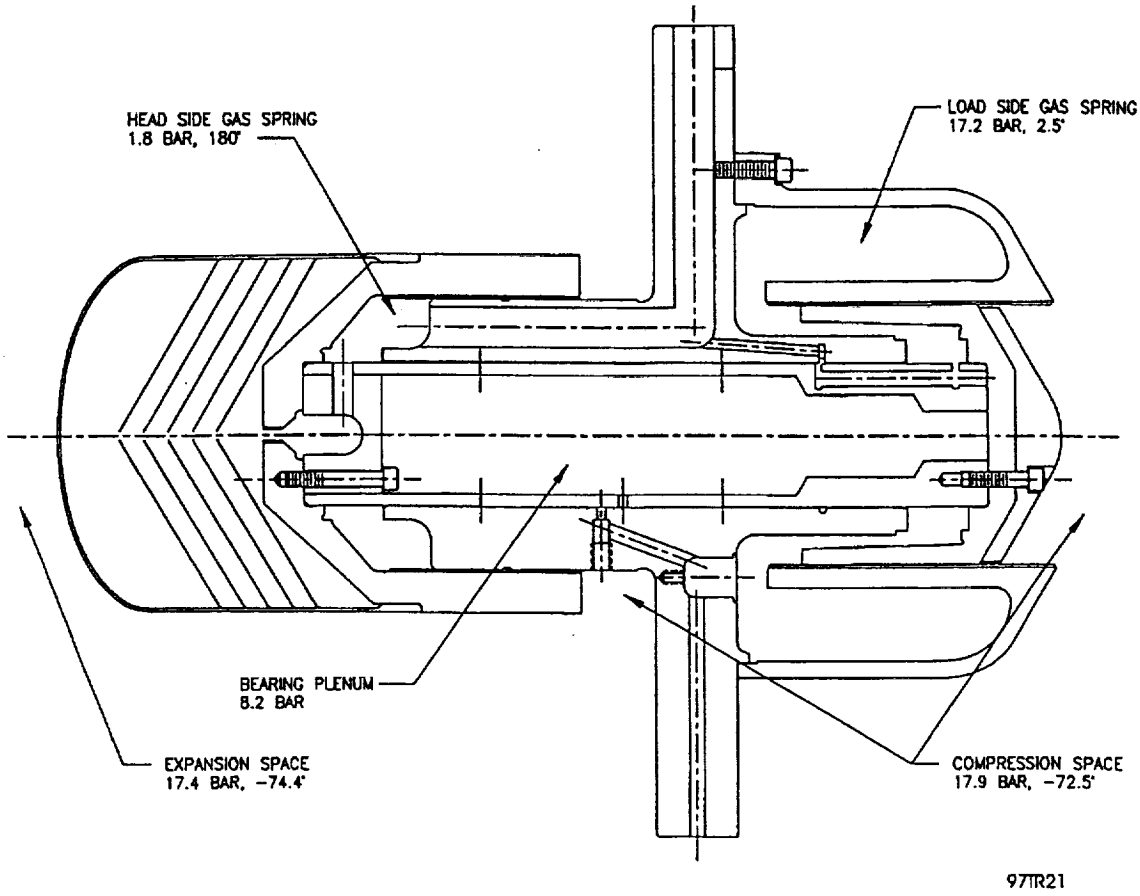

Figure 35. Pressure Amplitudes in Various Volumes of Displacer Drive (Pressure phase angles referred to are with respect to displacer motion.)

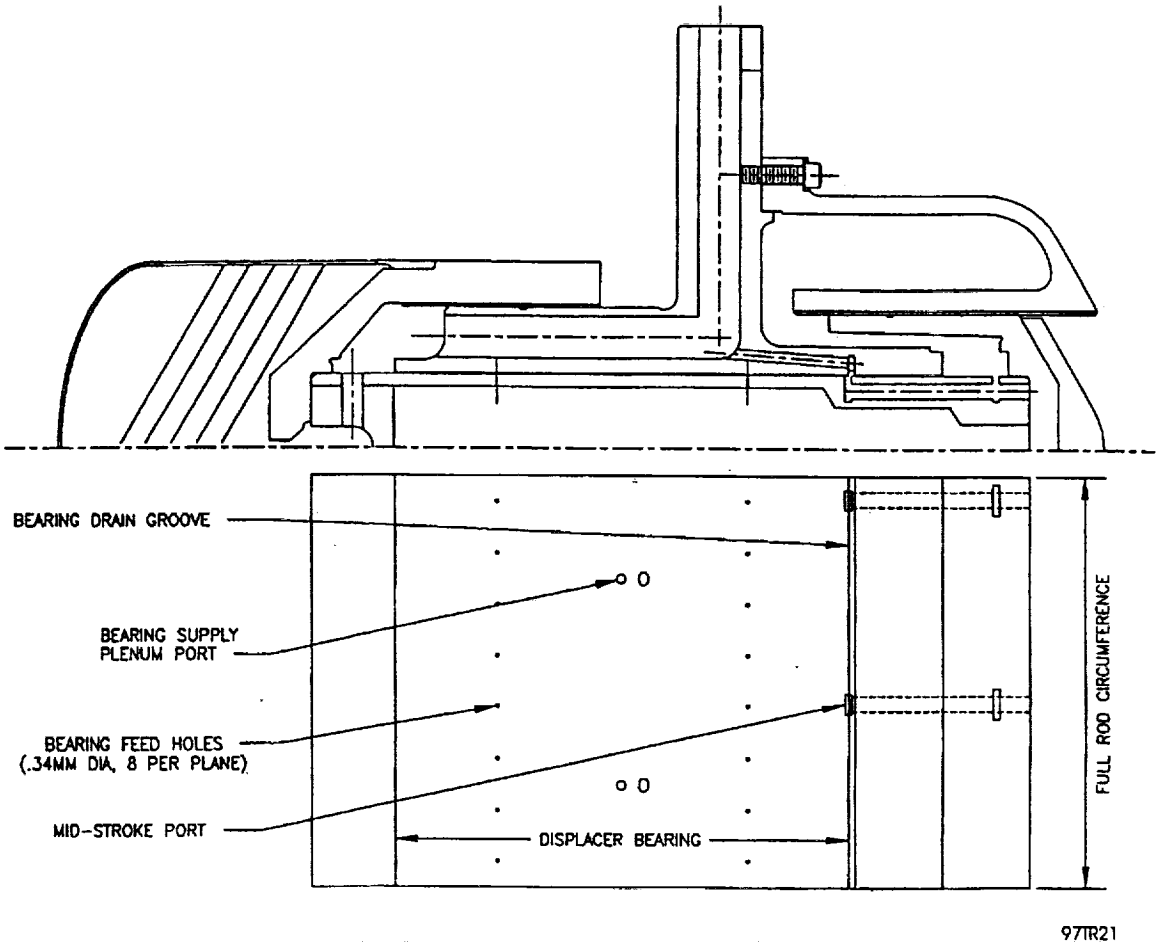

Figure 36. Displacer Bearing Ports, Groove, and Feed Holes Arrangement

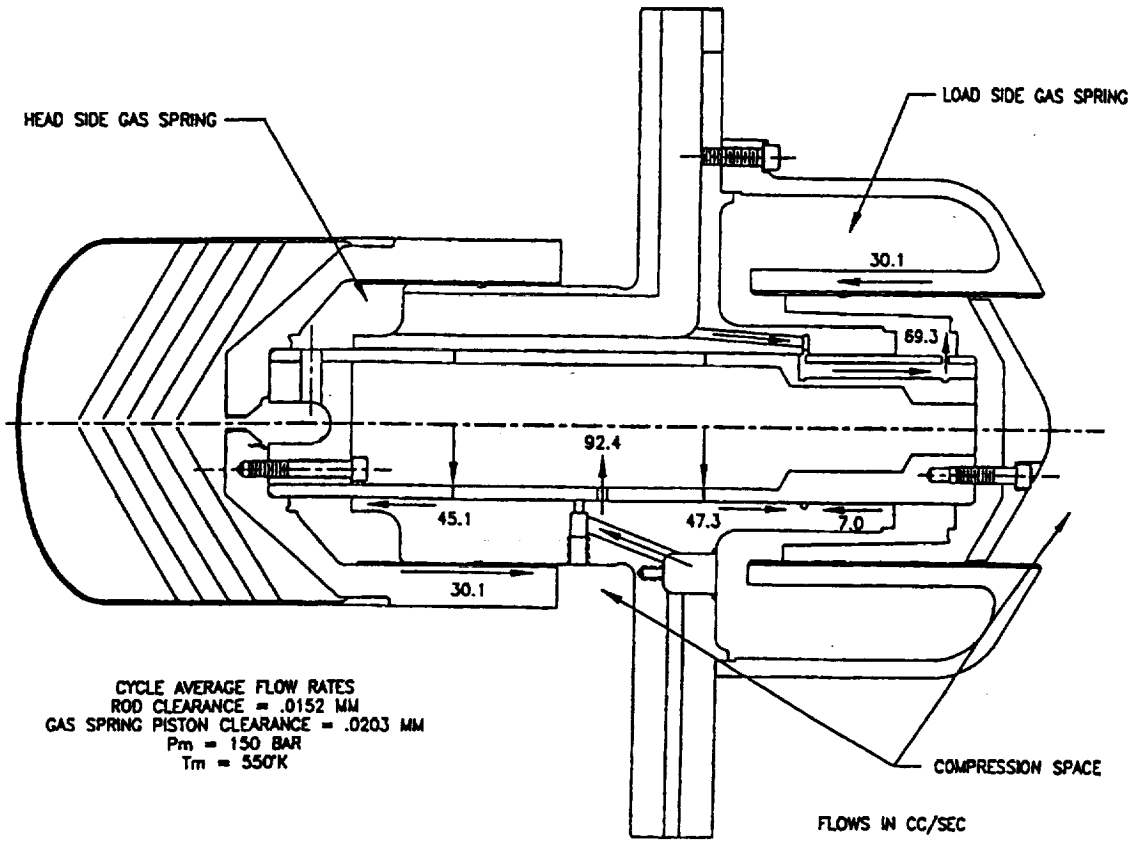

Figure 37. Flow Rates In Various Volumes of Displacer Drives

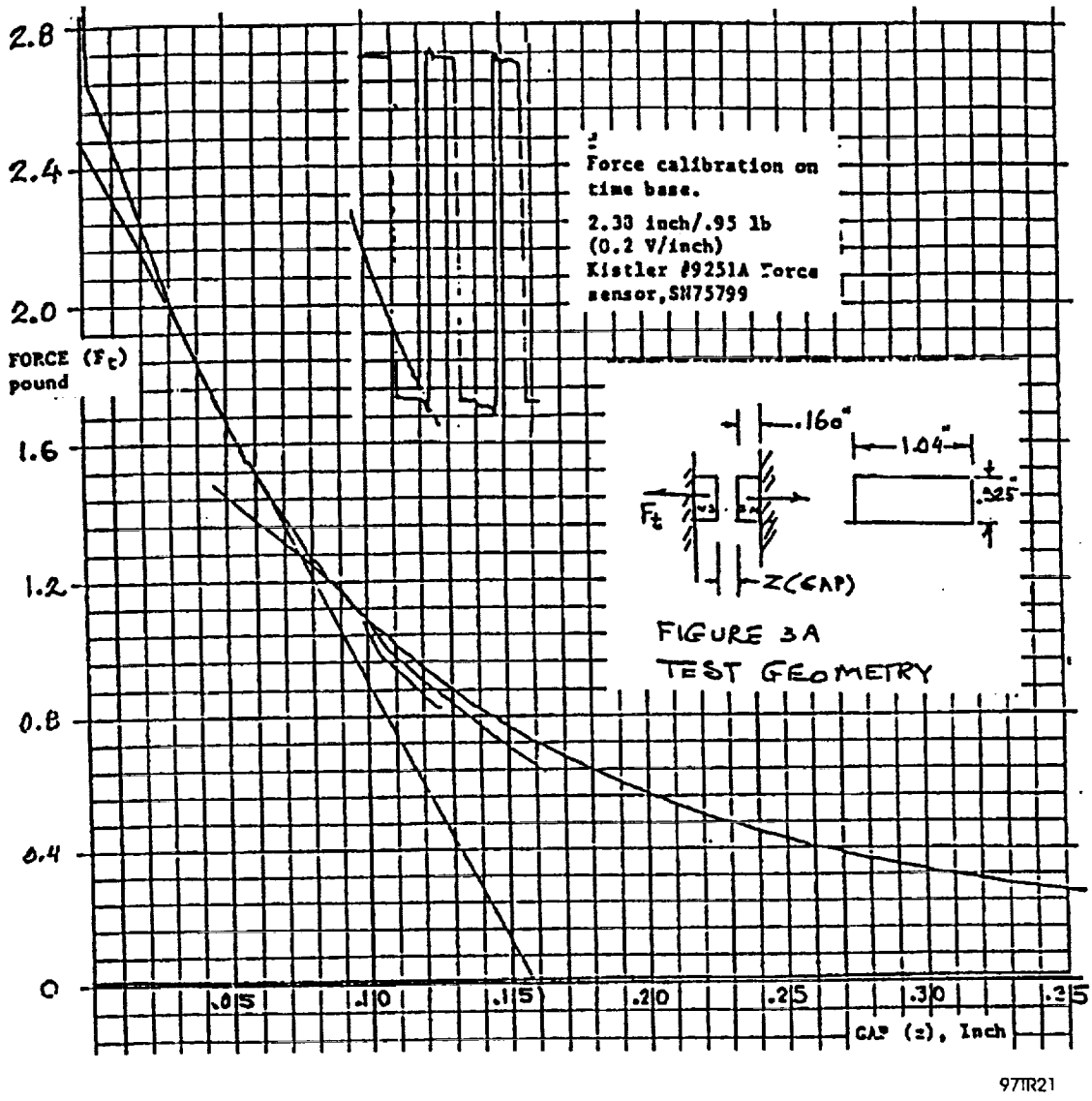

Figure 38. Displacer Sideloads: Radial Force versus Gap Characteristics

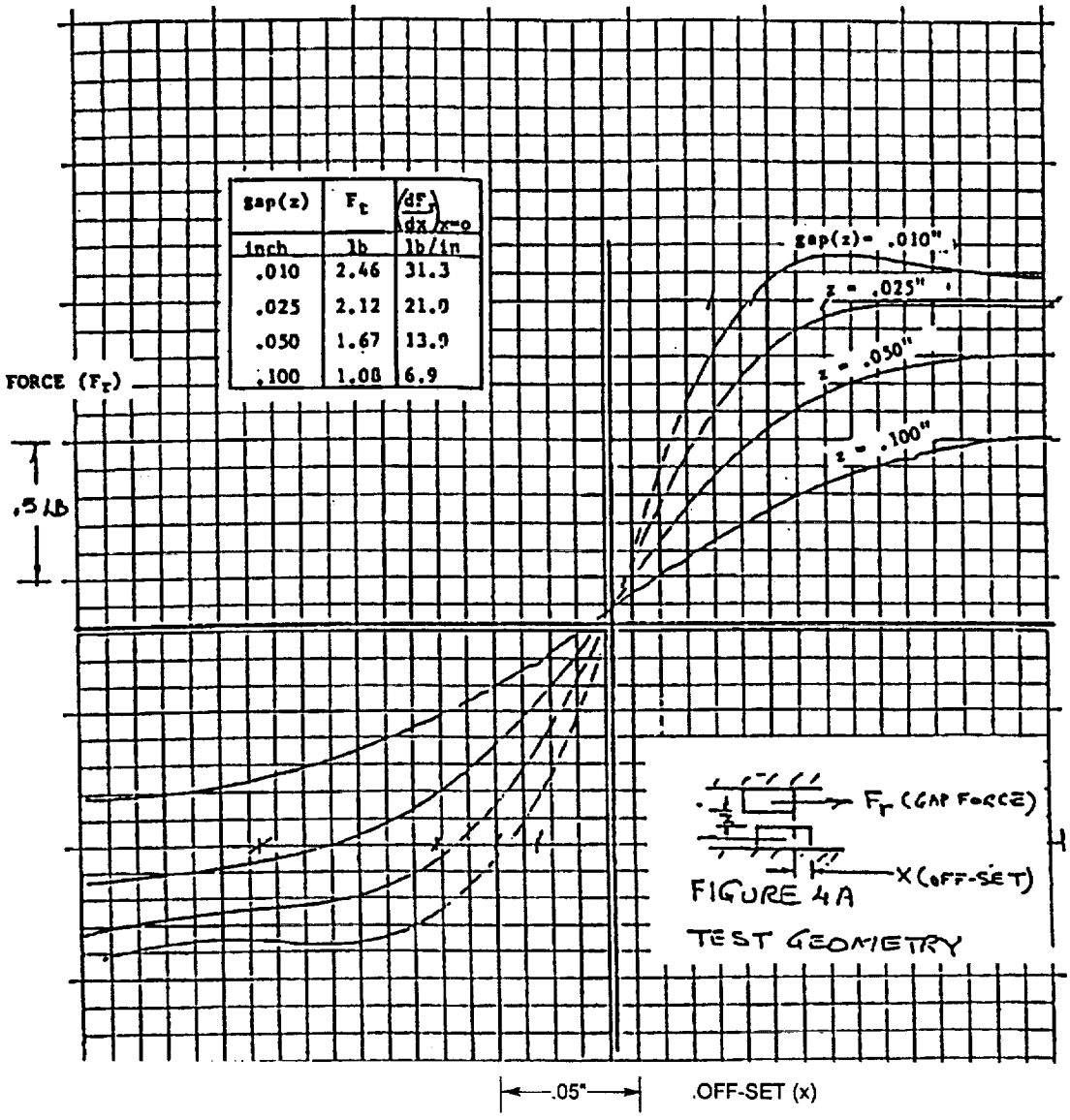

Figure 39. Displacer Sideloads: Circumferential

97TR21

6.0 STRUCTURAL ANALYSIS

6.1 Design Criteria

The design criteria used for the CTPC structural design are those established by the MTI Design Engineering Department as specific guidelines applicable to all Stirling system designs. These guidelines use definitions and safety factors generally accepted throughout the engineering profession.

6.1.1 Stress Definitions

The following stress definitions were used in the analysis.

- Membrane Stress: average stress on a component cross section due to pure tension or compression.
- Bending Stress: the stress on either surface of the cross section of a component due to a bending moment applied at the section.
- Primary Membrane Stress: a membrane stress which is not relieved by local deformation and is required to maintain equilibrium with applied mechanical loads, such as pressure, weight, etc.
- Primary Bending Stress: a bending stress which is not relieved by local deformation and is required to maintain equilibrium with applied mechanical loads.
- Secondary Stress: a stress which is limited by local plastic deformation if the elastic limit is exceeded. This type of stress is also referred to as strain limited. Sources of secondary stress are geometric discontinuities and thermal stresses.
- Effective Stress: the stress to be used in a multiaxial stress situation for comparison with material properties that are based on uniaxial tests. It is determined by the von Mises equivalent stress formula.

6.1.2 Stress Limits

The above-stated stresses are limited to certain values which are defined as follows:

- Primary membrane stress will have the following safety factors:
  - 2.0 versus the ultimate tensile strength
  - 1.5 versus the yield strength
  - 1.5 versus the creep rupture strength for the design life
  - 1.0 versus the 1% creep strength for the design life
- Primary membrane plus bending stress will have the following safety factors:
  - 1.33 versus the ultimate tensile strength
  - 1.0 versus the yield strength
  - 1.0 versus the creep rupture strength for the design life
  - 0.67 versus the 1% creep strength for the design life
- Primary plus secondary stress will have the following safety factors:
  - 1.5 versus the fatigue strength
  - 1.0 versus twice the yield strength (this criteria guards against ratcheting of the material).

6.2 Heater Head

6.2.1 Main Vessel

The heater head is exposed to large temperature gradients combined with a 150-bar steady pressure and an 18-bar cyclic pressure. To analyze these loading conditions on the complex geometry, finite element analysis (FEA) was used to determine the stress levels. Since the component is essentially axisymmetric, a two-dimensional (2-D) model was used. In the areas where the head is not axisymmetric, e.g., in the heater fins and the mounting nuts counterbores, 2-D planar elements with equivalent circumferential thicknesses were used. These elements provide stiffness in the X-Y plane, but do not provide stiffness in the hoop direction (Z-axis).

To facilitate code input and accurately define the thermal gradient along the outer wall of the heater head, a thermal analysis was first performed using the same finite element model as in the 2-D stress analysis. Boundary conditions for the thermal analysis are shown in Figure 40. In this analysis, the effects of radiation and conduction through the helium gap between the inside and outside walls of the regenerator were included.

For the structural analysis, the boundary conditions assumed are illustrated in Figure 41.

The CTPC heater head is made of Inconel 718. The creep life of the head at 1050 K is limited to tens of hours. By just changing the material to Udimet 720 (same geometry as the Inconel 718 heater head), the heater head life at 1050 K is more than 60,000 hr. Table 6 lists the pertinent properties of these two materials. Additional data on Inconel 718 and Udimet 720, creep, fatigue and weld properties, were developed and are reported in Appendixes B and C.

The primary stresses are determined by applying the pressure loading to the ANSYS model (no temperature gradients imposed). A summary of primary stresses in critical locations is shown in Figure 42. Safety factors for the primary membrane stresses are listed in Table 7, and those for the primary membrane plus bending stresses are listed in Table 8.

Since the CTPC Inconel 718 heater head is not expected to provide the full design life at 1050 K, actual life in hours is reported at each location rather than a safety factor. Additional information regarding expected life at 1000 K is listed since a significant amount of testing time will occur at this temperature or lower. Combined pressure and temperature stresses are summarized in Figure 43 and Table 9.

Since the high thermal stress component is expected to relax fairly rapidly due to creep, the indicated fatigue safety factor is lower than the actual condition. The modified value is listed at the bottom of Table 9. See Abdul-Aziz, et al., 1995 for a life assessment of the heater head using a combined finite-element viscoplastic, elastoplastic analysis.

6.2.2 Regenerator Wall

A separate FEA was performed for the regenerator wall. The wall carries the full temperature gradient of the engine and is exposed to the fluctuating pressure of the engine working fluid. The mean pressure has no effect because it is on both sides of the wall.

The finite element mesh and the assumed boundary conditions are shown in Figure 44. Since the piece is rigidly attached to the heater head and its stiffness is much lower than the rest of the heater head, the attached end was forced to have the same displacement and rotation as the corresponding point on the heater head.

Because there is no mean pressure force acting on the regenerator wall, all of the stresses are secondary stresses. Figure 45 shows the four highest stress locations along the wall under design point operating conditions. The temperature, the mean stress (due to the thermal gradient), and the alternating stress (due to the reciprocating pressure) are listed.

Safety factors for these locations are shown in Table 10 for the design point (1050 K) and also for 978 K (1300°F) and 922 K (1200°F) heater head operation.

Table 6. Material Properties

Properties	Udimet 720 CR		Inconel 718	
	MPa	ksi	MPa	ksi
Tensile Strength				
Room Temperature	1102	162	1347	198
1033 K (1400°F)	1014	149	844	124
Yield Strength				
Room Temperature	850	125	1109	163
1033 K (1400°F)	782	115	789	116
Creep Rupture, 60,000 hr				
1050 K (1430°F)	245	36	<70	<10

97TR21

Table 7. Heater Head Primary Membrane Stress Summary

Location*	Yield Strength**	Ultimate Strength**	1% Creep Life (1050 K)	1% Creep Life (1000 K)
P1	Stress value »0	Stress value »0	Stress value »0	Stress value »0
P2	6.10	7.15	134 hr	15,650 hr
P3	6.10	7.15	134 hr	15,650 hr
P4	3.57	4.19	40 hr	5,995 hr
P5	3.12	3.73	Stress value »0	Temperature below creep initiation level

*See Figure 42.

**Safety factor.

97TR21

Table 8. Heater Head Primary Membrane Plus Bending Stress Summary

Location*	Yield Strength**	Ultimate Strength**	1% Creep Life (1050 K)	1% Creep Life (1000 K)
P1	4.26	5.00	157 hr	16,680 hr
P2	3.28	3.84	49 hr	6,813 hr
P3	2.75	3.22	36 hr	4,948 hr
P4	3.57	4.19	40 hr	5,995 hr
P5	2.81	3.35	Temperature below creep initiation level	Temperature below creep initiation level

*See Figure 42.

**Safety factor.

97TR21

Table 9. Heater Head Primary Plus Secondary Stress Summary

Location*	Temperature, K	Stress, MPa (ksi)		Safety Factors	
		Mean	Alternating	Yield	Fatigue
H1	1050	181 (26.6)	39.5 (5.8)	2.31	2.16
H2	1050	333 (48.9)	16.3 (2.4)	1.46	1.61
H3	1050	335 (49.2)	18.4 (2.7)	1.45	1.58
H4	999	545 (80.1)**	15.0 (2.2)	1.20	1.28
H5	636	615 (90.4)	25.8 (3.8)	1.50	1.70

*See Figure 43.

97TR21

**Mean stress will creep down to approximately 408 MPa (60 ksi) in a short period of time, resulting in a safety factor of 1.67.

Table 10. Regenerator Wall Stress Summary: Safety Factors

Location*	1050 K		978 K		922 K	
	Yield	Fatigue	Yield	Fatigue	Yield	Fatigue
R1	2.39	2.15	3.61	3.02	4.26	3.58
R2	1.08	1.05	1.33	1.31	1.53	1.52
R3	3.43	2.51	3.73	2.72	4.00	2.92
R4	4.07	2.86	4.23	2.93	4.41	2.99

*See Figure 45.

97TR21

The safety factor versus fatigue does not meet the design criteria at the two higher temperatures. However, the high thermal stress will creep rapidly at these temperature levels, which will greatly ease the fatigue condition. The values in the table are extremely conservative, and failure is not expected. Combined creep and fatigue testing was initiated to confirm this (details for creep are given in Appendix B.4).

6.2.3 Fins

The helium flow passages in the heater head fins result in a relatively thin wall subject to high pressure. The wall thickness is nominally 0.030 in. but, due to tolerances, it can be as small as 0.014 in. To assess this, a separate FEA was performed. Figure 46 shows the finite element mesh and boundary conditions used in the analysis. The elements used in the analysis are 2-D planar elements of a single-unit thickness.

The maximum stress that occurs adjacent to the heater hole and the associated safety factors are given in Figure 47. Because the stress values are so low, creep is the only concern in this area. The maximum stress value is lower than stress values in other areas in the heater head hot section, resulting in an ample safety margin.

6.3 Heat Pipe

The heat pipe is exposed to the full hot-end temperature with a slight negative pressure acting on its surfaces. Stresses for this operating condition should be below the creep strength of the material. In the event of a heater fin failure, the structure must also withstand a 20-bar internal pressure for a very short time. A time transient analysis was performed to calculate the rate of pressure increase in the heat pipe in the event a heater head fin ruptured and helium leaked into the heat pipe. The size and shape of the

rupture disk was selected such that the maximum pressure in the heat pipe was limited to 300 psi. The heat pipe rupture disk has been designed to fail at 10-bar internal pressure. Stresses for this load condition are below the yield strength of the material at operating temperature.

Due to the complex construction of the heat pipe, a three-dimensional (3-D) FEA was performed to determine the peak stresses. Figure 48 shows the finite element mesh and boundary conditions used in the analysis. The elements used in the analysis are 3-D shell elements.

The maximum stress due to the pressure occurs in the middle of the top plate just outside the gusset. Since the vapor pressure of sodium varies with temperature, stress values under normal operating conditions are listed for different temperature levels. Table 11 summarizes the results of the analysis.

Table 11. Maximum Stress In Heat Pipe At Various Operating Temperatures

Temperature, K (°F)	811 (1000)	922 (1200)	978 (1300)	1005 (1350)	1033 (1400)	1050 (1430)
Maximum Stress, MPa (ksi)	29 (4.3)	27 (4.0)	25 (3.7)	23 (3.4)	21 (3.1)	19 (2.8)

97TR21

6.4 Cooler

6.4.1 Shell

Because of the complex geometry, the cooler shell was analyzed using a finite element code. As shown in Figure 49, the stiffness of each individual tube is represented by a beam element. The shell is represented by axisymmetric planar elements.

The maximum stress occurs in the outer shell and is indicated in Figure 50. As indicated in the figure, the safety factors against yield, rupture, and fatigue are well above those needed to meet the design requirements.

6.4.2 Tube

The insert inside the cooler tube is brazed to the tube over its full length to provide good thermal contact. To be conservative, the strengthening effect of the brazed insert was neglected, and the tube was analyzed assuming the full pressure is acting on the inner diameter.

The tube has an outside diameter (D) of 0.375 in. and an inside diameter (d) of 0.316 in. Using the conventional equation for calculating hoop stress:

$$\sigma_\theta = P_m \frac{\left(D^2 + d^2\right)}{\left(D^2 - d^2\right)}$$

the resulting stress due to the mean pressure (P_m) is 12.8 ksi (88.3 MPa), and the stress due to the cyclic pressure is 12% of the mean, or 1.5 ksi (10.6 MPa).

The safety factors associated with these stress levels are:

- Safety factor against yield: 3.19
- Safety factor against ultimate: 7.55
- Safety factor against fatigue: 6.33.

The cooler tubes have ample margin against yield, rupture, and fatigue.

6.5 Plunger

6.5.1 Carrier

To minimize the weight of the plunger carrier, the geometry was optimized using a finite element code to analyze the stresses. Because the carrier has many cutouts for gas flow and weight reduction, it is not axisymmetric. Consequently, a 3-D analysis was required to accurately model the geometry. Figure 51 shows three views of the finite element model used. The mesh and all boundary conditions are indicated. Since beryllium is a brittle material, all stresses must be held below yield to provide a factor of safety against rupture and fatigue failure.

Under normal operating conditions, the maximum load on the plunger carrier is due to the 300-g axial acceleration associated with the reciprocating motion at 70 Hz. This results in 28,450 N (6400 lbf) of force applied to the plunger by the magnet tie rods.

To provide a factor of safety against potential accident conditions, the plunger is designed to withstand 900 g which is the deceleration force associated with it engaging the snubbers at the maximum velocity attained during the stroke. This bounds the effect of a loss of alternator load (short circuit). For this condition, the dynamic force on the plunger carrier due to the weight of the magnet assembly is approximately 80,000 N (18,000 lbf). Results from this analysis are shown in Figure 52.

6.5.2 Tie Rods

The magnet tie rods are preloaded to resist the inertia loads quoted in the previous section. The preload is set by controlling the measured extension of the tie rod during assembly to 0.017 ±.002 in., which gives 95 ±10 ksi.

The maximum force per tie rod under normal operation is 1575 N (355 lbf). The stress in the tie rod due to this is 36 ksi. The stress at the accident condition is approximately 100 ksi. Inconel 718 has a yield strength above 150 ksi so that a preload of 100 ksi is ample to balance normal loads and adequate to react the bounding accident condition.

6.6 Volume Compensator

The volume compensator encloses part of the displacer forward gas spring. It is subject to the 150-bar engine mean pressure plus a 2-bar amplitude. A finite element stress analysis was performed to predict the stress levels. With the exception of the radial vent holes in the flange section volume, the component is axisymmetric. To simplify the analysis, the vent holes were not modeled because their effect on the stresses in the thin shell are negligible. As shown in Figure 53, 2-D axisymmetric planar elements were used in the analysis. The results of the analysis along with the safety factors are given in Figure 54. Since the pressure amplitude is so small, high cycle fatigue is not a concern.

6.7 Alternator Pressure Vessel

An FEA was performed to accurately estimate the stress levels in the alternator pressure vessel. A 2-D axisymmetric model representing the whole pressure vessel assembly (alternator pressure vessel, joining ring, and heater head) was constructed (see Figure 55). In order to properly represent the bolted flanges, 2-D beam elements were used for the studs, and 2-D interface elements were used between mating parts. The interface elements are used to model mating surfaces which can transmit compressive loads but, upon loss of preload and subsequent separation, cannot carry tensile loads. An initial elongation was imposed on the beam elements to represent initial preload on the studs. The ends of the beam elements were tied to neighboring nodes of the structure so that the tensile and bending loads transmitted to the stud elements were modeled. The maximum stress due to pressure for the whole structure occurs in the thin wall of the hemisphere. Figure 56 indicates the location and magnitude of the stress, along with the associated safety factors.

In the analysis of the alternator pressure vessel, the effects of the flanges were included. Beam elements were used to represent the studs. From this analysis, the stresses in the studs can also be determined. Effects due to the initial preload, additional tension due to the pressure load, and any bending effects that are transmitted to the studs are included. Figure 57 shows a detail of how the studs were modeled. The length used for the stud is equal to the unthreaded length plus half of the engaged thread length in the tapped hole. The results for the design point operation are listed in Table 12.

Table 12. Stud Summary: Design Point Operating Condition

Stud Summary	Heater Head	Alternator Pressure Vessel
Number of Studs	32	38
Preload	8.45 x10^4 N (19,000 lb)	8.45 x10^4 N (19,000 lb)
Blow-off Force	6.68 x10^5 N (150,200 lb)	1.09 x10^6 N (246,000 lb)
Clamping Force	2.70 x10^6 N (608,000 lb)	3.21 x10^6 N (722,000 lb)
Load Ratio	4.05	2.93
Preload Stress	1090 MPa (160 ksi)	1090 MPa (160 ksi)
Maximum Working Stress	1160 MPa (171 ksi)	1280 MPa (188 ksi)
Alternating Stress	8.8 MPa (1.3 ksi)	6.8 MPa (1.0 ksi)

97TR21

6.8 Hydrostatic Pressure Test

When the pressure vessel is first assembled, or whenever one of the mean-pressure-carrying components is replaced, an ambient temperature hydrostatic pressure test is performed to qualify the assembly. The test pressure is 1.5 times the expected maximum operating pressure increased by a factor to account for the operational temperature.

The alternator pressure vessel mounting studs are the most severely loaded components in the assembly. The maximum expected loading on the studs is 156 bar due to the 150 bar mean pressure and the 6-bar gas spring amplitude. At the 525 K operating temperature, the strength of the MP159 stud material is 17% lower than at room temperature. Inconel 718 has negligible loss in strength.

The hydrostatic pressure specified for the CTPC hydrotest is equal to 156 x 1.5 x 1.17 or 272 bar (3950 psi). At this pressure level, a significant amount of flange separation is expected. The analysis becomes nonlinear, and the predictions are sensitive to modeling accuracy. For this reason, the alternator pressure vessel stud joint was analyzed using a very detailed 3-D model.

Based on the 3-D analysis, the heater head joint does not see any significant flange separation due to the hydrostatic pressure, so the original 2-D model was sufficient for its analysis. The 3-D mesh used for the analysis is illustrated in Figure 58. The initial preload on the stud was simulated using constraint equations which force the displacements of the nut face relative to the flange face equal to an amount equivalent to the preload strain. A preliminary run was done without any pressure to confirm that the desired preload stress was obtained. The full hydrostatic test pressure was then added to the entire inner surface of the model. For this loading condition, the maximum stress in the stud shanks are allowed to reach the yield strength of the material, or a safety factor of 1.0. Table 13 lists the final stress results from this analysis.

Table 13. Stud Summary: Hydrostatic Pressure Test

Stud Summary	Heater Head	Alternator Pressure Vessel
Blow-off Force	1.21x10⁶ N (272,700 lb)	1.99x10⁶ N (446,700 lb)
Load Ratio	2.23	1.62
Maximum Stress	1224 MPa (180 ksi)	1530 MPa (225 ksi)
Safety Factor, Yield	1.28	1.02

97TR21

6.9 Seal Deflections

Because the leakage through the close-clearance seals is highly dependent on the size of the gap, it is critical to keep the gap from opening during operation. It is also necessary to limit the magnitude of gap closing during operation to prevent a possible rub from occurring. Since the displacer and power piston components are exposed to cyclic pressures, the walls must be sized so that gap changes during a cycle are small.

The design guideline used is to keep gap variations less than 10% of the design clearance. The equations used to calculate the radial deflection of the components are those for thick-walled cylinders exposed to either internal or external pressure.

6.10 Carbon Liners

In all areas where there are closely running clearances between mating parts, a carbon liner is used in the cylinder of the pair. These liners are held in position with a shrink fit. As a general design guideline, a nominal contact pressure of 7 bar (100 psi) under operating conditions was selected for all of the fits. The resulting magnitude of interference and wall thickness of each liner was then determined based on the strength of the carbon graphite used.

Carbon graphite has a much lower coefficient of thermal expansion than beryllium. Therefore, additional interference is required to maintain the 7-bar (100-psi) contact pressure at operating temperature. The most severe stress condition for the liners is at room temperature when the interference is the greatest. Table 14 lists the various geometries for each location where a carbon liner is used.

Handbook equations for the shrink fit of a low modulus liner into a high modulus, thick-walled cylinder were used to determine the stresses in the liners at installation and the interference at operating temperature. Table 15 summarizes the interference and stress conditions at installation and the safety factors against compressive strength for each liner.

Table 14. Carbon Liner Geometries

Location	Diameter, mm (in.)	Thickness, mm (in.)
Post and Flange	46.3 (1.823)	0.432 (0.017)
Displacer ID	87.9 (3.46)	0.762 (0.030)
Displacer Gas Spring Cylinder	84.3 (3.32)	0.94 (0.037)
Power Piston Cylinder	138.7 (5.46)	1.22 (0.048)

97TR21

Table 15. Carbon Liners Stress Summary (Room Temperature)

Location	Diametral Interference mm (in.)	Contact Pressure MPa (psi)	Hoop Stress MPa (psi)	Safety Factor
Post and Flange	0.221 (0.0087)	1.59 (231)	85.4 (12,390)	2.42
Displacer ID	0.442 (0.0174)	1.57 (227)	90.3 (13,090)	2.29
Displacer G.S. Cylinder	0.376 (0.0148)	1.78 (258)	79.9 (11,580)	2.59
Power Piston Cylinder	0.673 (0.0265)	1.53 (222)	87.1 (12,630)	2.38

97TR21

References

Abdul-Aziz, A., Bartolotta, P., Tong, M., and Allen, G. "An Experimental and Analytical Investigation of Stirling Space Power Convertor Heater Head." NASA TM-107013, 1995.

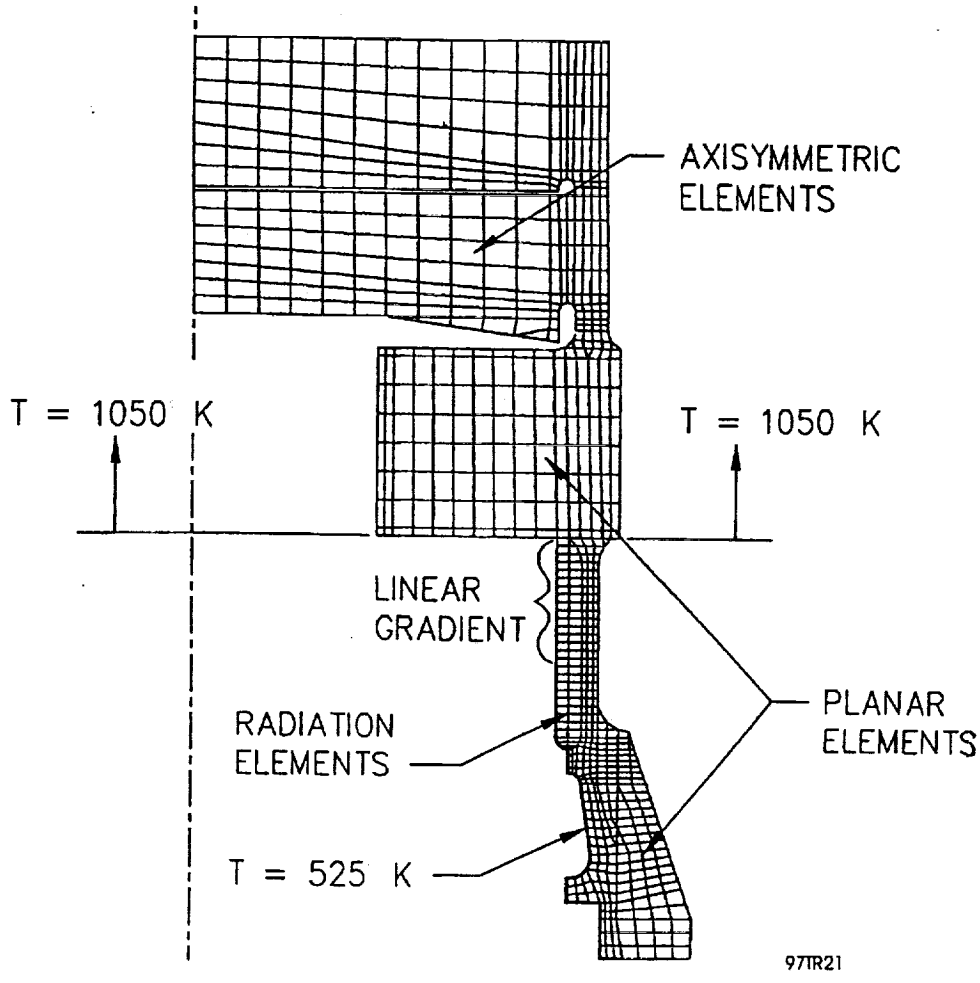

Figure 40. Boundary Conditions for Thermal Analysis: Heater Head Main Vessel

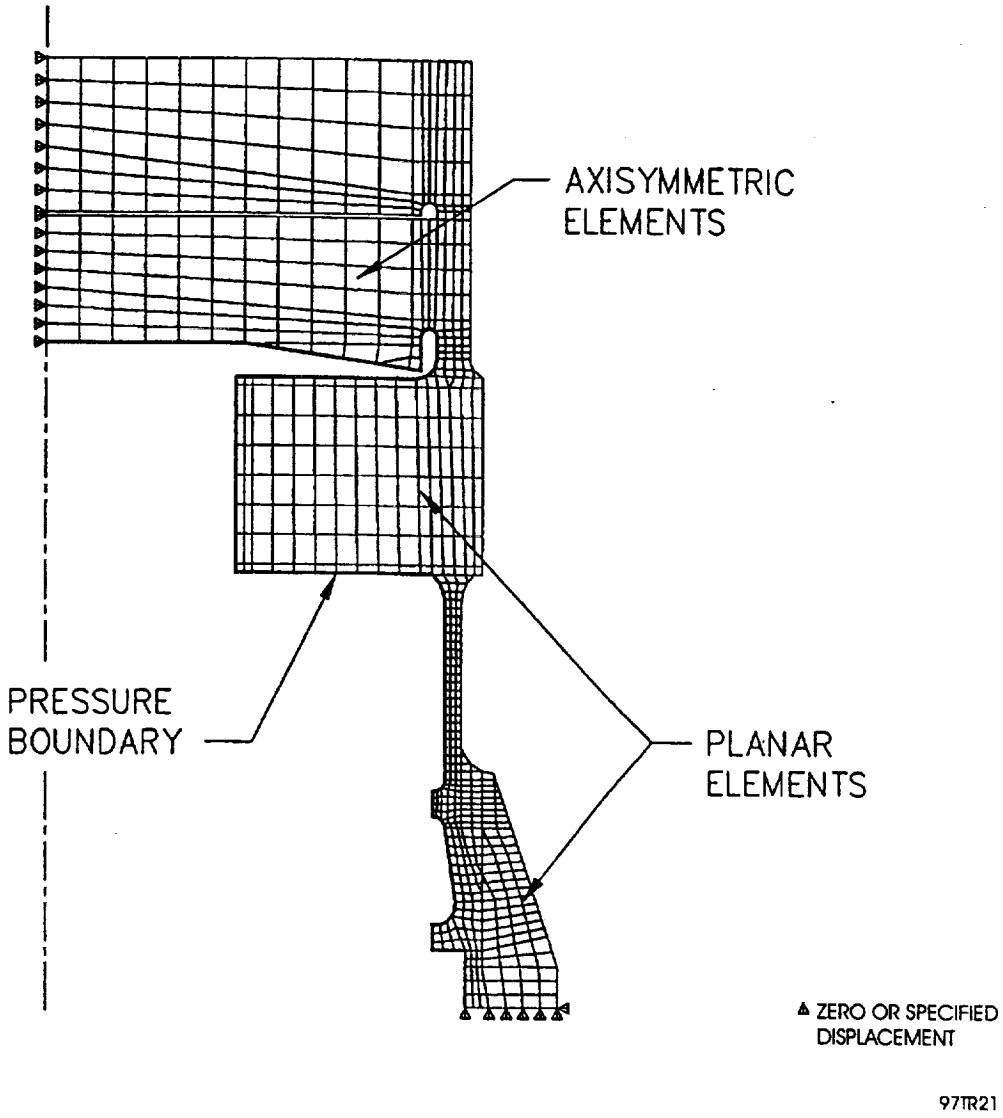

Figure 41. Boundary Conditions for Structural Analysis: Heater Head Main Vessel (Pressure boundary conditions of 150 ±18 bar)

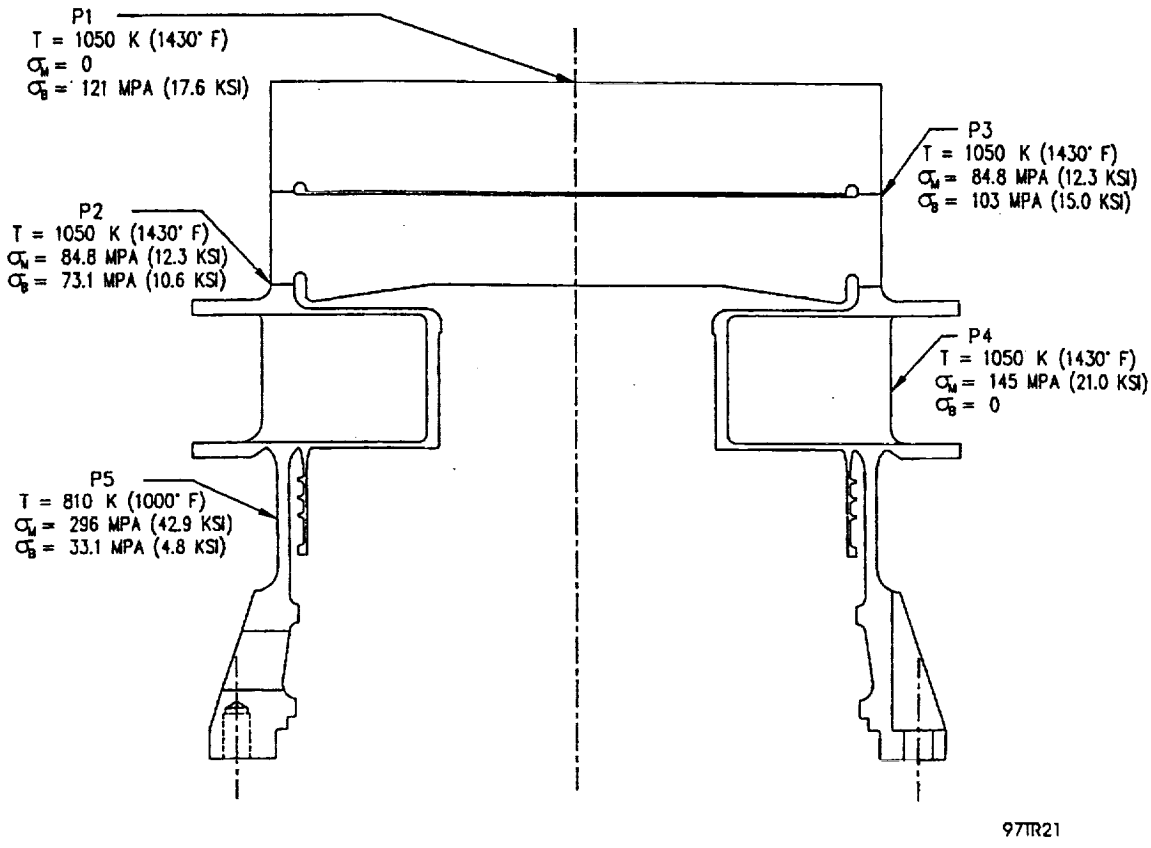

Figure 42. Summary of Primary Stresses in Critical Locations: Heater Head Main Vessel

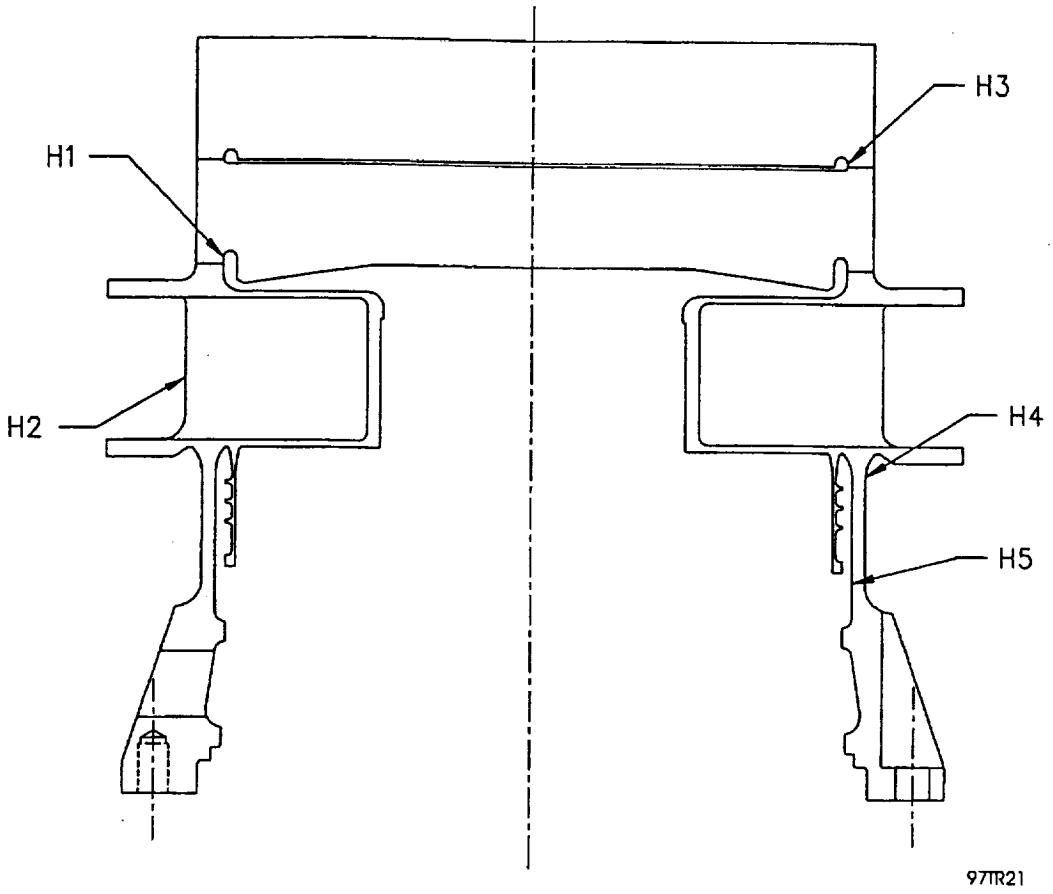

Figure 43. Locations of Heater Head Primary plus Secondary Stresses (Main Vessel)

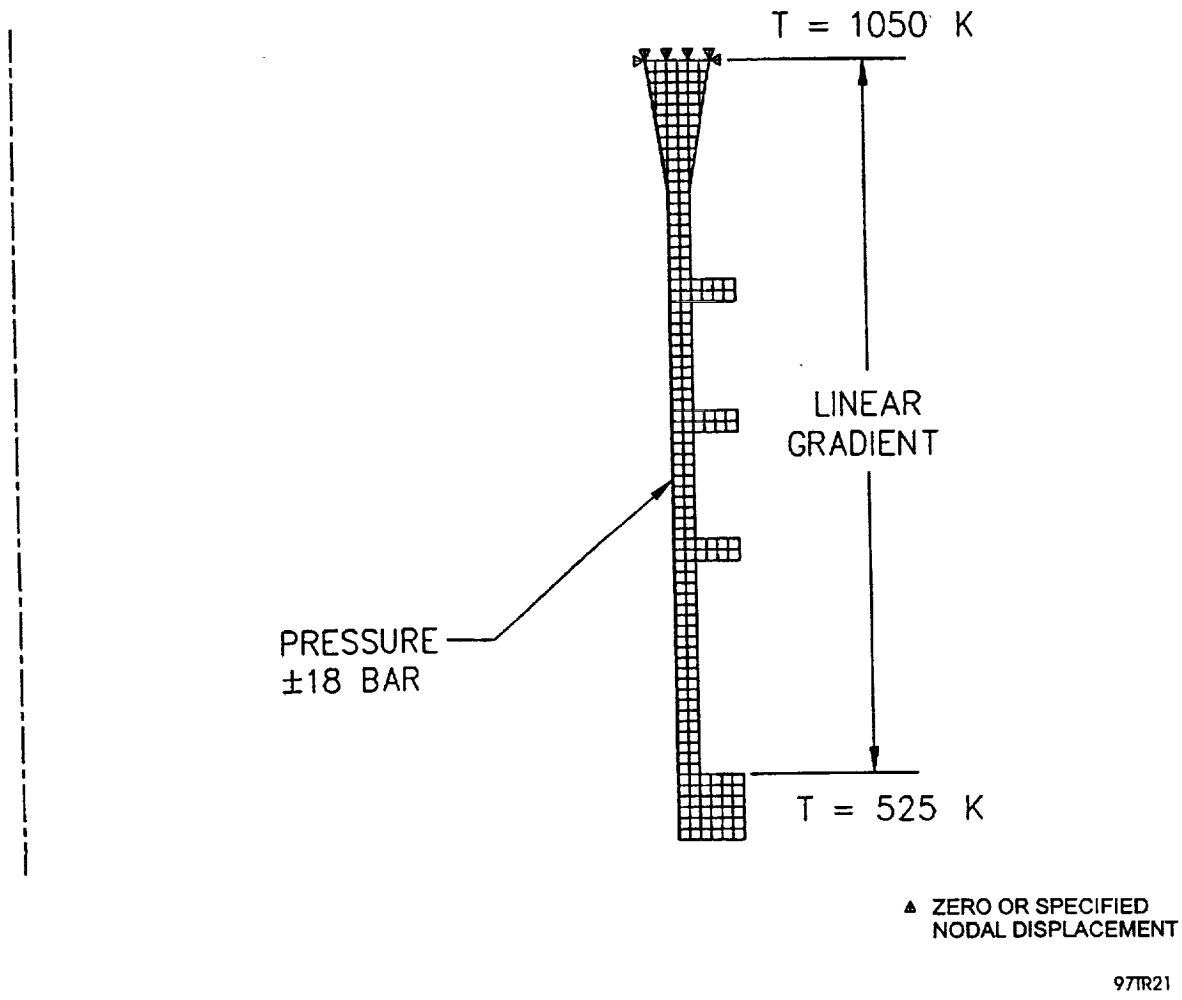

Figure 44. Finite Element Mesh and Assumed Boundary Conditions for Finite Element Analysis On Heater Head Regenerator Wall

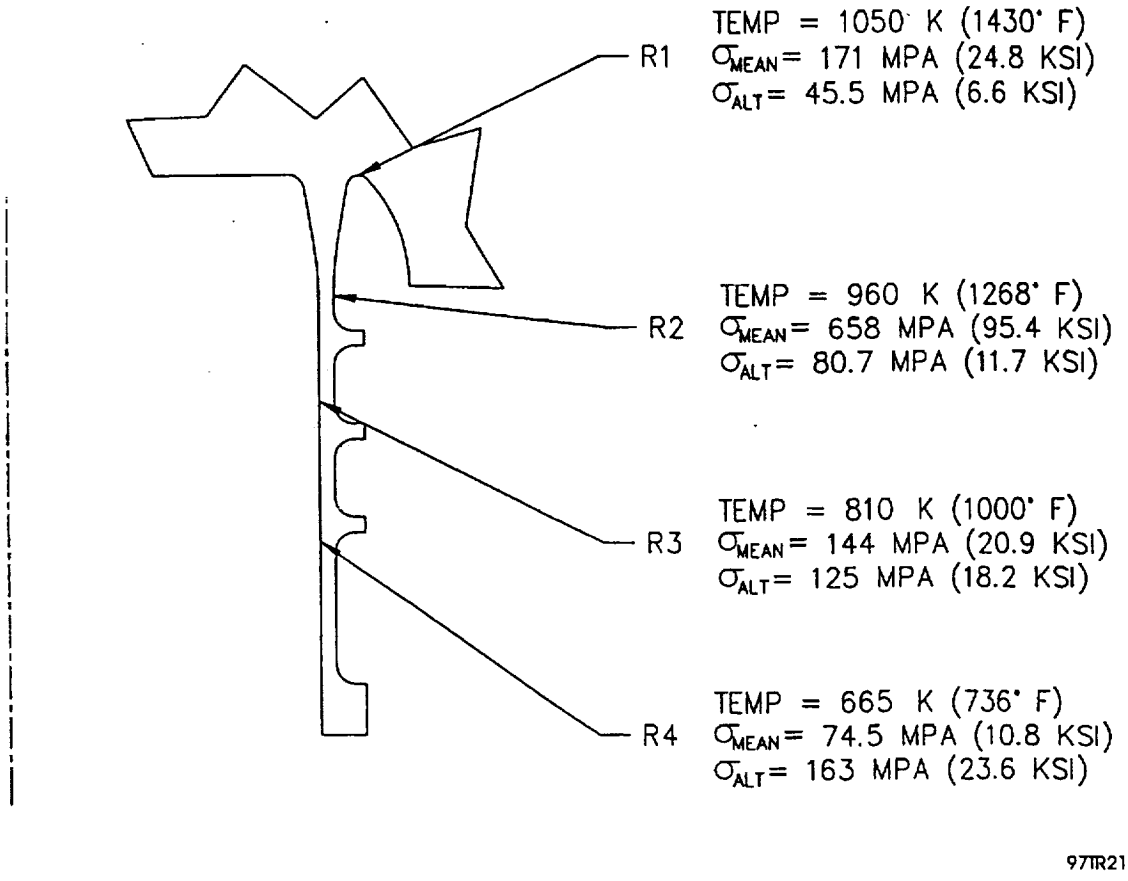

Figure 45. Four Highest Stress Locations along Regenerator Wall

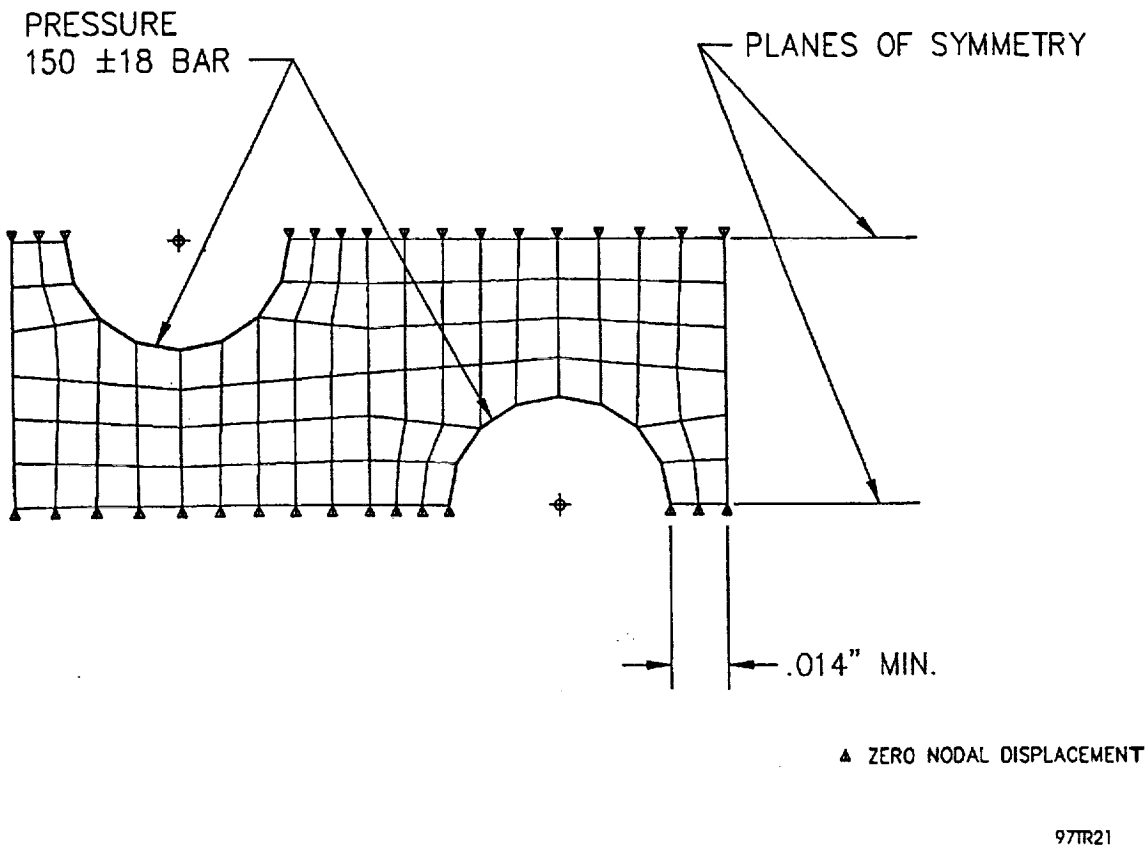

Figure 46. Finite Element Mesh and Boundary Conditions used in Heater Head Fin Analysis

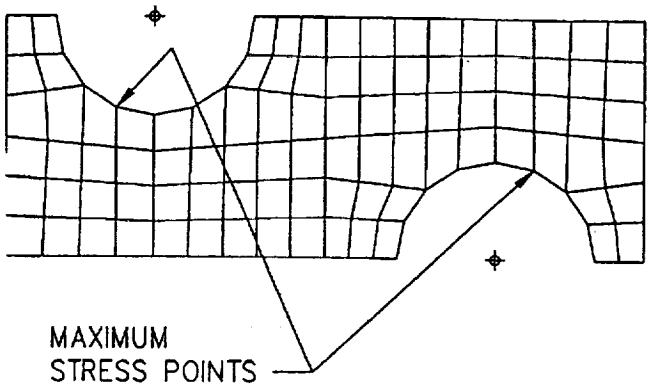

STRESS SUMMARY

σ_{MEAN} = 44.8 MPA (6.5 KSI)

σ_{ALT} = 5.4 MPA (.78 KSI)

n_{YIELD} = 9.9

$n_{ULTIMATE}$ = 10.5

$n_{FATIGUE}$ = 6.0

1% CREEP LIFE > 300 HRS.
@ 1050 K

97TR21

Figure 47. Safety Factors for Stress Locations: Heater Head Fins

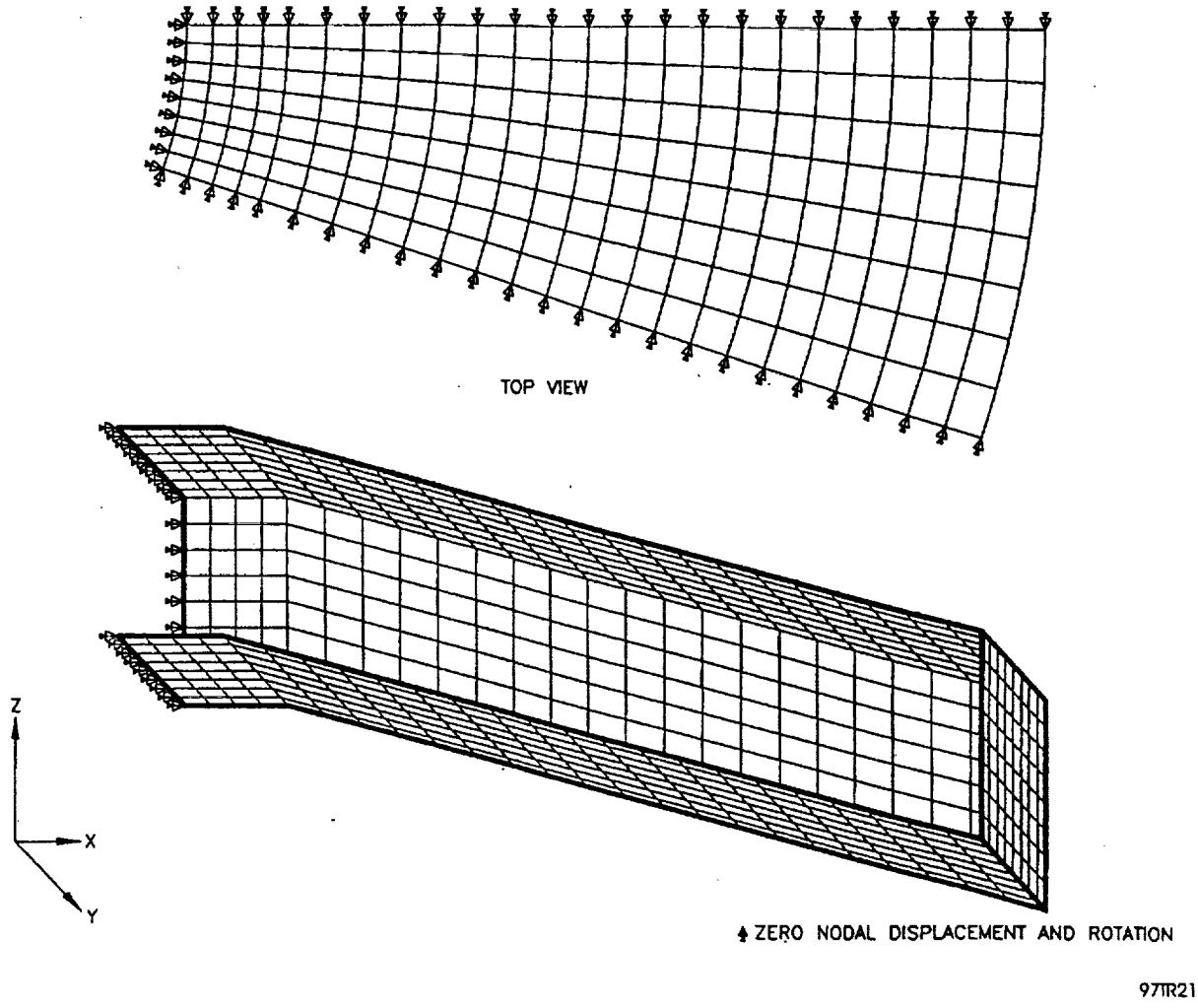

Figure 48. Finite Element Mesh used in Heat Pipe Analysis

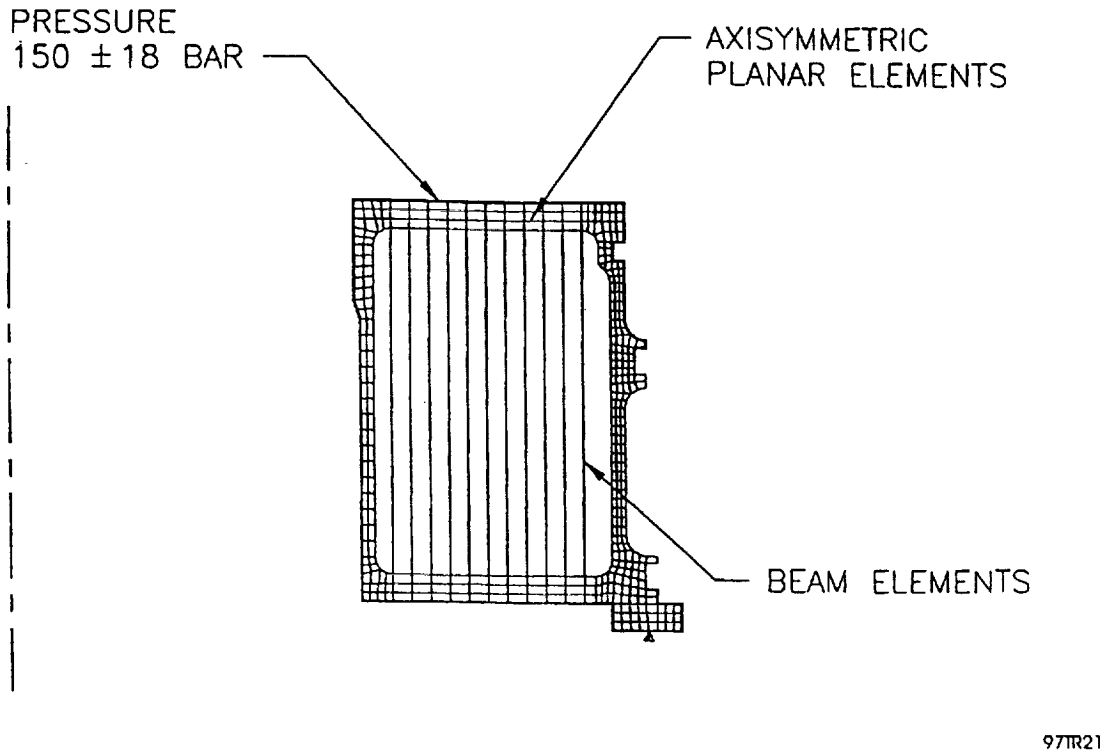

Figure 49. Finite Element Model of Cooler Shell

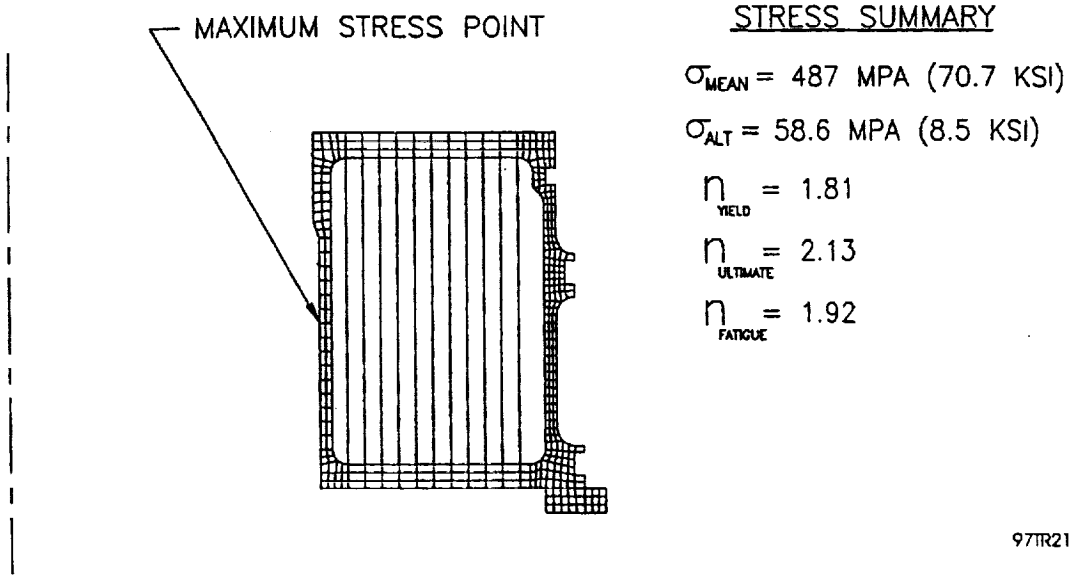

Figure 50. Maximum Stress Point in Cooler Shell

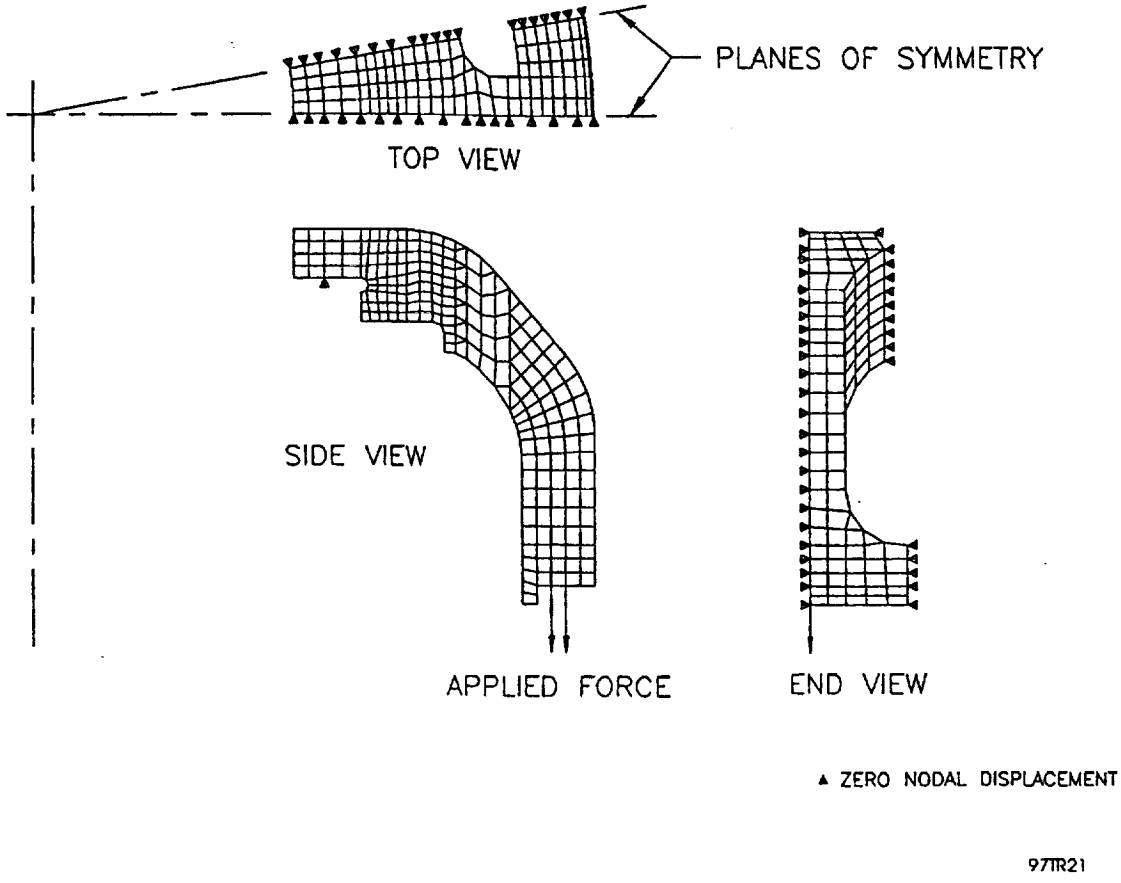

Figure 51. Three Views of Plunger Carrier Finite Element Model

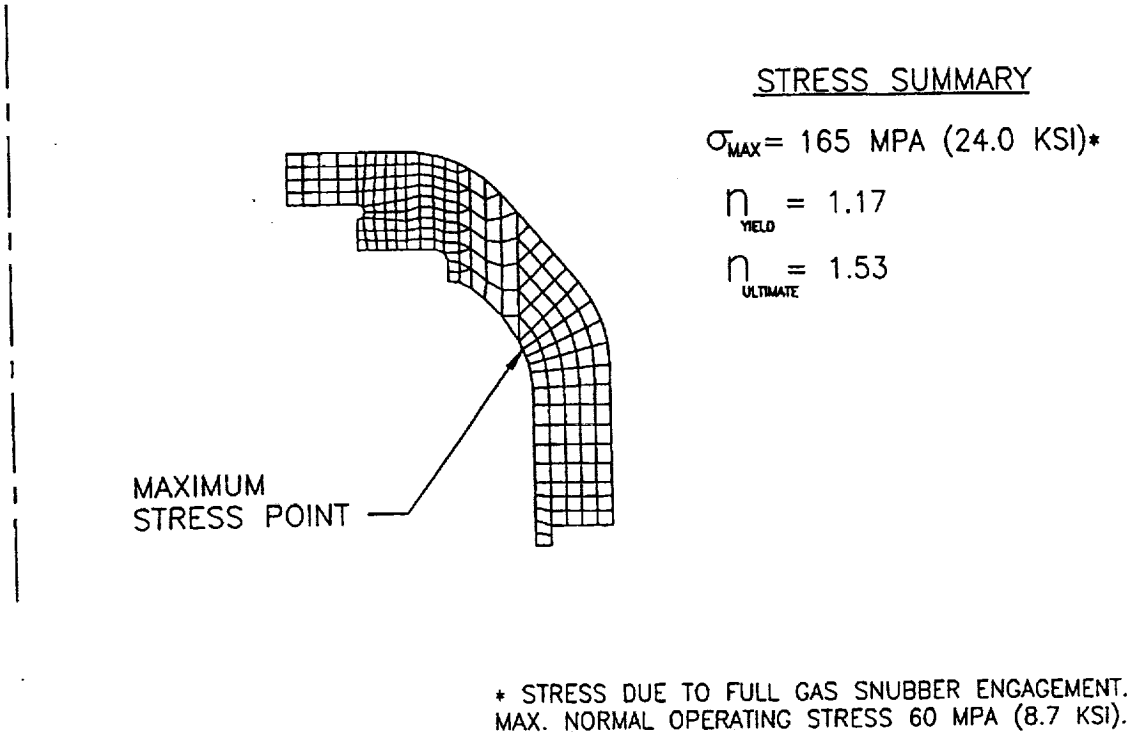

Figure 52. Results of Plunger Carrier Analysis

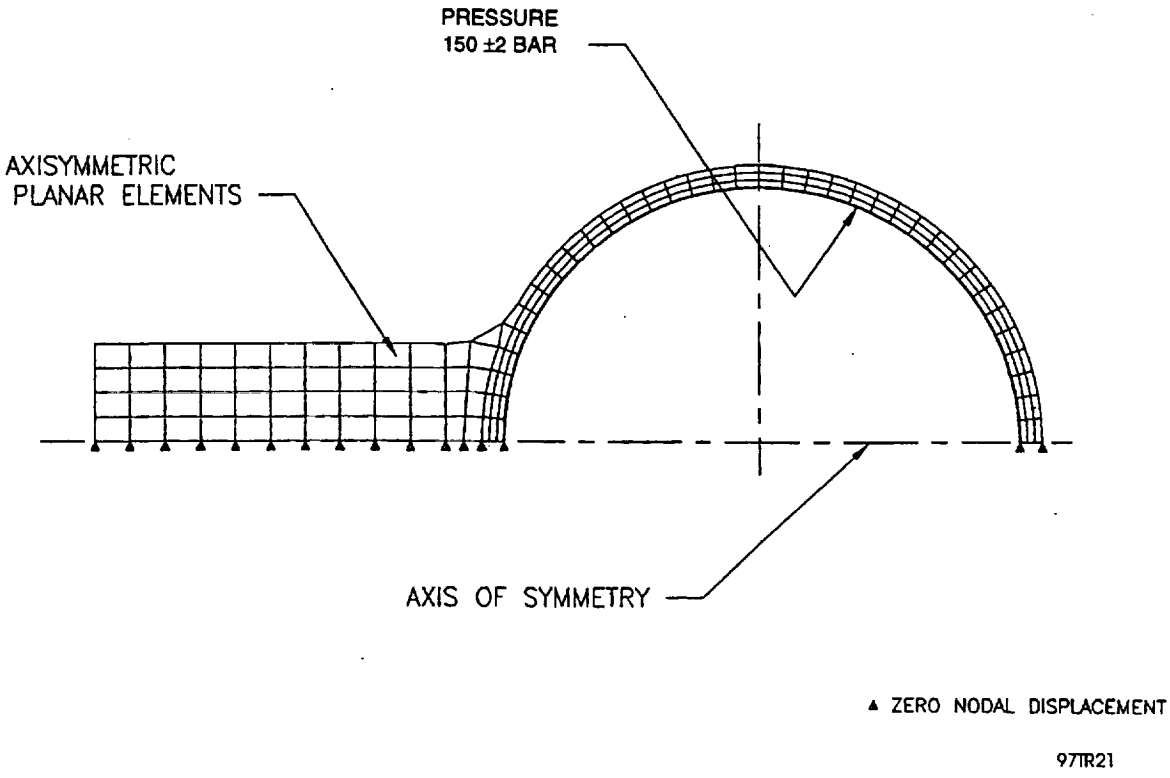

Figure 53. Finite Element Stress Analysis of Volume Compensator

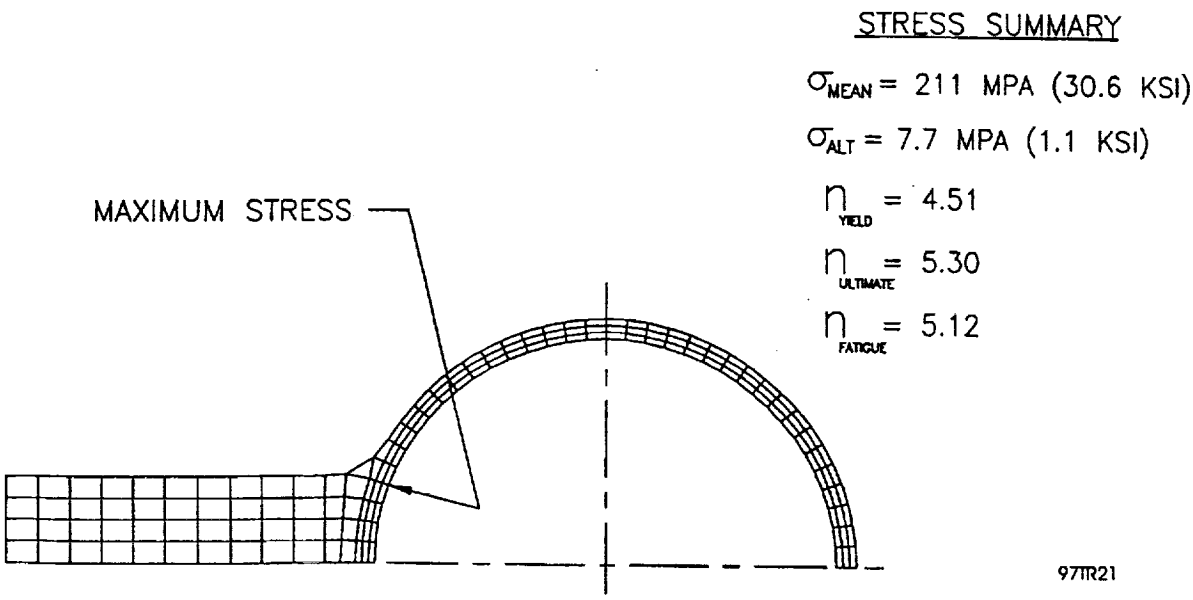

Figure 54. Results of Finite Element Analysis of Volume Compensator

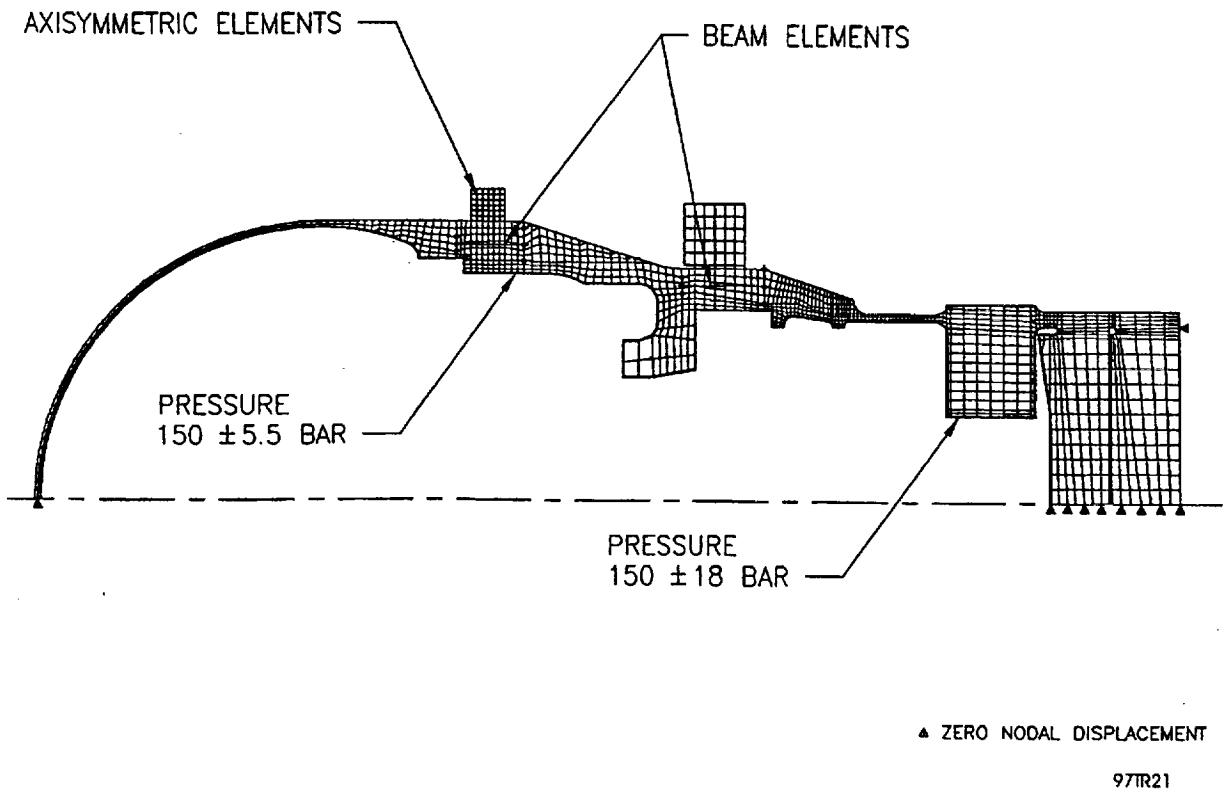

Figure 55. Pressure Vessel Finite Element Model (25°C)

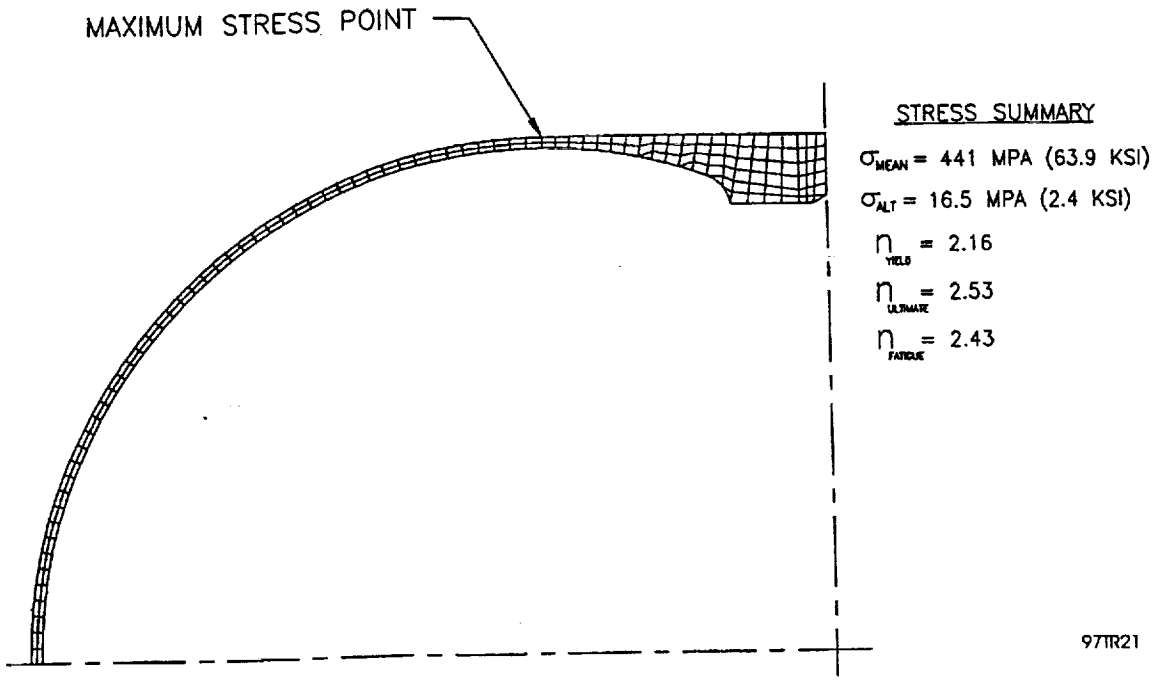

Figure 56. Results of Finite Element Analysis of Alternator Pressure Vessel

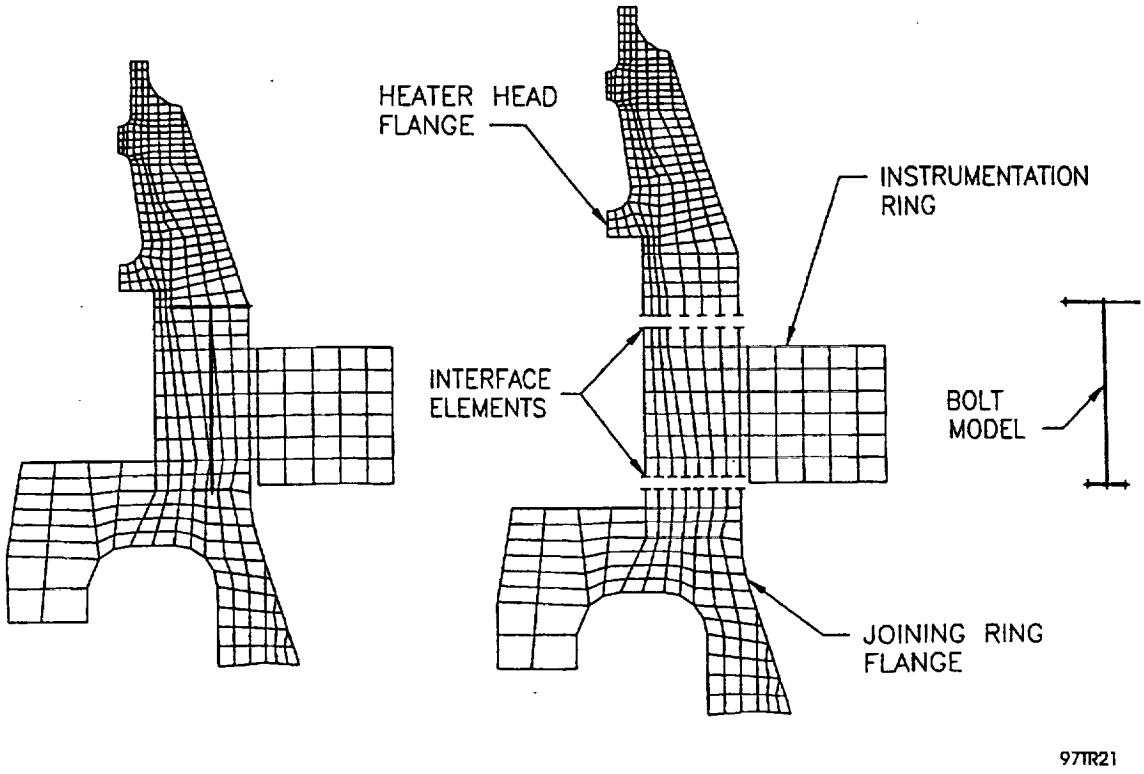

Figure 57. Finite Element Analysis: Detail of Studs in Alternator Pressure Vessel

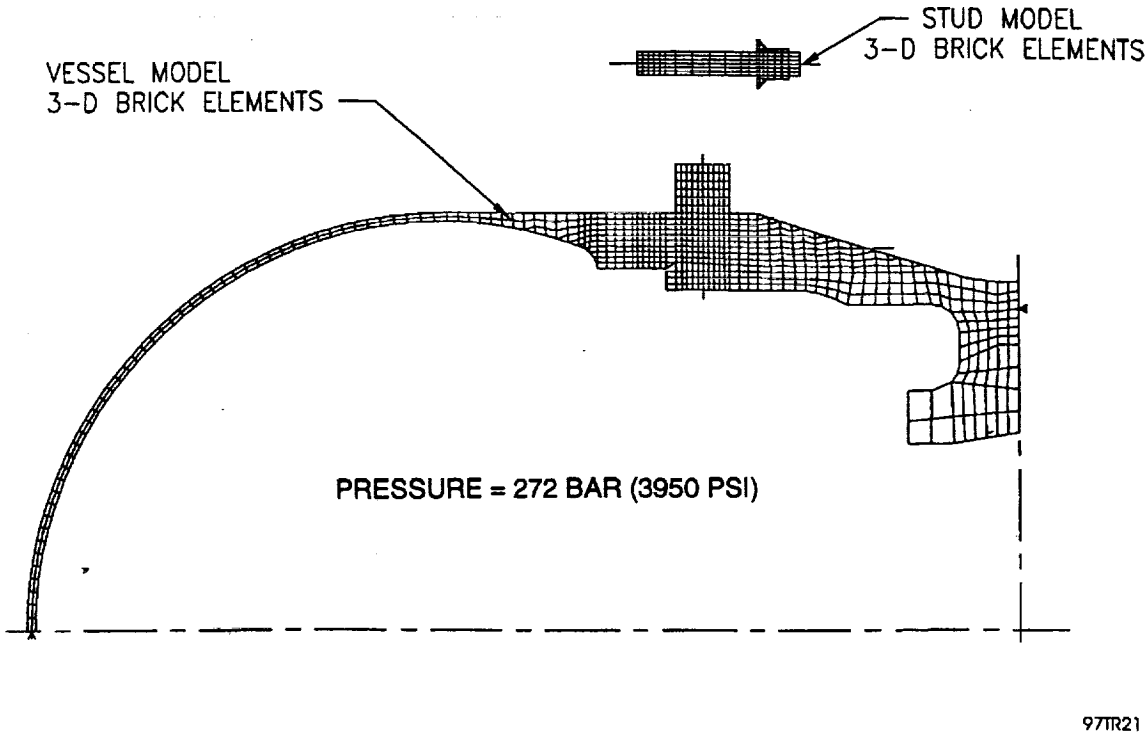

Figure 58. 3-D Mesh used in Analysis of Hydrostatic Pressure Test

7.0 ALTERNATOR DESIGN, DEVELOPMENT, AND TEST

7.1 Introduction

The CTPC alternator is a moving permanent magnet linear alternator, similar in configuration to the SPDE alternator. The CTPC alternator operates at an ambient temperature of 525 K, 200 K hotter than the SPDE. This temperature level is set by the basic specification for the power module which defines the average temperature of the engine cooler at 525 K (252°C). The elevated temperature requirement impacts mainly the design of the alternator plunger and the coil.

The best high-temperature permanent magnets available are samarium-cobalt magnets with a chemistry of 2 parts samarium and 17 parts cobalt and designated as 2-17 material. With an increase in temperature, the magnet strength decreases, as measured by the residual induction (B_r). Even more importantly for the CTPC design, the magnitude of the demagnetizing field which can be tolerated with no loss of B_r also decreases. As B_r drops, the coil current must be increased to maintain power output. An increase in coil current increases the magnitude of the demagnetizing field, and, therefore, a point can be reached where demagnetization limits the power density attainable. For the CTPC, this limit is about 550 K. Detailed design analyses have been conducted and are reported below which identify the margin against demagnetization at the 548 K (275°C) design temperature selected for the CTPC magnets. The magnet tests conducted and the acceptance criteria established are also described in detail.

Alternator coils typically use organic insulating and potting materials. Conventional materials are limited to applications where the coil temperatures do not exceed about 475 K. Since the requirements on the CTPC alternator coil are at least 100 K above this level, an unconventional approach to the design of the CTPC alternator coil was necessary. Significant development has been applied to evolve a coil with high-temperature capability.

7.2 Principle of Operation

A schematic diagram of the CTPC alternator is shown in Figure 59. In diagram "a", the magnets are shown in the left end of the stroke position. The arrows and dotted lines indicate the polarity of the magnets and also the direction of magnetic flux induced by the magnets in the stators. As shown in the diagram, flux encircles (links) the coil in a counterclockwise direction. Diagram "c" shows the magnets at the right end of the stroke position where the magnet-induced flux links the coil in a clockwise direction. Diagram "b" shows that at midstroke the magnet flux is localized, and the coil flux linkage is zero.

As the plunger oscillates at the 70-Hz frequency between the stroke limits, the flux linking the coil continuously changes. The instantaneous voltage generated in the coil is directly proportional to the rate of change of flux linking the coil. Since the flux magnitude is changing approximately linearly with the position of the plunger between the extremes shown in the diagrams, and since the displacement of the plunger varies sinusoidally with time, the voltage generated is also sinusoidal. The peak voltage occurs as the plunger crosses the midstroke position since this is the point at which maximum velocity and, consequently, maximum rate of change of flux linkage occurs.

By connecting the alternator terminals to an electrical load, an electrical current will flow, and power is transferred to the load. The current will cause a magnetic flux to link the coil and induce a voltage in the coil which lags the generated voltage by 90 degrees. This voltage is proportional to the coil inductance. At the coil terminals, the net voltage will be out of phase with the current, resulting in a power factor less than unity. To operate with a unity power factor, a tuning capacitor in series with the load is added to the electrical circuit.

The current flowing in the coil is sinusoidal with the peak occurring at midstroke for a tuned situation. Figure 60 shows the flux linking the coil due to the coil current with the plunger at its midstroke position. This flux opposes the magnet polarity of magnets "A" and "C" on the out stroke and opposes the magnet polarity of the magnets "B" and "D" on the in stroke. The magnets must be capable of withstanding this demagnetizing field.

7.3 Magnet Properties

The samarium-cobalt (Sm_2Co_{17}) magnets for the SPDE were supplied by Thomas and Skinner. In addition to supplying the magnets, Thomas and Skinner had also performed the assembly and machining on the SPDE plungers.

At the start of the CTPC program, Thomas and Skinner, Recoma, I G Technologies (IGT) and Electron Energy Corporation (EEC) were identified as potential suppliers of samarium-cobalt magnets and were asked to supply sample magnets for evaluation and any available high-temperature data.

Thomas and Skinner supplied sample Sm_2Co_{17} magnet material for testing but did not have high-temperature property data readily available. Recoma also supplied sample magnet material and had data available at several temperatures up to 350°C. These data had been generated at the University of Dayton, Ohio, and were used in the preliminary design analyses. The second quadrant demagnetization curves are shown in Figure 61. Based on these data and thermal analysis, 548 K (275°C) was selected as the design temperature for the alternator plunger.

Tests to determine the properties of the Sm_2Co_{17} material available from Thomas and Skinner were initiated. Thomas and Skinner decided to terminate its production of samarium-cobalt magnets and referred MTI to its subsidiary, EEC. Sample tests to determine the properties of EEC material were initiated, and, after several attempts, EEC advised MTI that they were not confident that the very stringent property requirements needed for the CTPC magnets could be guaranteed.

IGT was contacted and requested to supply magnet samples for high-temperature testing. KJS Associates of Dayton, Ohio, was contracted by IGT to perform these tests, and the sample material supplied showed very good properties. Figures 62 and 63 show the test results on one sample at room temperature and 548 K (275°C), respectively. Similar results were obtained on three other samples.

Based upon these test results, the magnet specification was finalized. Since no high-temperature test capability for full-size magnets (as opposed to samples) was available at that time, the acceptance criteria for magnets were based on room-temperature property requirements.

The parameter H_k is defined as the magnitude of the demagnetizing field at which the intrinsic induction has dropped 10% below the residual induction. The larger the value of H_k, the higher the resistance to demagnetization. It was observed from the IGT data that the samples with the highest value of H_k at room temperature also had the highest value of H_k at elevated temperature. The required room temperature value of H_k was specified as 13.5 kOe. It was estimated that a demagnetizing field in excess of 8.5 kOe could be tolerated at 548 K if the magnets met the room temperature specification. This is somewhat higher than the design level of 6.28 kOe and thus provides a modest margin against overcurrent or overtemperature fault conditions. Note that the residual induction used to design the CTPC alternator is 9.0 kgauss (0.9 tesla). The demagnetizing field imposed by the coil current at 12.5-kWe power output is 6.28 kOe.

IGT was acquired by Recoma and became a division of the Recoma company. The IGT division responded to the request for quotation and became the supplier of the magnets for CTPC.

During the magnet procurement phase, MTI developed a technique to measure the properties of full-size CTPC magnets at 548 K. This technique was applied to magnets which had met the room temperature specification and also some that were somewhat below the specification. This provided additional assurance that the magnets which were actually installed in the CTPC plunger had acceptable elevated temperature properties.

7.4 Preliminary Design and Analysis

This section describes the electromagnetic, thermal, and mechanical design of the CTPC alternator. Structural design is presented in Section 6.

7.4.1 Electromagnetic Design

The electromagnetic design of the CTPC alternator was performed using the computer codes LPMMA, MAXWELL, and FLUX.

LPMMA is a proprietary computer code developed by MTI for the design and analysis of linear motors and alternators. It uses a finite difference approach to the solution of the electromagnetic field equations. The code was also developed as an optimization tool in which changes to pertinent parameters can be easily entered and a rapid solution obtained. Although analytical simplifications were required in the development of the LPMMA code, compared to the more detailed finite element methods (MAXWELL and FLUX), comparisons with the more detailed analyses and experimental tests have shown the results from LPMMA to be quite accurate. The major LPMMA input parameters and output results are presented in the analytical results section below.

MAXWELL is a general-purpose finite element code which solves for the flux distribution in static electromagnetic models. For the CTPC, MAXWELL was used as follows:

1. For no coil current, the flux linking the coil is determined for the magnets in various positions between midstoke and end of stroke. From this, the rate of change of flux with respect to position ($d\phi/dx$) is determined. The rate of change of flux linking the coil with respect to time determines the voltage generated by the magnets and is calculated $(d\phi/dx)*(dx/dt)$.
2. Knowing the generated voltage from Step (1) and the load power factor (unity for the CTPC), the coil current is determined from the required shaft power.
3. To determine the voltage induced by the coil current, and, consequently, the coil inductance, a solution is obtained with the magnet B_r set to zero. The flux linking the coil, ϕ, due to the coil current is determined. The voltage induced in the coil is then determined by $\varpi\phi$ (where ϖ is the angular operating frequency).
4. To assess demagnetization, Maxwell solutions are obtained at midstoke with the magnets, and the coil current represented at end of stroke with zero coil current. The flux plots indicate directly the local flux conditions in the permanent magnets.

The FLUX code is a general-purpose dynamic electromagnetics code available at Rensselaer Polytechnic Institute (RPI). It is a time-consuming and relatively expensive code to run. Its use was limited to determining eddy current losses in the alternator support structure which are not readily calculated in the static code MAXWELL. After the design details of the alternator and surrounding structural components were finalized, FLUX provided an assessment of the eddy current losses in the final design configuration.

The two basic parameters that couple the design of the alternator to the design of the engine are piston stroke and frequency. Based on the optimization analyses for the CTPC engine geometry, the stroke and frequency were set at 28 mm and 70 Hz, respectively. The inner diameter of the inner stator was set at 7.00 in., and the outer diameter of the outer stator was set at 12.50 in. This established the envelope of the alternator for detailed design.

The final design configuration selected is shown in Figure 64. The key parameters are listed in the Table 16, with the predicted design performance characteristics listed in Table 17. The first column of Table 17 lists the performance calculated at the nominal design point using the properties and geometry as they were known at the preliminary design stage. The second column revises the design calculations based on as-built dimensions and properties. In both cases, the frequency is assumed to be 70 Hz. Alternator weight breakdown is given in Table 18.

7.4.2 Thermal Analysis and Cooling Design

As discussed in Section 7.3, the magnets in the alternator plunger are sensitive to demagnetization if operated above their design temperature. The design temperature for the magnets was set at 548 K (275°C). The engine cooler average wall temperature is 525 K at the design point. The general

Table 16. Key Parameters of Final Design Configuration

Components	Parameter Values
Magnets	
B_r at 275°C	9.0 kgauss (0.90 tesla)
Thickness	9.0 mm (0.355 in.)
Thickness-to-gap ratio	0.8
Effective length, each	28 mm (1.1 in.)
Mean diameter	220 mm (8.695 in.)
Effective circumference	671 mm (26.4 in.)
Number of magnets/ring	18
Total number of magnets	72
Number of segments per magnet	3 (single used in as-built CTPC)
Coil	
Copper area	1135 mm^2 (1.76 $in.^2$)
Number of turns	80
Copper geometry	2 flat wires, 0.55 x 0.04 in.
Conductor insultation	Polyimide (≈ 2-mil thick)
Net packing factor	88%* and 65%**
Laminations	
Material	Permendur V (Hiperco 50)
Insulation	Oxided surface (Danco)
Outer stator O.D.	317.5 mm (12.50 in.)
Outer stator I.D.	232.2 mm (9.14 in.)
Overall length	95.3 mm (3.75 in.)
Pole face length	31.7 mm (1.25 in.)
Inner stator O.D.	209.8 mm (8.26 in.)
Inner stator I.D.	177.8 mm (7.0 in.)
Outer stator cross-section area Flat laminations Tapered laminations Wire ways	3512 mm^2 (15.2 $in.^2$) 2786 mm^2 (12.06 $in.^2$) 809 mm^2 (3.5 $in.^2$) 81 mm^2 (0.35 $in.^2$)
Inner stator cross-sectional area Flat laminations Tapered laminations Slots	3489 mm^2 (15.1 $in.^2$) 2241 mm^2 (9.70 $in.^2$) 1280 mm^2 (5.54 $in.^2$) 23 mm^2 (0.1 $in.^2$)

*Coil only.

97TR21

**Includes filler rings.

Table 17. CTPC Alternator Predicted Performance Characteristics

Parameter Units	Design Point	As-built Calculation
Stroke, mm	28	28
Shaft power, kW	14.1	14.1
Magnet temperature, K	548	548
B_r, tesla	0.90	0.92
E_{gen}, V peak/turn	4.87	4.98
Number of turns	80	80
E_{gen}, V rms	275.6	281.7
NI, A turns peak	5790	5662
Current, A rms	51.2	50.1
Inductance, mH	14.9	14.9
V_{ind}, V rms	335.7	328.5
V-terminal, V rms	434.3	432.7
Beta (V_{ind}/E_{gen})	1.22	1.17
Tuning capacitor, μF	346	346
Flux density iron, tesla	1.70	1.62
Minimum magnet flux density, tesla	0.20	0.22
Average coil temperature, K	593	593
Coil loss/shaft power, %	3.9	3.55
Lamination loss/shaft power, %	1.6	1.6
Magnet loss/shaft power, % Eddy current Hysteresis	 0.3 3.0	 1.8 3.0
Structural Loss/Shaft power, %	2.0	3.0
Efficiency, %	89.0	87.05
Output power, kW	12.54	12.25

97TR21

*Table 18. Weight Breakdown**

Component	Weight, kg (lb)
Magnet	5.82 (12.84)
Laminations	21.34 (47.05)
Copper	8.60 (18.96)
Insulation	0.30 (0.66)
Subtotal	36.06 (79.5)
Inconel in plunger	1.4 (3.08)
Filler rings (PMR-15)	0.16 (0.35)
Outer stator end rings	2.8 (6.22)
Inner stator end rings	2.9 (6.41)
Subtotal	7.26 (16.0)
TOTAL	43.32 (95.5)

*Stator assemblies and plunger, excluding carrier and support ring.

temperature level of the alternator assembly is established by control of the temperature of the fluid flowing over the outside of the pressure vessel. To simplify the mechanical design of the power module, it is desirable that the pressure vessel coolant and the engine coolant be a single loop. The pressure vessel will be cooled by fluid at a temperature of about 520 K (245°C). Thus, there is about a 30°C difference between the pressure vessel coolant and the magnet temperature limit.

The primary source of heat in the cold end of the engine is the alternator. The coil I^2R loss is about 600 W, and losses in the laminations, magnets, and adjacent structure are about 800 W.

Prediction of heat transfer between the solid surfaces and the helium which is agitated by the motion of the piston and plunger requires that the helium flow and convective heat transfer coefficients be predictable over all surfaces. Both the geometry of the alternator section of the engine and the helium flow patterns are very complex, making accurate heat transfer predictions difficult. To enhance the transfer of heat from the alternator region to the vessel, controlled flow paths are introduced. Figure 65 shows the approach selected for the CTPC. Directional orifices are located in series with flow passages located at the I.D. of the inner stator, the O.D. of the outer stator, and the inside of the lower section of the vessel. Directional orifices are shaped such that the resistance to flow in one direction is less than in the opposite direction.

As the plunger moves, gas is displaced as shown in Figure 66. Flows in each of the four parallel paths are established by the requirements of continuity and equal pressure drop along each path. To make the analysis tractable, simplifying assumptions are made. The surface friction and orifice pressure drop, which balances the pressure drop along a passage, are based on steady flow conditions. Under rapidly oscillating flow conditions, this may not be accurate.

Due to the directional orifices, more gas flows down along the vessel on the up stroke than on the down stroke, resulting in a circulation superimposed on the 70-Hz oscillating flow. Figure 67 shows the temperatures calculated for design point conditions.

Due to the limitations on the capability of inorganic materials to survive high-temperature conditions, the coil construction approach was selected to minimize the maximum coil temperature.

Temperature levels inside the coil were calculated using the ANSYS code. The ANSYS model is shown in Figure 68. Figure 69 shows the boundary conditions, heat generation, thermal conductivities, and

calculated temperature distribution. As coil development proceeded, the wrap was changed from alumina-filled Kapton to polyimide-coated fiberglass. The thermal conductance (conductivity divided by thickness) is approximately the same as the 0.006-in. wrap assumed in the thermal analysis. The heat flow is primarily axial as expected, and the maximum temperature in the coil is 320°C. This value was used as a reference for evaluating the stability of insulation and adhesives.

7.5 Mechanical Design and Fabrication

As mentioned above, the permanent-magnet linear alternator in CTPC is conceptually similar to the SPDE design. The primary consideration which resulted in most of the detail design changes from the SPDE is the temperature requirement. This section describes the development effort performed to address the high-temperature requirement for the CTPC alternator.

7.5.1 Coil Fabrication

The geometry of the coil is shown in Figure 70. During the detail design phase, the alternator envelope and slot geometry were finalized. The final number of turns selected was 80, resulting in a nominal generated voltage at design point conditions of 280 V rms. Two 15-turn end coils and two 25-turn inner coils are connected in series. The end coils are connected to the inner coils on the inside diameters; the inner coils and the terminals are connected at the outer diameter.

Several polyimide adhesives were evaluated before finally selecting Matrimid 5218. Matrimid 5218 requires a controlled high-temperature oven cure to develop its properties.

Several trial coils were made to develop the winding procedure and make adjustments to the winding fixture so that the coil dimensions were within the tolerance requirements.

To avoid a joint at the interconnection of the edge coil and the inner coil, an approach was developed in which the larger coil was wound first with sufficient extra wire for the small coil included. The winding fixture and coil were placed in an oven to cure the adhesive. Following cool down, the second coil was then wound, and the fixture and coils were returned to the oven to cure the adhesive of the second winding. In the final assembly, two similar coils were joined together to form the full coil.

Following fabrication of the individual coil halves, they were overwrapped with fiberglass, coated with high-temperature silicone (Castol), and cured. This provided protection and additional insulation where the coil contacted the laminations, taking the place of a slot liner in a conventional construction.

A flattened fiberglass tube of appropriate thickness was placed in the central gap between the two coil sections. This serves the function of making the final width of the coils the same as the slot. It also introduces some compliance to accommodate axial differential expansion between the coil assembly and the laminations.

Finally, the braze joints are made to interconnect the coils and add the terminal connection strips.

7.5.2 Outer Stator Fabrication And Test

An inverted shoe geometry was selected for the outer stator. To assemble a coil into such a geometry requires the use of two-piece laminations. Fourteen-mil-thick flat laminations of the geometry shown in Figure 64 were made from Permendur V material. These were split in the back iron as shown. During assembly, the long and short pieces are alternated so that a split in one lamination is adjacent to solid material in the next lamination. Because the laminations are flat, they are stacked in a way such that there are no gaps at the I.D.; the circumference difference between the I.D. and O.D. results in gaps between the laminations at the O.D. To take up the extra space, taper-ground laminations are used to fill the gaps. This improves the structural rigidity of the assembly and also provides magnetic flux carrying capability to provide margin against saturation.

An assembly fixture was designed and built to position the coil, the laminations, and the end rings during the final welding operations.

7.5.3 Inner Stator Construction

The inner stator construction did not present any unusual difficulties. It is a solid array of laminations held together by rings at each end fillet welded to the laminations. To eliminate gaps for structural integrity and to maximize iron area, 20% of the laminations were taper ground from 25-mil stock. The unground laminations were made from 14-mil stock. A fixture was used to hold the components in position for welding, and the outer diameter was ground to final drawing dimension.

7.5.4 Plunger Construction

Figure 71 shows the plunger which is comprised of 4 rows of 18 magnets with 3 Inconel 718 spacer rings between the magnet rows, an Inconel 718 end ring at the free end, and an Inconel 718 ring between the beryllium carrier and the first row of magnets. Eighteen tie rods are located in narrow gaps between the magnets. These are threaded into helicoiled holes in the plunger and have self-locking nuts at the free end. The ends of the magnets have ears ground on them that fit closely into the spacer and end rings.

A requirement of the plunger design is that low electrical resistance current paths must be avoided to minimize power losses associated with eddy currents during operation. Initially, magnets made from three pieces with insulated joints in the individual magnets were proposed to limit eddy currents in the individual magnet blocks. Based on a concern expressed by the magnet vendor regarding the reliability of such a construction method, it was decided to use single-piece magnets and accept the 1.6% predicted penalty on alternator efficiency.

The spacer rings incorporated an insulated joint to break up the circumferential continuity of the rings (Figure 72). The magnets were insulated from the rings by placing a layer of KAPTON in the groove. This technique was evaluated using three magnets in a flat mockup.

Since samarium-cobalt magnets are very brittle and easily damaged, two plungers were ordered so that the program had a backup available in the event one was damaged accidentally.

7.6 Alternator Static Tests

The objectives of the static tests were to measure the following alternator parameters using various test setups:

- Sidepull gradient and magnitude
- Plunger axial stiffness and plunger force due to coil current
- Coil flux linkage by magnets: generated voltage
- Direct current resistance and coil inductance
- Power loss (see Section 7.7).

The alternator static tests were performed either with the plunger locked in position at various locations or with the plunger entirely removed from the test setup. Different magnitudes of electrical voltages were supplied across the alternator terminals either by the variable frequency DMAC power supply or by the 60-Hz line power. The alternator losses were determined by sequentially removing individual subassemblies or components (plunger, inner and outer stators, stator mounting plate, power piston cylinder, joining ring, pressure vessel) and comparing the required electrical power input. These tests showed that the characteristics of the alternator agreed reasonably well with the design predictions. The results for plunger S/N #1 at 60 Hz, 425 V rms and 50.6 A rms are summarized in Table 19. Note the test was performed at room temperature (approximately 300 K). The last two columns of the table represent the expected values when the alternator is operating at its design temperature of 525 K.

Table 19. Plunger Test Results

Parameter	Units	Measured 300 K	Predicted 300 K	Measured Extrapolated 525 K	Predicted 525 K
Sidepull gradient	lb/mil	9.1*	8.1	8.0	7.0
BETA (based on coil flux linkage)	V/(m/s)	74.2	73.1	65.0	64.1
Force per unit coil current (plunger at midstroke)	N/A	77.7	77.9	68.1	68.3
Axial stiffness (midstroke average)	lb/in.	741	799	649	699
Coil inductance	mH	14.5	14.9	14.5	14.9
Coil dc resistance	ohm	0.087	0.087	0.183	0.183
I^2R loss	W	221	221	465	465
Stator loss	W	274	274	274	274
Structure loss	W	237	201	237	201
Plunger loss	W	787	750	787	750
Total loss	W	1519	1446	1763	1690

*±10% angular variation.

97TR21

7.7 Power Loss

The alternator losses can be broken down as follows:

- Stator losses
  - Coil I^2R
  - Coil eddy currents
  - Lamination hysteresis
  - Lamination eddy currents
  - End rings and weld eddy currents
- Plunger losses
  - Magnet eddy currents
  - Magnet hysterisis
  - Structure eddy currents
- Engine structure eddy current losses
  - Stator mounting plate
  - Power piston cylinder
  - Joining ring
  - Pressure vessel.

The following series of power loss static tests (plunger stationary or not present) were conducted:

1. In the first series, the first-build stator assemblies, including end rings, were tested with the stator mounting plate installed on a modified lathe. Testing at low currents was performed with the plunger installed.

2. The second series of tests were conducted on the engine assembly stand. In these tests, all the subassemblies except the pressure vessel could be included in the build. Tests with various subassemblies sequentially removed from the setup were conducted.
3. The third series of tests were conducted on the backup stators prior to the lamination and end ring welding to determine the losses in a bare assembly.

By performing back-to-back tests with various subassemblies or components sequentially removed, it is possible, by comparing the tests, to determine the loss in each subassembly.

The coil I^2R loss was determined at each data point from the measured resistance and current values. Subtracting this loss from the total power supply gave the remaining loss, which is referred to as core loss.

In Table 20, losses based on the static test measured data are compared with analytical predictions. The coil I^2R losses are based on 50.6-A rms coil current and the resistance at the design temperature of 573 K. (This is 2.1 times the room temperature value of 0.087 ohm). The analytical predictions are based upon final as-built dimensions (Br = 0.92 tesla at 548 K and a coil temperature of 573 K) but do not include the magnet hysteresis losses shown in Table 17.

Table 20. Comparison of Measured Losses with Analytical Predictions

Component	Based on Test Data		Analytical Prediction	
	Loss (W)	% Power, Shaft	Loss (W)	% Power, Shaft
Coil I^2R	465	3.30	465*	3.30*
Laminations				
Hysteresis	–	–	128*	0.91*
Eddy current	–	–	0.29*	–
Coil eddy current	–	–	105*	0.74*
Total	274	1.94	274*	1.94*
Stator end rings				
Outer	–	–	30**	0.21**
Inner	83	0.59	0.11**	–
Total	–	–	46**	0.33**
Stator mount plate	66	0.47	40**	0.28**
Engine structure				
Power piston cylinder	–	–	–	–
Joining ring	–	–	–	–
Pressure vessel	Not included	–	–	–
Total	88	0.62	115	0.82
Plunger				
Magnet hysteresis	–	–	0	0
Magnet eddy current	–	–	327***	2.32
Structure eddy current	–	–	0	0
Total	435	5.58	327	2.32
Total	1411	10.0	1267	9.0
Efficiency	90.0	–	91.0	–

*LPMMA. 97TR21

**MAXWELL.

***MTI eddy current analysis code.

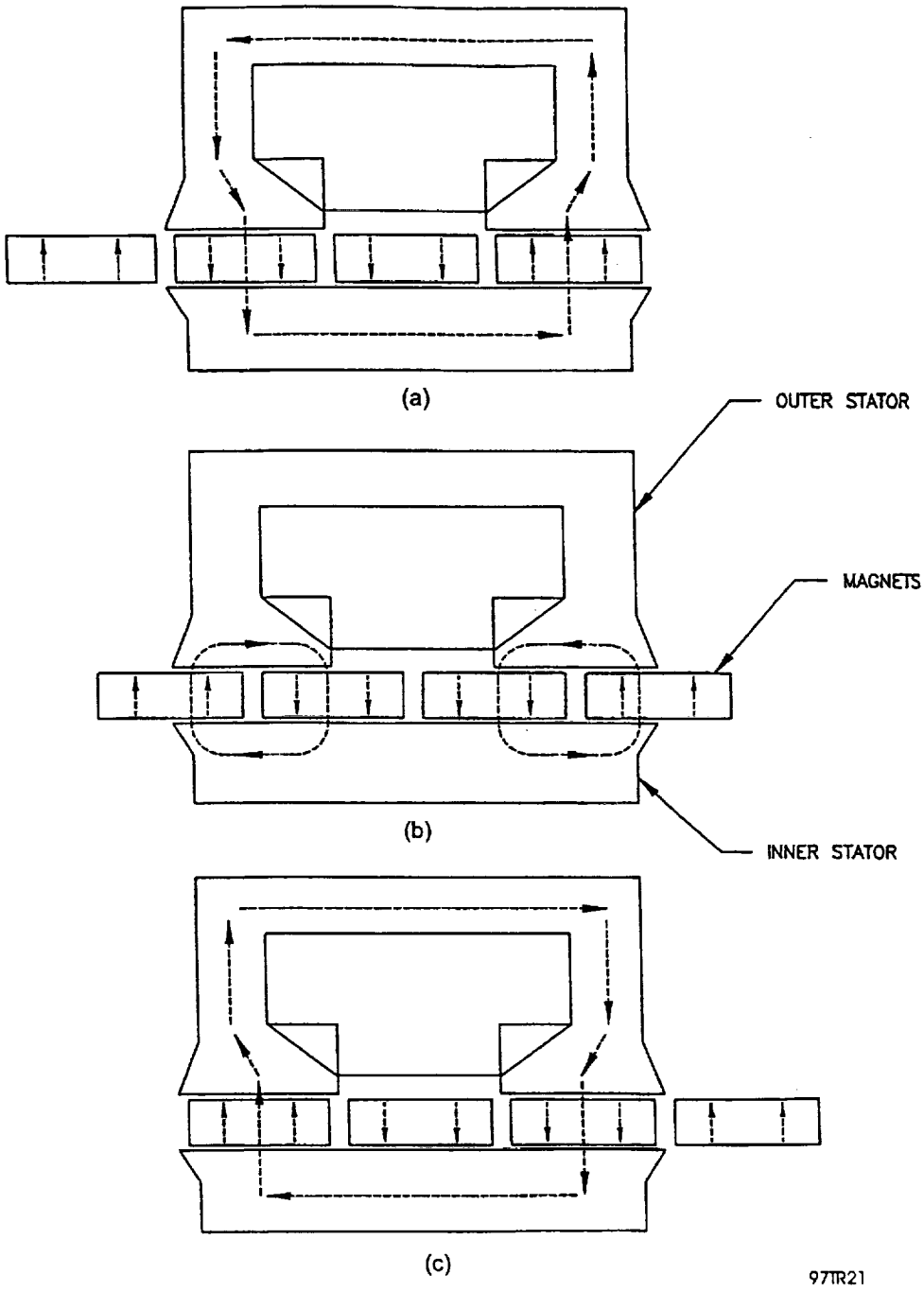

Figure 59. Schematic of CTPC Alternator

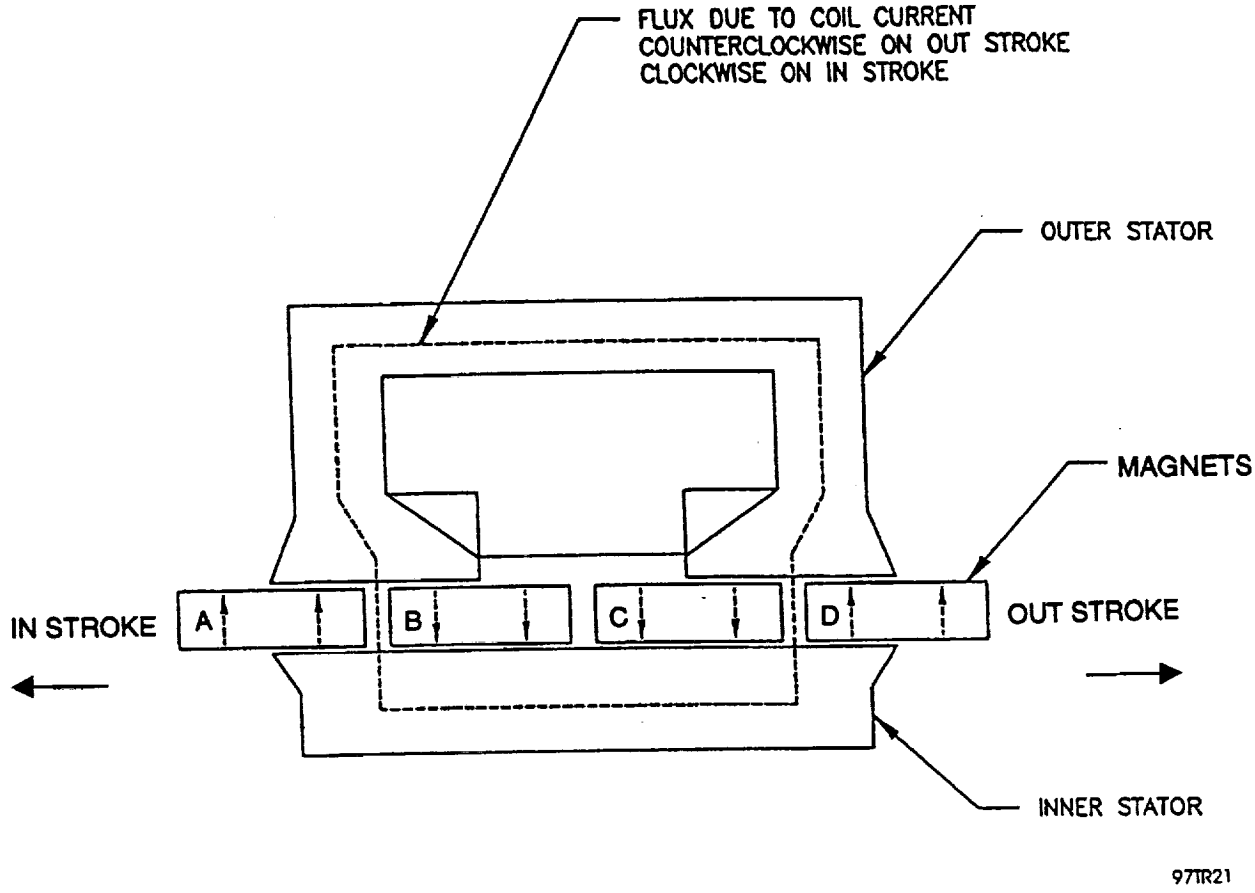

Figure 60. Flux Linking Coil due to Coil Current

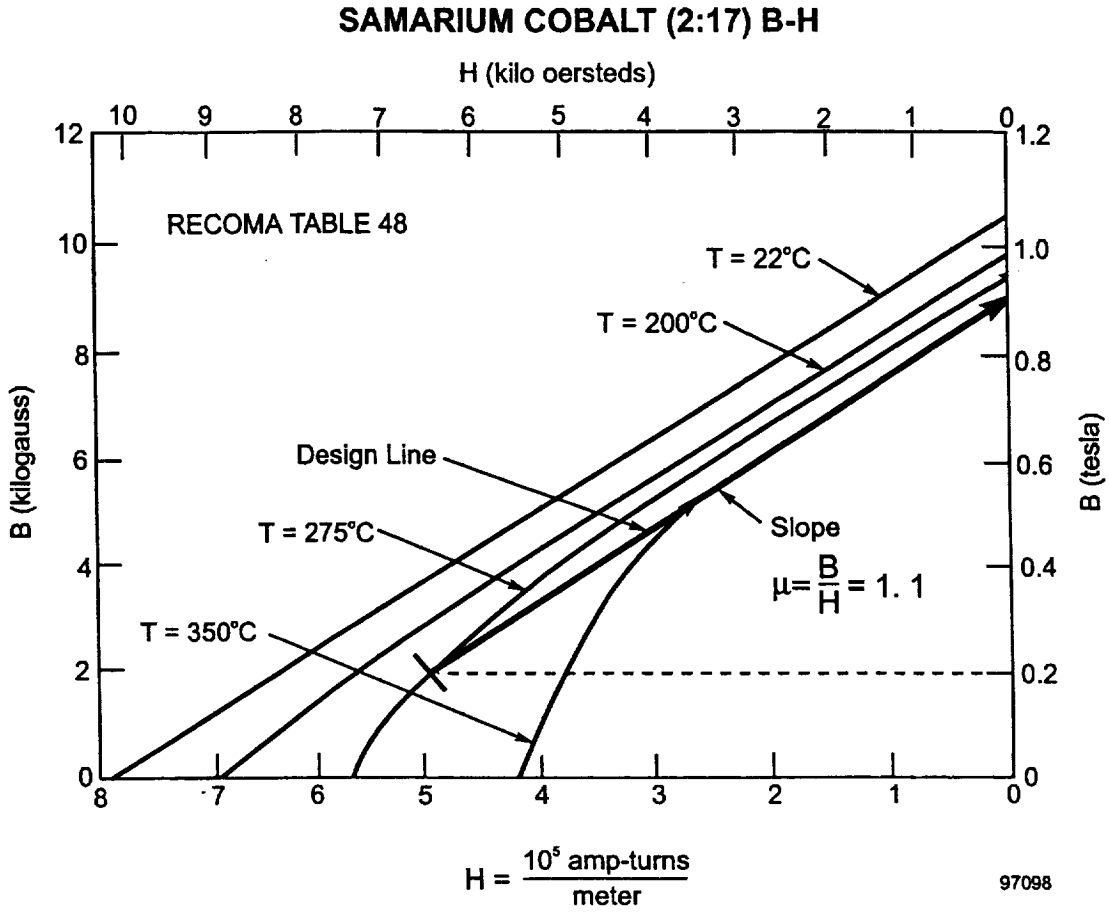

Figure 61. Second Quadrant Demagnetization Curves

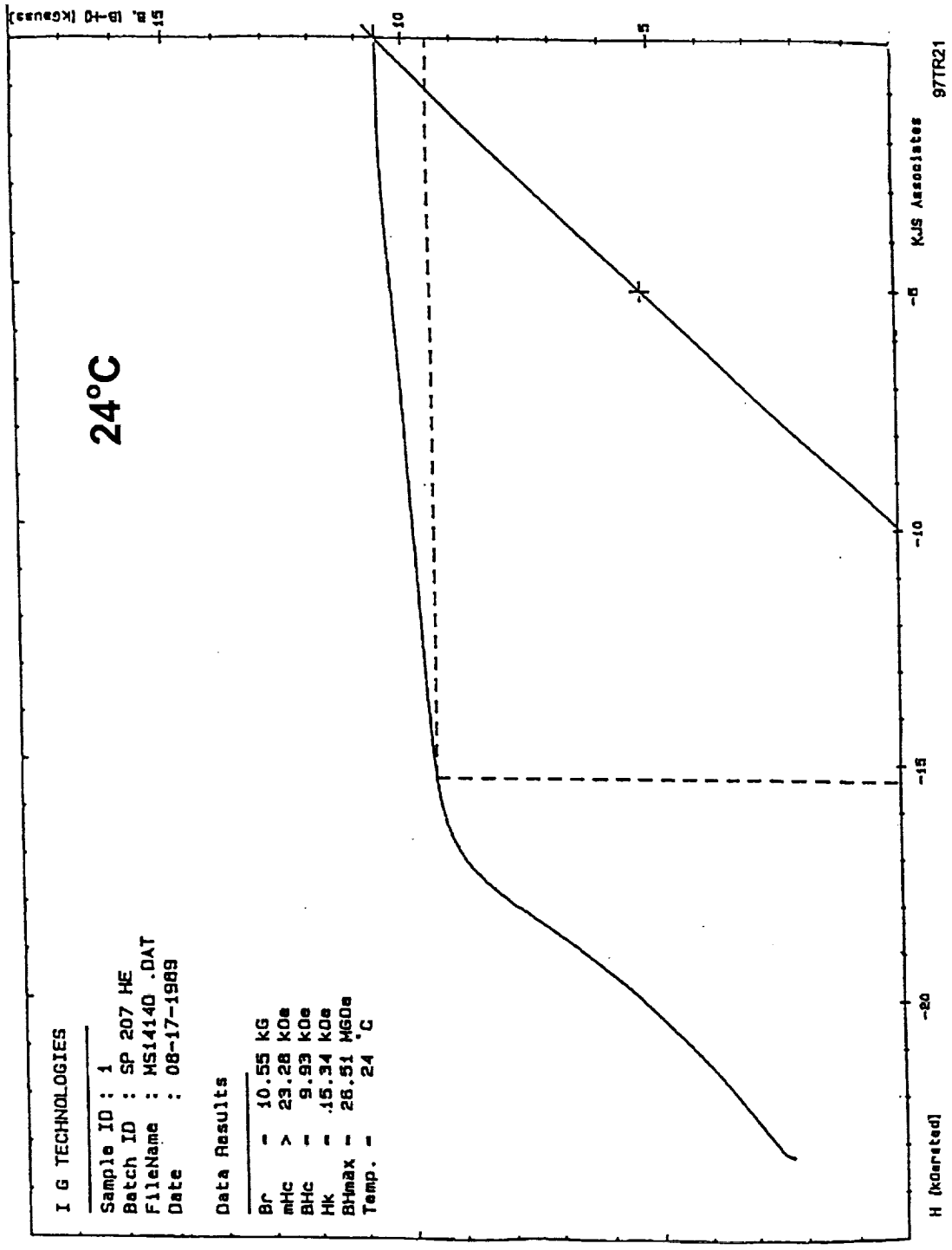

Figure 62. Test Results on Sample at Room Temperature

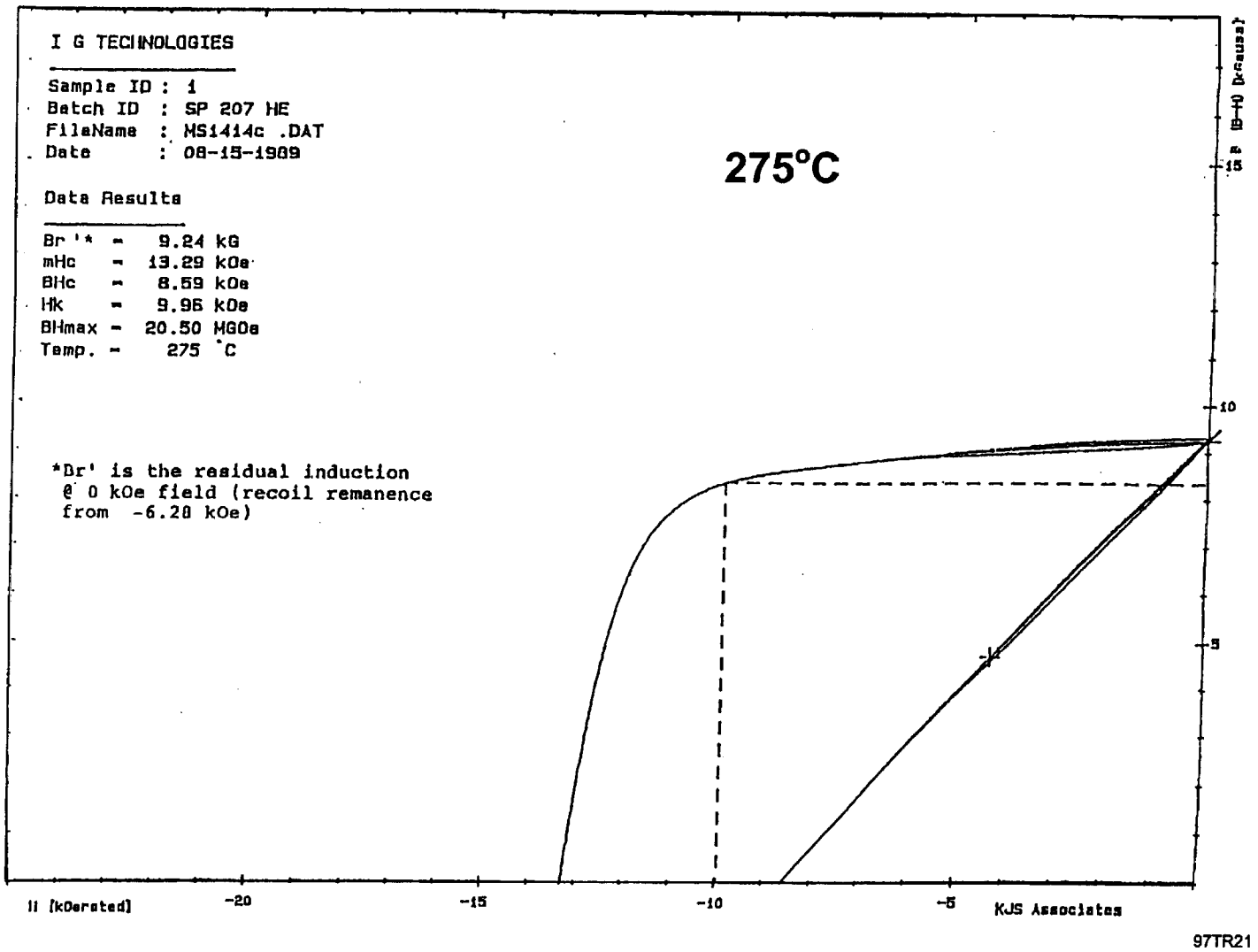

Figure 63. Test Results on Sample at 548 K

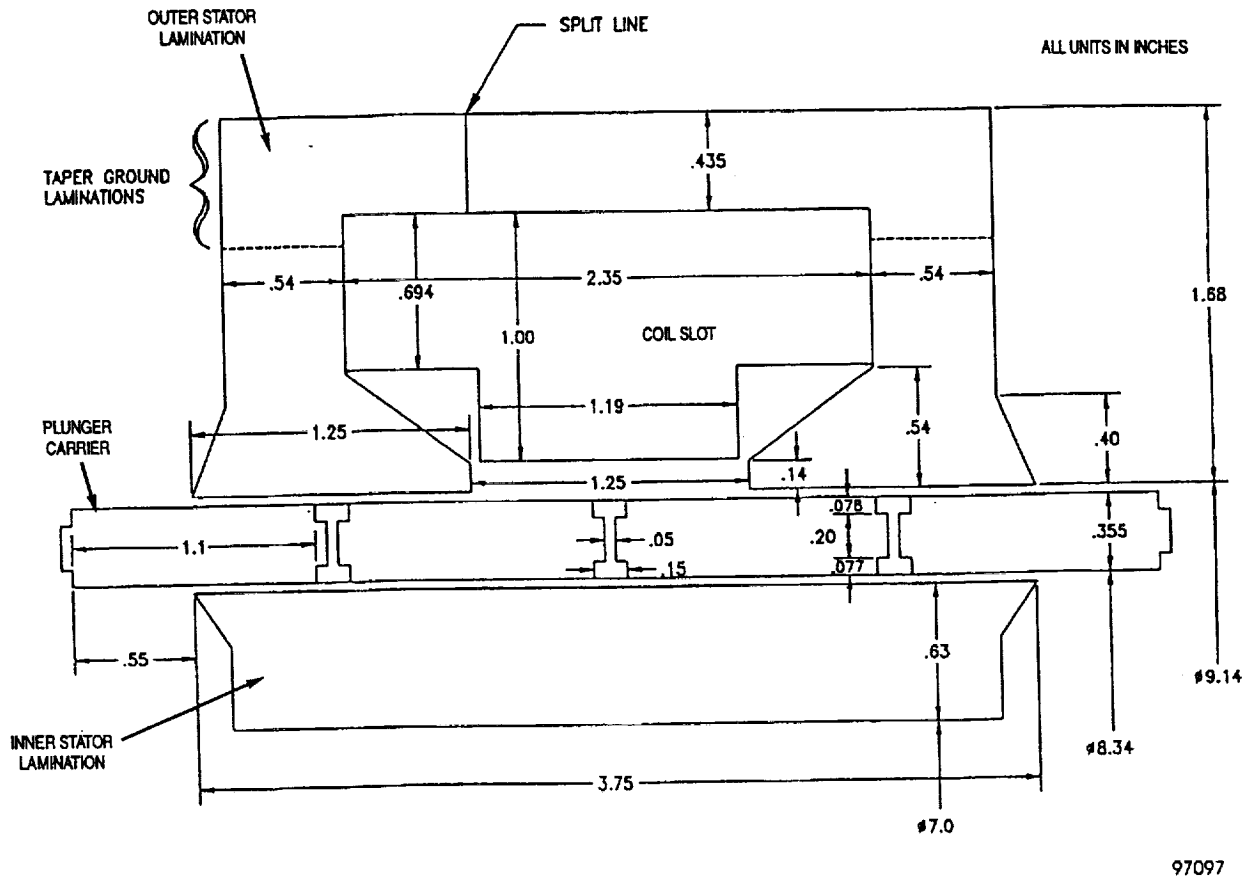

Figure 64. Final Alternator Design Configuration

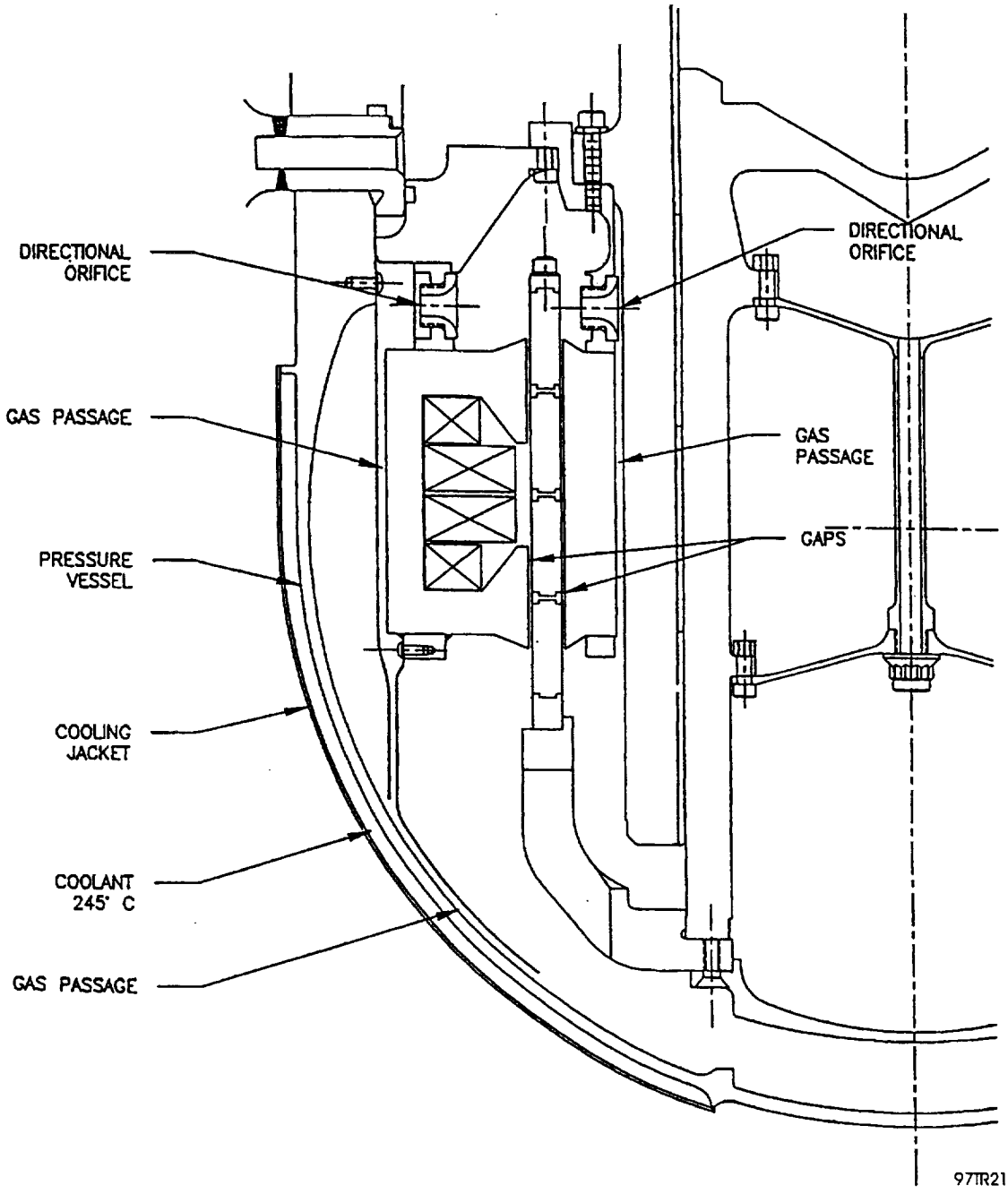

Figure 65. Approach to CTPC Alternator Cooling

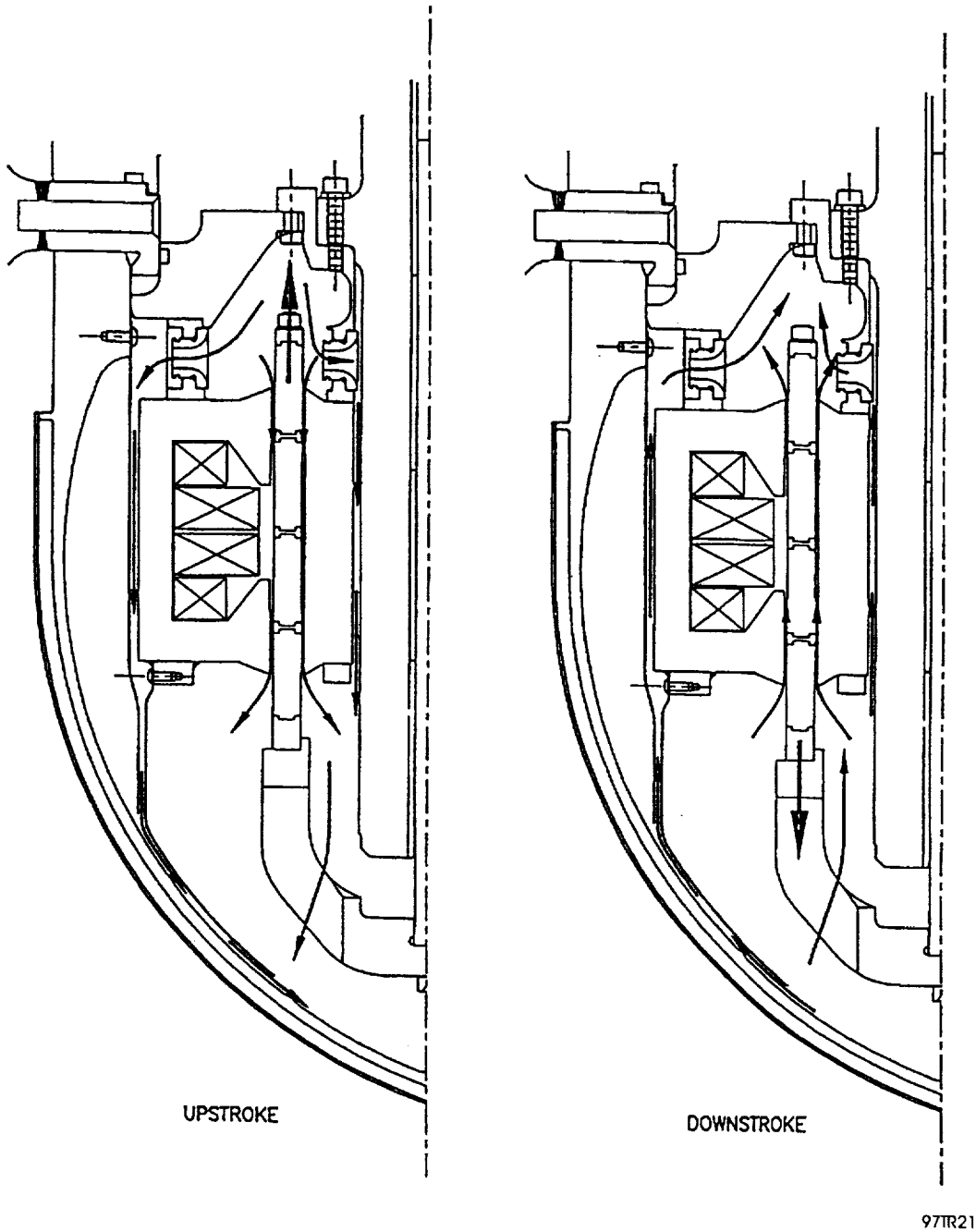

Figure 66. Gas Displacement in Alternator Cooling Flow

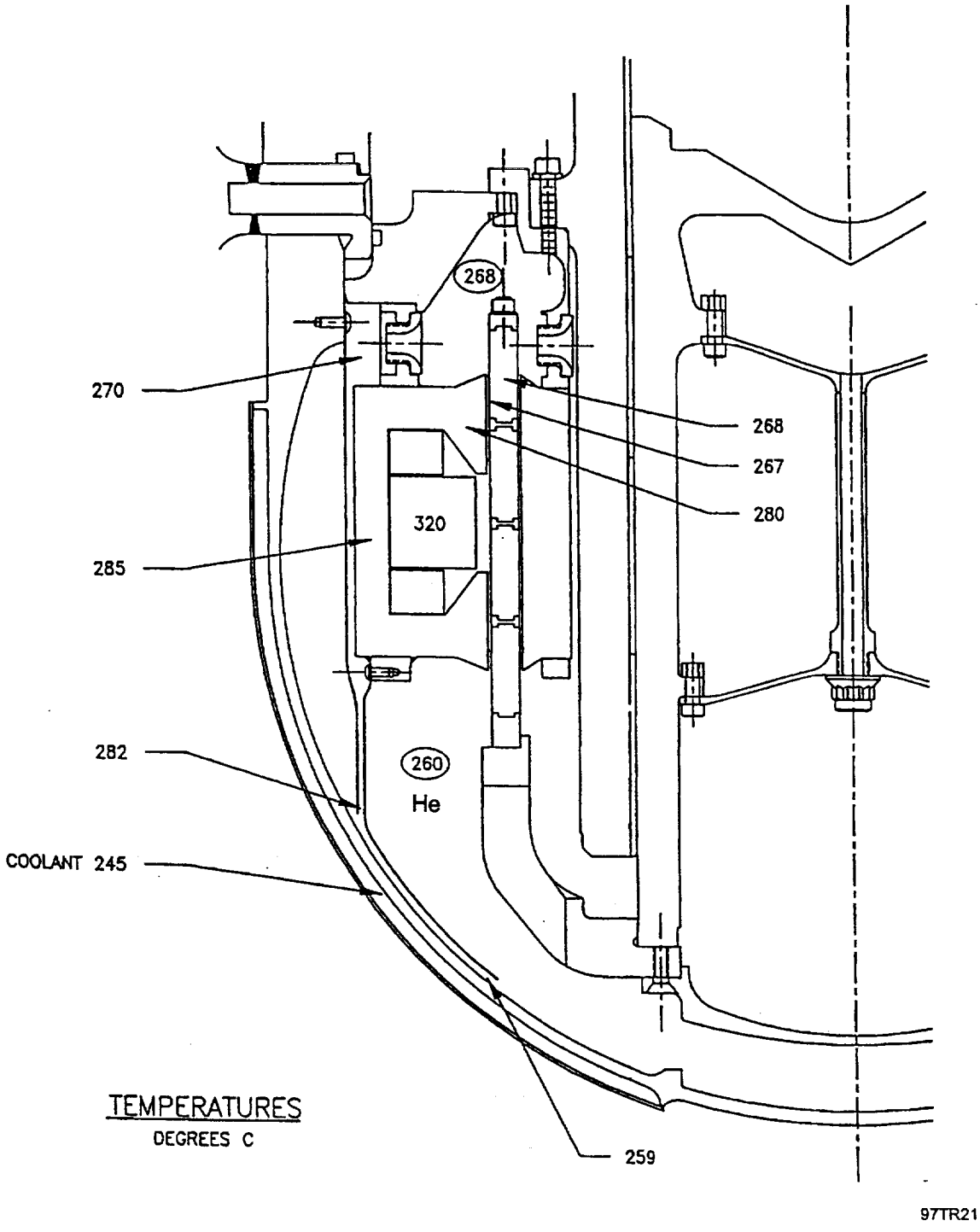

Figure 67. Calculated Temperature for Design Point Conditions

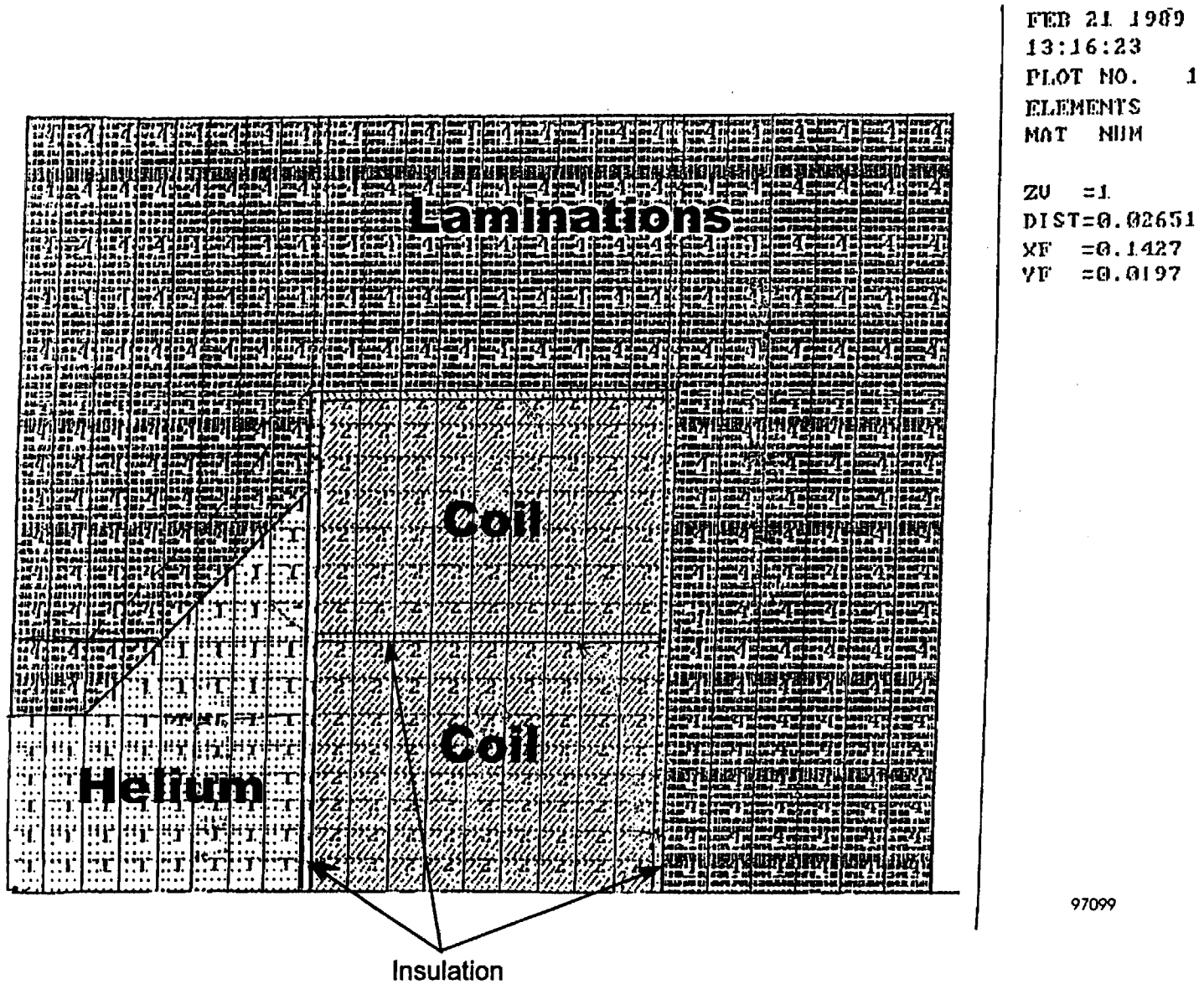

Figure 68. ANSYS Model of Temperature Levels Inside Coil

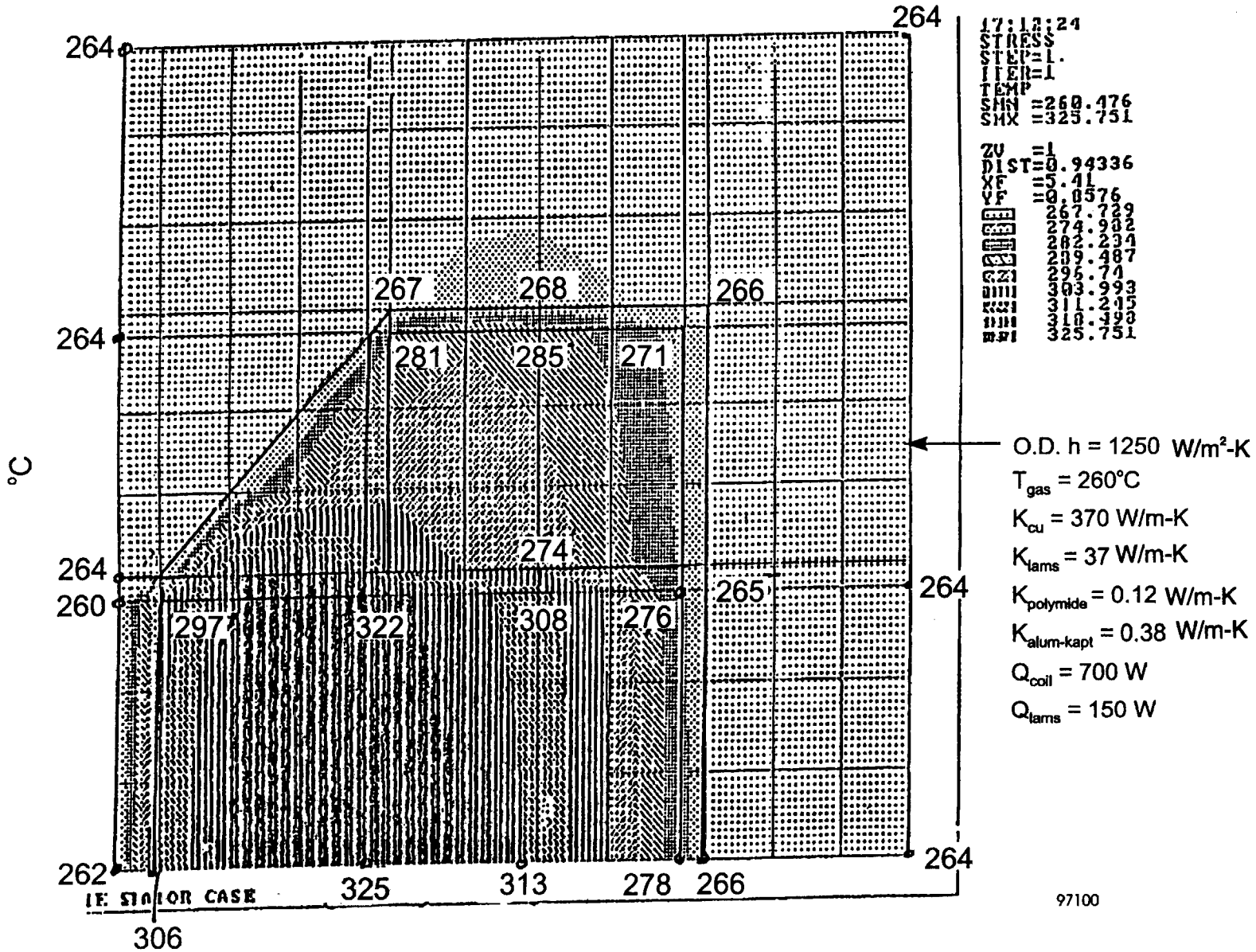

Figure 69. ANSYS Model Parameters

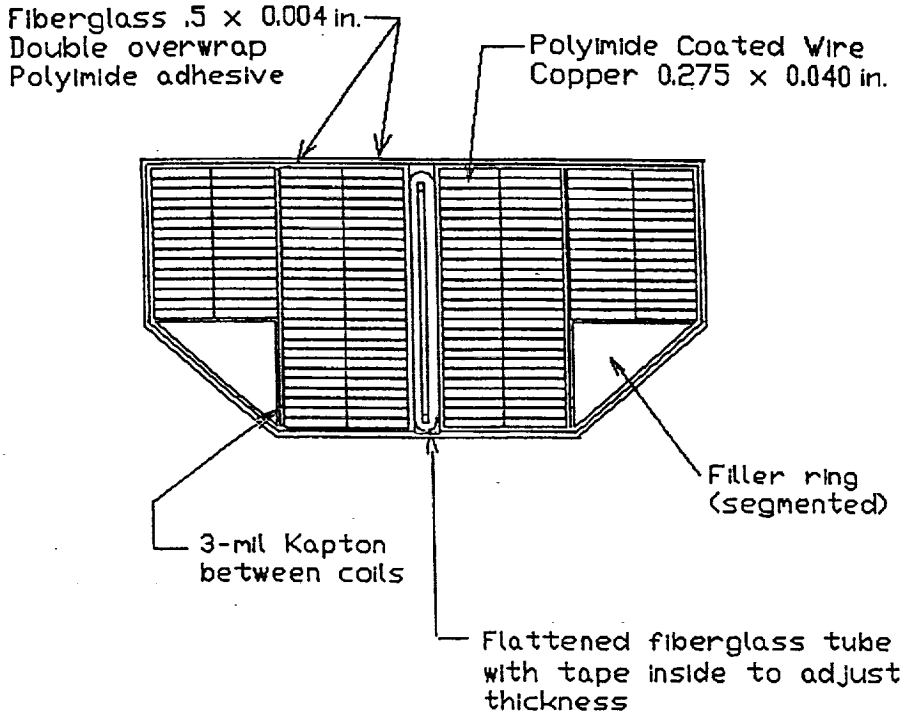

Figure 70. Coil Geometry

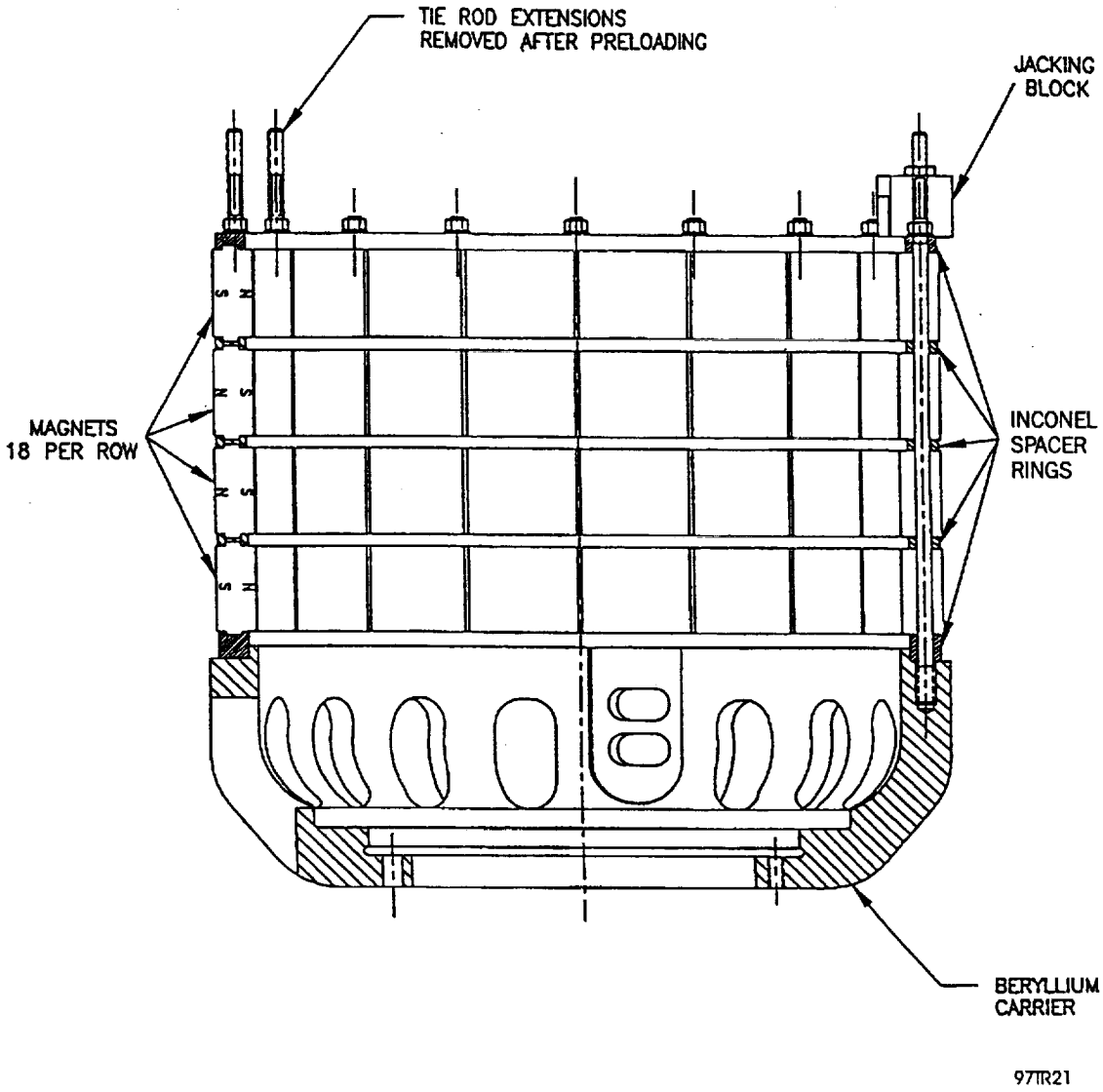

Figure 71. Plunger Construction

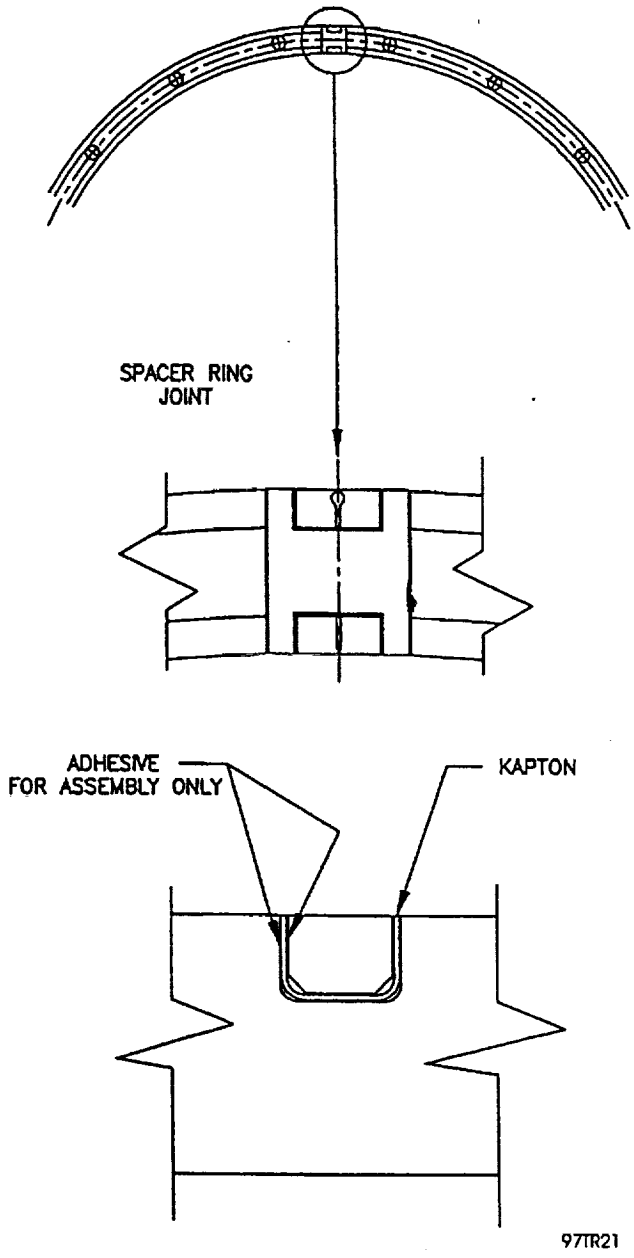

Figure 72. Incorporation of Insulated Joint in Spacer Rings

8.0 HEAT PIPE DEVELOPMENT

Stirling engine power converters for electrical power generation in space will be coupled to either a nuclear or solar heat source. If multiple power converters are coupled to a large energy source, such as a nuclear reactor of the SP100 size, it is desirable to isolate the reactor system from the engine-alternator system so that a single failure in one power converter cannot disable the complete system. Coupling each power converter to the reactor loop via a heat pipe provides the desired isolation and transfers the heat with a minimum temperature drop.

Even in smaller systems, the heat pipe approach has advantages in that the heat exchanger at the engine is decoupled from the heat exchanger connected to the heat source, permitting the geometry of each to be optimized independently.

For the CTPC, it was decided to use a heat pipe to transfer heat into the engine at the heater head. The maximum operating temperature for the CTPC was set at 1050 K based on the creep strength of the heater head material. Sodium was selected as the heat transfer fluid based on its thermodynamic properties (primarily vapor pressure) in the 900 to 1110 K range. Below about 800 K, the vapor pressure is so low that relatively little power can be transferred. Above 1100 K, the internal pressure imposes nontrivial structural requirements on a large heat pipe.

The heat pipe for the CTPC is intended to represent a space engine concept at the engine heater head but not necessarily represent a typical interface to the heat source. For lab testing, it was decided to use site electric power and electric heaters for the heat source.

Since it was not intended to represent a configuration that would be used in space, the heat pipe concept for the CTPC was designed to minimize technical risks to the maximum extent practical.

The Starfish heater head described in Section 3 was designed to provide a near-optimum geometry for heat transfer into the helium. The faces of the fins adjacent to the helium passages become the condenser section of the heat pipe and result in a surface area of 2440 cm^2. At a reference maximum power input to the engine of 60 kW (1200 W/slot), the flux density in the condenser is approximately 25 W/cm^2. At the specified design point of 75 kW (1500 W/slot), the heat flux is approximately 30 W/cm^2. Based on previous sodium heat pipe experience, this was determined to be acceptable.

The heat flux at the evaporator at 60 kW is approximately 18 W/cm^2, and at 75 kW is approximately 23 W/cm^2. Ample margin against the various heat pipe limits (boiling, sonic flow, capillary pumping, and viscous transport) was maintained by design.

Initially, the reference number of radial slots was 82, and detailed analyses were conducted on this arrangement. As the detail design proceeded, the slots were widened to facilitate the installation of wicks on the slot surfaces. Based on detailed analyses and gas passage drilling limitations, the final arrangement contained 50 slots with a double row of round helium gas passages in the fins between the slots.

Before proceeding to build the final unit, it was decided that a test of a heat pipe incorporating the key features of the reference design should be performed to verify the thermal performance and also work out details in the fabrication, heat treating, cleaning, and sodium-filling procedures. A $1/10^{th}$ segment was built and tested and demonstrated successful heat transfer at the maximum power condition (see Appendix A). Fabrication and sodium-filling issues that were addressed are summarized in Appendix A.2 and A.3.

8.1 Design Description

Figure 72A shows a cross section of the heat pipe, heater head, and the heaters. The top cover plate, the edge rings, and the bottom plate (which is the heat pipe evaporator) form an enclosed annulus surrounding

the Starfish section of the heater head. All internal surfaces of the annulus and the slots are covered with a wick. The wick is two layers of 100-mesh stainless steel screen.

A set of silicon-carbide radiant heaters provides heat to the bottom plate. Liquid sodium in the wick on the bottom plate absorbs heat and boils. The vapor produced flows into the heater head slots and condenses on the surface giving up the heat of vaporization to the helium flowing in the passages in the slot walls. The condensed liquid is returned to the bottom plate by arteries beneath the wicks. The arteries are small diameter tubes constructed of 200-mesh stainless steel screen.

The material of construction for the CTPC heat pipe was Inconel 718. This material was chosen for its compatibility with the CTPC heater head, which was also made of Inconel 718. For the long-life Udimet heater head, Inconel 617 will be the material used for the heat pipe structure.

MTI was responsible for generating the detail drawings, establishing the overall assembly procedure, and coordinating the procurement of the complete assembly. Thermacore was responsible for heat pipe thermal design and applying the wicks and arteries and final processing after sodium filling. Energy Technology Engineering Center (ETEC) developed fill procedures to ensure low oxygen content in the sodium heat pipe. ETEC used these procedures to fill and process the 1/10-segment heat pipe. Thermacore modified their fill techniques based on the ETEC procedures and then filled and processed the final CTPC heat pipe. Thermacore first demonstrated their revised procedure by successfully filling a cylindrical heat pipe.

The following outlines the assembly steps:

1. Electron-beam weld lower plate to heater head.
2. Electron-beam weld outer ring to lower plate.
3. Gas-tungsten-arc weld ribs to bottom plate.
4. Gas-tungsten-arc weld lifting lugs and burst diaphragm housing to outer ring.
5. Machine tops of ribs.
6. Apply wicks (including lower surface of top plate).
7. Electron-beam weld top plate to heater head and top of ribs.
8. Attach fill and drain valves/argon fill per MTI specification.
9. Remove valves and heat treat per MTI specification, argon fill per MTI specification.
10. Charge with sodium.
11. Optimize per Thermacore procedure. Heat and remove incondensible gases and excess sodium. Seal and remove valves.

The processing procedures associated with removing condensible gases and excess sodium involve heating the completed assembly to temperature in the age-hardening range for Inconel 718.

8.2 1/10-Segment Tests

A pie-shaped segment of the heat pipe and Starfish heater head was fabricated (see Appendix A.1). The slot geometry is the same as in the CTPC heater head. However, the fins between the slots were about twice as wide to accommodate the water-cooling approach used in the test to simulate the heat removal by helium in the engine.

For the tests, a cooling system was built on the gas gap calorimeter principle. Water flows through tubes which pass through 3.175-mm (1/8-in.) diameter holes drilled through the fins with a gas gap between the tubes and the fin metal.

By selecting the gap dimension and adjusting the gas conductivity by varying the proportions of a nitrogen-helium mixture used to trickle through the gap, it was possible to maintain the slot wall at heat pipe condenser temperature (1050 K), remove the design heat load, and keep the water below its boiling point (373 K).

Heat removal is determined by measuring water flow rate and the temperature rise of the water as it passes through the setup. A quartz heater located beneath the bottom plate provided heat input to the assembly.

The thermal load in the tests in which 10 kW is being transferred from the bottom plate to the Starfish section corresponds to 100 kW into the evaporator of the full-scale unit. This corresponds to approximately 31 W/cm^2 at the evaporator. As indicated early, 60 kW is the reference operating condition and 75 kW was selected as the design requirement to provide operating margin.

Since the fins between the slots were wider than in the actual heater head, the surface area for condensation is reduced. The thermal flux at the condenser for these 1/10-segment tests is thus significantly well above the levels experienced in the actual engine tests.

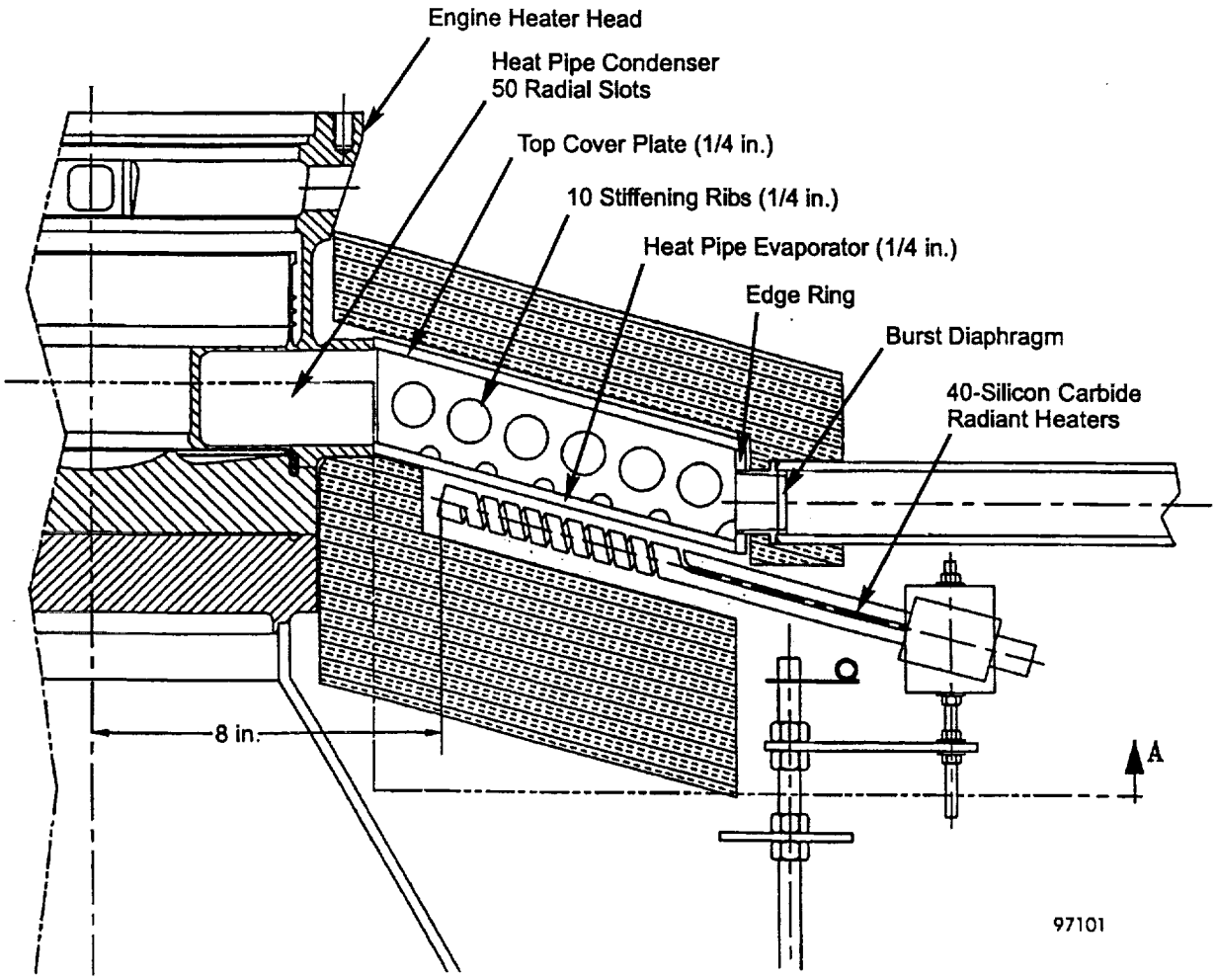

Figure 72A. CTPC Heat Pipe

9.0 ENGINE TEST DATA ANALYSIS

The CTPC gave a feeling of confidence to the design approach since it achieved its performance goals in the very first test, and significant endurance test hours were accumulated before the program concluded.

- Cold motoring test: 40.00 hr
- Hot engine tests: 1473.7 hr
  Slot heater head (with radiant heaters): 26.76 hr
  Heat pipe heater head: 1446.98 hr
  — Initial test: 7.08 hr
  — Phase I endurance test: 496.59 hr
  — Phase II endurance test: 943.31 hr

These test hours were accumulated from 30 April 1990 through 8 September 1996. The endurance tests were performed with a heater temperature of 800 K and a cooler temperature of 400 K. A brief test of 3-4 hours duration was run at 1050 K heater temperature and 525 K cooler temperature; performance was similar to that achieved in the 800 K/400 K testing.

9.1 Cold Motoring Engine Tests

For the thermodynamic and dynamic performance of the engine, the HFAST version 2.00 code was used to analyze the data. For the linear alternator, the MTI-developed LPMMA code and the Ansoft finite-element program MAXWELL were used.

9.1 Cold Motoring Engine Tests

The cold motoring tests were performed with the entire engine assembled, but without the regenerator and the heater head. The coolers (engine and alternator) were active in order to maintain the temperature. For various tests, the displacer assembly was either installed or removed. For the latter case, a dummy head was used in the compression space in place of the displacer drive. The internally supplied hydrostatic bearings were successfully tested at ambient and high temperatures (525 K) without the need for external centering mechanisms.

During the period of the cold motoring tests, several instrumentation and hardware problems were identified and corrected. The calibration procedures of the dynamic signals (position probes, pressure transducers, electrical measurements) were progressively refined. Pressure probes were calibrated at the mean pressure as used in the engine tests.

Because of the diagnostic nature of the cold motoring tests, no test results will be presented. It is worth mentioning that the gas spring stiffness and damping coefficients were continuously monitored during the tests to identify potential measurement and hardware problems. By making proper adjustments based on the measured gas spring performance, the HFAST code was used successfully to guide the hot engine tests.

9.2 Radiant Heater Engine Tests

The first radiant heater engine test was performed on November 17, 1992. To reduce the risk of damaging the heater, most tests were performed with the heater temperature at 800 K and the cooler temperature at 400 K. (See Appendix B.9 for a description of the radiant heaters.)

Because of insufficient space, the surface temperature of the starfish fins of the engine heater could not be directly measured. To overcome the problem, gas temperatures in the cylinder spaces (expansion space and compression space) were measured and used to guide the engine tests. To obtain the desired heater-to-cooler wall temperature ratio of 2.0, the corresponding gas temperature ratio was determined by HFAST

version 2.00 to be approximately 1.82 to 1.84. The engine tests were conducted by maintaining the gas temperature ratios close to this predicted value. Using gas temperatures to conduct engine tests was only a short-term solution and was not needed after the heat pipe was installed in the engine.

The effect of a volume stuffer on the engine performance was tested on January 21, 1993. The volume stuffer reduced the dead volume in the working space, mainly in the cold connecting duct, by about 4.6%. The reduced volume was expected to give higher pressure amplitude and increased power output.

For the purpose of comparison, the test results of April 21, 1993, (without the volume stuffer) were used as the reference. A wide range of gas temperature ratios was tested on both days. To make the comparison meaningful, the comparison was based on the gas temperature ratios between 1.81 and 1.83. The choice of the temperature ratios to use in the comparison was determined mainly by the number of available test data points that were under similar operating conditions.

Since exact duplication of test conditions was difficult to achieve, comparing tests of different dates and engine builds involved some degrees of uncertainties. The observed difference between different engine builds could be a result of measurement errors or unintended hardware variations. This was especially true if the difference to be identified was small. To further complicate the problem, it was noted that not all data were taken when the engine was thermally stabilized. The recorded difference between engine builds could also be due to the transient behavior of the engine. Thus, the comparisons to be presented could only be interpreted qualitatively.

Figure 73 shows the measured and predicted displacer amplitude. With the volume stuffer installed, the pressure wave in the working space was increased, and, consequently, the displacer amplitude was also increased. The increase in the displacer amplitude as predicted by the code agreed reasonably well with the test. Note the physical constraint of the displacer amplitude (0.015 m) was reached before the potential benefits of the volume stuffer could be fully realized.

Figure 74 shows the measured and predicted alternator power output. With the volume stuffer installed, the test showed a slight increase in the power output over the range the engine could be operated with the stuffer. The code predicted an increase of the power output of about 300 W. The difference between the two configurations was within the uncertainty band of the measurement. Both code and test indicated the system efficiency should remain virtually the same with or without the volume stuffer.

Most hot engine tests were performed using regenerator S/N #1. The effect of regenerator S/N #2 on engine performance was tested on April 30, 1993. Table 21 summarizes the differences between the two regenerators.

Table 21. Summary of Differences between Regenerators

S/N	Wire Diameter (mil)	Porosity (%)	Matrix Material
#1	2.0	72.8	SS 347
#2	1.5	79.9	SS 304

97TR21

As noted, the regenerator S/N #2 had higher porosity. The higher porosity of the regenerator increased the dead volume in the working space by about 3%, which, in turn, reduced the pressure wave amplitude in the working space. The loss in the pressure amplitude was somewhat offset by reduced pumping power.

For the purpose of comparison, the test results of May 24, 1993, (with regenerator S/N #1) were used as the reference. To make the comparison meaningful, the comparison was based on the gas temperature ratios between 1.84 and 1.86. The choice of the test days and the temperature ratios for the comparison reference was determined mainly by the available number of data points that were under similar operating conditions.

Figure 75 shows the measured and predicted alternator power output. As shown, regenerator S/N #1 gave higher alternator power output than regenerator S/N #2. The code predicted that the difference between the two regenerators was about 500 W, which was in good agreement with the test.

Figure 76 shows the measured and predicted system efficiency. The system efficiency includes the efficiencies of the engine (including the internally pumped gas bearings) and the linear alternator. For the test, the system efficiency was based on the cold-end measurements. The test showed a slight decrease in efficiency with regenerator S/N #2. However, the difference was well within the uncertainty band of the measurement. The code predicted a slight increase in efficiency with regenerator S/N #2.

9.3 Engine Heat Pipe Tests

The first heat pipe engine test was performed successfully on August 16, 1993. For the heat pipe engine tests, the heater-to-cooler temperature ratio was based on the thermocouple measurements of the heat pipe vapor temperature and the gas-side cooler wall temperature. In the following, the test results of September 8, 1993, (15 MPa mean engine pressure, 400 K cooler temperature) will be used.

Figure 77 shows the relation between the measured heater-to-cooler temperature ratio and the measured gas temperature ratio of the cylinder spaces. During the test, the wall temperature ratio was held slightly higher than the design value of 2.0 to compensate for the temperature drop (about 10 K) from the heat pipe vapor temperature to the working-gas-side heater wall temperature. As shown, for several intermediate piston amplitudes, the wall temperature ratios were slightly higher than the set value of about 2.03. This was due to the difficulty in setting the electrical input to the heater to obtain the desired temperature ratios. On the average, the measured gas temperature ratio was about 1.85, which was slightly higher than the code-predicted value used in the radiant heater engine tests. Otherwise, the engine was expected to repeat the performance of previous radiant heater engine tests.

To better understand the engine performance, HFAST version 2.00 was used to simulate the test. Two modes of simulation were performed: constraint and dynamic. In the constraint simulation mode, the measured displacer and power piston motions and frequency were used as code inputs. This allowed the thermodynamic performance of the engine to be compared under identical piston dynamics. In the dynamic simulation mode, the piston dynamics were determined from an equivalent mass-damper-spring model, and its effect was coupled with the thermodynamic simulation of the HFAST code. This mode allowed the complete engine, which included the working space, the gas springs and the linear alternator, to be simulated and analyzed. For both simulation modes, the mean pressure and heater and cooler temperatures were specified according to the measured values. The results of the constrained simulation will be presented first, followed by the dynamic simulation results. Except for modeling the gas spring performance, no calibration factors were used.

Figure 78 shows the piston PV power. For the test, the piston PV power was obtained from the measured compression space pressure wave and the piston motion. It is well known that the measured PV power is sensitive to the phase errors between the two quantities. Thus, the uncertainty band could be significant. As shown, the code overpredicted the piston PV power by approximately 6%.

Figure 79 shows the piston PV efficiency. For the test, the efficiency was calculated by two methods: the hot end and the cold end. The hot-end efficiency was calculated by using the measured heat input to the heater. The measured heat input had been corrected for estimated heat loss to the engine test cell. The cold-end efficiency was calculated by using the deduced heat input to the engine heater. The deduced heat input was equal to the sum of the measured heat rejection (engine and alternator coolers) and the alternator electrical power output. According to the principle of energy conservation, the deduced heat input should equal the measured heat input under ideal testing conditions.

As shown, the code agreed reasonably well with the cold-end efficiency. The difference between the cold-end and hot-end efficiencies was about 5 percentage points and indicated the potential uncertainty band of the measurement. The discrepancy between the cold-end and hot-end efficiencies showed that, in the test results, there were energy flows that were not properly accounted for.

Note the heat rejection measurements were made with both primary and backup instruments (orifice and turbine flow meters, RTDs, and differential RTDs). The agreement between the primary and backup instruments appeared to be good. Thus, there were reasons to believe that the cold-end efficiency was more reliable.

Figure 80 shows the cycle power. For the test, the cycle power was obtained by adding the measured displacer power losses to the piston PV power. As shown, the code overpredicted the cycle power by about 5%. Figure 81 shows the cycle efficiency. As shown, the code agreed reasonably well with the cold-end cycle efficiency. The results were similar to the piston PV power and efficiency comparisons.

Figures 82 and 83 show the pressure wave amplitude and phase angle (relative to the piston motion) in the compression space. As shown, the code overpredicted the pressure amplitude by about 5%. The difference of the code predicted phase angle was about 0.2 degrees. These discrepancies were the reason that the code overpredicted piston PV power.

Figures 84 and 85 show the amplitude and phase angle of the pressure drop between the compression space and the expansion space. The expansion space pressure was not directly measured but was estimated from the force balance on the displacer. Because of the estimation procedure, the uncertainty band could be significant. Thus, the comparison could only be regarded as qualitative. As shown, the pressure drop amplitude as predicted by the code was slightly less than the deduced value. The difference in the phase angles was significant but could be a result of the errors in the estimation procedure.

Figures 86 and 87 show the gas temperatures in the expansion and compression spaces. As shown, the code underpredicted the gas temperatures in both cylinder spaces. The difference in the expansion space was about 20 K. The difference in the compression space was about 5 K. The net result was a code-predicted gas temperature ratio that was less than that measured.

Before the dynamic simulation of the entire system was made, the measured and predicted gas spring stiffness and damping coefficients were compared.

Figure 88 shows the displacer (aft and forward) gas spring stiffness. As shown, the measured gas spring stiffness was lower than the predicted stiffness by about 5%. However, the difference appeared to be higher than can be explained by the heat transfer alone. It was possible that the difference was caused by measurement errors. But it was also possible that the difference was caused by the gas spring mean volume used in the prediction. The gas spring mean volume was obtained from the design drawings and had not been verified by independent tests. In the dynamic simulation (to be presented below), the displacer gas spring stiffness was reduced relative to the prediction by 3.6E4 N/m.

Figure 89 shows the piston gas spring stiffness. As shown, the measured piston gas spring stiffness was lower than the expected value by about 10%. Again, the heat transfer alone could not explain the discrepancy. As to be discussed later in this section, the alternator BETA value was checked, and no apparent measurement error could be identified. Thus, it was more likely that the discrepancy was caused by the piston gas spring mean volume used in the prediction. No tests had been conducted to determine the mean volume in the piston gas spring. In the dynamic simulation, the piston gas spring stiffness used was reduced relative to the prediction by 1.0E5 N/m.

Figure 90 shows the displacer (aft and forward) gas spring damping coefficient. As shown, the measured damping coefficients were lower than the expected value. Thus, some of the gas spring losses could have been overpredicted. In the dynamic simulation, the displacer gas spring damping coefficient was reduced relative to the prediction by 10 N-s/m.

Figure 91 shows the piston gas spring damping coefficient. As shown, the measured damping coefficients were higher than the prediction. In the dynamic simulation, no adjustment was made to the piston gas spring damping coefficient.

The results of the dynamic mode simulation will be presented below. As discussed above, the gas spring stiffness and damping coefficients were adjusted according to the measured results (except for the piston gas spring damping coefficient). Without the adjustments, the predicted dynamic behavior of the system would be less satisfactory.

Figure 92 shows the predicted operating frequency. As shown, the code predicted the frequency reasonably well.

Figures 93 and 94 show the displacer motion. As shown, the code predicted the displacer amplitude well. However, the displacer phase angle was off by 6 degrees. Note the amplitude of the displacer was higher than the piston amplitude by about 10%. Thus, the physical constraint on the displacer motion was reached first and became a limiting factor during the test.

Figure 95 shows the alternator power output. As shown, the code predicted the alternator power output very well. Recall that the code overpredicted the cycle power under constraint simulations. The error in the displacer motion simulation appeared to offset the error in the cycle power prediction. Thus, the agreement in the alternator power output was better than expected. As shown, the alternator power output at the full power point was above the design goal of 12.5 kW.

Figure 96 shows the system efficiency. The system efficiency includes the efficiencies of the engine (including the internally pumped gas bearings) and the linear alternator. Both hot-end and cold-end efficiencies are presented. As shown, the code agreed with the cold-end system efficiency reasonably well. At the maximum power point, the cold-end system efficiency was about 22% and was above the design goal. On the other hand, the hot-end system efficiency was about 3 percentage points less than the cold end.

Figure 97 shows the alternator efficiency. For the test, the alternator efficiency was based on the piston PV power measurement. Thus, the accuracy of the piston PV power measurement would also affect the alternator efficiency. The HFAST-predicted alternator efficiency was obtained from a simplified equivalent circuit model so the results were only approximate. As shown, the measured alternator efficiency was about 92%, which was higher than the expected efficiency at the design point of 525 K. This was because the test was conducted at a lower cooler temperature of 400 K, and the alternator efficiency was expected to decrease with increasing operating temperature.

The mechanical-electrical coupling of the alternator was represented by the BETA value. Since the electrical measurements were usually more reliable, the alternator BETA value was used to identify potential mechanical measurement errors. The alternator BETA value was defined as the ratio of the induced voltage in the coil divided by the plunger velocity. The induced voltage was deduced from the measured alternator terminal voltages and the alternator inductance. The alternator inductance was determined from the static tests. From the principle of conservation of energy, the alternator BETA value could also be defined as the plunger force divided by the coil current. The plunger force could be deduced from the piston force balance by using the measured pressure waves and the stiffness of the plunger magnet forces. The magnet stiffness was obtained from the alternator static tests.

Figure 98 shows the alternator BETA value. As shown, the measured BETA values using different measured parameters and calculation methods were in good agreement. The measured BETA values were lower than the values predicted from the static tests by 2 to 3%. Since the alternator BETA value decreases with decreasing operating temperature, the discrepancy could be due to the temperature effect. Because of the deduction procedure involved, the alternator BETA value could not detect errors that were within the uncertainty band of the test.

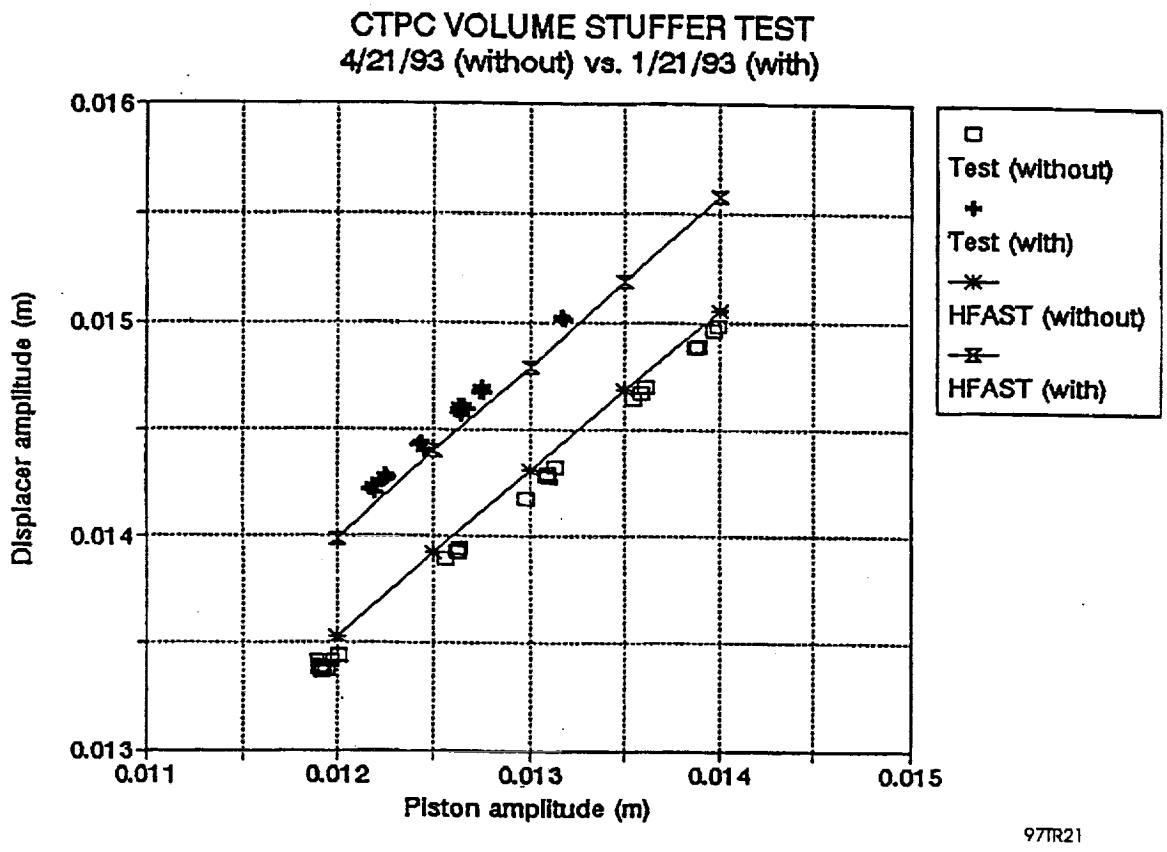

Figure 73. Measured and Predicted Displacer Amplitude

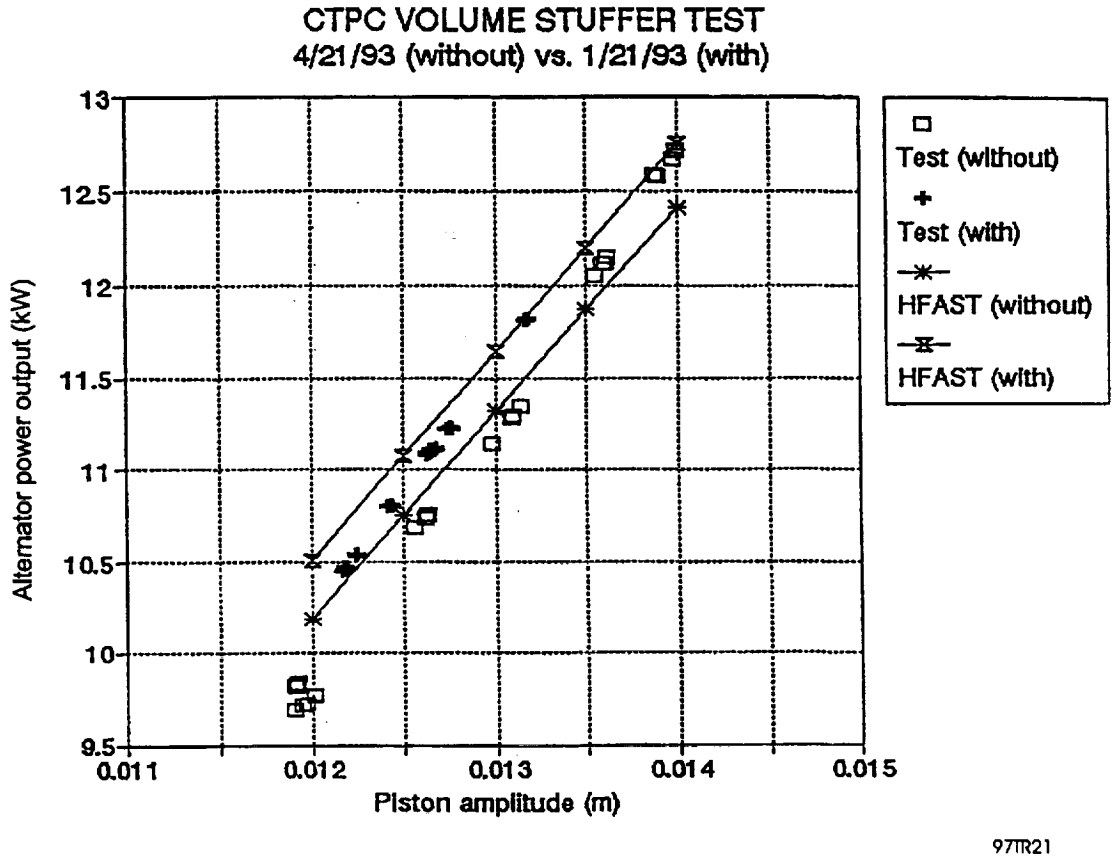

Figure 74. Measured and Predicted Alternator Output

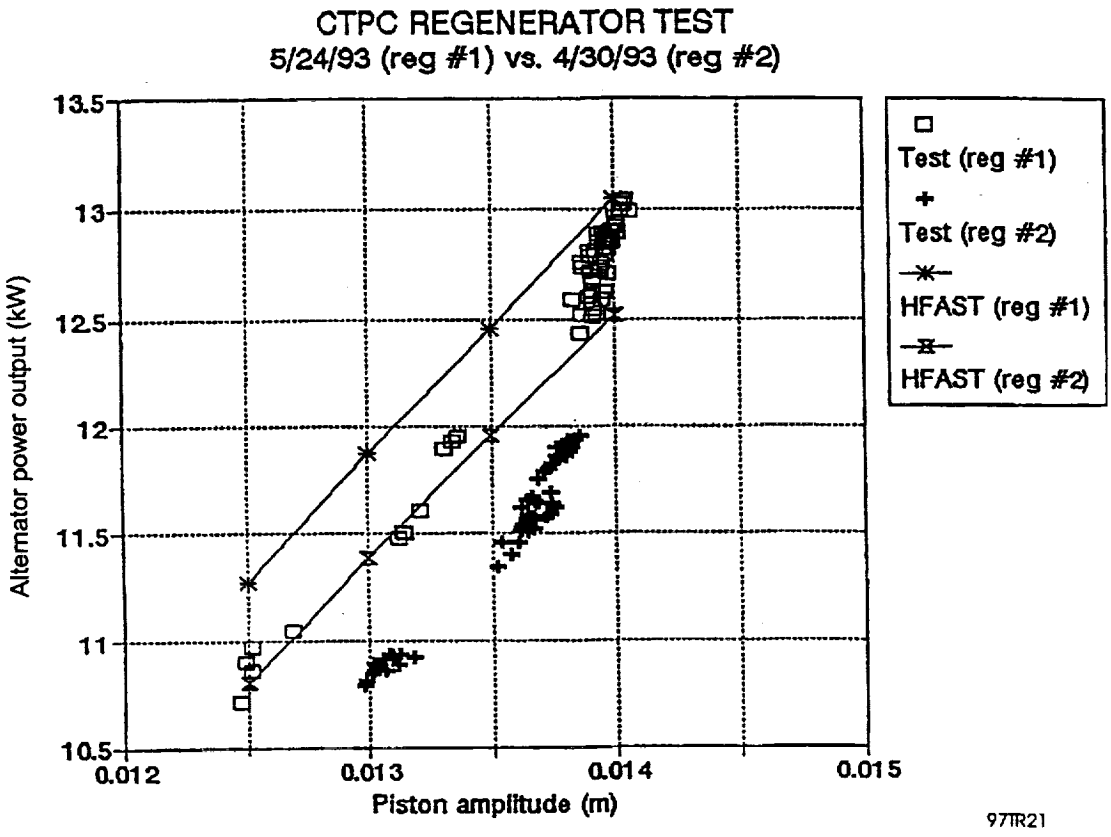

Figure 75. Measured and Predicted Alternator Power Output for Two Regenerators

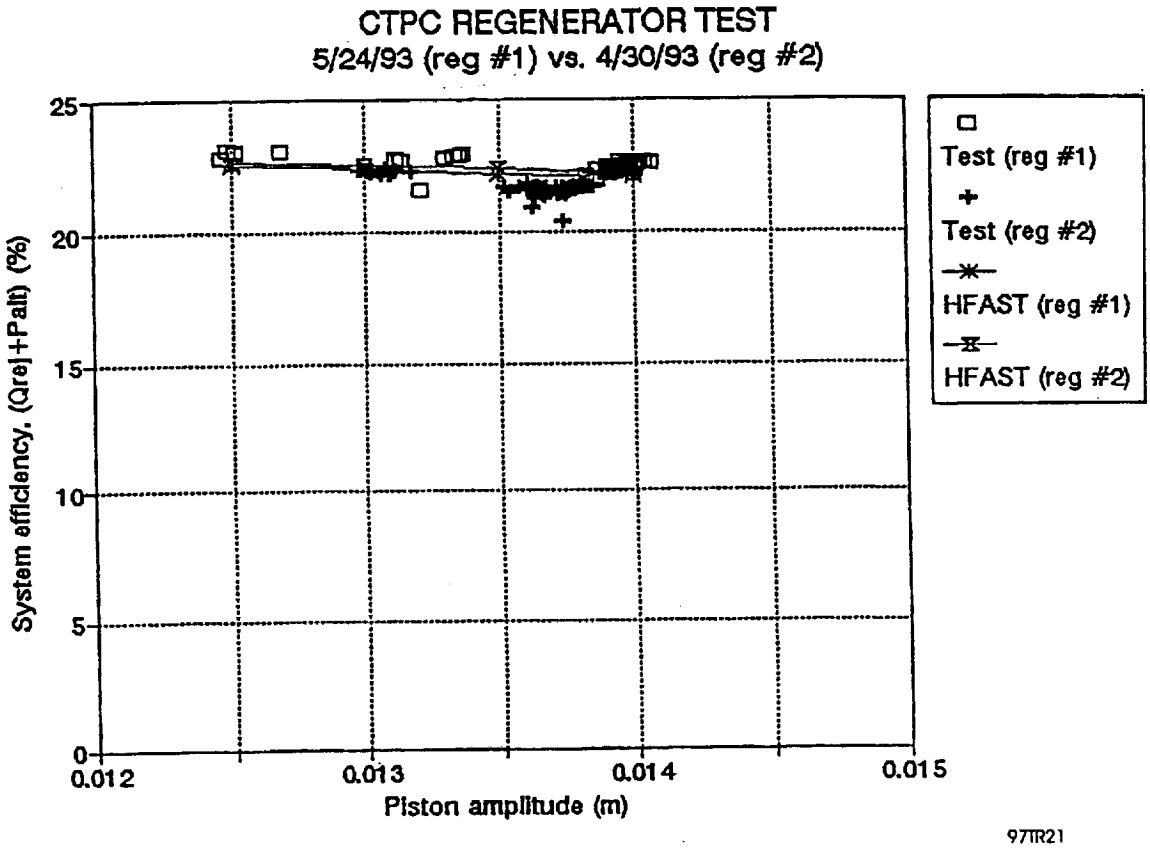

Figure 76. Measured and Predicted System Efficiency

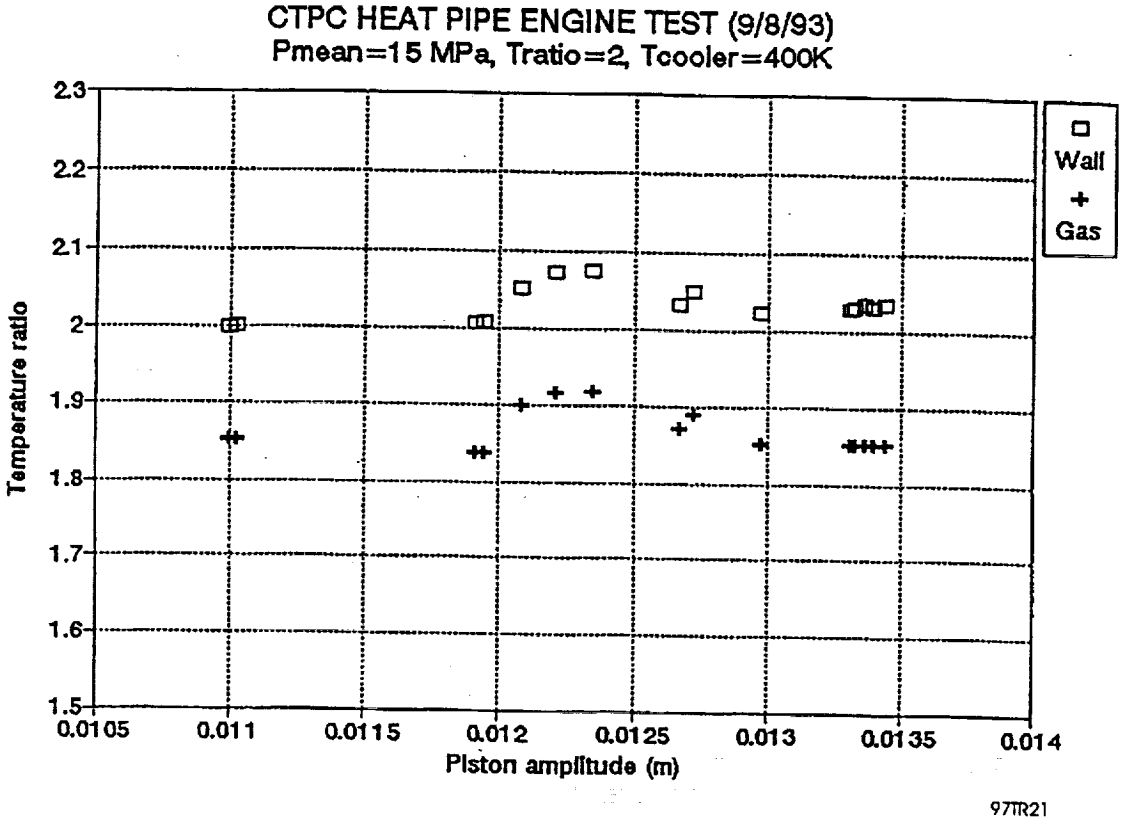

Figure 77. Relationship between Measured Heater-to-Cooler Temperature Ratio and Measured Gas Temperature Ratio of Cylinder Spaces

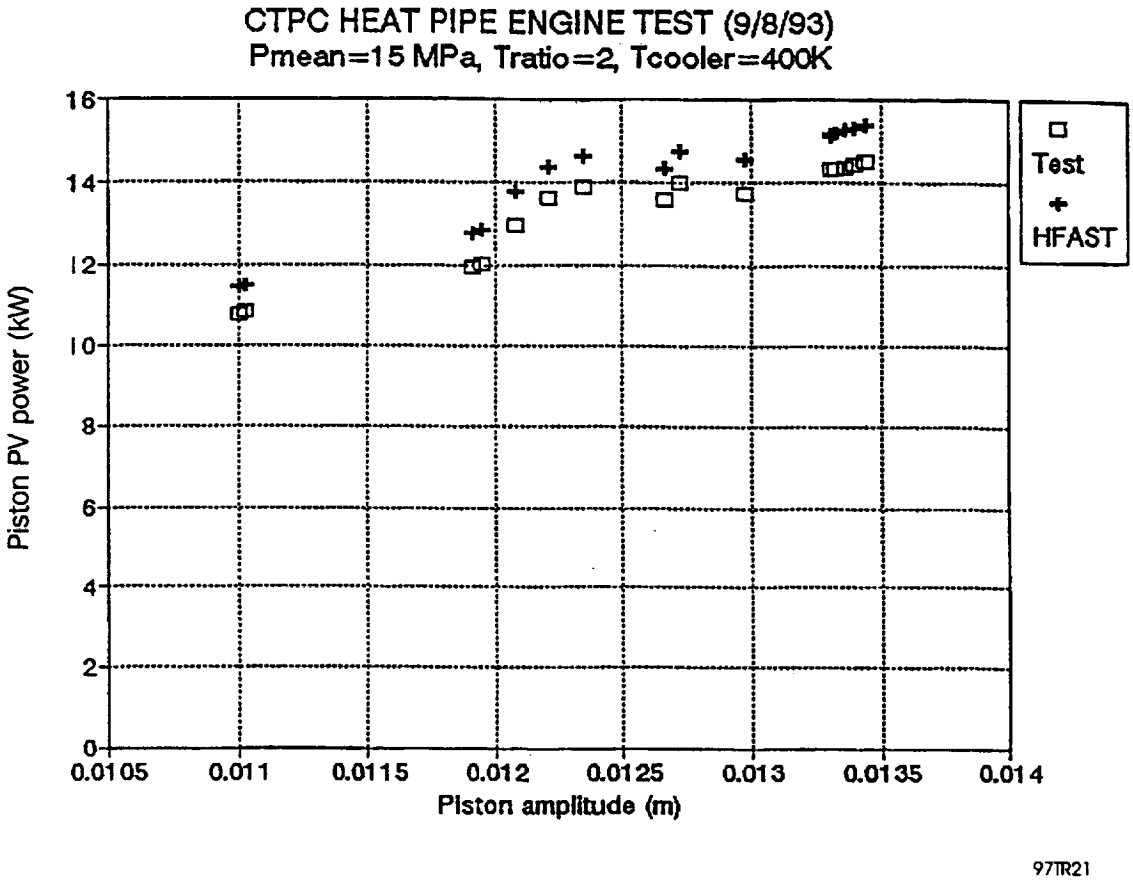

Figure 78. Piston PV Power

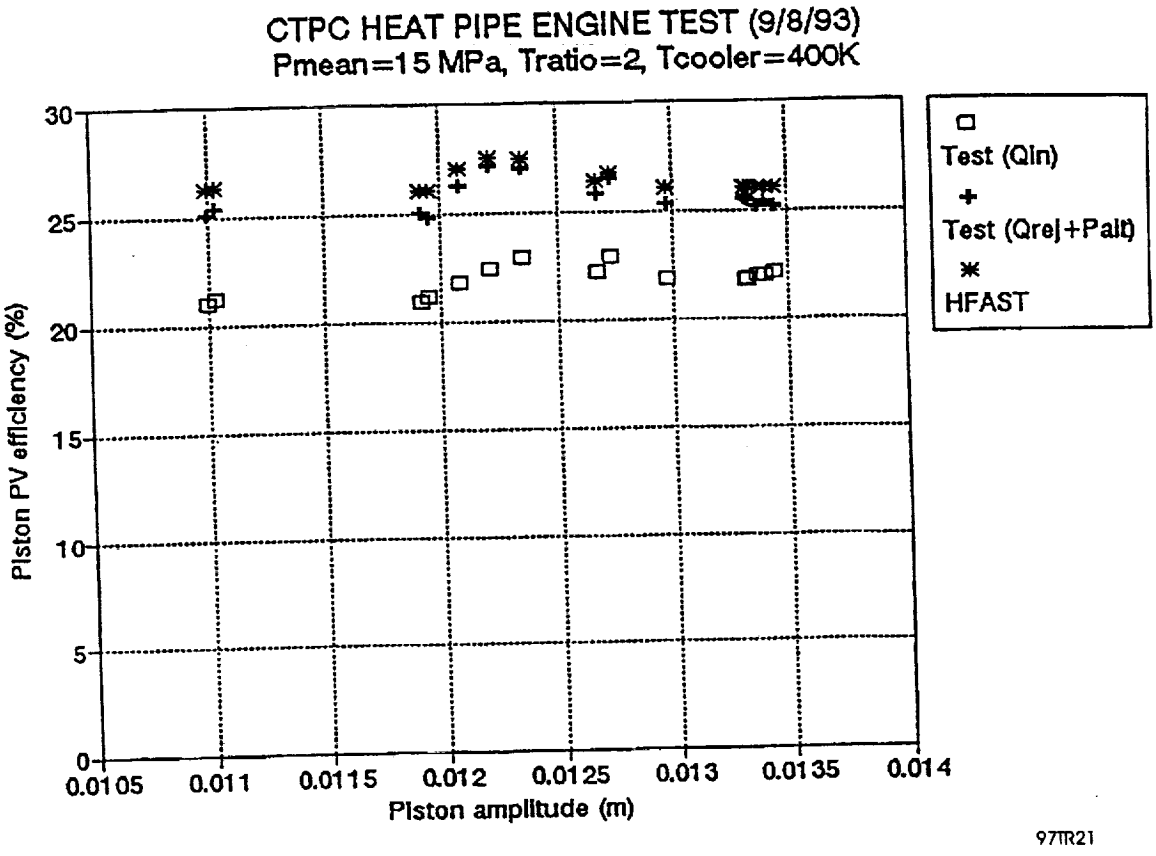

Figure 79. Piston PV Efficiency

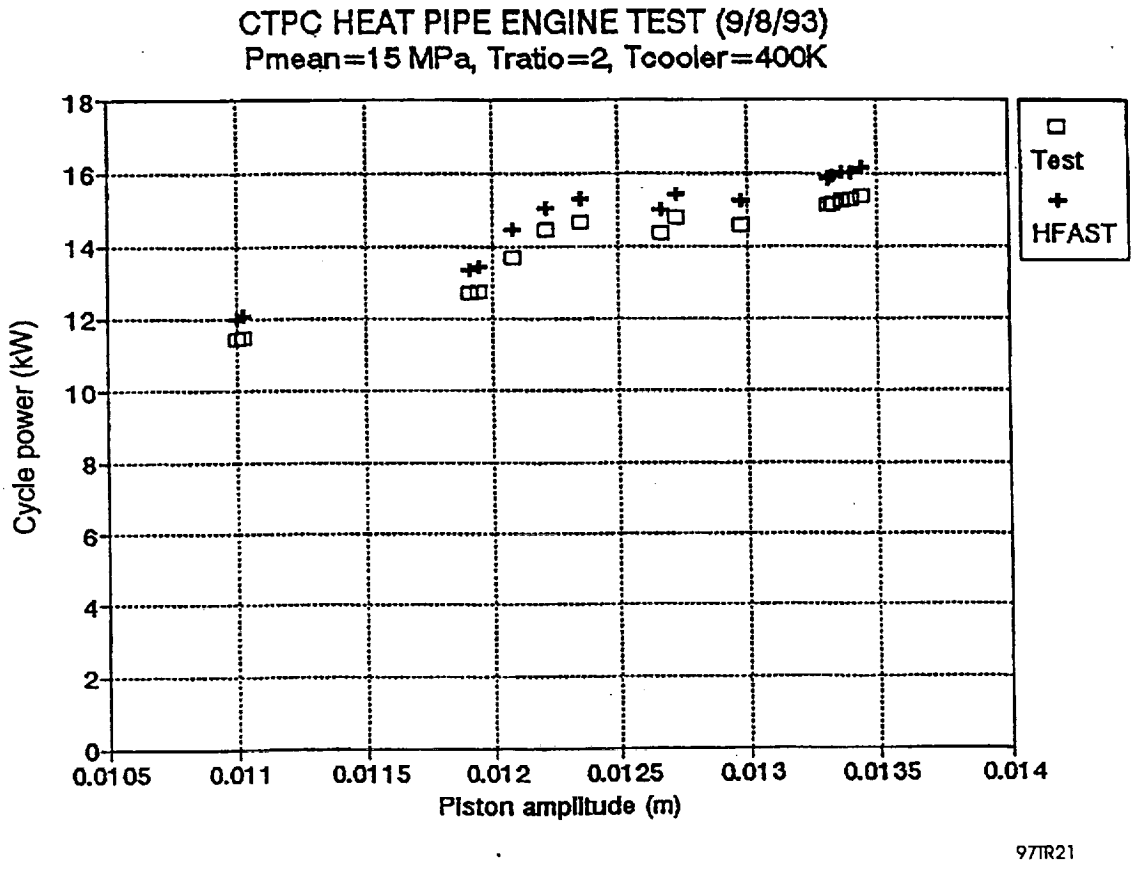

Figure 80. Cycle Power

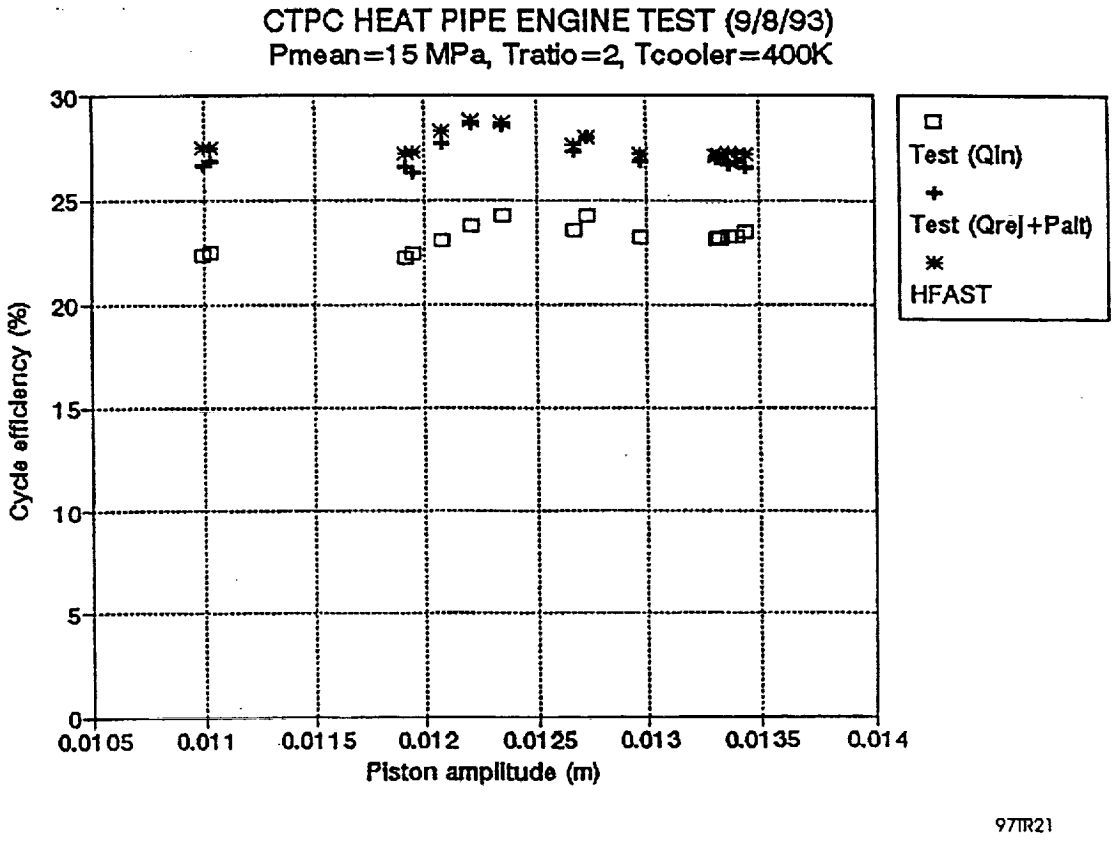

Figure 81. Cycle Efficiency

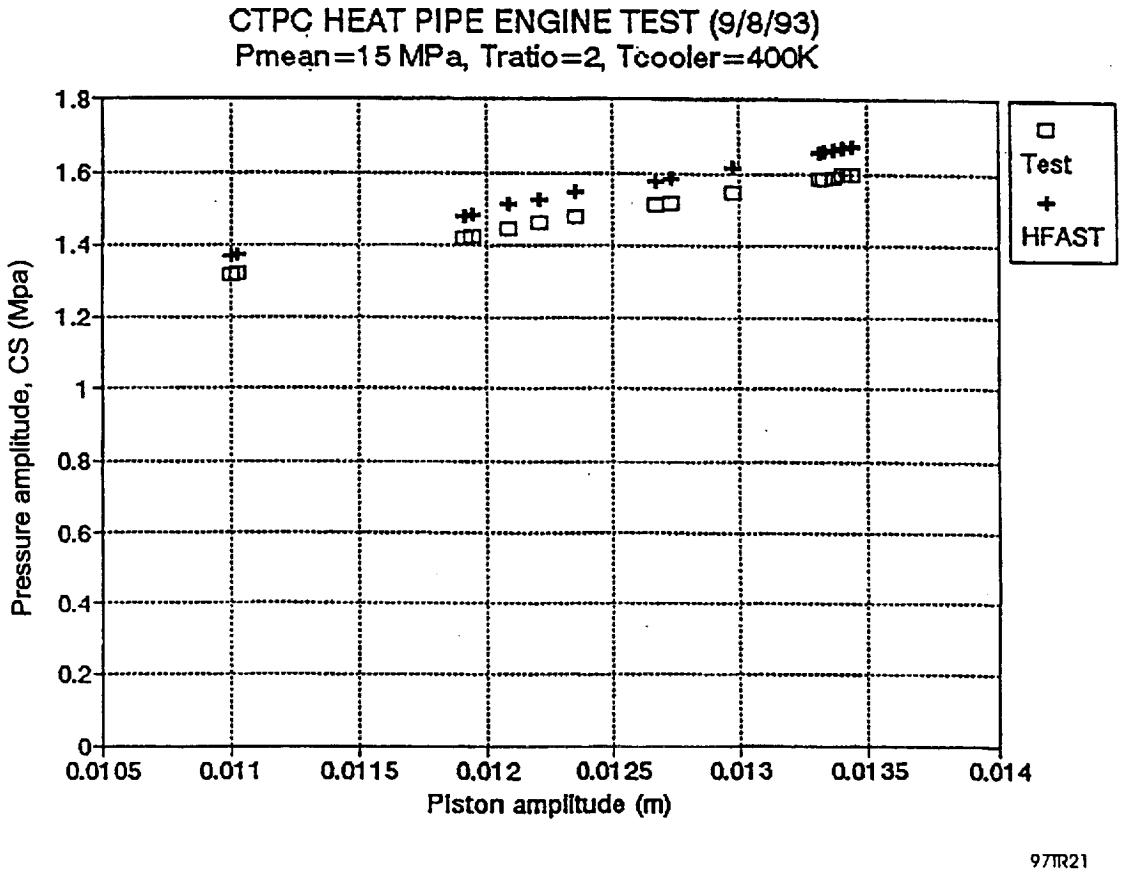

Figure 82. Compression Space Pressure Amplitude versus Piston Amplitude

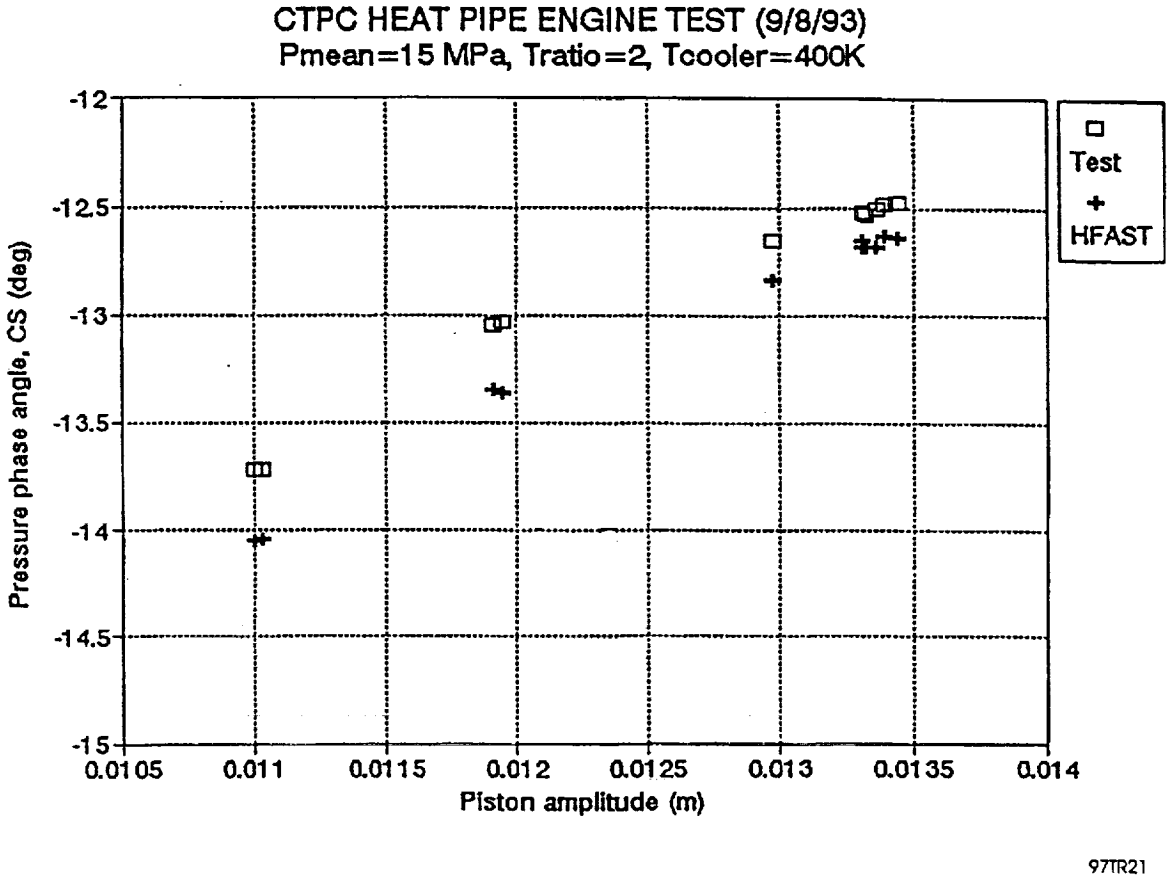

Figure 83. Pressure Phase Angle versus Piston Amplitude

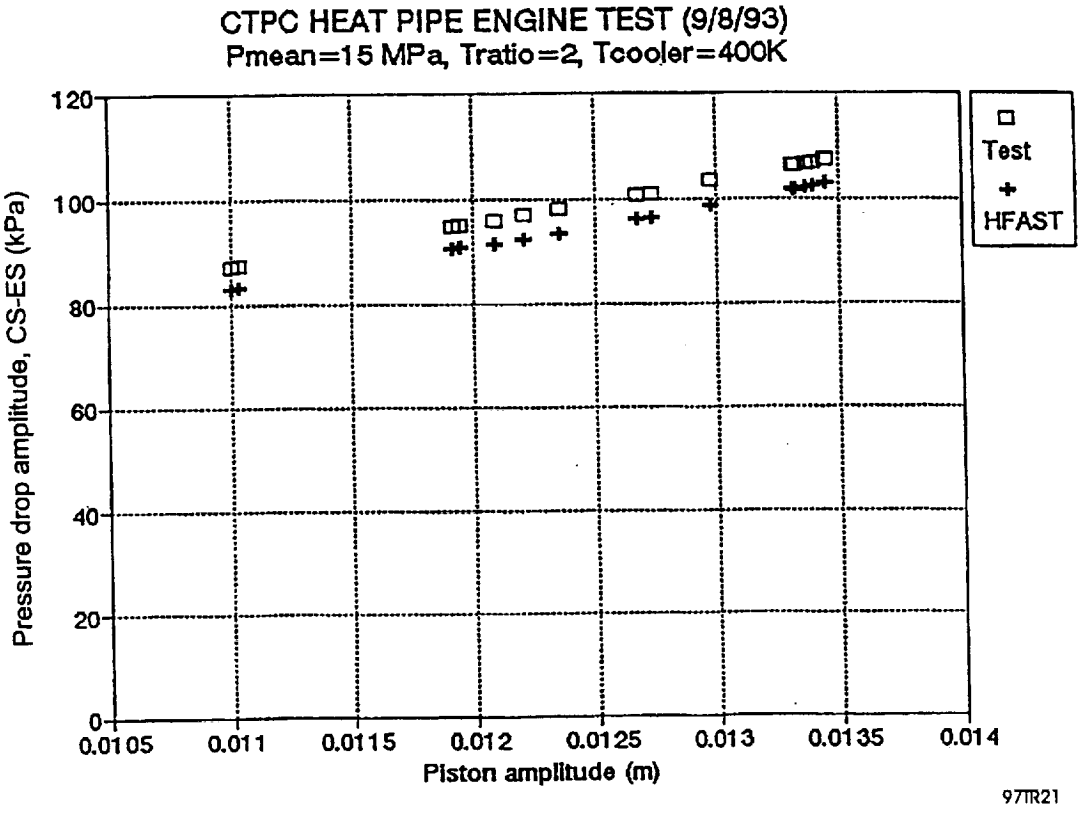

Figure 84. Amplitude of Pressure Drop between Compression and Expansion Spaces

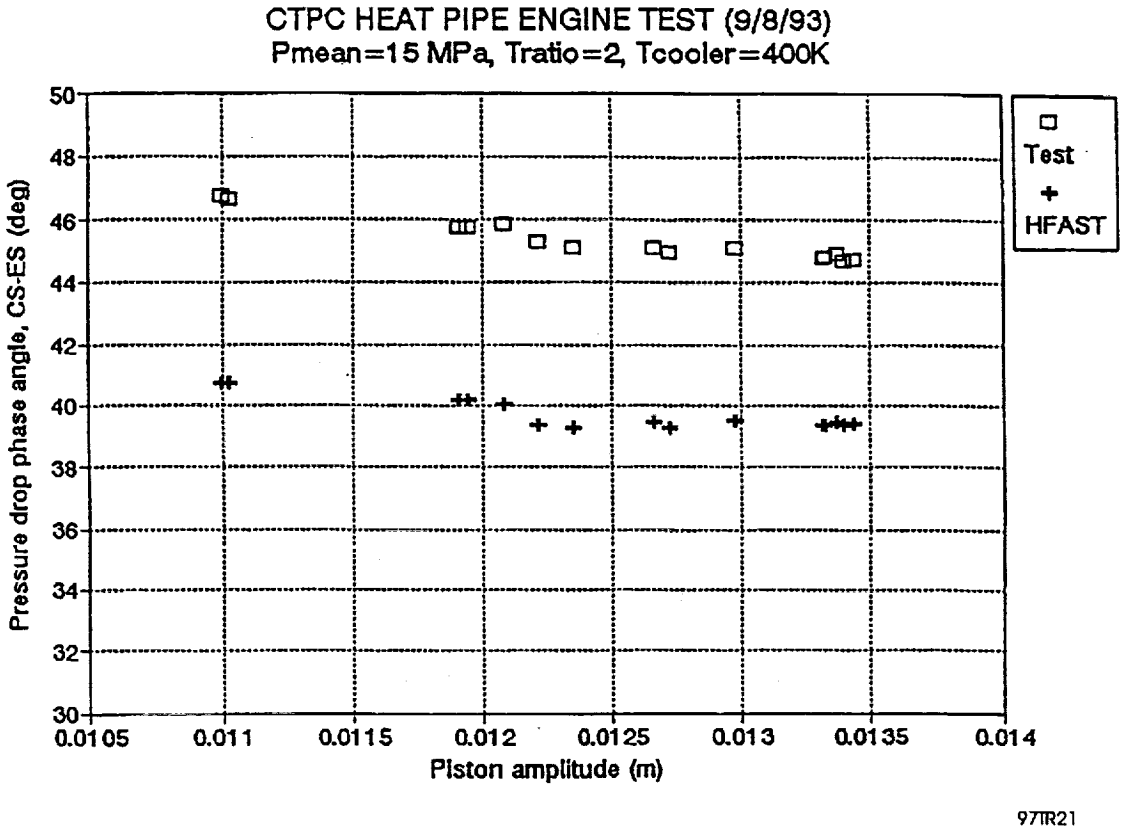

Figure 85. Pressure Drop Phase Angle versus Piston Amplitude

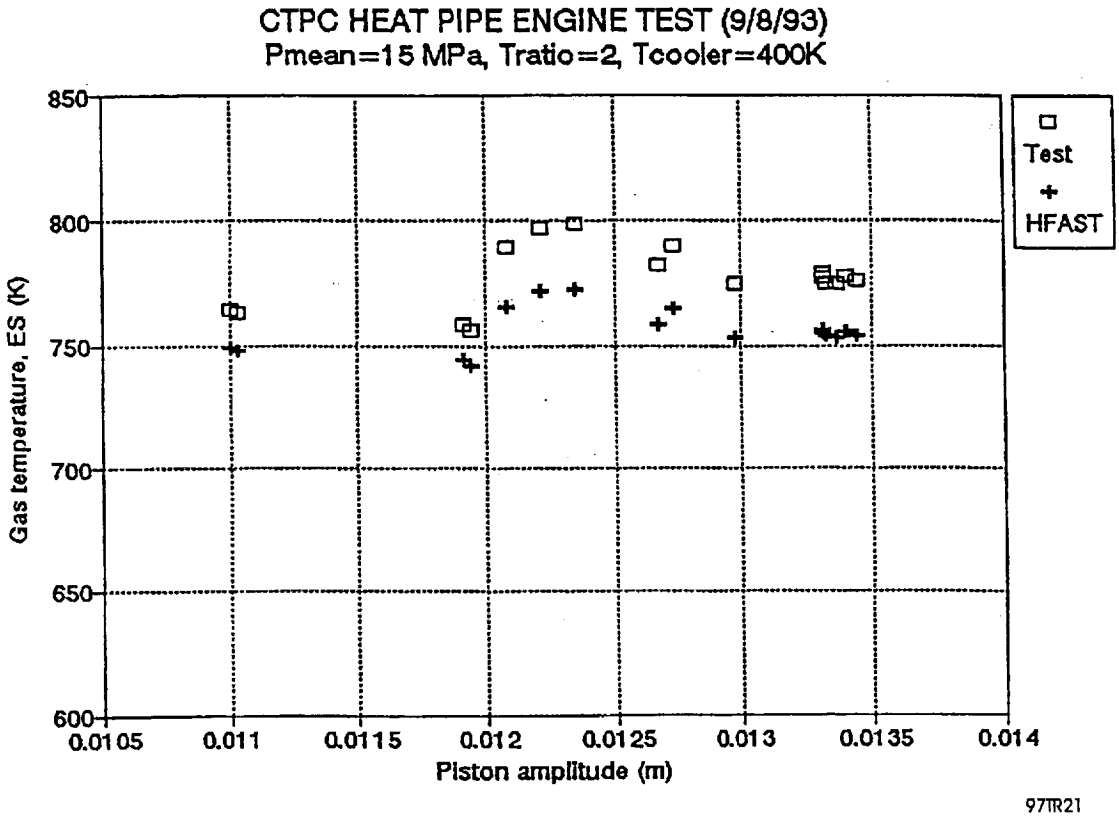

Figure 86. Gas Temperature in Expansion Space

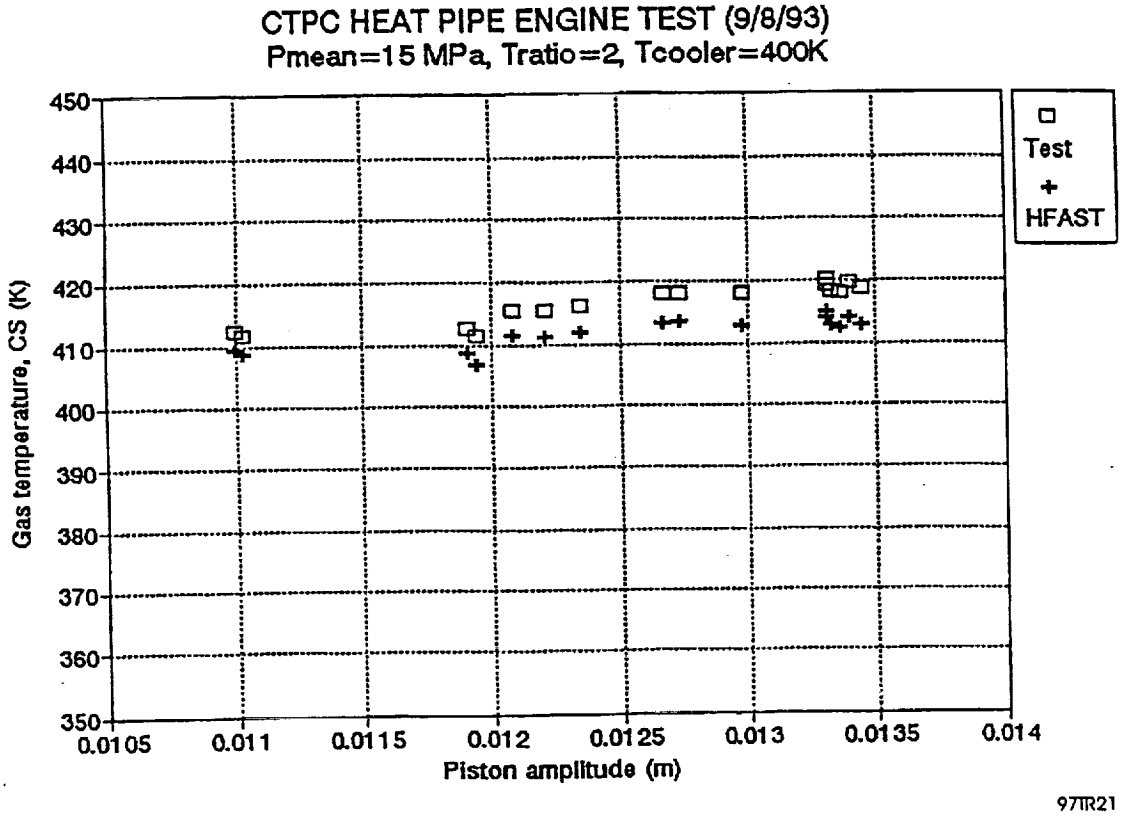

Figure 87. Gas Temperature in Compression Space

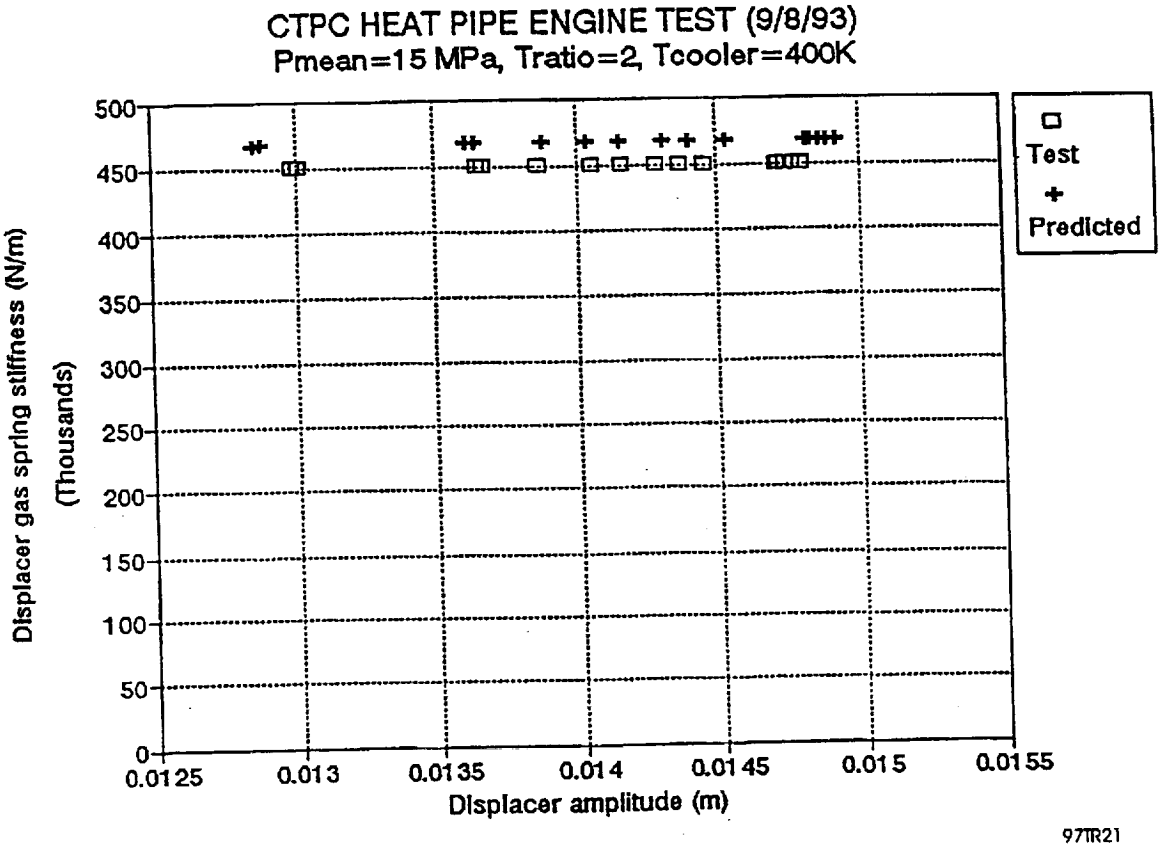

Figure 88. Displacer (aft and forward) Gas Spring Stiffness

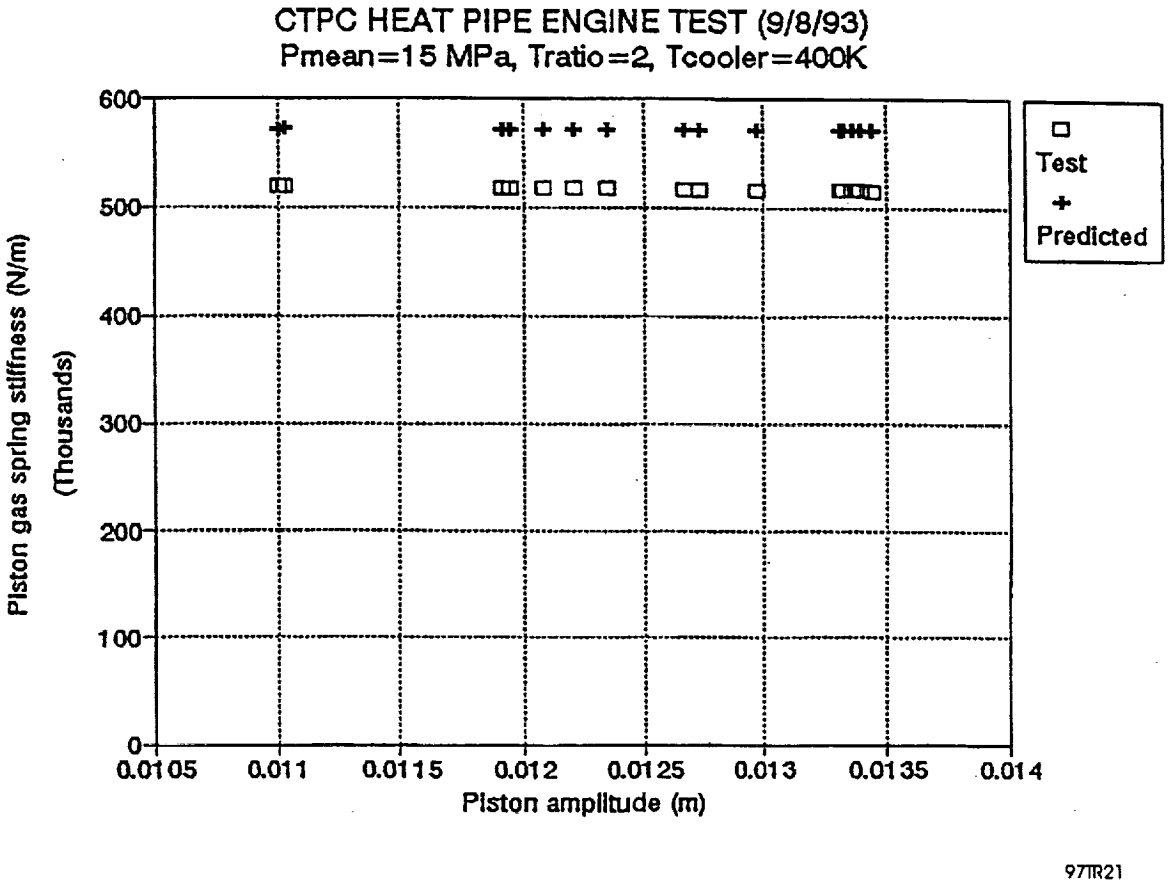

Figure 89. Piston Gas Spring Stiffness

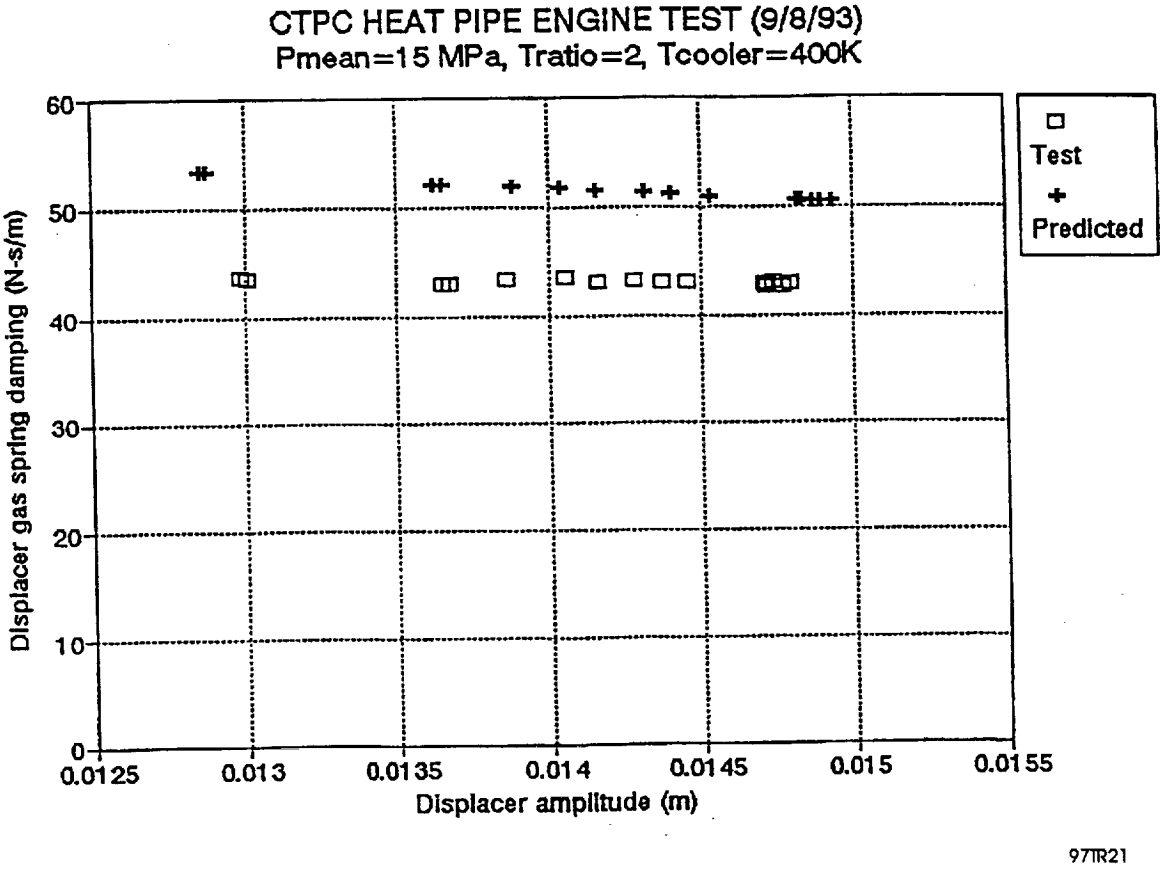

Figure 90. Displacer (aft and forward) Gas Spring Damping Coefficient

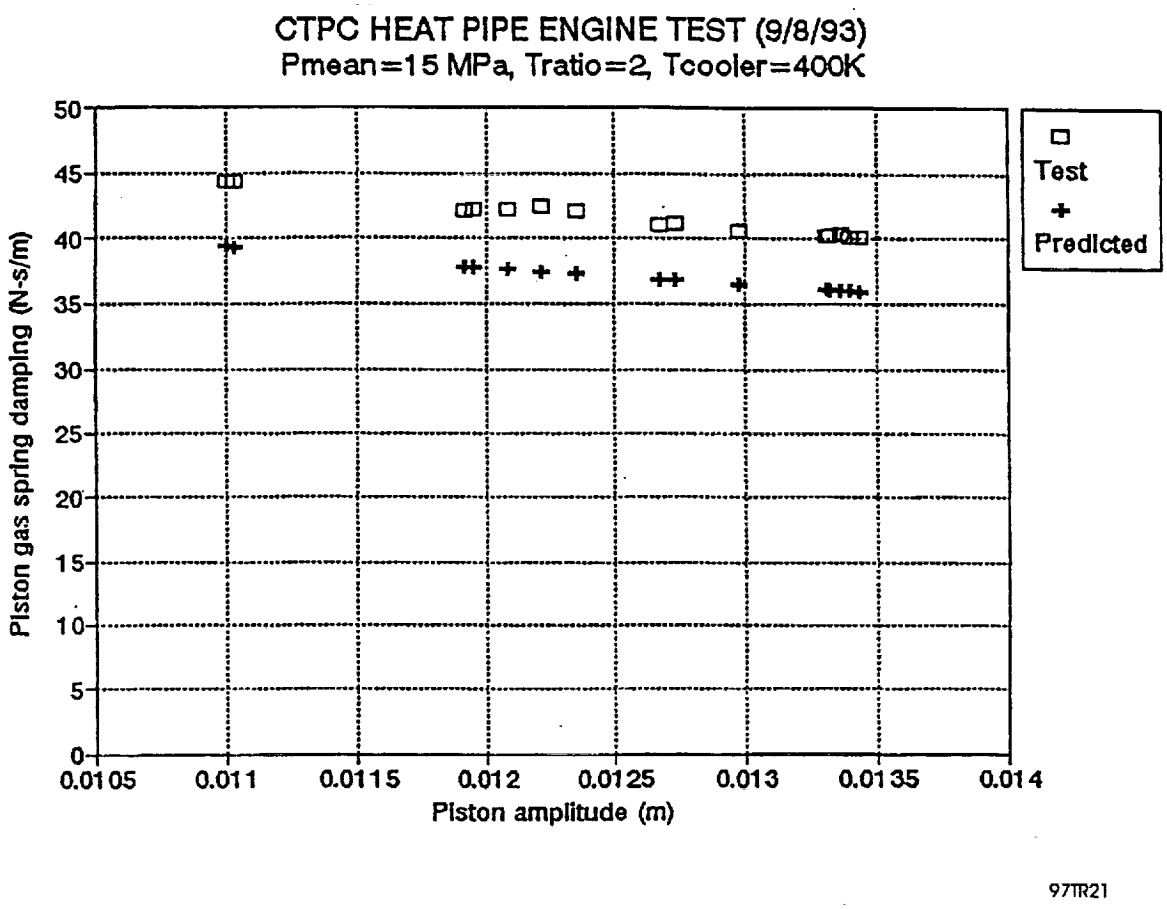

Figure 91. Piston Gas Spring Damping Coefficient

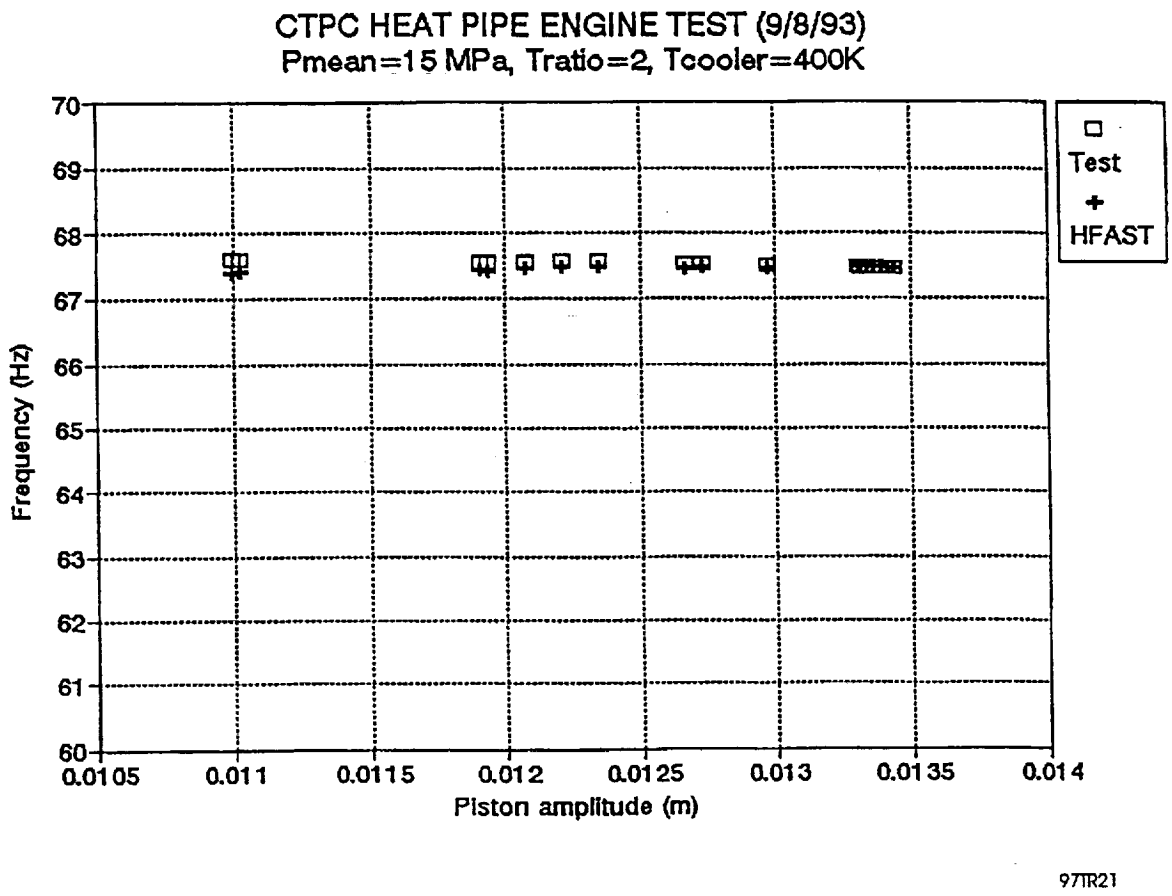

Figure 92. Operating Frequency

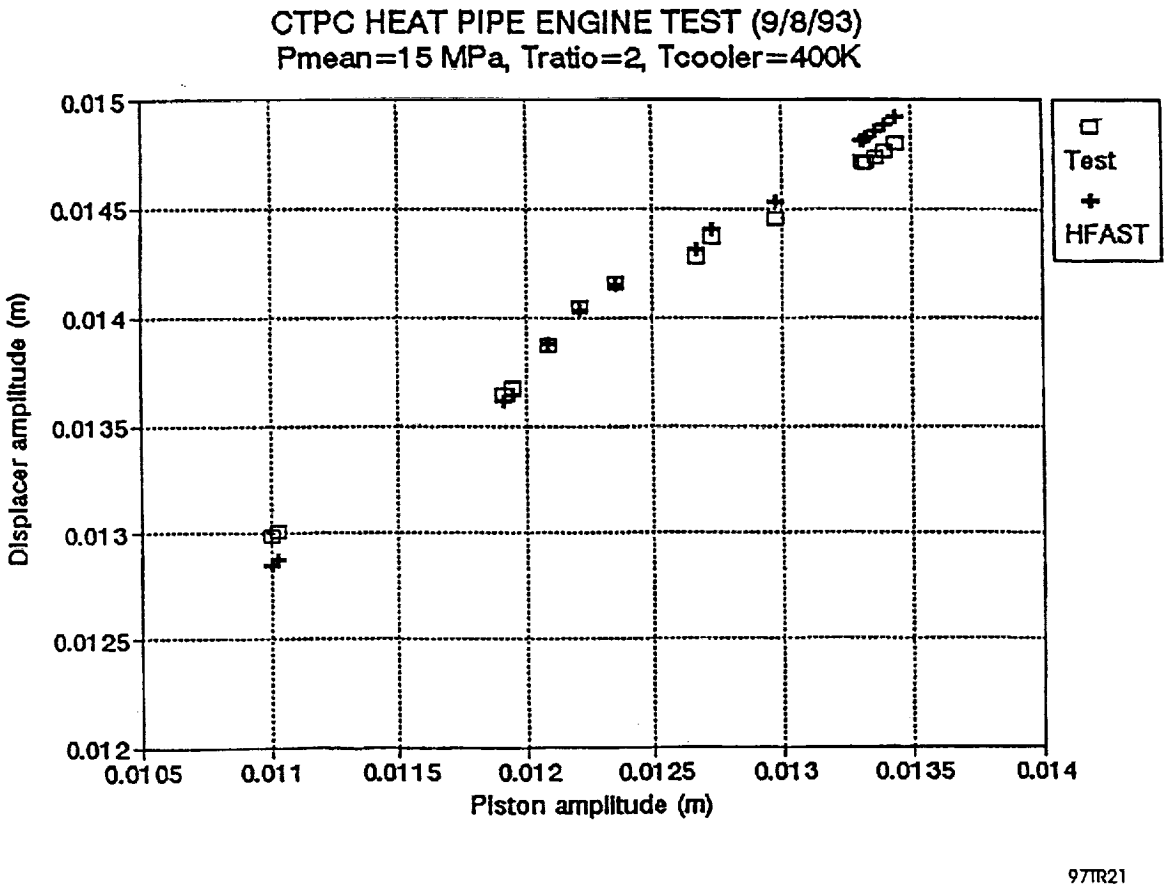

Figure 93. Displacer Motion

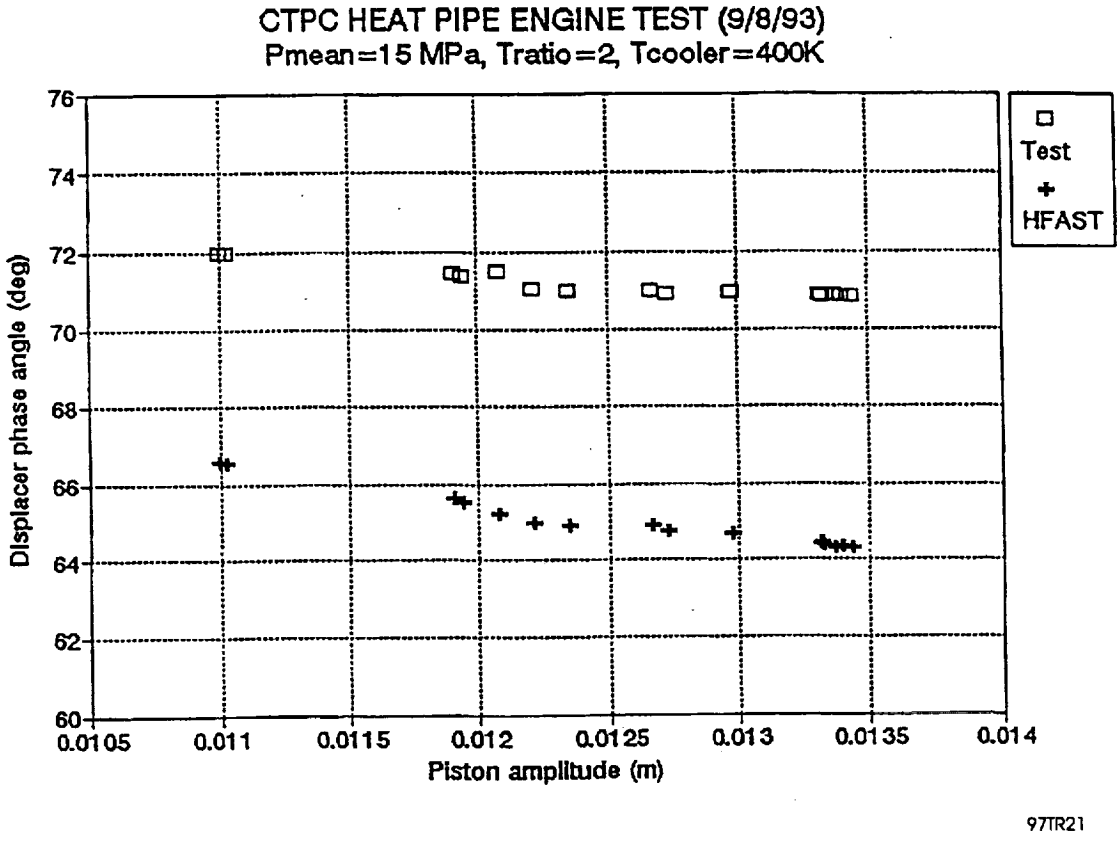

Figure 94. Displacer Phase Angle versus Piston Amplitude

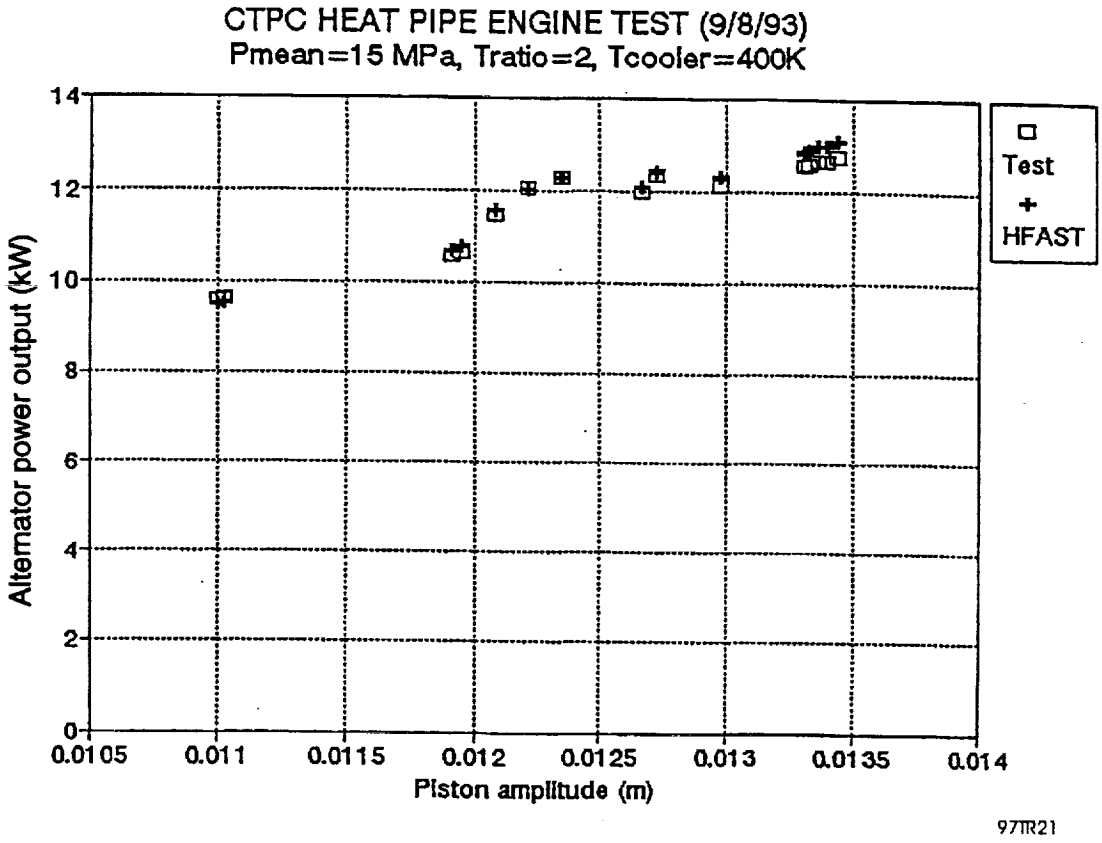

Figure 95. Alternator Power Output

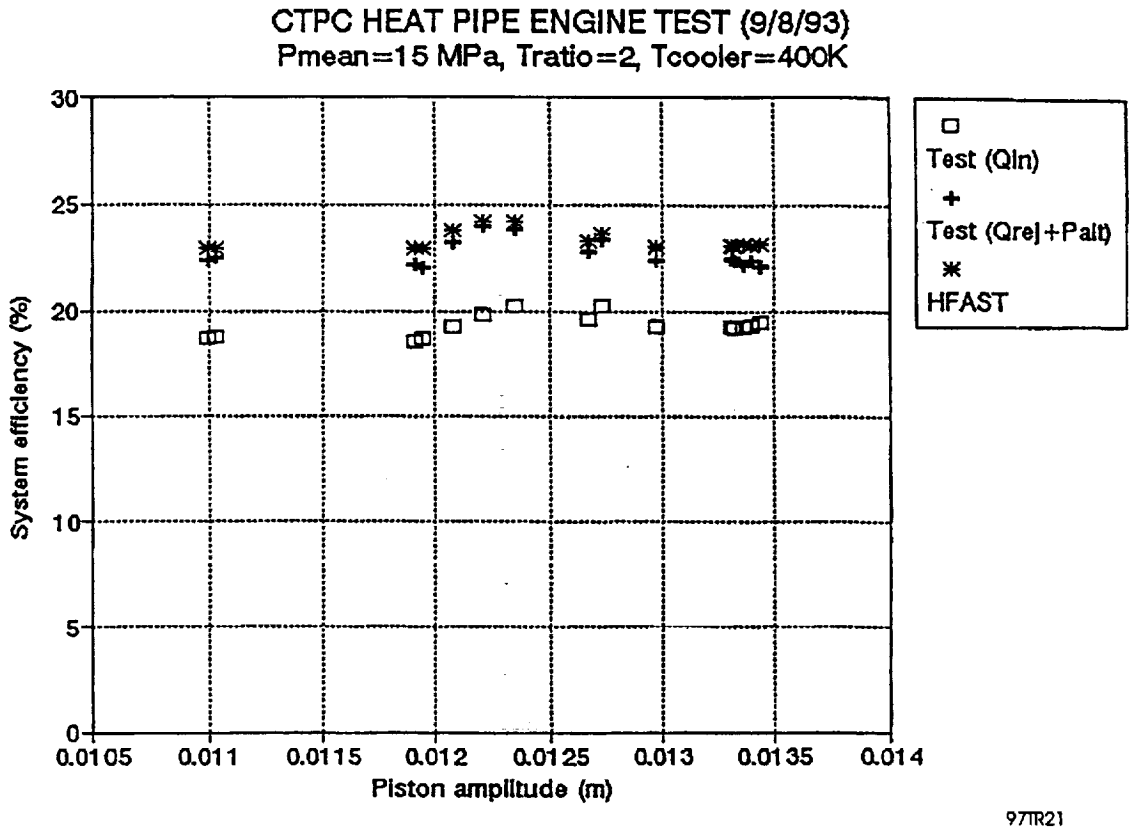

Figure 96. System Efficiency

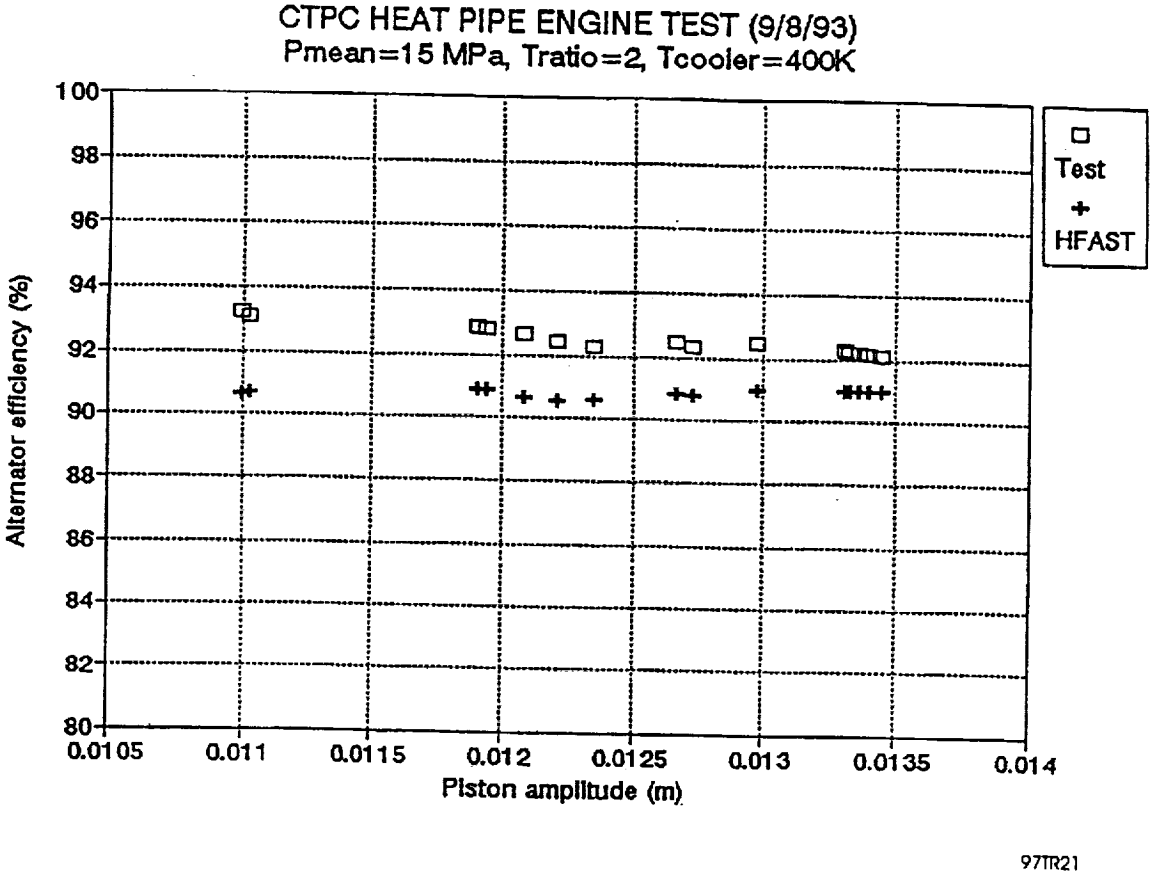

Figure 97. Alternator Efficiency

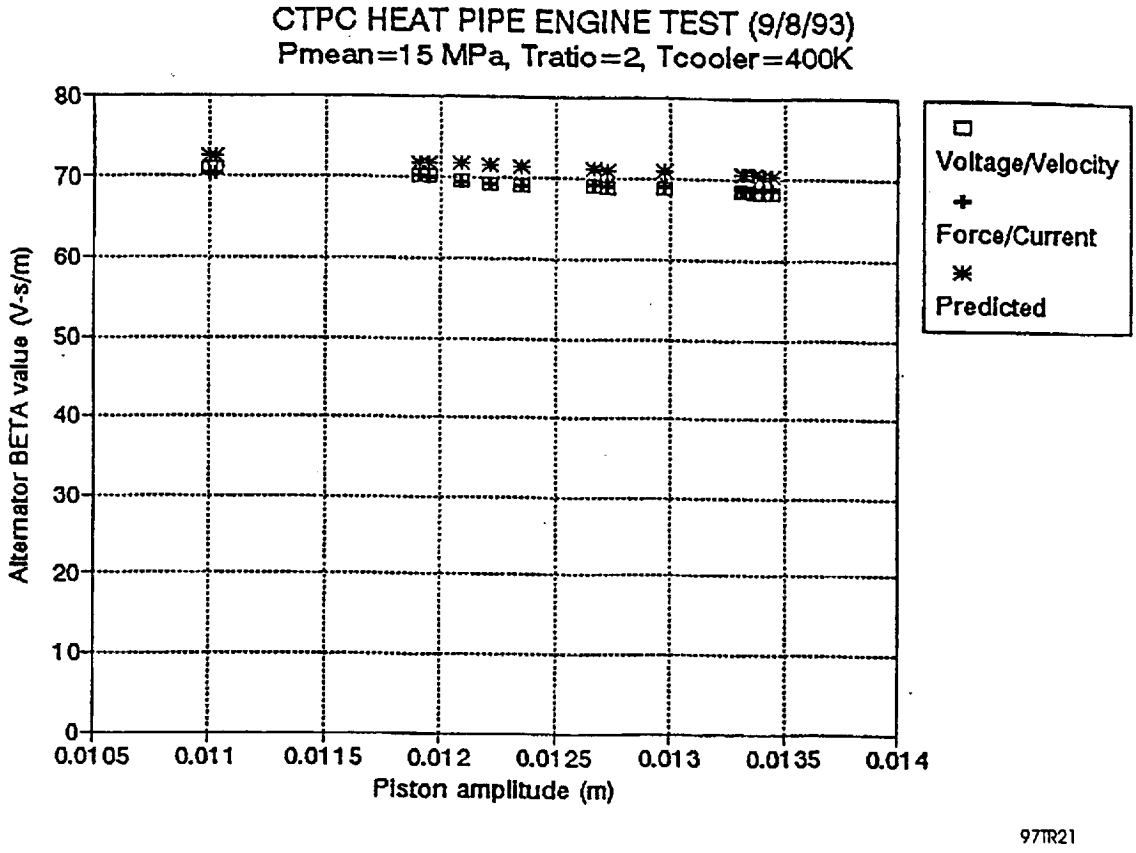

Figure 98. Alternator BETA Value

10.0 COMPONENT DEVELOPMENT SUMMARY

The CTPC is required to operate at higher temperatures than the SPDE on both the hot side and the cold side of the engine. To minimize joints and the potential unreliability associated with them, unconventional fabrication approaches were required in the heater and cooler.

Due to the unproven character of the Starfish heater head heat pipe concept, a separate development program on the heat pipe was conducted prior to initiating fabrication of the full-sized unit. Details on this program are provided in Appendix A.

Various component development activities were conducted to support the design and fabrication of the engine, alternator, and test facility (see Appendix D for photographs of development hardware). The conclusions reached from these activities are summarized in this section, with supporting details presented in Appendix B.

10.1 High-Temperature Inorganic Materials

Organic materials are commonly used in low-temperature applications for adhesives, electrical wire and slot insulation, potting compounds, O-rings, gaskets, feedthrough glands, etc. In general, most commonly used organics have a useful upper temperature limit of about 200°C. The cold side of the CTPC engine operates in the temperature range of 250°C to 325°C. For eventual space application, an engine alternator may be required to have a design life of several years. The goal for the CTPC was set at 7 years or 60,000 hours.

In the search for acceptable adhesives, various ceramic materials were evaluated. They were, in general, very brittle and a source of abrasive debris that could damage or jam the close clearance seals. None were judged to be acceptable for engine application. In general, mechanical joints will be required in place of adhesives where the long-life requirement must be met.

The area of the design where elimination of inorganic materials is most difficult is in the alternator coil. The development activities followed for the coil are covered in Section 7. The development of a coil using inorganic materials and readily available construction techniques was not successful. As an interim measure, high-temperature polyimide insulation and adhesives were used in conjunction with a fiberglass wrap. This resulted in a construction which can tolerate the 320°C coil temperatures for several hundred hours. There was insufficient data to predict whether this would be adequate for thousands of hours. It was judged that an approach using inorganics such as glass encapsulation was likely to be required, which involved significant development beyond the scope of the CTPC program. Further detail on materials behavior at elevated temperature is covered in Section B.2 of Appendix B.

For the CTPC, high-temperature silicone was found to be useful for the following:

- Making seals at internal instrumentation line feedthroughs
- Encapsulating alternator power connections
- Sealing internal feedthrough plug thread
- Bonding the wire and the fiberglass overwrap
- Alternator coil.

For O-rings, the material Kalrez was identified as capable of meeting temperature requirements. This is a very expensive material and, for budgetary reasons, replaceable Viton was used for the CTPC tests. Metallic gaskets and seals using Grafoil or copper were used for seals between flat surfaces where O-rings are not required.

10.2 Heat Exchanger Fabrication

10.2.1 Pocket Machining

The technique for removing material to create the pockets in the Starfish heater head is to rough out the pocket by end milling, final machining by a plunge electron-discharge machining (EDM) process and removal of the recast layer from the surface by chemical milling.

To establish and confirm the process details, two single pocket samples were made. The chemical milling operation was verified on the bore of a tube which was used as a heat pipe sample. Five fin segments were also made to develop the final process details.

Metallographic analyses performed at MTI are reported in Section B.3 of Appendix B.

10.2.2 Fin Passage Drilling

The initial design of the Starfish head called for oval passages with a dimension of 2.54 x 1.0 mm (0.100 x 0.040 in.) The approaches considered for passage drilling were:

- Electron discharge machining
- Shaped-tube electrochemical milling (STEM).

The EDM process was successful in producing prototypic oval passages in a material sample but was rejected in favor of STEM drilling based on a lower projected cost and shorter machining time.

In the STEM process, a hollow electrode of a similar dimension to the hole to be drilled is used to transfer material from the part being machined to the electrode using 20% sulfuric acid supplied through the electrode. Periodic reversal of the current is used to flush the deposit from the electrode. The straightness of the electrode determines the straightness of the drilling. For small deep holes, such as in the Starfish head, maintaining adequate straightness of the electrode proved to be a problem. The vendor had successful previous experience with round drillings using a die-spinning process to maintain tube straightness. A design change was made in which the single row of oval holes was replaced by a double row of round holes (see Table 3 for specifications). Several single fin samples were used to develop the process and two five-fin samples which had been made to develop the pocket machining process were used to finalize the procedures.

10.2.3 Cooler Assembly

In the cooler assembly, a solid nickel rod with longitudinal grooves on the outer diameter is inserted inside an Inco 625 tube. Good thermal contact between the rod and the tube is needed for efficient heat transfer between the helium in the passages formed by the grooves and the coolant which flows over the outside of the tube. The array of tubes are joined to a tube sheet at each end.

Initially, it was intended to shrink fit the insert into the tube and then braze the tube-to-tube sheet joints. Based on trials on samples, shrink fitting the relatively long, small diameter insert into the tube proved impractical. Good braze joints require well-controlled small clearances. The fit up of rigid tubes into tube sheets at both ends with the required clearance also proved to be impractical. Clearances on both the insert and at the tube sheet were opened up. The insert was brazed into the tube and the tube sheet joints were EB welded. Metallographic examination showed the braze joint had a high fraction of coverage providing adequate thermal contact. The weld joints were also determined to be good.

10.3 Inconel 718 Strength Issues

10.3.1 Creep Strength

Udimet 720 was selected as the heater head material with sufficient creep strength to meet the 60,000 hours life at 1050 K. Due to uncertainties regarding joining processes and the lack of data on some possible material forms, a separate development program was initiated. Inconel 718 was selected for the CTPC engine builds. It was required to perform engine testing up to the design temperature of 1050 K, but the life requirements at this temperature were relaxed.

Since 1050 K is above the normal operating range for Inconel 718, creep tests were performed to establish the operating time/temperature limits for the CTPC. Based upon creep strength tests, a creep damage versus time at various temperature levels was developed (see Section B.4 of Appendix B for details). The conclusions reached were that for short-duration performance tests, operation up to 1000 K will not be restricted, but operation between 1000 and 1050 K will be limited to about 50 hours. Extended (endurance) testing could be conducted at 950 K without restriction based on creep considerations.

10.3.2 Fatigue Strength

An inherent feature of Stirling engines is that there is a large thermal gradient along the pressure containing structure adjacent to the regenerator. For large diameter engines with short regenerators located inside the main vessel, this gradient is a source of significant thermal stresses in the vessel wall. The pressure loading on the wall creates stresses due to the mean pressure (15 MPa, (150 bar)) and the alternating pressure (1.8 MPa, (18 bar)). The alternating stresses are relatively small but, being superimposed on the mean pressure and thermal stresses, fatigue cannot be dismissed.

In the SPDE and CTPC, the vessel wall is not in direct contact with the regenerator. By tailoring the geometry, the stress levels have been maintained at a level where an ample factor of safety against fatigue failure is predicted based upon the application of a standard Goodman diagram.

Increasing the frontal area of the CTPC regenerator would improve the thermodynamic efficiency of the CTPC design. To minimize the specific weight, it may be desirable to place the regenerator in direct contact with the vessel wall. This will increase the thermal stress levels such that adequate fatigue resistance may not be predicted by applying the standard Goodman diagram.

A series of tests were initiated and consulting advice sought to determine if a less restrictive design basis could be justified to provide more flexibility in optimizing Stirling engine heater head designs. Test data on Inconel 718 indicates that there is a failure threshold for the cyclic stress component at high mean stress. This justifies a less restrictive criterion for future designs than was previously being applied.

10.3.3 Weld Creep

The weld between the Starfish and the closure plates is subject to a tensile load due to engine pressure. Tests on samples demonstrated that weld creep strength was no lower than in the unwelded material. Results of these tests are presented in Section B.4 of Appendix B.

10.3.4 Weld Fatigue

Electron-beam-welded test samples were prepared to evaluate the fatigue performance of the closure plate welds. The standard 6.35-mm (0.25-in.)-diameter smooth bar test was run at 1050 K in an air environment. The fatigue test was run with a mean load of 248 MPa and an alternating load of ±62 MPa. The test specimen was run to 10,000,000 cycles without failure.

10.4 Beryllium Issues

10.4.1 Beryllium-Inconel 718 Braze

The Inconel 718 (In718) dome of the displacer must be joined to the beryllium (Be) displacer body at its outer diameter. This joint is subject to the inertia loads associated with the 70-Hz displacer motion (about 300 g). The joint must also seal to avoid a loss due to gas pumping across the joint. The outside of the joint is exposed to the cyclic expansion space pressure and the inside is at a constant pressure. A brazing technique was developed and tested. The details are reported in Section B.5 of Appendix B.

During subsequent engine testing, it was determined from a bench test that the joint was not leak tight. This introduced an uncertainty regarding the strength of the joint. Radial shear pins were added as a backup to the braze. A displacer was reworked using a shrink fit and shear pins with no braze. The leak rate was very low in this assembly and calculations indicated the pumping loss during engine operation was negligible.

10.4.2 Nickel and Aluminum Oxide Coatings

All surfaces of beryllium are coated with electroless nickel. Based on spalling observed on a chrome oxided test sample, an evaluation of the adhesion of nickel to beryllium was initiated. Tests before and after heating were conducted. Based on these tests, it was decided to perform all beryllium braze operations prior to nickel coating. The adhesive strength of aluminum oxide coatings was also assessed. Results of these test are given in Section B.5 of Appendix B.

10.4.3 Beryllium-Magnet Bond

Magnets are located in the displacer assembly on the gas spring piston and post and flange to keep the displacer from rotating. This is required to maintain port alignment. Space is very limited and an adhesive would simplify the installation. Based on the testing evaluation discussed earlier, it was decided that the available adhesives were inadequate at 300°C, and a mechanical attachment was devised.

10.4.4 Beryllium-Beryllium Braze

A beryllium plug is brazed into one end of the displacer rod. An aluminum braze was used on the SPDE. Samples were made to permit tests at 300°C to be conducted to verify the strength of the joint. Rupture and fatigue tests were conducted and ample strength was demonstrated. Details are presented in Section B.5 of Appendix B.

10.4.5 Beryllium-Helicoil Interaction

Helicoils are used on several joints in the CTPC. The attachment of the plunger to the power piston is typical and is the most highly loaded joint in the engine. Samples were procured, and tightening and untightening torque tests conducted before and after temperature cycling to 320°C. No damage was observed. A tightening torque of 11.8 N-m (105 in.-lb) was applied. The loosening torque was 9.9 N-m (88 in.-lb.)

A tensile test was performed using a sample with helicoils in each end to evaluate the load-bearing capacity of the Be helicoil assembly. The test specimen was heated to approximately 320°C during the testing schedule. The total load applied to the fastener was 9785 N (2200 lbf), which translates into a stress of approximately 4.65 10^8 N/m^2 (67,484 psi) at the thread root.

10.5 Heat Pipe Processing and Sodium Issues

10.5.1 Heat Pipe Processing

Fabrication of the sodium heat pipe structure requires a series of thermal processing steps to ensure proper sodium charging and cleanliness. Sodium filling is performed at temperatures below 427 K and will not alter the mechanical properties of Inconel 718. The higher temperature heat pipe processing and sodium charge optimization takes place in the age-hardening range of Inconel 718 and will therefore affect the mechanical properties. A thermal cycle for sodium charge optimization and processing which maintained the optimum mechanical properties in Inconel 718 was defined by MTI and the sodium processing vendors. The thermal cycle was to be performed after age hardening and allowed a maximum of 10 hours at temperatures up to 1000 K and 3 hours at temperatures up to 1060 K. Tensile tests performed on materials subjected to full aging followed by the heat pipe processing and thermal optimization cycle showed no degradation when compared to material given the conventional Inconel 718 heat treatment only.

10.5.2 Sodium Issues

The CTPC heat pipe and heater head assembly will require Inconel 718 to survive static and fatigue loads in a 1050 K sodium heat pipe environment. Concerns of general corrosion and degradation of Inconel 718 mechanical properties in sodium prompted MTI to run a Heat Pipe Fatigue Test (HPFT) to evaluate Inconel 718 performance under engine operating conditions. The details of the testing performed are presented in Section B.6 of Appendix B. The results of the heat pipe fatigue test confirmed that Inconel 718 could perform without incident under the stress, temperature, time, and sodium conditions expected in the CTPC.

An evaluation of various refractory coatings was made in the early stages of the procurement. Results are covered in Section B.6 of Appendix B. It was decided that for the relatively short life, Inconel CTPC heater head coatings would not be used.

Section B.6 of Appendix B presents test results of a 25.4-mm (1-in.) diameter by 254-mm (10-in.) long Inconel heat pipe that was operated at 1050 K and at approximately 20 W/cm^2 heat flux. During these tests, heat was input over a 101.6-mm (4-in.)-long section by a large (69.8 mm (2.75 in.) in O.D., 45.9 mm (1.81 in.) in I.D.) silicon-carbide heater. Heat was removed by a 101.6-mm (4-in.)-long water jacket. A mixture of helium and nitrogen was trickled through a small gap between the pipe O.D. and the jacket I.D. to control the heat loading. Approximately 1000 hours of operation were accumulated. Regions of oxygen-accelerated corrosion were present in areas of crevices with the depth of attack less than 35 microns.

10.6 Wear Couple Selection

The power piston and displacer have running clearances in the range 10 to 18 microns (0.0004 to 0.0007 in.) Past experience has shown that small debris particles or small distortions due to thermal and/or pressure effects can occasionally cause local rubbing and even jamming of the piston or displacer. During startup on internally pumped hydrostatic gas bearings, it takes about seven cycles to develop the full bearing supply pressure. During this period, rubbing contact will occur.

The CTPC is designed to operate at an elevated cold-side temperature. The potential for thermal distortion is higher than in a lower temperature engine. Several engines built and tested at MTI prior to the CTPC used chrome oxide on both surfaces where the potential for sliding contact existed. This is referred to as a 'hard on hard' wear couple combination. It was decided for CTPC to investigate several wear couple combinations. The objective here was to identify a low friction pair which would wear rather than jam under light rubbing conditions.

Screening tests were conducted using a pad-on-disc test rig. The reference wear couple selected was the aluminum oxide hard face (applied by Speedring's procedure) and carbon graphite P-3310 (Pure Carbon Co.). Additional tests were conducted on a wear couple test rig that uses round bushings in contact with a cylindrical rod. The test details and results are presented in Section B.7 of Appendix B.

10.7 Pressure Boundary Penetrations

10.7.1 Capacitance Probe Feedthroughs

Reciprocating motion of the power piston and displacer is determined by measuring the change in the radial dimension of a tapered gap. Capacitance probes supplied by CAPACITEC were selected for this measurement based on their thermal stability at an operating temperature of approximately 300°C. These probes use a shielded cable and a microdot connector. To bring these cables through the joining ring and instrumentation ring, pressure-tight feedthroughs supplied by CONAX were selected. To avoid having to remove the microdot connector, a split gland is used in the fitting. To meet the temperature requirement (250°C), lava seal glands were specified. These fittings were tested in helium at temperature.

Problems occurred during engine operations because the lava seal did not provide the necessary insulation to ground. The lava element was replaced with Teflon, and the stainless steel elements that compress the Teflon gland were replaced with Vespel pieces made at MTI. These worked fairly well but shorts were sometimes experienced due to the wear and tear associated with assembly and disassembly.

A change in lead size from 1.5- to 0.75-mm (60- to 30-mil) diameter was made due to damage experienced at the probe connection associated with the bending stiffness of the lead wire. This necessitated a change in the lead feedthroughs. An arrangement was made in which a microdot connector is located on both sides of the feedthrough. A length of 9.5-mm (3/8-in.)-diameter triax cable is passed through a Swagelock connector which seals on the stainless steel outer sheath. The outer sheath was removed on either side of the feedthrough, and high-temperature epoxy used to seal against helium flow through the inner region of the cable.

10.7.2 Thermocouple Feedthroughs

The thermocouple feedthroughs are similar to the capacitance probe feedthroughs with the exception that a split gland is not required.

10.7.3 Instrumentation Ring Seal

There are multiple instrumentation wires and several gas lines which must cross the joint between the beryllium post and flange and the Inconel 718 instrumentation ring. The seal arrangements considered and tested are covered in Section B.8 of Appendix B. The arrangement which has worked successfully is the Belleville washer seal. The original design was modified by adding a high-temperature silicone washer between the Belleville washer and the seat in the beryllium.

10.8 Heating System

10.8.1 Slot Heaters

Heat pipe development and engine hardware procurement were planned to proceed in parallel. When it was recognized that the engine heater head would be available several months before the heat pipe, it was decided to seek an interim means of supplying heat to the head.

A 12.5-kW alternator output at a thermal efficiency of 20% requires a 62.5-kW thermal input to the heater head. Flat silicon-carbide radiant heaters that could be located in the slots of the Starfish head were identified as a possible approach. An Inconel 718 block was available in which a sample pocket had been machined. This was modified for thermocouple installation and used for heater evaluation tests. The details are reported in Appendix B.9. The conclusions reached were that these heaters could supply over 60 kW to the head for several hundred hours. At power levels over 70 kW into the engine, the life expectancy of some heaters could be in the tens of hours. This capability was sufficient to cover all near-term performance testing needs.

A setup was built to evaluate temperature conditions and determine if cooling of the fin edge or electrical connection inside the holder was needed. Based on the tests, cooling is not required. However, exact conditions in the engine could not be closely simulated. The capability to add air cooling was provided on the test stand and would have been added if engine test experience dictated a need.

10.8.2 Heat Pipe Heaters

Heat is input to the heat pipe by an array of cylindrical silicon-carbide heaters located in an annular cavity beneath the bottom plate of the heat pipe. A test setup was built to simulate the cavity. The simulated heat pipe bottom plate was jet cooled using shop air. Details are presented in Section B.9 of Appendix B. The conclusions reached were that over 75 kW can be supplied to the engine for an extended period without heater failure. This capability is expected to cover all foreseeable needs.

10.8.3 Mosfet Circuit

A characteristic of silicon-carbide heaters is that the resistance is not closely controlled. Variations of ±20% is typical. The slot heaters are closely coupled to the heater head. To maintain a circumferentially uniform heat input to the heater head, it is necessary to control the voltage across each heater. This is less critical for the heat pipe heaters because the sodium will even out heat input variations. For heater head life considerations, however, it is an advantage to be able to minimize power variations between heaters.

In the control approach selected, each heater is controlled by a dc circuit in which a high-frequency duty cycle signal is supplied to a solid-state switching circuit in which the main control component is a MOSFET. Three prototype circuits were built and tested prior to building the final heating system assemblies.

10.9 Cooler Flow Test

To evaluate the flow distribution in the engine cooler and select the geometry of inlet and/or outlet flow distributors, a mockup of the cooler was built and tested. Details of this test are presented in Section B.10 of Appendix B. The conclusions reached were that no flow distributors were needed at the entrances or exits to the cooler.

11.0 CONCLUSIONS

Operation in space requires the power converter to absorb heat from a high-temperature source and radiate unused heat to space via a radiator. Since the size of the radiator is proportional to the fourth power of the absolute temperature, the heat reject temperature for the space application optimizes, for a minimum specific mass, to a temperature (525 K) much higher than the near-ambient reject temperature for terrestrial systems. To provide the converter with an acceptable efficiency, heat must be supplied to the converter through heat pipes at a temperature of 1050 K.

Due to the high-temperature operation requirement for both the hot and cold sides of the power converter, critical component, material, and manufacturing technologies were developed for long-term, reliable operation in space. The readiness of these technologies was demonstrated through the 12.5-kWe CTPC tests. The conclusions that can be drawn from the results of this technology development work are summarized below for each key technology area.

- Starfish Heater Head. The Starfish heater head was designed as a monolithic structure with an annular sodium heat pipe as an integral part of the head. This design minimized the number of brazed or welded joints in the assembly and eliminated any joints that see both high stress and a sodium environment. This design resulted in a significant increase in the reliability of the heater head by reducing the number of potential leak sites.

  Udimet 720 was selected as the long-life material for the heater head. Since Udimet is not readily joined to itself or other alloys, welding and transient liquid phase (TLP) brazing techniques were identified and preliminary evaluations completed. High cycle fatigue, low cycle fatigue, and creep data were generated to form the design basis. Fatigue data were also generated for Inconel 718 at 525, 1000, and 1050 K, which formed the design basis for the cold end of the heater head.

  The Starfish heater head was a new approach to Stirling engine heater design. The two critical manufacturing steps are the precise machining of 50 radial pockets into a solid ring of superalloy material followed by the machining of almost 2,000 1-mm (40-mil) diameter holes, 50-mm (2-in.) long through a 3.8-mm (0.150-in.) thick wall between the pockets. Positional tolerances on the hole position are very tight since the edges of the holes are about 0.75 mm (30 mils) from the surface. This machining was accomplished successfully using a shaped tube electrochemical milling process.

- Heat Pipe. Heat pipe development was conducted primarily at Thermacore with support by ETEC for sodium filling. A 1/10th segment was built and tested. The thermal performance of the concept was verified, and various processing procedures developed. Based on these processing procedures, a full-scale heat pipe was designed, fabricated, integrated with the engine, and successfully tested.

- Long Life, High Performance Regenerator. A regenerator design was developed and tested that eliminated bypass losses and thus resulted in a more efficient, reliable unit. This long-life regenerator is constructed of a single stack of sintered felt metal. Coarse screen mesh is sintered to each end of the felt metal to give the matrix rigidity and to prevent small pieces from breaking off during engine operation. The inside and outside diameters are brazed to metal liners to prevent bypass leakage from occurring.

- Cooler. By providing slotted inserts in relatively larger diameter tubes, the number of joints in the cooler was drastically reduced as compared to the SPDE design without any significant performance penalty. Metallographic examination showed the braze joints between the insert and the tube had a high fraction of coverage, providing adequate thermal contact. This design modification further enhanced cooler reliability.

- Elevated Temperature Alternator. The alternator is required to operate in a helium environment of about 275°C. The magnet design temperature of 275°C is near the upper bound of practical application for the best rare earth magnets. Based on sample tests, samarium cobalt (Sm_2Co_{17})

magnets were selected, and a very stringent procurement and test specification was developed. A technique for measuring the properties of full-size CTPC magnets at 275°C was developed. This was applied to magnets that had met the room temperature specifications.

Alternator coils typically use organic insulating and potting materials. Conventional materials were limited to applications where the coil temperatures did not exceed about 200°C. Since the requirements for the CTPC alternator coil were at least 100°C above this level, an unconventional approach to design of the CTPC alternator coil was mandated. Significant development effort was applied to devise a coil with high-temperature capability.

- Internally Charged Hydrostatic Gas Bearings. Internally charged hydrostatic gas bearings were developed for both the power piston and displacer with adequate stiffness to carry the sideloads generated by the alternator. Wear couples for the bearings and seals were also developed that permitted startup and shutdown without debris generation, thus resulting in a long-life bearing design. Carbon graphite and aluminum oxide were selected as mating surfaces (for bearings and close clearance seals) based on friction and wear tests conducted at 525 K. In addition to the hydrostatic bearing, a spiral-groove hydrodynamic bearing was also developed and demonstrated.

- The CTPC gave a feeling of confidence to the design approach since it achieved its performance goals in the very first test, and significant endurance test hours were accumulated before the program concluded. Over 1470 hours were accumulated in hot engine tests and nearly 1450 hours for the heat pipe heater head (7.08 hr for the initial test, 496.59 for the Phase I endurance test, and 943.31 hr for the Phase II endurance test).

- Key issues remaining for development include the long-life/high temperature (1050 K) Udimet heater head and a ceramic-coated coil identified as the best long-life option for an alternator operating in an ambient environment of 525 K. Since development of these components was initiated but not completed during the program, issues regarding their design, fabrication, and demonstration remain and offer an opportunity for future work.

BIBLIOGRAPHY

The documents listed in this bibliography primarily describe work performed as part of the overall project that included development of the Stirling Space Engine (SSE). Certain other documents have been included that were not part of this effort but provide related information that may be of interest. The bibliography is organized by topic areas to provide an easy reference for the reader.

Programmatic/Status Updates

Alger, D.L.: Overview of the 1986 Free-Piston Stirling Activities at NASA Lewis Research Center, NASA TM-88895, 1986.

Alger, D.L.: Progress Toward the Evolution of a Stirling Space Engine, NASA TM-100221, 1987.

Dudenhoefer, J.E. and Winter, J.M.: Status of NASA's Stirling Space Power Converter Program, NASA TM-104512, prepared for the 26th Intersociety Energy Conversion Engineering Conference, Boston, MA, 1991.

Dudenhoefer, J.E.: Programmatic Status of NASA's CSTI High Capacity Power Stirling Space Power Convertor Program, NASA TM-103142, prepared for the 25th Intersociety Energy Conversion Engineering Conference, Reno, NV, 1990.

Dudenhoefer, J.E., Alger, D., and Winter, J.M.: Progress Update of NASA's Free-Piston Stirling Space Power Converter Technology Project, NASA TM-105748, prepared for the Nuclear Technologies for Space Exploration Conference, Jackson Hole, WY, 1992.

Slaby, J.G.: Overview of NASA Lewis Research Center Free-Piston Stirling Engine Activities, NASA TM-83649, DOE/NASA/1005-2, prepared for the 19th Intersociety Energy Conversion Engineering Conference, 1984.

Slaby, J.G.: Overview of the 1985 NASA Lewis Research Center SP-100 Free-Piston Stirling Engine Activities, NASA TM-87028, DOE/NASA/1005-5, prepared for the 20th Intersociety Energy Conversion Engineering Conference, Miami Beach, FL, 1985.

Slaby, J.G.: Overview of the 1986 Free-Piston Stirling SP-100 Activities at the NASA Lewis Research Center, NASA TM-87305, DOE/NASA/1005-9, prepared for the 21st Intersociety Energy Conversion Engineering Conference, San Diego, CA, 1986.

Slaby, J.G.: Overview of Free-Piston Stirling SP-100 Activities at the NASA Lewis Research Center, NASA TM-87224, DOE/NASA/1005-8, prepared for the 3rd International Stirling Conference, Rome, Italy, 1986.

Slaby, J.G. and Alger, D.L.: A 1987 Overview of Free-Piston Stirling Technology for Space Power Application, NASA TM-89832, 1987.

Slaby, J.G.: Overview of Free-Piston Stirling Engine Technology for Space Power Application [Final Report], NASA TM-88886, DOE/NASA/1005-12, 1987.

Slaby, J.G.: Overview of NASA Lewis Research Center Free-Piston Stirling Engine Technology Activities Applicable to Space Power Systems, NASA TM-88815, DOE/NASA/1005-10, prepared for the 4th Symposium on Space Nuclear Power Systems, Albuquerque, NM, 1987.

Slaby, J.G.: The 1988 Overview of Free-Piston Stirling Technology for Space Power at the NASA Lewis Research Center, NASA TM-100795, 1988.

Slaby, J.G.: Free-Piston Stirling Technology for Space Power, NASA TM-101956, prepared for the International Conference on Space Power, Cleveland, OH, 1989.

Sovie, R.J.: SP-100 Advanced Technology Program, NASA TM-89888, 1987.

Winter, J.M.: CSTI High Capacity Power, NASA TM-102059, prepared for the 24th Intersociety Energy Conversion Engineering Conference, Washington, D.C., 1989.

Winter, J.M.: The NASA CSTI High Capacity Power Program, NASA TM-105240, prepared for the Conference on Advanced Space Exploration Initiative Technologies, Cleveland, OH, 1991.

Winter, J., Dudenhoefer, J., Juhasz, A., Schwarze, G., Patterson, R., Ferguson, D., Titran, R., Schmitz, P., and Vandersande, J.: The NASA CSTI High Capacity Power Project, NASA TM-105813, Proceedings of the 27th Intersociety Energy Conversion Engineering Conference, vol. 6, pp. 6.79-6.85, held in San Diego, CA, 1992.

Mission and System Analyses

Bents, D.J.: Preliminary Assessment of Rover Power Systems for the Mars Rover Sample Return Mission, NASA TM-102003, prepared for the International Conference on Space Power, Cleveland, OH, 1989.

Bents, D.J., Geng, S.M., Schreiber, J.G., Withrow, C.A., Schmitz, P.C., and McComas, T.J.: Design of Multihundred Watt DIPS for Robotic Space Missions, NASA TM-104401, prepared for the 26th Intersociety Energy Conversion Engineering Conference, Boston, MA, 1991.

Bents, D.J.: Small Stirling Dynamic Isotope Power System for Multihundred-Watt Robotic Missions, NASA TM-104460, prepared for the International Pacific Air and Space Technology Conference, Gifu City, 1991.

Bents, D.J., McKissock, B.I., Hanlon, J.C., Schmitz, P.C., Rodriguez, C.D., and Withrow, C.A.: Comparison of Dynamic Isotope Power Systems for Distributed Planet Surface Applications, NASA TM-4303, 1991.

Bents, D.J., Schreiber, J.G., Withrow, C.A., McKissock, B.I., and Schmitz, P.C.: Design of Small Stirling Dynamic Isotope Power System for Robotic Space Missions, NASA TM-105919, prepared for the 10th Symposium on Space Nuclear Power and Propulsion, Albuquerque, NM, 1992.

Bents, D.J.: Small Stirling Dynamic Isotope Power System for Robotic Space Missions, NASA TM-105785, prepared for the Nuclear Technologies for Space Exploration Conference, Jackson Hole, WY, 1992.

Bloomfield, H.S.: A Reliability and Mass Perspective of SP-100 Stirling Cycle Lunar-Base Powerplant Designs, NASA TM-103736, 1991.

Harty, R.B. and Durand, R.E.: Lunar Electric Power Systems Utilizing the SP-100 Reactor Coupled to Dynamic Conversion Systems [Final Report], NASA CR-191023, 1993.

Hoang, D., Ludwigs, S., Schmitz, P., and Wright, J.: Mars Sample Return Power Supply [Final Report], NASA CR-184708, 1988.

Littman, F.D.: Power System Commonality Study [Final Report], NASA CR-190765, 1992.

Marshall, A.C. and McKissock, B.: Scaling Study for SP-100 Reactor Technology, NASA TM-897140, SAND-89-1635C, prepared for the 7th Symposium on Space Nuclear Power Systems, Albuquerque, NM, 1990.

Mason, L.S., Bloomfield, H.S., and Hainley, D.C.: SP-100 Power System Conceptual Design for Lunar Base Applications, NASA TM-102090, prepared for the 6th Symposium on Space Nuclear Power Systems, Albuquerque, NM, 1989.

McComas, T.J. and Dugan, E.T.: Thermal Analysis of Conceptual Designs for GPHS/FPSE Power Systems of 250 We and 500 We, NASA CR-187145, 1991.

Schmitz, P.C. and Mason, L.S.: Space Reactor/Stirling Cycle Systems for High Power Application, NASA TM-103698, prepared for the 8th Symposium on Space Nuclear Power Systems, Albuquerque, NM, 1991.

Schmitz, P.C., Kenny, B.H., and Fulmer, C.R.: Preliminary Design of a Mobile Lunar Power Supply, NASA TM-104471, prepared for the 26th Intersociety Energy Conversion Engineering Conference, Boston, MA, 1991.

Stofan, E.R., Dudenhoefer, J.E., et al: Venus Interior Structure Mission (VISM): Establishing a Seismic Network on Venus, Workshop on Advanced Technologies for Planetary Instruments, Part 1, pp. 23-24, 1993.

MTI Reports

Brown, A.T.: Space Power Demonstrator Engine, Phase I Final Report, NASA CR-179555, 1987.

Dhar, M., Jones, D., Huang, S., and Rauch, J.: Design and Performance of a 25-kWe Free-Piston Stirling Space Power Demonstrator Engine, Proceedings of the 22nd Intersociety Energy Engineering Conference, vol. 1, pp. 133-137, held in Philadelphia, PA, 1987.

Dhar, M., Rauch, J., Huang, S., and Bolton, R.: Space Power Demonstration Engine Linear Alternator Dynamometer Test Results, Proceedings of the 24th Intersociety Energy Conversion Engineering Conference, vol. 2, pp. 1103-1107, held in Washington, D.C., 1989.

Dochat, G.R.: Stirling Space Power Demonstrator Engine Test/Analytical Comparison, 37th International Astronautical Congress, Innsbruck, Austria, vol. 15, pp.341-346, 1986.

Dochat, G.R. and Dhar, M.: Free-Piston Space Stirling Technology Program, Proceedings of the 24th Intersociety Energy Conversion Engineering Conference, vol. 2, pp. 849-854, held in Washington, D.C., 1989.

Dochat, G.R.: Free-Piston Space Stirling Technology Program - An Update, Proceedings of the 25th Intersociety Energy Conversion Engineering Conference, vol. 5, pp. 219-223, held in Reno, NV, 1990.

Dochat, G. and Dhar, M.: Free-Piston Stirling Component Test Power Converter, Proceedings of the 26th Intersociety Energy Conversion Engineering Conference, vol. 5, pp. 239-244, held in Boston, MA, 1991.

Dochat, G.R.: Free-Piston Stirling Engine System Considerations for Various Space Power Applications, Proceedings of the 8th Symposium on Space Nuclear Power Systems, pt. 2, pp. 598a-604a, held in Albuquerque, NM, 1991.

Dochat, G.R.: Free-Piston Stirling Component Test Power Converter Test Results and Potential Stirling Applications, Proceedings of the 27th Intersociety Energy Conversion Engineering Conference, vol. 2, pp. 2.225-2.231, held in San Diego, CA, 1992.

Dochat, G.: SPDE/SPRE Final Summary Report, NASA CR-187086, 1993.

Huang, S.C.: HFAST, A Harmonic Analysis Program for Stirling Cycles, Proceedings of the 27th Intersociety Energy Conversion Engineering Conference, vol. 5, pp. 5.47-5.52, held in San Diego, CA, 1992.

Jones, D.: Space Power Free-Piston Stirling Engine Scaling Study, NASA CR-182218, 1989.

Rauch, J. and Dochat, G.: Free-Piston Stirling Engine/Linear Alternator 1000-Hour Endurance Test, NASA CR-174771, DOE/NASA/0333-1, 1985.

Rauch, J.S., Bolton, R.J., and Short, H.F.: SPRE Alternator Dynamometer Test Report, NASA CR-182251, MTI 89TR15, 1990.

Spelter, S. and Dhar, M.: Space Power Research Engine Power Piston Hydrodynamic Bearing Technology Development, NASA CR-182136, 1989.

Walak, S.E., Cronin, M.J., and Grobstein, T.: Heat Pipe Fatigue Test Specimen: Metallurgical Evaluation [Topical Report, Oct. 1990-1991], NASA CR-189120, 1992.

Miscellaneous

Dudenhoefer, J.E., Cairelli, J.E., Schreiber, J.G., Wong, W.A., Thieme, L.G., Tew, R.C., Geng, S.M., Bloomfield, H.S., Alger, D.A., Rauch, J.S., and Overholt, D.M.: Chapter "Dynamic Power Conversion Systems for Space Nuclear Power," A Critical Review of Space Nuclear Power and Propulsion—1984-1993; M.S. El-Genk, Editor; American Institute of Physics, 1994.

Penswick, L.B.: 1050 K Stirling Space Engine Design, NASA CR-182149, 1988.

Penswick, L.B., Beale, W.T., and Wood, J.G.: Free-Piston Stirling Engine Conceptual Design and Technologies for Space Power, Phase I Final Report, NASA CR-182168, 1990.

Ross, B. and Dudenhoefer, J.E.: Stirling Machine Operating Experience, NASA TM-104487, prepared for the 26th Intersociety of Energy Conversion Engineering Conference, Boston, MA, 1991.

Component Technology - General

Alger, D.L.: Component Improvement of Free-Piston Stirling Engine Key Technology for Space Power, NASA TM-100950, 1988.

Thieme, L.G.: Component Technology for Stirling Power Converters, NASA TM-104387, Proceedings of the 26th Intersociety Energy Conversion Engineering Conference, vol. 5, pp. 223-228, held in Boston, MA, 1991.

Thieme, L.G. and Swec D.M.: Summary of the NASA Lewis Component Technology Program for Stirling Power Converters, NASA TM-105640, 1992.

Thieme, L.G. and Swec, D.M.: Overview of the NASA Lewis Component Technology Program for Stirling Power Converters, Proceedings of the 27th Intersociety Energy Conversion Engineering Conference, vol. 5, pp. 5.283-5.288, held in San Diego, CA, 1992.

Linear Alternators/Magnets

Corey, J.A. and Yarr, G.A.: Hots to Watts: The FPSE Linear Alternator System Re-Invented, Proceedings of the 27th Intersociety Energy Conversion Engineering Conference, vol. 5, pp. 5.289-5.294, held in San Diego, CA, 1992.

Holliday, J.C.: Advanced Analysis Technique for the Evaluation of Linear Alternators and Linear Motors, NASA CR-198434, 1995.

Nasar, S.A. and Chen, C.: Study of Free-Piston Stirling Engine Driven Linear Alternators [Final Report], NASA CR-181425, 1987.

Niedra, J.M. and Overton, E.: 23 To 300 C Demagnetization Resistance of Samarium-Cobalt Permanent Magnets, NASA TP-3119, 1991.

Niedra, J.M. and Schwarze, G.E.: Makeup and Uses of a Basic Magnet Laboratory for Characterizing High-Temperature Permanent Magnets, NASA TM-104508, prepared for the First International High Temperature Electronics Conference, Albuquerque, NM, 1991.

Niedra, J.M.: M-H Characteristics and Demagnetization Resistance of Samarium-Cobalt Permanent Magnets to 300 C, NASA CR-189194, Proceedings of the 27th Intersociety Energy Conversion Engineering Conference, vol. 5, pp. 5.303-5.308, held in San Diego, CA, 1992.

Niedra, J.M.: Lightweight Linear Alternators With and Without Capacitive Tuning, NASA CR-185273, 1993.

Niedra, J.M.: Comparative M-H Characteristics of 1-5 and 2-17 Type Samarium-Cobalt Permanent Magnets to 300 C, NASA CR-194440, 1994.

Materials, Joining, and Structural Analysis

Abdul-Aziz, A., Bartolotta, P., Tong, M., and Allen, G.: An Experimental and Analytical Investigation of Stirling Space Power Convertor Heater Head, NASA TM-107013, 1995.

Baggenstoss, W. and Mittendorf, D.: Materials Technology for Stirling Space Power Convertors, NASA CR-189102, 1992.

Halford, G.R. and Bartolotta, P.A.: Stirling Engine: Available Tools for Long-Life Assessment, NASA TM-103660, prepared for the 8th Symposium on Space Nuclear Power Systems, Albuquerque, NM, 1991.

Kalinowski, J.M.: Weldability of a Nickel-Based Superalloy [Final Report], NASA CR-195376, 1994.

Mittendorf, D.L. and Baggenstoss, W.G.: Transient Liquid Phase Diffusion Bonding for Stirling Engine Application, Proceedings of the 25th Intersociety Energy Conversion Engineering Conference, vol. 5, pp. 231-236, held in Reno, NV, 1990.

Mittendorf, D.L. and Baggenstoss, W.G.: Transient Liquid Phase Diffusion Bonding of Udimet 720 for Stirling Power Converter Applications, Proceedings of the 27th Intersociety Energy Conversion Engineering Conference, vol. 5, pp. 5.393-5.397, held in San Diego, CA, 1992.

Park, J.: Creep Rupture Data Analysis by Association with a Large Database on Numerous Materials Tested to Long Times, Ph. D. Thesis, Case Western Reserve University, 1993.

Scheuermann, C.M., Moore, T.J., and Wheeler, D.R.: Preliminary Study of Niobium Alloy Contamination by Transport Through Helium, NASA TM-88952, DOE/NASA/16310-2, 1987.

Scheuermann, C.M., Dreshfield, R.L., Gaydosh, D.J., Kiser, J.D., Mackay, R.A., McDaniels, D.L., Petrasek, D.W., Vannucci, R.D., Bowles, K.J., and Watson, G.K.: Materials Technology Assessment for a 1050 K Stirling Space Engine Design, NASA TM-101342, 1988.

Sliney, H.E., Lukaszewicz, V., and Dellacorte, C.: The Tribology of PS212 Coatings and PM212 Composites for the Lubrication of Titanium 6Al-4V Components of a Stirling Engine Space Power System, NASA TM-106462, 1994.

Tong, M.T., Bartolotta, P.A., Halford, G.R., and Freed, A.D.: Stirling Engine - Approach for Long-Term Durability Assessment, Proceedings of the 27th Intersociety Energy Conversion Engineering Conference, vol. 5, pp. 5.209-5.214, held in San Diego, CA, 1992.

Heat Exchangers and Heat Pipes

Alger, D.L.: Heat-Pipe Heat Transport System for the Stirling Space Power Converter (SSPC), NASA CR-191065, Proceedings of the 27th Intersociety Energy Conversion Engineering Conference, vol. 5, pp. 5.455-5.459, held in San Diego, CA, 1992.

Dussinger, P.M.: Insoluble Coatings for Stirling Engine Heat Pipe Condenser Surfaces, NASA CR-191188, 1993.

Dussinger, P.M. and Lindemuth, J.E.: Insoluble Coatings for Stirling Engine Heat Pipe Condenser Surfaces, Phase II Final Report, NASA CR-202323, 1997.

Hull, D.R., Alger, D.L., Moore, T.J., and Scheuermann, C.M.: Fatigue Failure of Regenerator Screens in a High Frequency Stirling Engine, NASA TM-88974, 1987.

Knowles, T.R.: Composite Matrix Regenerator for Stirling Engines [Final Report], NASA CR-202322, 1997.

Moore, T.J., Cairelli, J.E., and Khalili, K.: Failure Analysis of a Stirling Engine Heat Pipe, NASA TM-101418, 1989.

Noble, J.E., Hickman, G.L., and Grobstein, T.: Alkali Metal Compatibility Testing of Candidate Heater Head Materials for a Stirling Engine Heat Transport System, Proceedings of the 26th Intersociety Energy Conversion Engineering Conference, vol. 6, pp. 166-170, held in Boston, MA, 1991.

Oldson, J.C., Knowles, T.R., and Rauch, J.: Pulsed Single-Blow Regenerator Testing, Proceedings of the 27th Intersociety Energy Conversion Engineering Conference, vol. 5, pp. 5.399-5.403, held in San Diego, CA, 1992.

Schmitz, P., Tower, L., Dawson, R., Blue, B., and Dunn, P.: Preliminary SP-100/Stirling Heat Exchanger Designs, NASA TM-106444, prepared for the 11th (1994)Symposium on Space Nuclear Power and Propulsion, Albuquerque, NM, 1993.

Schmitz, P., Tower, L., Dawson, R., Blue, B., and Dunn, P.: Preliminary Design of a SP-100/Stirling Radiatively Coupled Heat Exchanger, NASA TM-107069, 1995.

Schreiber, J.G.: The Design and Fabrication of a Stirling Engine Heat Exchanger Module With an Integral Heat Pipe, NASA TM-101296, 1988.

Schreiber, J.G.: Initial Characterization of a Modular Heat Exchanger with an Integral Heat Pipe, NASA TM-102097, prepared for the 24th Intersociety Energy Conversion Engineering Conference, Washington, D.C., 1989.

Skupinski, R.C., Tower, L.K., Madi, F.J., and Brusk, K.D.:Test Results of Stirling Engine Utilizing a Modular Heat Exchanger with an Integral Heat Pipe, NASA TM-105883, 1993.

Tower, L.K., Baker, K.W., and Marks, T.S.: NASA Lewis Steady-State Heat Pipe Code Users Manual, NASA TM-105161, 1992.

Tower, L.K.: Simple Analysis of Nickel Transport in Heat Pipes of Stirling Engine Power Conversion Systems, Proceedings of the 27th Intersociety Energy Conversion Engineering Conference, vol. 5, pp. 5.461-5.466, held in San Diego, CA, 1992.

Bearings

Curwen, P.W., Fleming, D.P., Rao, D.K., and Wilson, D.S.: Magnetic Bearings for Free-Piston Stirling Engines, NASA TM-105730, Proceedings of the 27th Intersociety Energy Conversion Engineering Conference, vol. 5, pp. 5.381-5.386, held in San Diego, CA, 1992.

Curwen, P.W., Rao, D.K., and Wilson, D.S.: A Feasibility Assessment of Magnetic Bearings for Free-Piston Stirling Space Power Converters [Final Report, July 1990 - Aug. 1991], NASA CR-189135, 1992.

Dimofte, F. and Liebler, K.: Free-Piston Stirling Converter Dynamic Gas Bearings, Proceedings of the 27th Intersociety Energy Conversion Engineering Conference, vol. 5, pp. 5.387-5.392, held in San Diego, CA, 1992.

Load Interaction and Dynamic Analysis

Gordon, L.B.: Loss Terms in Free-Piston Stirling Engine Models [Final Technical Report], NASA CR-189840, 1992.

Kankam, M.D. and Rauch, J.S.: Comparative Survey of Dynamic Analyses of Free-Piston Stirling Engines, NASA TM-104491, Proceedings of the 26th Intersociety Energy Conversion Engineering Conference, vol. 5, pp. 314-319, held in Boston, MA, 1991.

Kankam, M.D., Rauch, J.S., and Santiago, W.: Dynamic Analysis of Free-Piston Stirling Engine/Linear Alternator-Load System - Experimentally Validated, NASA TM-106034, Proceedings of the 27th Intersociety Energy Conversion Engineering Conference, vol. 5, pp. 5.315-5.323, held in San Diego, CA, 1992.

Kankam, M.D. and Rauch, J.S.: Controllability of Free-Piston Stirling Engine/Linear Alternator Driving a Dynamic Load, NASA TM-106497, prepared for the 28th (1993)Intersociety Energy Conversion Engineering Conference, Atlanta, GA, 1994.

Kankam, M.D. and Rauch, J.S.: Transient and Steady-State Performance of Space Power Research Engine with Resistive/Motor Loads, Proceedings of the 31st Intersociety Energy Conversion Engineering Conference, vol. 2, pp. 1277-1282, held in Washington, D.C., 1996.

Niedra, J.M.: Analog Synthesized Fast-Variable Linear Load, NASA CR-187155, 1991.

Rauch, J.S., Kankam, M.D., Santiago, W., and Madi, F.J.: A Free-Piston Stirling Engine/Linear Alternator Controls and Load Interaction Test Facility, NASA TM-105825, Proceedings of the 27th Intersociety Energy Conversion Engineering Conference, vol. 5, pp. 5.309-5.314, held in San Diego, CA, 1992.

Rauch, J.S. and Kankam, M.D.: Transient and Steady-State Tests of the Space Power Research Engine with Resistive and Motor Loads, NASA TM-106832, 1995.

NASA-Lewis Testing

Cairelli, J.E.: SPRE I Free-Piston Stirling Engine Testing at NASA Lewis Research Center, NASA TM-100241, Proceedings of the Tenth Annual ASME Solar Energy Conference, pp. 375-382, held in Denver, CO, 1988.

Cairelli, J.E., Geng, S.M., and Skupinski, R.C.: Results from Baseline Tests of the SPRE 1 and Comparison with Code Model Predictions, NASA TM-102044, prepared for the 24th Intersociety Energy Conversion Engineering Conference, Washington, D.C., 1989.

Cairelli, J.E., Swec, D.M., Skupinski, R.C., and Rauch, J.S.: Update on Results of SPRE Testing at NASA, Proceedings of the 25th Intersociety Energy Conversion Engineering Conference, Vol. 5, pp. 237-244, held in Reno, NV, 1990.

Cairelli, J.E., Swec, D.M., Wong, W.W., Doeberling, T.J., and Madi, F.J.: Update on Results of SPRE Testing at NASA Lewis, NASA TM-104425, Proceedings of the 26th Intersociety Energy Conversion Engineering Conference, vol. 5, pp. 217-222, held in Boston, MA, 1991.

Miller, E.L. and Dudenhoefer, J.E.: On the Dynamic Response of Pressure Transmission Lines in the Research of Helium-Charged Free Piston Stirling Engines, NASA TM-102121, Proceedings of the 24th Intersociety Energy Conversion Engineering Conference, vol. 5, pp. 2243-2248, held in Washington, D.C., 1989.

Schreiber, J.G., Geng, S.M., and Lorenz, G.V.: RE-1000 Free-Piston Stirling Engine Sensitivity Test Results [Final Report], NASA TM-88846, DOE/NASA/1005-11, 1986.

Wong, W.A., Cairelli, J.E., Swec, D.M., Doeberling, T.J., Lakatos, T.F., and Madi, F.J.: NASA Lewis Stirling SPRE Testing and Analysis with Reduced Number of Cooler Tubes, NASA TM-105767, Proceedings of the 27th Intersociety Energy Conversion Engineering Conference, vol. 5, pp. 5.443-5.448, held in San Diego, CA, 1992.

Loss Understanding - General

Tew, Jr., R.C.: Overview of Heat Transfer and Fluid Flow Problem Areas Encountered in Stirling Engine Modeling, NASA TM-100131, 1988.

Tew, R.C., Thieme, L.G., and Dudenhoefer, J.E.: Recent Stirling Engine Loss-Understanding Results, NASA TM-103122, prepared for the 25th Intersociety Energy Conversion Engineering Conference, Reno, NV, 1990.

Tew, R.C. and Geng, S.M.: Overview of NASA Supported Stirling Thermodynamic Loss Research, NASA TM-105690, Proceedings of the 27th Intersociety Energy Conversion Engineering Conference, vol. 5, pp. 5.489-5.494, held in San Diego, CA, 1992.

Oscillating Flow Pressure Drop and Heat Transfer Loss Understanding - Experimental

Dean, C.E., Grassmyer, W.A., Smith, J.L., Jr., Lienhard, J.H. V: Experiments on Heat Transfer under Conditions of Oscillating Pressure and Flow, Presented at the 1993 Winter Annual Meeting of the ASME (Session on Heat Transfer in Reciprocating Machinery), 1993.

Dean, C.E.: Establishing Baseline Data for an Experimental Apparatus that Measures Heat Transfer under Conditions of Oscillating Pressure and Flow, NASA CR-193772, Massachusetts Institute of Technology, Master's Thesis, 1993.

Friedman, G.T.: Experimental Investigation of Fluid Mechanics in Oscillating Flow: A Detailed Study at a Single Operation Point, Master's Thesis, U. of Minnesota, 1991.

Gedeon, D. and Wood, J.G.: Oscillating-Flow Regenerator Test Rig: Woven Screen and Metal Felt Results [Topical Status Report, 1 Apr. 1991 - 30 June 1992], NASA CR-190689, 1992.

Gedeon, D. and Wood, J.G.: Oscillating-Flow Regenerator Test Rig: Hardware and Theory With Derived Correlations for Screens and Felts, NASA CR-198442, 1996.

Kafka, B.C. and Kornhauser, A.A.: Measurements of In-Cylinder Heat Transfer with Inflow-Produced Turbulence, Proceedings of the 29th Intersociety Energy Conversion Engineering Conference, pt. 4, pp. 1890-1895, held in Monterey, CA, 1994.

Koester, G., Howell, S., Wood, G., Miller, E., and Gedeon, D.: Oscillating Flow Loss Test Results in Stirling Engine Heat Exchangers, NASA CR-182288, 1990.

Kornhauser, A.A. and Smith, J.L. Jr.: The Effects of Heat Transfer on Gas Spring Performance, Proceedings of the 26th Intersociety Energy Conversion Engineering Conference, vol. 5, pp. 180-185, held in Boston, MA, 1991.

Kornhauser, A.A., Kafka, B.C., Finkbeiner, D.L., and Cantelmi, F.C.: Heat Transfer Measurements for Stirling Machine Cylinders, NASA CR-197128, Virginia Polytechnic Institute and State University, Final Report for NASA Grant NAG3-1285, 1994.

M. I. T. Stirling Cycle Heat Transfer Apparatus", Proceedings of the 27th Intersociety Energy Conversion Engineering Conference, vol. 5, pp. 5.509-5.516, held in San Diego, CA, 1992.

Qui, S. and Simon, T.W.: Visualization of Entry Flow Separation for Oscillating Flow in Tubes, Proceedings of the 27th Intersociety Energy Conversion Engineering Conference, vol. 5, pp. 5.517-5.521, held in San Diego, CA, 1992.

Qui, S. and Simon, T.W.: Measurements of Heat Transfer and Fluid Mechanics within an Oscillatory Flow in a Pipe, prepared for presentation at the Winter Annual Meeting of the ASME, 1994.

Seume, J.R. and Simon, T.W.: Oscillating Flow in Stirling Engine Heat Exchangers, Proceedings of the 21st Intersociety Energy Conversion Engineering Conference, vol.1, pp. 533-538, held in San Diego, CA, 1986.

Seume, J. R. and Simon, T.W.: Flow Oscillation Effects in Tubes and Porous Material: Unresolved Issues, In: Morel, T.E., Dudenhoefer, J.E., Uxkan, T., Singh, P.J. (eds.): Fluid Flow and Heat Transfer in Reciprocating Machinery. Proceedings, ASME Winter Annual Meeting, held in Boston, MA, FED-Vol. 62, HTD-VOL. 93, pp. 55-62, 1987.

Seume, J. R., Goldberg, L.F., and Simon, T.W.: Description of an Oscillating Flow Test Program, Proceedings of the 22nd Intersociety Energy Conversion Engineering Conference, vol.4, pp. 1753-1758, held in Philadelphia, PA, 1987.

Seume, J. R. and Simon, T.W.: Effect of Transition on Oscillation Flow Losses in Stirling Engine Coolers and Heaters, Proceedings of the 23rd Intersociety Energy Conversion Engineering Conference, vol. 1, pp. 127-132, held in Denver, CO, 1988.

Seume, J. R.: An Experimental Investigation of Transition in Oscillating Pipe Flow, Ph. D. Thesis, U. of Minnesota, 1988.

Seume, J., Friedman, G., and Simon, T.W.: Fluid Mechanics Experiments in Oscillatory Flow, Volume I - Report, NASA CR-189127, 1992.

Seume, J., Friedman, G., and Simon, T.W.: Fluid Mechanics Experiments in Oscillatory Flow, Volume II - Tabulated Data, NASA CR-189128, 1992.

Simon, T.W. and Seume, J.R.: A Survey of Oscillating Flow in Stirling Engine Heat Exchangers, NASA CR-182108, 1988.

Simon, T.W., Ibrahim, M., Kannapareddy, M., Johnson, T., and Friedman, G.: Transition of Oscillatory Flow in Tubes: An Empirical Model for Application to Stirling Engines, Proceedings of the 27th Intersociety Energy Conversion Engineering Conference, vol. 5, pp. 5.495-5.502, held in San Diego, CA, 1992.

Smith, J.L. Jr., Lienhard, J.H., Tziranis, A.K., and Ho, Y.: Tziranis, A.K.: Temperature, Heat Flux, and Velocity Measurements in Oscillating Flows with Pressure Variations, Massachusetts Institute of Technology, Master's Thesis, 1992.

Wood, J.G., Miller, E.L., Gedeon, D.R., and Koester, G.E.: Description of an Oscillating Flow Pressure Drop Test Rig, NASA TM-100905, 1988.

Wood, J.G.: Oscillating-Flow Loss Test Results in Rectangular Heat Exchanger Passages, NASA CR-185297, 1991.

Oscillating Flow Pressure Drop and Heat Transfer Loss Understanding - Analysis

Ahn, K.H. and Ibrahim, M.B.: A 2-D Oscillating Flow Analysis in Stirling Engine Heat Exchangers, Joint ASME-JSME Fluids Engineering Conference, FED-Vol. 113, pp. 159-164, Portland, OR, 1991.

Ahn, K.H. and Ibrahim, M.B.: Laminar/Turbulent Oscillating Flow in Circular Pipes, International Journal of Heat and Fluid Flow, vol. 13, pp. 340-346, 1992.

Bauer, C.: Low-Reynolds Number Kappa-Epsilon and Empirical Transition Models for Oscillatory Pipe Flow and Heat Transfer, NASA TM-109785, Master's Thesis, Cleveland State University, 1993.

Gedeon, D.: Computational Techniques for the Two-Dimensional Gasdynamic Equations in Stirling Engine Regenerators and Associated Manifolds," Proceedings of the 20th Intersociety Energy Conversion Engineering Conference, pp. 3.354-3.359, held in Miami Beach, FL, 1985.

Gedeon, D.: Manifest: A Computer Program for 2-D Flow Modeling in Stirling Machines, NASA CR-182290, 1989.

Gedeon, D.: Advection-Driven vs. Compression-Driven Heat Transfer, prepared for NASA Lewis Research Center under Purchase Order C-23433, Task 2, 1992.

Goldberg, L.F.: The Simulated Systems Impact of Two-Dimensional Oscillating Flows In a Stirling Machine Heat Exchanger, In: Morel, T.E., Dudenhoefer, J.E., Uxkan, T., Singh, P.J. (eds.): Fluid Flow and Heat Transfer in Reciprocating Machinery. Proceedings, ASME Winter Annual Meeting, held in Boston, MA, FED-Vol. 62, HTD-VOL. 93, pp. 63-68, 1987.

Hashim, W.: Effect of Flow Oscillations on Friction Factor and Heat Transfer Coefficient in a Channel with Sudden Change in Cross Section, Master's Thesis, Cleveland State University, 1992.

Ibrahim, M.B., Tew, R.C., and Dudenhoefer, J.E.: Two-Dimensional Numerical Simulation of a Stirling Engine Heat Exchanger, NASA TM-102057, Proceedings of the 24th Intersociety Energy Conversion Engineering Conference, vol. 6, pp. 2795-2802, held in Washington, D.C., 1989.

Ibrahim, M.B., Tew, R.C., and Dudenhoefer, J.E.: Further Two-Dimensional Code Development for Stirling Space Engine Components, Proceedings of the 25th Intersociety Energy Conversion Engineering Conference, vol. 6, pp. 329-335, held in Reno, NV, 1990.

Ibrahim, M.B. and Kwan, C.F.: Prediction for Hydrodynamically and Thermally Developing Pulsatile Flows, Proceedings of the 4th International Symposium on Transport Phenomena in Heat Transfer, vol. 4, pp. 1570-1581, Sydney, Australia, 1991.

Ibrahim, M.B., Kannapareddy, M., Tew, R.C., and Dudenhoefer, J.E.: Instantaneous Heat Transfer Coefficient Based Upon Two-Dimensional Analyses for Stirling Space Engine Components, Proceedings of the 26th Intersociety Energy Conversion Engineering Conference, vol. 6, pp. 149-159, held in Boston, MA, 1991.

Ibrahim, M.B., Mankbadi, R.R., and Ahn, K.: Evaluation of Turbulence Models in Unsteady Flows, prepared for the 4th International Conference for Fluid Mechanics, Alexandria, Egypt, 1992.

Ibrahim, M.B. and Hashim, W.: Oscillating Flow in Channels with Sudden Change in Cross Section, (submitted for publication to Computers and Fluids, An International Journal), 1992.

Ibrahim, M.B., Hashim, W., Tew, R.C., and Dudenhoefer, J.E.: Heat Transfer in Oscillating Flows with Sudden Change in Cross Section, NASA TM-105692, Proceedings of the 27th Intersociety Energy Conversion Engineering Conference, vol. 5, pp. 5.503-5.508, held in San Diego, CA, 1992.

Ibrahim, M. and Hashim, W.: Oscillating Flow and Heat Transfer in a Channel with Sudden Cross Section Change [Final Report, 2 Jan. 1989 - 30 June 1993], NASA CR-199358, 1993.

Ibrahim, M. and Kannapareddy, M.: Computational Heat Transfer Analysis for Oscillatory Channel Flows, NASA CR-199238, 1993.

Ibrahim, M., Bauer, C., Simon, T.W., and Qui, S.: Modeling of Oscillatory Laminar, Transitional, and Turbulent Channel Flows in Heat Transfer, 10th International Heat Transfer Conference, Brighton, England, 1994.

Jeong, E.S.: Heat Transfer with Oscillating Pressure in Reciprocating Machinery, Ph. D. Thesis, Massachusetts Institute of Technology, 1991.

Kannapareddy, M.: Numerical Thermal Analysis of Heat Exchangers for the Stirling Engine Application, NASA CR-199120, 1995.

Koehler, W.J.: On the Heat Transfer in Oscillatory Flow - A Numerical Study, Ph. D. Thesis, U. of Minnesota, 1990.

Koehler, W.J., Patankar, S.V., and Ibele, W.E.: Numerical Prediction of Turbulent Oscillating Flow and Associated Heat Transfer, NASA CR-187177, 1991.

Kornhauser, A.A.: Dynamic Modeling of Gas Springs, Proceedings of the 26th Intersociety Energy Conversion Engineering Conference, vol. 5, pp. 176-179, held in Boston, MA, 1991.

Kornhauser, A.A.: A Model of In-Cylinder Heat Transfer with Inflow-Produced Turbulence, Proceedings of the 27th Intersociety Energy Conversion Engineering Conference, vol. 5, pp. 5.523-5.528, held in San Diego, CA, 1992.

Kwan, C.: Compressibility Effects on Periodic Unsteady Flows, Master's Thesis, Cleveland State University, 1992.

Oseid, K.L.: Numerical Prediction of Turbulent Oscillating Flow and Heat Transfer in Pipes with Various End Geometries, NASA CR-198416, Ph. D. Thesis, U. of Minnesota, 1995.

Patankar, S.V., Koehler, W.J., and Ibele, W.E.: Numerical Prediction of Turbulent Oscillating Flow in a Circular Pipe, Proceedings of the 25th Intersociety Energy Conversion Engineering Conference, vol.5, pp. 398-406, held in Reno, NV, 1990.

Smith, J.L. Jr. and Romm, M.: Thermodynamic Loss at Component Interfaces in Stirling Cycles, Proceedings of the 27th Intersociety Energy Conversion Engineering Conference, vol. 5, pp. 5.529-5.532, held in San Diego, CA, 1992.

Stirling Cycle Analysis

Geng, S.M.: Calibration and Comparison of the NASA Lewis Free-Piston Stirling Engine Model Predictions with RE-1000 Test Data, NASA TM-89853, prepared for the 22nd Intersociety Energy Conversion Engineering Conference, Philadelphia, PA, 1987.

Geng, S.M. and Tew, R.C.: Comparison of GLIMPS and HFAST Stirling Engine Code Predictions with Experimental Data, NASA TM-105549, Proceedings of the 27th Intersociety Energy Conversion Engineering Conference, vol. 5, pp. 5.53-5.58, held in San Diego, CA, 1992.

Goldberg, L.F.: One- and Two-Dimensional Stirling Machine Simulation Using Experimentally Generated Reversing Flow Turbulence Models, NASA CR-185285, 1990.

Goldberg, L.F.: An Investigation of the Information Propagation and Entropy Transport Aspects of Stirling Machine Simulation, NASA CR 189143, 1992.

Hall, C.A. and Porsching, T.A.: Multidimensional Computer Simulation of Stirling Cycle Engines [Final Technical Report], NASA CR-190497, 1992.

Kalaani, L.K., Geng. S., and Ibrahim, M.B.: Stirling Engine Code Validation for RE-1000 Free-Piston Stirling Engine, First AIAA Mini-Symposium on Aerospace Technology in Northern Ohio, Cleveland State University, Cleveland, OH, 1990.

REPORT DOCUMENTATION PAGE

Form Approved
OMB No. 0704-0188

1. AGENCY USE ONLY (*Leave blank*)

2. REPORT DATE
August 1999

3. REPORT TYPE AND DATES COVERED
Final Contractor Report

4. TITLE AND SUBTITLE
Stirling Space Engine Program
Volume 1—Final Report

5. FUNDING NUMBERS
WU–632–1A–1G–00
NAS3–25463

6. AUTHOR(S)
Manmohan Dhar

7. PERFORMING ORGANIZATION NAME(S) AND ADDRESS(ES)
Mechanical Technology Incorporated
968 Albany-Shaker Road
Latham, New York 12110

8. PERFORMING ORGANIZATION REPORT NUMBER
E–11751–1

9. SPONSORING/MONITORING AGENCY NAME(S) AND ADDRESS(ES)
National Aeronautics and Space Administration
John H. Glenn Research Center at Lewis Field
Cleveland, Ohio 44135–3191

10. SPONSORING/MONITORING AGENCY REPORT NUMBER
NASA CR—1999-209164-VOL1
MTI 97TR21

11. SUPPLEMENTARY NOTES
Technical Agent, D. Alger, Sverdrup Technology, Inc. Project Manager, James E. Dudenhoefer, Power and On-Board Propulsion Technology Division, NASA Glenn Research Center, organization code 5440, (216) 433–6140.

12a. DISTRIBUTION/AVAILABILITY STATEMENT
Unclassified - Unlimited
Subject Categories: 20 and 44

This publication is available from the NASA Center for AeroSpace Information, (301) 621–0390.

12b. DISTRIBUTION CODE

13. ABSTRACT (***Maximum 200 words***)
The objective of this program was to develop the technology necessary for operating Stirling power converters in a space environment and to demonstrate this technology in full-scale engine tests. Hardware development focused on the Component Test Power Converter (CTPC), a single cylinder, 12.5-kWe engine. Design parameters for the CTPC were 150 bar operating pressure, 70 Hz frequency, and hot- and cold-end temperatures of 1050 K and 525 K, respectively. The CTPC was also designed for integration with an annular sodium heat pipe at the hot end, which incorporated a unique "Starfish" heater head that eliminated highly stressed brazed or weld joints exposed to liquid metal and used a shaped-tubed electrochemical milling process to achieve precise positional tolerances. Selection of materials that could withstand high operating temperatures with long life were another focus. Significant progress was made in the heater head (Udimet 700 and Inconel 718 and a sodium-filled heat pipe); the alternator (polyimide-coated wire with polyimide adhesive between turns and a polyimide-impregnated fiberglass overwrap and samarium cobalt magnets); and the hydrostatic gas bearings (carbon graphite and aluminum oxide for wear couple surfaces). Tests on the CTPC were performed in three phases: cold end testing (525 K), engine testing with slot radiant heaters, and integrated heat pipe engine system testing. Each test phase was successful, with the integrated engine system demonstrating a power level of 12.5 kWe and an overall efficiency of 22% in its maiden test. A 1500-hour endurance test was then successfully completed. These results indicate the significant achievements made by this program that demonstrate the viability of Stirling engine technology for space applications.

14. SUBJECT TERMS
Free-Piston Stirling Engines; Stirling Space Power Systems; Nuclear electric power generation

15. NUMBER OF PAGES
202

16. PRICE CODE
A10

17. SECURITY CLASSIFICATION OF REPORT	18. SECURITY CLASSIFICATION OF THIS PAGE	19. SECURITY CLASSIFICATION OF ABSTRACT	20. LIMITATION OF ABSTRACT
Unclassified	Unclassified	Unclassified	